2D Transit Dosimetry Using Electronic Portal Imaging Device

Yun Inn Tan

Submitted in fulfilment of the requirements for the
Degree of Doctor of Philosophy

College of Medical, Veterinary and Life Sciences
Department of Clinical Physics

2016

Abstract

The amorphous silicon electronic portal imaging device (a-Si EPID) was originally designed for positional verification in radiotherapy. Several feature of the a-Si EPID, such as the high-resolution detector array and ease of operation, have made this imaging device an attractive tool for dose measurements. The main challenge with a-Si EPID dosimetry is the deviation in scatter and dose response characteristics from a water-equivalent detector that makes the conversion of EPID signal to dose not straightforward.

The aim of this thesis is to develop a model to perform 2D transit dosimetry for patient-specific treatment verification with a-Si EPID. The transit model can be used for both pre-treatment and actual treatment verification to ensure safety in different stages of the radiotherapy process.

The model was based on a quadratic equation that relates the reduction in radiation intensity, represented by the ratio of exit to entrance dose, to the water-equivalent path length (EPL) of the attenuator. Coefficients in the quadratic equation were derived from a set of calibration dose planes measured for a reference beam with water phantoms of known thicknesses. Two sets of coefficients were derived separately from calibration dose planes measured with EPID and ionisation chamber (IC) in water. Consequently, with two sets of coefficients, the EPL of any attenuator can be calculated using either EPID measured dose planes or treatment planning system (TPS) computed dose planes for the treatment field to be verified. The calculated EPL, which is a property of the attenuator and independent of the dosimeter, was used to link the different dosimetry systems and provide a two-way relationship for either: (Path 1) reconstruction of in-phantom or in-vivo dose from EPID measured dose planes, for comparison with TPS planned dose; or (Path 2) prediction of EPID transit dose from TPS computed dose planes, for comparison with EPID measurement during treatment.

The developed model was first tested with homogeneous and heterogeneous slab phantoms using open, enhanced dynamic wedge (EDW) and intensity modulated radiation therapy (IMRT) fields. Results showed that the model could accurately

detect deviation between delivered and planned doses. Further evaluation with an anthropomorphic pelvic phantom and 65 test fields (open, 3D conformal, EDW, IMRT) at different gantry angles showed a mean gamma pass rate (4%/4mm criterion) of 97.6% (range: 90.0% to 100%) for in-phantom exit dose comparisons (Path 1) and 97.1% (range: 92.9% to 99.8%) for EPID transit dose comparisons (Path 2). In addition, the methods in Path 1 were expanded to reconstruct dose at other levels besides the exit level. In-phantom isocentre dose comparisons resulted in a mean gamma pass rate of 98.2% (range: 91.7% to 100%).

Finally, clinical feasibility of the EPID transit dosimetry model was demonstrated for three patients (11 3D conformal fields, 18 verifications) who were undergoing radiotherapy treatment at the pelvic region. Gamma analyses with 5%/5mm criterion resulted in a mean pass rate of 97.0% (range: 92.4% to 99.6%) and 98.6% (range: 96.1% to 100%) for in-vivo comparisons at the exit level and isocentre level respectively (Path 1). The mean gamma pass rate for EPID transit dose comparisons (Path 2) was 95.6% (range: 90.7% to 99.9%).

In conclusion, the 2D EPID transit dosimetry model developed in this thesis has been proven to be valid and suitable for clinical implementation. The model is: (1) practical, involving only general measurements and does not require any modification to the EPID panel, (2) generic, with the methods applicable to all a-Si EPID and TPS regardless of manufacturer and (3) flexible, allowing users to verify the accuracy of treatment delivery either at multiple planes in-vivo or at the EPID level. These are important characteristics to encourage widespread implementation of EPID transit dosimetry in different clinical setting for safer radiotherapy.

Table of Contents

List of tables

List of figures

Acknowledgements

First and foremost, I would like to express my deep gratitude to Professor Alex Elliott for giving me the opportunity to accomplish, first, the MSc and then, this PhD. Thank you for always believing in me. I will be forever grateful for your support and unwavering commitment in ensuring the best educational journey a student could ever hope for. Also thank you for your patience and dedication in reviewing (many times!) manuscripts and drafts of this thesis.

I am also deeply appreciative of the support and guidance provided by Martin Glegg. Thank you for always finding time from your busy schedule, to share your clinical experience in this research project. The meetings always leave me with a better understanding of the issue at hand.

This research project would not have been possible without Dr. Mohamed Metwaly, whose ideas have had a profound influence on this work. Thank you for showing me how to be a good researcher. More than that, thank you for showing me that everything is possible. I am so lucky to have you as a guiding light through this long and sometimes difficult journey. You have been a great inspiration.

I am indebted to Shàun Baggarley for accommodating to the special work arrangement, allowing me the time and space to complete this PhD. Thank you for being such a supportive boss. Not forgetting the amazing team of medical physicists in National University Cancer Institute, Singapore (NCIS): Poh Wee, Fahdil, Yuh Fun, Teh and Joan. Thank you for taking up more than your fair share of duties during my frequent absence from work.

Special thanks goes to Professor Jay Lu Jiade and Dr. Ivan Tham, past and present Head of Department of Radiation Oncology, NCIS, for their assurance and continuous support in promoting research work in the department. Thank you for opening doors and creating opportunities. It is a great honour to be part of this forward-looking and enthusiastic family.

I am equally thankful to all staff and friends from the Beatson West of Scotland Cancer Centre: Garry Currie, Head of Radiotherapy Physics, for granting me the permission to learn from many outstanding physicists in your department; Dr. Mark McJury, Consultant Clinical Scientist, for helping to clear the administrative hurdles; Dr. Kurian Oommen, for showing me how to be a good teacher; Magda Skikiewicz, Laura Hammond and Pamela Ocampo, for the laughter and great memories; Martin Ford, Kirsty Brown and Gillian McKee, for your generosity and kindness; Abdullah Abuhaimed, for your company on this arduous PhD journey. A sincere thank you also goes to many others, whose names are too many to list, for providing warmth in the cold Scottish weather.

I would also like to thank my sponsors, National University Health System (NUHS) and Ministry of Health (MOH), Singapore, for the Academic Medicine Development Award (AMDA). In our own ways, big and small, we make this nation extraordinary.

Last but not least, the biggest thank you goes to my parents, siblings and husband. To my parents and siblings, thank you for providing a safe environment so that the littlest one in the family can go out and explore the world with confidence. To my husband, thank you for putting up with the missing wife and for always cheering me on to reach for the stars.

Author's declaration

I declare that, except where explicit reference is made to the contribution of others, that this thesis is the result of my own work and has not been submitted for any other degree at the University of Glasgow or any other institution. Part of the Matlab code used in this thesis was based on the script written by Kavuma Awusi. The original code had been substantially re-developed and expanded to perform the functions described in this thesis, which were novel and different from the methods employed by Kavuma.

Signature: 

Printed name: Yun Inn Tan

Abbreviations

1D	One-dimensional
2D	Two-dimensional
3D	Three-dimensional
a-Si	Amorphous silicon
AAA	Analytical anisotropic algorithm
AgBr	Silver bromide
Al_2O_3	Aluminium oxide
AXB	AcurosXB
BCF	Backscatter correction factor
CBCT	Cone-beam computed tomography
CC	Compact chamber
CCD	Charge-coupled device
cGy	Centigray
CT	Computed tomography
d	Depth
D_{dmax}	Dose at depth of maximum dose
DICOM	Digital imaging and communications in medicine
d_{max}	Depth of maximum dose
DRR	Digitally reconstructed radiograph
DVH	Dose volume histogram
EDW	Enhanced dynamic wedge
EPID	Electronic portal imaging device
EPL	Equivalent path length
EPL_{rel}	Equivalent path length relative to water
FFF	Flattening filter free
FFT	Fast-fourier transform
fs	Field size
FSF	Field size correction factor
Gd_2O_2S	Gadolinium oxysulphide
GSTT	Golden segmented treatment table
Gy	Gray
HU	Hounsfield unit
IAEA	International atomic energy agency

IC	Ionisation chamber
ICRU	International commission on radiation units and measurements
IMRT	Intensity modulated radiation therapy
Inst.	Institution
ISQL	Inverse square law
KV	Kilovoltage
LiF	Lithium fluoride
linac	Linear accelerator
M	Exit
M0	Entrance
MC	Monte Carlo
MF	Modulation factor
MLC	Multi-leaf collimator
MOSFET	Metal oxide semiconductor field effect transistor
MU	Monitor unit
MV	Megavoltage
NRLS	National reporting and learning system
OAR	Organ at risk
OD	Optical density
OF	Output factor
OSLD	Optically stimulated luminescence detector
PBC	Pencil beam convolution
PDD	Percentage depth dose
PETD	Percentage exit thickness dose
PMT	Photomultiplier
PSDL	Primary standard dosimetry laboratory
PSRT	Patient safety in radiotherapy steering group
PT	Physical thickness
QA	Quality assurance
RTE	Radiotherapy error
SAD	Source to axis distance
SBRT	Stereotactic body radiotherapy
SD	Standard deviation
SiO_2	Silicon dioxide
SLIC	Scanning liquid-filled ionisation chamber

SRS	Stereotactic radiosurgery
SSD	Source to surface distance
Th	Thickness
TLD	Thermoluminescent detector
TMR	Tissue maximum ratio
TMR^t	Transit tissue maximum ratio
TPR	Tissue phantom ratio
TPS	Treatment planning system
UK	United Kingdom
VMAT	Volumetric modulated arc therapy
V_{TH}	Threshold voltage
W	Weighting
WF	Wedge factor
z	Atomic number

Chapter 1: General introduction

1.1 Aim of radiotherapy

The aim of radiotherapy is to deliver as much radiation dose as possible to a tumour site to kill cancerous cells, while limiting the damage to surrounding healthy tissues. This can be achieved: (1) biologically, through dose fractionation and (2) physically, through conformal treatment techniques.

Dose fractionation refers to the delivery of a total therapeutic dose in smaller fractions over a protracted period of time. For example, instead of delivering the total prescribed dose of 70 Gy in one treatment session, 2 Gy is delivered daily for 35 sessions. The rationale of dose fractionation is based on the knowledge that early responding tissues (such as cancer cells) and late responding tissues (such as normal lung, kidney, heart, liver and other normal cells) possess different radiobiological properties (Orton, 2007). At lower doses, the repair of sub-lethal damage of normal cells exceeds that of cancer cells. Also, prolonging the overall treatment time optimally, allows early responding normal cells to repopulate and reduces acute side effects. At the same time, fractionation increases damage to cancer cells through reoxygenation and redistribution of cells into radiosensitive phases of the cell cycle between fractions. In short, the practice of dose fractionation maximises the killing of cancer cells while limiting the damage to surrounding healthy tissues.

Meanwhile, conformal treatment techniques allow geometrical sparing of organs at risk and healthy tissues. Modern linear accelerators use the multi-leaf collimator (MLC) to shield part of the radiation field to limit the dose to organs at risk (OARs) and healthy tissues. These MLC leaves are controlled and moved independently to create a field of any shape. The automation of beam shaping with the MLC system makes it possible to incorporate a large number of beam shapes into a treatment plan. As a result, the MLC system enables the practical delivery of complex radiotherapy techniques such as intensity modulated radiation therapy (IMRT) and volumetric modulated arc therapy (VMAT). These treatment techniques are capable of delivering highly conformal dose

distributions with steep dose gradients that allow better sparing of adjacent healthy tissues.

Although dose fractionation and conformal treatment techniques can possibly improve tumour control and reduce side effects, the treatment outcome depends on the ability to accurately deliver the treatment in a reproducible manner over many days or even weeks. The accuracy and reproducibility of treatment delivery is especially important for complex treatment techniques with steep dose gradients, where the margin of error is small and slight inaccuracy may lead to under-dosing of target and/or over-dosing of the OARs. Moreover, these complex treatment techniques require input from many different modalities and professionals and thus may create an environment with more potential for error.

1.2 Errors in radiotherapy

An error in radiotherapy is defined as:

> "… a non-conformance where there is an unintended divergence between a radiotherapy treatment delivered or a radiotherapy process followed and that defined as correct by local protocol." (The Royal College of Radiologists et al., 2008)

In an effort to improve the safety and quality of radiotherapy in the United Kingdom (UK), a voluntary National Reporting and Learning System (NRLS) is in place to encourage clinical departments and radiotherapy professionals to report radiotherapy error (RTE). The purpose of NRLS is to promote nationwide sharing of RTE so that the radiotherapy community can learn from these incidents and prevent future occurrence of similar errors. The Patient Safety in Radiotherapy Steering Group (PSRT) analyses RTEs in the NRLS database and publishes quarterly newsletter and biennial reports with recommendations and guidance on how to minimise the occurrence of common errors (Patient Safety in Radiotherapy Steering Group, 2010, 2012, 2014).

During the period December 2011 to November 2013, a total of 7,655 RTE reports were recorded out of an estimated 413,730 radiotherapy sessions

delivered in the UK (Patient Safety in Radiotherapy Steering Group, 2014). Although the number of RTEs appears to be large, the majority of RTEs were lower-level incidents that have little or no critical effect on the patient treatments. Only 1.7% (n = 128) of the total RTEs were higher-level incidents (defined as dose error of 10% or more than that intended for a whole treatment course, or 20% or more than that intended for a given fraction). The risk of a radiotherapy error having a clinically significant adverse outcome was estimated at 30 per million courses of radiotherapy (The Royal College of Radiologists et al., 2008). Meanwhile the risk of death arising from radiotherapy error was estimated at two per million courses (Munro, 2007). Although the risk is small, the radiotherapy community must not be complacent. Ford et al. (2009) identified as many as 127 possible failures in the whole radiotherapy process. Therefore, it is important that systems are put in place to prevent the occurrence of error or to maximize the detection of error before any harm can be done.

1.3 Quality assurance (QA) in radiotherapy

QA in radiotherapy is:

> "… all procedures that ensure consistency of the medical prescription, and safe fulfilment of that prescription, as regards the dose to the target volume, together with minimal dose to normal tissue, minimal exposure of personnel and adequate patient monitoring aimed at determining the end result of the treatment." (Thwaites et al., 2005)

QA checks should be omnipresent in all stages of a radiotherapy process. The purpose of QA checks is twofold. First, QA checks improve safety in radiotherapy treatment through early detection of errors and prevent severe consequence that could affect the outcome of patients' treatment. Second, QA checks can reduce uncertainties in each stage of the radiotherapy process and improves the overall treatment accuracy. The International Commission on Radiation Units and Measurements (ICRU) has recommended that the delivered dose must be within 5% of the prescribed dose (ICRU Report No. 24, 1976). To meet this requirement, the accuracy within each step of the radiotherapy process must be much better than 5% (Kutcher et al., 1994).

The role of QA checks becomes even more critical with the introduction of complex treatment techniques such as the IMRT and VMAT. The IMRT and VMAT treatments use inverse planning whereby an optimisation engine works to produce a treatment plan that best matches the criteria specified by the user. The number of monitor units (MU) for IMRT and VMAT plans are dependent on the optimal fluence distribution and plan modulation. Unlike the case of a conventional treatment, where MU is a straightforward function of beam output, field size and depth, the MU values for IMRT and VMAT fields are less intuitive and not easy to verify. Furthermore, the numbers of MU for IMRT and VMAT treatments are typically much higher than a conventional treatment. For example, the total MU for an IMRT treatment can be in the order of thousands, roughly five times higher than a conventional treatment for the same prescription dose. As a result, the correct delivery of treatment becomes critically important because an error in delivery may lead to catastrophic consequence or even death. This risk was clearly highlighted in the accident at St Vincent's Medical Center in New York City, where a patient was irradiated with a large number of MU, which was planned for an IMRT technique but was delivered with an open field due to a corrupted MLC file (NYC Department of Health and Mental Hygiene, 2005, ICRP Publication 112, 2010).

1.4 Patient-specific treatment verification

An international review of major radiotherapy incidents over three decades (1976 to 2007) found that 45% of radiotherapy incidents occurred during the introduction of new systems and/or equipment (Shafiq et al., 2009). The high probability of an error occurring in a new technique combined with the high severity should an error occur, has prompted several international bodies to publish new QA guidelines when IMRT was first introduced for clinical application (Ezzell et al., 2003, Mijnheer & Georg, 2008, Moran et al., 2011). The main highlight of the IMRT guidelines is the recommendation to perform patient-specific treatment verification. Patient-specific treatment verification refers to the validation of individual patient treatment as opposed to a more general system verification. Although patient-specific treatment verification is emphasized for IMRT treatment, it is applicable to all types of radiotherapy

treatment. There are many variations to the practice of patient-specific treatment verification such as the time of verification and the materials and methods used for the verification.

1.4.1 Time of verification

Patient-specific treatment verification can be performed prior to the start of treatment (pre-treatment QA), during the actual treatment or both.

Pre-treatment QA is the common term used to describe the verification of an individual treatment plan before delivery to the patient. The advantage of pre-treatment QA is that it allows the detection and rectification of an error before it can affect the patient treatment. This is especially important for high dose hypo-fractionation radiotherapy and radiosurgery, where an error in the first treatment fraction would be difficult or impossible to compensate. Pre-treatment QA is effective in checking the integrity of data transfer, that the correct version of the plan was sent to the record and verify system and the deliverability of a treatment plan. However, there has been much debate on the value of pre-treatment QA (Ramsey et al., 2003, Smith et al., 2011). Despite the wide adoption of pre-treatment QA, roughly 30% of institutions evaluated by the Radiological Physics Centre (RPC) in an IMRT credentialing exercise failed to meet the 7% dose agreement and 4 mm distance-to-agreement criteria between measured and planned dose distribution (Ibbott et al., 2006, Ibbott et al., 2008). A retrospective analysis of RPC results from 2003 to 2013 (n = 745 plans) showed that institution pre-treatment QA was a poor indicator of delivery accuracy and could only detect 18% of plans that failed the RPC phantom evaluation (Kry et al., 2014). Also interesting is a study that found pre-treatment QA to be the least effective among all the common QA checks, detecting only 1.4% of the errors investigated (Ford et al., 2012).

On the other hand, verification during the actual treatment delivery such as in-vivo dosimetry can serve as an ultimate check to the accuracy of treatment delivered to the patient (ICRU Report No. 24, 1976). In addition to the errors that can be detected by pre-treatment QA, actual treatment verification can also detect patient positioning error, change in patient anatomy, obstruction from immobilisation devices or table arm and performance of machine on a

particular treatment day (van Elmpt et al., 2008a). Mans et al. (2010b) reported that nine out of the 17 serious errors detected in their in-vivo treatment verification would not have been detected with pre-treatment verification. However, in-vivo treatment verification is expensive, cumbersome and difficult to implement. For instance, the capital cost to start an in-vivo dosimetry program is estimated to be £6000 per linear accelerator with a subsequent annual revenue cost of £19000 (Williams & McKenzie, 2008). Furthermore, in-vivo dosimetry can only detect an error after the treatment has been delivered.

Therefore, the time of verification should be carefully considered, taking into account the risk of different treatment techniques and practical issues such as cost, additional machine time and other resources (Williams & McKenzie, 2008, Mackay & Williams, 2009). In addition, legal requirements of a country also determine when the patient-specific verification should be performed. For example, in-vivo dosimetry is legally required in some European countries such as France, Sweden, Denmark, Norway and the Czech Republic.

1.4.2 Methods of verification

There are various methods to perform patient-specific treatment verification.

Firstly, treatment can be verified using either measurement- or software-based methods (Siochi et al., 2013). The measurement-based method refers to the type of verification where the dose is physically measured and compared against the expected dose, to check the accuracy of treatment delivery. On the contrary, software-based verification does not require the physical measurement of each treatment plan. Instead, an independent calculation is performed and verified against the dose computed by the treatment planning system (TPS). The input to the independent calculation system can be either field parameters exported from the TPS (Siochi et al., 2009) or machine treatment log files that contain delivery information such as the MLC position (Rangaraj et al., 2013). In recent years, software-based treatment verification of IMRT plans has gained popularity mainly because of the time saving factor. Besides being more efficient, the use of a software-based QA also helps physicists to make better judgements since errors in treatment planning and machine delivery can be segregated (Siochi et al., 2008). However, the use of software-based QA in place

of physical measurement is still debatable (Childress et al., 2015). For example, in the use of treatment log files for software-based QA, concerns were raised on the reliability of data recorded in the log files and the fact that this type of QA would not detect changes in dose parameters such as beam output, quality and profiles (Childress et al., 2015). Pawlicki et al. (2009) highlighted the need to perform an initial evaluation of consistency between the two methods using control charts before replacing measurement-based QA with software-based QA.

Secondly, treatment verification can be performed for either a single point or multiple points, depending on the choice of detector or the capability of the software. Clearly, compared to multiple point verification, single point verification is inferior because of the lack of information at other areas in the treatment field. Furthermore, in the case of modulated field, it is often difficult to find a verification point that is located in a high-dose and low-gradient region so as to minimise the effect of positioning uncertainty. Instead of single point verification, a more efficient and effective method is to perform simultaneous verification of dose distributions in a 2D plane or 3D volume. The widely used method to evaluate the agreement between evaluated and referenced dose distributions is gamma analysis (Low et al., 1998). The gamma analysis calculates an index for each point based on the dose difference and distance-to-agreement (DTA), as shown in Equation 1-1. A point with gamma index less than 1 represents good agreement ($\gamma \leq 1$, pass) and a point with gamma index more than 1 represents disagreement exceeding the specified tolerances ($\gamma > 1$, fail). The acceptance of a test depends on the number of points that passed the gamma analysis.

$$\Gamma(r_e, r_r) = \sqrt{\frac{r^2(r_e, r_r)}{\Delta d^2} + \frac{\delta^2(r_e, r_r)}{\Delta D^2}} \tag{1-1}$$

Where:

$r(r_e, r_r)$ is the spatial distance between evaluated point (r_e) and reference point (r_r);

$\delta(r_e, r_r)$ is the dose difference between point r_e and point r_r;

Δd is the distance-to-agreement criterion; and

ΔD is the dose difference criterion.

Although the gamma analysis method provides a quick representation of the quality of agreement between two dose distributions, the region of failure is difficult to interpret and the clinical relevance remains unclear. This is mainly due to the fact that the gamma result does not provide information on the magnitude of disagreement and the location of disagreement relative to patient's anatomy. Several investigators found a weak or no correlation between gamma passing rates and deviation in clinical dose volume histogram (DVH) metrics and concluded that gamma analysis lacks predictive power to detect clinically relevant differences (Nelms et al., 2011, Zhen et al., 2011, Carrasco et al., 2012, Stasi et al., 2012, Coleman & Skourou, 2013, Lin et al., 2014). Instead of verifying with gamma analysis, verification of anatomical doses based on DVH metrics using clinical tolerance would provide more information on the impact of delivery inaccuracy (McDermott et al., 2008, Oldham et al., 2012).

Thirdly, patient-specific treatment verification can be analysed either field-by-field or as a composite delivery. Verification of a composite delivery provides a more realistic representation of patient treatment but small differences may be masked because of normalisation to higher overall dose. On the other hand, field-by-field (or per-beam) verification may magnify irrelevant error in fields with low dose weighting (Carrasco et al., 2012). However, field-by-field analysis may help to indicate a problem in a particular field especially when troubleshooting a plan that failed the QA test.

Finally, in the case of pre-treatment verification, there is a choice of either performing the QA in a homogeneous or heterogeneous phantom. Most commercial QA devices use homogenous phantoms with simple geometry, such as a cube or cylinder. Verification with a homogeneous phantom may not be adequate since it does not check for TPS inaccuracies in computing doses in the presence of inhomogeneity and the use of phantoms with simple geometry does not correctly represent the human body. The use of anthropomorphic phantoms with humanoid external shape and organs that mimic the human body (Molineu et al., 2005) would allow a more comprehensive evaluation of the treatment accuracy. Apart from the choice of phantoms, pre-treatment verification can also be performed using either variable treatment gantry angles or a fixed

gantry angle of zero degrees. For measurement-based QA, collapsing all gantry angles to zero saves delivery time. In addition, by measuring all beams perpendicular to the detectors, no correction is required for detectors that show angular dependence. However, irradiation with the gantry at zero degrees neglect the effect of gravity on different mechanical parts such as the MLC leaves positions and the accuracy of gantry angles.

In summary, it is important to have a thorough understanding of the strengths and weaknesses of a particular practice. The method adopted by a department should depend on the perceived risk of a certain treatment technique and the availability of equipment and manpower. The practice of patient-specific treatment verification should be reviewed and updated from time to time as technology evolves and risk changes. As a rule of thumb, more vigorous checks should be put in place for new techniques to ensure safe implementation. The frequency of checks can be reduced and the methods simplified as experience and confidences in a treatment technique are gained.

1.5 Types of detectors

Measurement-based patient-specific treatment verification can be performed using different types of detectors such as ionisation chamber (IC), diode, metal oxide semiconductor field effect transistor (MOSFET), thermoluminescent detector (TLD), optically stimulated luminescence detector (OSLD), radiographic film, radiochromic film and electronic portal imaging device (EPID). The principle of operation and characteristics for each of the detectors are described in the following section. An overview of these detectors is provided in Table 1-1. Gel dosimeter and alanine are excluded since they are not commonly used for routine patient-specific treatment verification.

1.5.1 Ionisation chamber (IC)

Principle of operation

The IC consists of an air filled sensitive volume with three electrodes: polarizing electrode, collecting electrode and guard electrode. Exposure to radiation produces ion pairs in the air cavity. The ionisation charge is collected by the collecting electrode, which is held at high bias voltage, and measured by an

electrometer. The measured charge is converted to absorbed dose to water using a calibration factor (N_{D,W,Q_o}) traceable to a Primary Standard Dosimetry Laboratory (PSDL).

Characteristics

The IC is used to measure absolute dose output and is considered the gold standard in radiation dosimetry because of its high accuracy. The overall standard uncertainty for the determination of absorbed dose to water under reference conditions is estimated to be only 1.5% (IAEA Technical Reports Series No. 398, 2000). The other advantages of ICs include excellent long-term stability, good reproducibility, linear response to dose, small angular dependence for cylindrical IC and immediate dose-readout. Although the IC is affected by changes in environmental temperature and pressure, ion recombination and polarity effect, the correction factors are straightforward and well established (IAEA Technical Reports Series No. 398, 2000, Khan, 2010c).

For patient-specific treatment verification, the IC is used to perform pre-treatment QA measurement. A cylindrical IC is inserted into a phantom to measure absolute point dose for comparison with the TPS computed dose. The main issue with using an IC to measure modulated fields is the finite size of the chamber. Using an IC to measure IMRT subfields smaller than the chamber dimension may be inaccurate due to the lack of charged particle equilibrium. Therefore, as a general rule, an IC with small volume (0.125 cc or less) should be used for IMRT pre-treatment QA measurement (Laub & Wong, 2003, Sánchez-Doblado et al., 2007). Besides chamber volume, the positioning of the IC also plays an important role in minimising uncertainties; it must be positioned in a low-gradient region to avoid any fluence-averaging perturbation effect. Using a small volume IC (0.007 cc), Capote et al. (2004) found that the dose measured within the IMRT subfield could be accurate to within 3%, but 9% deviation was observed at the penumbra region.

Alternatively, patient-specific pre-treatment QA can be verified in 2D using an array of ICs. Commercially available IC-based 2D array devices include MatriXX (IBA Dosimetry GmbH, Schwarzenbruck, Germany) and Octavius (PTW, Freiburg, Germany). Typically, the device consists of more than 1000 small volume ICs

(0.06 cc to 0.08 cc) embedded in a phantom of different dimensions. Although the problem with chamber positioning encountered for single point measurement is not applicable to a 2D array device, the poor resolution of a 2D array (around 0.7 cm) is still considered not ideal for IMRT/VMAT measurements. The other disadvantage of 2D array devices is the limited active area (usually less than 27 x 27 cm^2) that constrains the maximum field size that can be measured. It is also crucial to keep the measurement field size within the recommended limit to avoid direct exposure of the electronics, which are prone to radiation damage. Nevertheless, the 2D array device remains very popular because it is easy to use and provides a relatively efficient method to perform patient-specific treatment verification.

1.5.2 Diode

Principle of operation

Diode detectors are made of silicon crystal doped with impurities to create p-type silicon (an electron receptor that contains 'holes') and n-type silicon (an electron donor). An example of the type of diode detector used in radiotherapy is a p-n junction diode, where a bulk of p-type silicon is mixed with a thin layer of n-type material to create a junction. This junction, also known as depletion zone, is the sensitive volume of the detector. When irradiated, electron-hole pairs are created in the depletion zone. The movement of electrons and holes across the depletion zone to the p- and n-regions produces a measurable current proportional to the incident radiation.

Characteristics

The main advantage of the diode detector compared to an IC is the high sensitivity. The energy needed to produce an electron-hole pair in silicon is almost 10 times less than that needed to produce an ion pair in air. Moreover, the silicon has a density 1,800 times higher than air. Combining both factors, the relative efficiency per unit volume for a diode detector is 18,000 times higher than the IC (Khan, 2010c). The high efficiency makes it possible for diode detectors to be small in size. Besides the good spatial resolution, the diode is also a very reliable detector, with a reproducibility of better than 1% (IAEA Human Health Reports No. 8, 2013) and an excellent linear response with dose (Jornet et al., 2004). Other advantages of the diode detector include ruggedness

and real-time dose readout, making it a suitable detector for in-vivo dose measurement.

However, a diode detector shows energy, angular, temperature and dose per pulse dependence (Mijnheer et al., 2013). The energy dependence is because of the high atomic number of silicon (z = 14) that causes over-response to low energy radiation. The response of a diode detector to 48 keV photons was 7.7 times more than at 6 MV (Edwards et al., 1997). Adding a build up cap to absorb low energy radiation can mitigate the energy dependence of the diode but the build up cap could perturb the dose to patient. Depending on the beam energy, field size and the type of diode, the presence of a build up cap could increase the patient's surface dose by 50% to 90% and decrease the dose at depth by 4% to 13% (Nilsson et al., 1988, Alecu et al., 1997). Meanwhile, the angular dependence of a diode can affect the detector response by 10% to 15% (Nilsson et al., 1988, Seco et al., 2014) and the variation in temperature can cause 0.1% to 0.3% deviation in response per degree Celsius (°C) (Lanson et al., 1999, Jornet et al., 2004, Seco et al., 2014). As for the dose-per-pulse dependence, Saini & Zhu (2004) varied the source to detector distance and found sensitivity variation of around 1% to 3% for most of the commercial diode detectors investigated in the study. Before a diode detector can be used for in-vivo dose measurement, it must be cross-calibrated against an IC according to beam energies and preferably as close to the clinical set-up as possible. Additional correction factors must be derived to account for non-reference conditions during actual patient measurement such as difference in field size, distance from source, angle of incidence and the presence of wedge. Although the diode detector has a very long lifespan, it must be routinely re-calibrated to account for reduction in diode sensitivity due to radiation damage. Typically, the diode sensitivity is reduced by about 0.7% for every kGy of radiation (Lanson et al., 1999).

Besides in-vivo dosimetry, diodes are also used as detectors for 2D array pre-treatment QA devices. Examples of commercially available diode-based 2D array device include ArcCHECK (Sun Nuclear, Melbourne, FL, USA) and Delta4 (ScandiDos AB, Uppsala, Sweden). Similar to IC-based 2D array devices, a large number of diode detectors (>1000) are embedded in the phantom in different

configurations. Although the diode detector is small in size, the spacing between detectors in the phantom is large, resulting in poor resolution (0.5 cm to 1 cm). While the characteristics of diode detectors in a 2D array are similar to those described in the previous paragraph for a single detector, the number of correction factors that must be derived by the user is greatly simplified mainly because of automated correction by the software and also because of less variation in pre-treatment set-up compared to in-vivo measurement. Depending on the frequency of use, it is still necessary to re-calibrate the diode-based 2D array periodically due to reduction in diode sensitivity with irradiation. Overall, the diode-based 2D array device is still relatively easy to use and provides an efficient way to perform pre-treatment verification in more than one dimension.

1.5.3 Metal oxide semiconductor field effect transistor (MOSFET)

Principle of operation

The MOSFET is a semiconductor detector, which consists of a silicon substrate and three terminals: 'source', 'drain' and 'gate'. In a p-channel MOSFET, the main substrate is composed of n-type silicon and two p-type regions. The space between the two p-type regions is known as the p-channel and above this channel is an insulating layer of silicon dioxide (SiO_2) with the 'gate' terminal. Without voltage to the 'gate' terminal, the p-channel is not conductive and current cannot flow between the 'source' and 'drain' terminals located above the two p-type regions. Threshold voltage (V_{TH}) is the amount of voltage needed to allow current, I_{DS}, to flow. When a MOSFET is irradiated, the charge generated in the oxide layer is permanently trapped and causes the V_{TH} to increase linearly as a function of absorbed dose. The principle of MOSFET is based on measuring the change in V_{TH} to derive the amount of absorbed dose.

Characteristics

Similar to the diode, MOSFET has the advantages of real-time readout, high sensitivity and small size. In fact, the size of a micro MOSFET is only 1 mm x 1 mm x 3.5 mm, allowing excellent spatial resolution and less dose perturbation when used for in-vivo dosimetry. The MOSFET also showed excellent linear response to dose (Jornet et al., 2004). Meanwhile, the temperature and angular response of MOSFET detector varies with its design. A single-detector MOSFET system showed strong temperature dependence of as high as 50 mV for a 25°C

change in temperature during the readout process (2 mV/°C) (Cheung et al., 2004) but a double-detector MOSFET system showed negligible temperature dependence of around 0.02 mV/°C (Soubra et al., 1994) or 0.5% response deviation from 20°C to 40°C (Ramaseshan et al., 2004). The findings on MOSFET angular dependence vary substantially between authors from 2% (Ramaseshan et al., 2004, Rowbottom & Jaffray, 2004, IAEA Human Health Reports No. 8, 2013) to 12% (Lonsdale, 2012) to 27% (Scalchi et al., 2005). The variation in reported angular dependence could be due to differences in the thickness of silicon dioxide layer and the shape of the detector.

Also, as with diodes, a MOSFET detector exhibits over-response to low energy radiation because of the high atomic number of silicon and silicon oxide. The response of MOSFET was 4.4 times higher for 33 keV photons compared to 6 MV photons (Edwards et al., 1997). Compared to a diode, the reproducibility of MOSFET detector was lower at 2% to 3% (Soubra et al., 1994, Ramaseshan et al., 2004, Scalchi et al., 2005). Lastly, the main disadvantage of the MOSFET detector is the short lifespan. Although the MOSFET sensitivity did not change with accumulated dose, the detector can no longer be used after approximately 50 Gy (Jornet et al., 2004). This is because the permanent trapping of charge will saturate the traps after accumulating a certain amount of dose.

1.5.4 Thermoluminescent detector (TLD)

Principle of operation

A TLD is made of crystalline material that is doped with impurities to create traps in the lattice structure. Electrons that are produced during irradiation can fall into these traps to create a metastable state. When heated, these trapped electrons are released and visible light is produced, a process known as thermoluminescence. A photomultiplier (PMT) then converts the visible light to electrical current and the amplified current can be related to absorbed dose received by the material.

Characteristics

The most common type of TLD for clinical dosimetry is made of doped lithium fluoride (LiF). The TLD can come in many different forms (such as powder or solid) and shapes (such as chips, rods or pellets), making it a very adaptable

dosimeter for in-vivo dose measurement in various situations. Furthermore, the TLD is easy to use because it is not attached to any cables and bias voltage is not needed for its operation. Similar to semiconductor dosimeters, TLD has high sensitivity and is small in size. But unlike diodes, TLD has small temperature and angular dependence (Essers & Mijnheer, 1999, IAEA Human Health Reports No. 8, 2013, Mijnheer et al., 2013). As TLD is almost tissue equivalent, the over-response to low energy radiation (33 keV) was only 1.31 times more than to 6 MV photons (Edwards et al., 1997).

The major disadvantage of TLD is the requirement for time consuming pre- and post-processing and consequently, delayed dose results. A typical TLD processing involves annealing the TLD for 1 hour at 400°C and then cooling it for 24 hours at 80°C, although the procedure may vary with manufacturer. The processing of TLD must be carried out carefully and consistently to get accurate and reproducible results. Generally, the reproducibility of TLD was around 2% (IAEA Human Health Reports No. 8, 2013), about 1% to 2% worse than diode detectors (Loncol et al., 1996). The poorer reproducibility of TLD was attributed to the deviation in the crystal and impurities concentration as well as other uncertainties related to the PMT, annealing and readout procedures (Loncol et al., 1996). Lastly, the TLD response is only linear to dose up to 1 Gy for LiF doped with magnesium and titanium (LiF:Mg,Ti) and 10 Gy for LiF doped with phosphorus, magnesium and copper (LiF:Mg,Cu,P). Above the dose threshold, the TLD response is supralinear and may cause deviation up to 9% if uncorrected (IAEA Human Health Reports No. 8, 2013).

1.5.5 Optically stimulated luminescence detector (OSLD)

Principle of operation

An OSLD is made of aluminium oxide doped with carbon (Al_2O_3:C). The principle of OSLD is very similar to TLD except that light, instead of heat, is used to stimulate the release of trapped electrons. To discriminate the stimulation light from the resultant light produced by the released electrons, the wavelength of the stimulation light must be different from the resultant light. In addition, an optical filter is placed in front of the PMT to selectively absorb and prevent stimulation light from reaching the counter.

Characteristics

OSLD is used for in-vivo dosimetry and shares many of the TLD advantages such as high sensitivity, small detector size, no cables and does not require bias voltage. The characteristics of OSLD are also rather comparable to TLD with small angular and temperature dependence. The angular dependence for OSLD was 3% to 4% (Kerns et al., 2011) and the variation in response was less than 1% when temperature was varied from 21°C to 36°C (Yukihara et al., 2008). Even though the OSLD requires processing, the readout process is much faster than TLD and the OSLD response was found to stabilise at 8 minutes post-irradiation (Reft, 2009). The ability to re-read the OSLD signal is also an added advantage. With careful and consistent processing, the reproducibility of OSLD results was reported to be 1.5% (IAEA Human Health Reports No. 8, 2013).

The main disadvantage of OSLD is its change in reproducibility and sensitivity with accumulated dose, resulting in a short lifespan. The OSLD dose response was observed to be linear up to 2 Gy and supralinear above 2 Gy (Reft, 2009) but this dose response relationship altered with historical dose (Jursinic, 2010). The change in response with historically accumulated dose is due to the ineffectiveness of optical bleaching in emptying electrons in deeper energy traps and causes residual signal to build up with repeated use. The IAEA Human Health Reports No. 8 (2013) observed substantial changes in OSLD sensitivity and reproducibility and advised against using the OSLD without optical bleaching after an accumulated dose of 2.5 Gy to 3 Gy. Because of the higher atomic number of aluminium oxide (z = 11.2), the OSLD response was 3.6 times higher for 35 keV photons compared to 6 MV photons (Reft, 2009).

1.5.6 Radiographic Film

Principle of operation

Radiographic film consists of a transparent plastic coated on one or both sides with radiation sensitive emulsion containing crystals of silver bromide (AgBr). A chemical reaction takes place when the film is exposed to radiation and a latent image is formed. Through processing, the AgBr crystals affected by radiation are reduced to metallic silver. Subsequently, the remaining unaffected crystals are removed through fixing. The degree of darkening of a film, or optical density (OD), depends on the amount of deposited silver and is a function of absorbed

dose. The conversion of OD to dose is done through the sensitometric curve, which is a plot of OD versus dose.

Characteristics

Radiographic film is used for patient-specific pre-treatment QA. The main advantage of radiographic film is the 2D spatial information with excellent resolution. However, there are many challenges in using radiographic film for dose measurement. First, the relationship between OD and dose may not be linear and is dependent on the film emulsion. In addition, the film response is very sensitive to variation in developer chemistry composition, temperature and processing time. Childress et al. (2002) observed a 7.5% standard deviation due to variation in processor conditions. Therefore, it is important to establish the sensitometric curve for each batch of film and to process the subsequent films carefully and consistently following the exact conditions used during calibration to minimise uncertainties (Pai et al., 2007). By following a strict protocol, the reproducibility of radiographic film is estimated to be better than 2% (Mijnheer et al., 2013).

The main disadvantage of radiographic film is the substantial energy dependence because of the high atomic number of silver (z = 45) in the film emulsion. The radiographic film exhibits over-response at large field size and depths due to the increased proportion of low energy scattered photons. Reports on the extent of film energy dependence vary between different authors, ranging from less than 3% (Martens et al., 2002) to up to 9% (Yeo et al., 2004) outside the penumbra region of IMRT fields where the low energy photons are abundant. The discrepancies in results from different studies was later attributed to variation in phantom material and dimension (Palm & LoSasso, 2005). Also, the radiographic film response is dependent on the film plane orientation with respect to the beam direction. The sensitivity of film was found to be greater when the radiographic film was positioned perpendicular rather than parallel to the beam axis (Oldham & Webb, 1997). Danciu et al. (2001) reported a maximum of 4% to 6% increase in response for films positioned perpendicular to beam axis and became negligible at depth more than 5 cm. For small fields with diameter less than 4 cm, the angular dependence of film was less at 1.5% (Robar & Clark, 1999). The other drawback of radiographic film is the limited dynamic range. For

instance, the commonly used XV2 film (Eastman Kodak, Rochester, NY, USA) is only suitable for dose measurement within 0.05 Gy to 0.8 Gy. Irradiation with doses below this range will be obscured by background density while above this range the film saturates. The dynamic range has been extended in later versions of radiographic film such as the Kodak EDR2 (Eastman Kodak, Rochester, NY, USA), with a useful range of 0.1 Gy to 5 Gy.

1.5.7 Radiochromic film

Principle of operation

Radiochromic film has one or two thin radiosensitive layer(s) on clear polyester base(s). The radiosensitive layer, consisting of microcrystals of a monomer dispersed in gelatin binder, undergoes polymerisation when irradiated with ionising radiation (Niroomand-Rad et al., 1998). The polymerisation causes the film to progressively change colour to different shades of blue. The darkness of the film is proportional to absorbed dose and can be measured as OD using a commercial flatbed document scanner in transmission mode (Devic et al., 2005, Paelinck et al., 2007). The absorbed dose can then be derived from the OD using the sensitometric curve.

Characteristics

Radiochromic film is also used for patient-specific pre-treatment QA but it has many advantages over radiographic film such as insensitivity to visible light and does not require tedious chemical processing. Also, radiochromic film has a larger dynamic range suitable for verification of a wide range of megavoltage treatments (e.g. GafChromic EBT2 film (Ashland, Covington, KY, USA) has a dynamic range of 0.01 Gy to 40 Gy). The major advantage of radiochromic film is the near tissue equivalence of the sensitive layer that leads to low energy dependence (Arjomandy et al., 2010, Borca et al., 2013). This is an important characteristic that eliminates some of the uncertainties seen with radiographic film.

One of the disadvantages of radiochromic film that is similar to radiographic film is the large inter-batch variation in sensitivity up to 13.7% (Reinhardt et al., 2012). This requires the re-establishment of sensitometric curve for each batch of film, resulting in extra workload. Although radiochromic film does not involve

processing due to its self-developing nature, the read-out process still requires careful handling and strict adherence to standardised protocol. Factors such as time of scan, scanner warm up, scan orientation and film position can affect the accuracy of results. Because the radiochromic film continues to polymerise post-irradiation, a consistent wait-time of at least 24 hours (preferably 48 hours) is needed (Niroomand-Rad et al., 1998, Arjomandy et al., 2010, Reinhardt et al., 2012) delaying the availability of results. Meanwhile, the OD reading is also sensitive to film orientation due to the polarization effect of the scanner light. Depending on the scanner and dose, the OD scanned with landscape orientation could be 4% higher than portrait (Butson et al., 2006, Borca et al., 2013) and the error due to misalignment of film on scanner bed could be as much as 1% per degree of rotation (Butson et al., 2009). So, it is crucial that the film is consistently placed on the scanner, possibly with the help of a template.

The other disadvantage of radiochromic film is the additional requirement to correct for non-uniformity of film and scan field (Zhu et al., 1997, Paelinck et al., 2007). The non-uniform film response and scan field could be up to 3.7% (Hartmann et al., 2010) and 8% (Paelinck et al., 2007) respectively, depending on the film and scanner model. Furthermore, the read-out process also showed temperature dependence and requires proper warm-up of the scanner to reduce uncertainty (Paelinck et al., 2007, Buchauer et al., 2009). Additional steps to improve read-out accuracy were explicitly described by Devic et al. (2005) that included taking an average of five successive scans of non-irradiated and irradiated film to reduce noise, scans of empty scanner bed to remove defective pixels and an additional scan of an opaque film to account for scanner background signal. Only by following a strict read-out protocol consistent with calibration, the reproducibility of radiochromic film dosimetry could be kept to within 2% (Devic et al., 2005) to 3% (Mijnheer et al., 2013).

1.5.8 Electronic portal imaging device (EPID)

The electronic portal imaging device (EPID) was first invented to replace film for positional verification in radiotherapy. In general, the EPID is advantageous because it provides immediate 2D high-resolution digital images without the need of manual processing. The EPID is particularly attractive for dose measurement because the panel is readily available as an attachment to most

linear accelerators (linacs) and the measurement requires only minimal set-up. Most importantly, the EPID can potentially be used for both pre-treatment and actual treatment dose verification.

1.5.8.1 Scanning liquid-filled ionisation chamber (SLIC) EPID

Principle of operation

The earliest EPID model was a scanning liquid-filled ionisation chamber (SLIC) EPID. A prototype SLIC EPID was developed at The Netherlands Cancer Institute, Amsterdam (Meertens et al., 1985, Van Herk & Meertens, 1988) and was later commercialised as PortalVision (Varian, Palo Alto, CA, USA). The PortalVision ionisation chamber matrix is constructed from a layer of Isooctane liquid (the active volume) sandwiched between two electrode printed circuit boards. Each printed circuit board has 256 parallel electrode strips and the strips are arranged perpendicular to each other between the two boards. The cross-points of the electrode strips form the 256 x 256 matrix detector. A simplified diagram of the SLIC EPID is illustrated in Figure 1-1. With an active area of 32.5 x 32.5 cm^2, the corresponding detector resolution is 0.13 x 0.13 cm^2. Apart from the detector matrix, the EPID panel also consists of a 256-channel high voltage switch, 256-channel electrometer and other control electronics. To form one image frame, high voltage is applied sequentially row-by-row across the matrix. During the time when voltage is applied, the multi-channel electrometer scans the activated row to measure the charge of each ionisation chamber simultaneously. The acquisition time for one full-frame varies between 1.5 s and 6 s (Boyer et al., 1992, Essers et al., 1995). The measured charge (or pixel value) has been found to be proportional to the square root of the dose rate (Van Herk, 1991, Zhu et al., 1995, Parsaei et al., 1998), with a small correction term linear to the dose rate (Essers et al., 1995, Boellaard et al., 1996). Using a calibration curve, an image represented in pixel value can be converted to a 2D dose rate matrix. Subsequently, the dose rate matrix is multiplied by the time interval or MU for that image to form a 2D dose matrix. Finally, multiple 2D dose matrices are summed to give an integrated dose matrix.

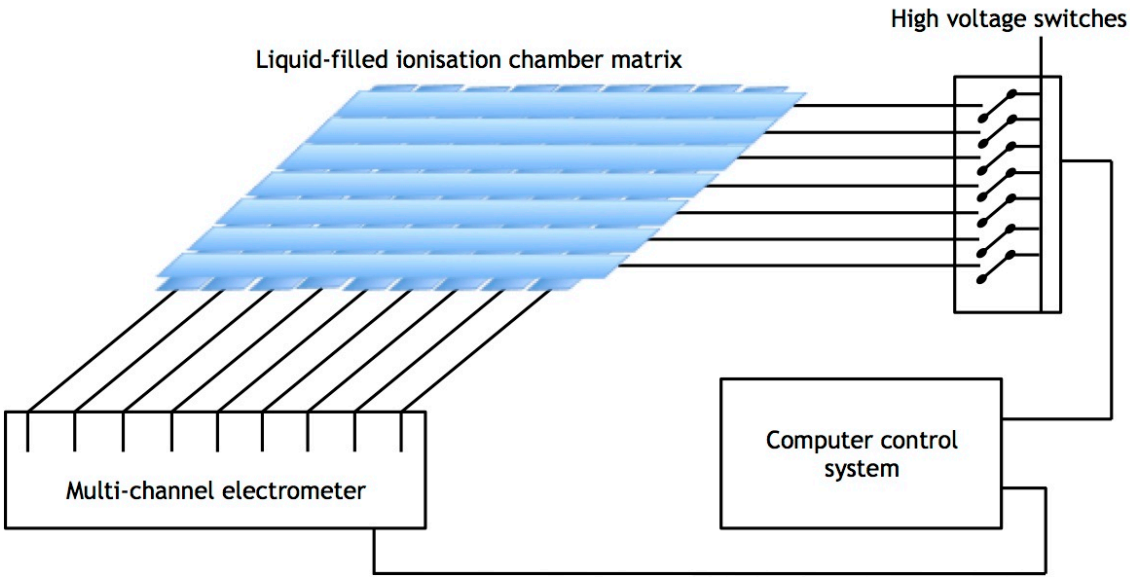

Figure 1-1 A simplified illustration of a scanning liquid-filled ionisation chamber (SLIC) EPID.

Characteristics

As a dosimeter, the SLIC EPID has the advantage of good short- and long-term stability with variation less than 1% (Essers et al., 1995, Zhu et al., 1995). More importantly, the SLIC EPID exhibited tissue equivalent response with minimal energy dependence (Curtin-Savard & Podgorsak, 1999). The response was consistent regardless of field size (Parsaei et al., 1998) and comparable to IC measurements to within 0.5% (Zhu et al., 1995). The main disadvantage of the SLIC EPID is the relatively long acquisition time (or dead time where signal is lost), which resulted in poor detector efficiency. Using a commercial SLIC EPID with a standard mode, the acquisition of one image frame including storage can take up to 9 s (5.5 s to read-out and 3.5 s to store the image) (Chang et al., 2000). When measuring a dynamic IMRT delivery with continuous MLC movements, it is important that leaf motion is small during the sampling time between image frames in order to correctly measure a continuous data. Because of the slow sampling of SLIC EPID, Chang et al. (2000) deliberately reduced the speed of MLC movements by increasing the MU nearly nine-fold from the original prescription, thus restricting the application to only pre-treatment verification. Although the acquisition rate was improved in a later version of the commercial SLIC EPID, the detector was slow in returning to equilibrium state and caused a change in response (or memory effect) when continuously irradiated and sampled at a fast speed of 1 s/image (Chang et al., 2003). To minimise variation due to memory effect, Curtin-Savard & Podgorsak (1999) employed a 1 min per

segment wait-time for a step-and-shoot IMRT verification and as a result, the delivery time for an IMRT field with 88 segments took 1.5 h. The other problem with SLIC EPID dosimetry is the effect of beam hold-off during a dynamic IMRT delivery, where the linac beam pauses while MLC leaves move to position (Chang et al., 2003). Because the SLIC EPID measures in dose rate, the inappropriate increase in delivery time would result in inaccurate dose conversion. The other factor that may affect SLIC EPID dosimetric accuracy is the variation in local detector response with different gantry angles. This gantry-dependent sensitivity variation, also known as the bulging effect, is caused by the non-uniform pressure distribution in the liquid layer due to gravity (Yin et al., 1994) and can amount to about 3% deviation if uncorrected (Van Esch et al., 2001).

1.5.8.2 Charge-coupled device camera-based (CCD) EPID

Principle of operation

Another earlier model of EPID is the camera-based (CCD) EPID. This type of EPID comprises a fluorescent screen, mirror(s) and a CCD-based camera (Figure 1-2). The fluorescent screen, which consists of a steel plate coated with a phosphor layer (gadolinium oxysulphide, Gd_2O_2S:Tb), converts radiation to visible photons. The visible photons are reflected via mirror(s) and imaged by the CCD-based camera. The mirror allows the camera to be positioned away from direct radiation exposure that could damage the CCD chip. A prototype CCD EPID was described by Visser et al. (1990) and was later commercialised as SRI-100 (Philips Medical Systems, Best, The Netherlands). The SRI-100 CCD EPID has a fluorescent screen that is 40 x 30 cm^2 in size, a CCD camera with 512 x 256 pixels and consequently a detector resolution of 0.08 x 0.12 cm^2. Other commercially available CCD EPID includes Beamview Plus (Siemens, Concord, CA, USA) and TheraView (Cablon Medical, Leusden, The Netherlands).

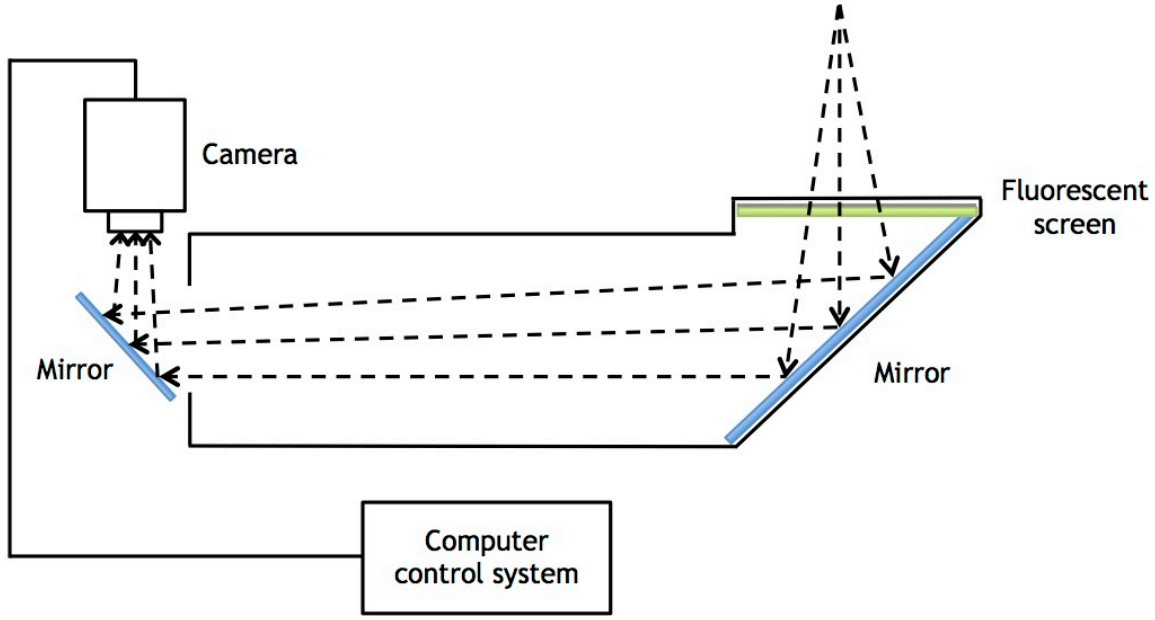

Figure 1-2 A simplified illustration of a charge-coupled device camera-based (CCD) EPID.

Characteristics

Unlike SLIC EPID, CCD EPID does not require row-by-row scanning of the detector matrix. Instead, signals for the whole matrix are detected simultaneously, resulting in a fast image acquisition. The image acquisition for CCD EPID involves the following steps. First, signals are accumulated in the CCD chip for a pre-set amount of time (typically ranging from 0.24 s to 1 s). Then, the accumulated signal is transferred from the CCD chip to the frame grabber to form one image frame. Although no signal is measured during this transfer, the dead time is negligible at only 0.0002 s for newer models of CCD EPID (Franken et al., 2004). The final image is formed by the accumulation of multiple image frames in the frame processor. For dosimetry purposes, the number of accumulated image frames is dependent on the irradiation time and is calculated to capture the whole delivery. As an example, if the irradiation time for a treatment field is 30 s and the accumulating time for one frame is set to 0.24 s, then a total of at least 125 frames are needed to capture the complete delivery.

Besides fast acquisition, the CCD EPID also showed good stability with less than 1% variation in its short- and long-term response (Dirkx, 1995, Heijmen et al., 1995, De Boer et al., 2000, Franken et al., 2004). The CCD EPID response was also found to be independent of gantry angle (De Boer et al., 2000). As for the dose-response relationship, the CCD EPID showed linear response to dose (Dirkx,

1995, Heijmen et al., 1995, De Boer et al., 2000) but non-linearity was observed for certain EPID models when the EPID dose (or pixel value) was high (Pasma et al., 1998, Franken et al., 2004). The under-response at high dose was mainly attributed to out-dated electronics (Pasma et al., 1998) and was not observed for a modified CCD EPID investigated by the same group of researchers (De Boer et al., 2000). The other advantage of the CCD EPID is the energy independence. Although the fluorescent layer is not water-equivalent, the CCD EPID response was not affected by changes in energy spectrum when phantoms of different thicknesses were placed in the beam (Heijmen et al., 1995, Pasma et al., 1998).

The general weakness of CCD EPID is the low collection efficiency, with only 0.01% to 0.1% of the total light emitted by the phosphor layer reaching the camera (Herman et al., 2001). In fact, the poor efficiency of system is one of the main reasons that both SLIC and CCD EPIDs are now obsolete. For dosimetry purposes, the main disadvantage of CCD EPID is the presence of light scattering that requires complicated correction. The light scattering, commonly referred to as glare or cross-talk, occurs when a photon incident on a point in the fluorescent layer emits visible light that gets reflected by the mirror not only directly towards the camera but also back to another point on the fluorescent layer. In the second scenario, the light then scatters off the fluorescent layer again and is reflected by the mirror towards the camera and detected as an additional signal (Heijmen et al., 1995, Partridge et al., 1999). The increase in signal due to multiple light scattering is dependent on field size and can reach up to 20% of the primary signal (Partridge et al., 1999). Partridge et al. (1999) proposed the use of an anti-scatter grid placed in contact with the fluorescent screen to remove light scattering. Although the anti-scatter grid successfully reduced the light scattering to less than 2%, the method involves in-house modification of a commercial CCD EPID and causes a uniform 25% reduction in overall signal. Alternatively, the measured EPID signal can be de-convolved with a cross-talk kernel derived from a set of on-axis measurements with different square fields (Heijmen et al., 1995, Pasma et al., 1998). Because the cross-talk effect is dependent on position, a more extensive correction method was demonstrated by Franken et al. (2006) using a database of 64 x 64 kernels measured at different positions on the EPID.

1.5.8.3 Amorphous-silicon (a-Si) EPID

Principle of operation

Currently, the most widely used EPID model is the indirect detection flat panel amorphous silicon (a-Si) EPID. This type of a-Si EPID consists of a copper plate, a fluorescent layer and a photodiode system (Figure 1-3). The functions of the copper plate are to produce electrons from incident photons to improve detective quantum efficiency and to absorb low energy scattered radiation that reduces image contrast. For an indirect detection flat panel, an additional fluorescent layer with gadolinium oxysulphide (Gd_2O_2S:Tb) phosphor is used to convert incident radiation into visible light. Underneath the fluorescent layer is the photodiode system comprising an array of photodiodes coupled to thin-film transistors (TFT) embedded on an amorphous-silicon panel. The photodiode absorbs visible light and integrates the resulting charge while the TFT acts as a switch for the row-by-row read-out process. The read-out, amplification and digitisation of signals are controlled by acquisition electronics. A prototype a-Si EPID was first described by Antonuk et al. (1995) and Antonuk et al. (1998) and it has since become the most popular megavoltage imaging system provided by major linac manufacturers. Examples of commercially available a-Si EPIDs are iViewGT (Elekta, Stockholm, Sweden), aS500/aS1000 (Varian, Palo Alto, CA, USA) and OptiVue 500/1000ST (Siemens, Concord, CA, USA).

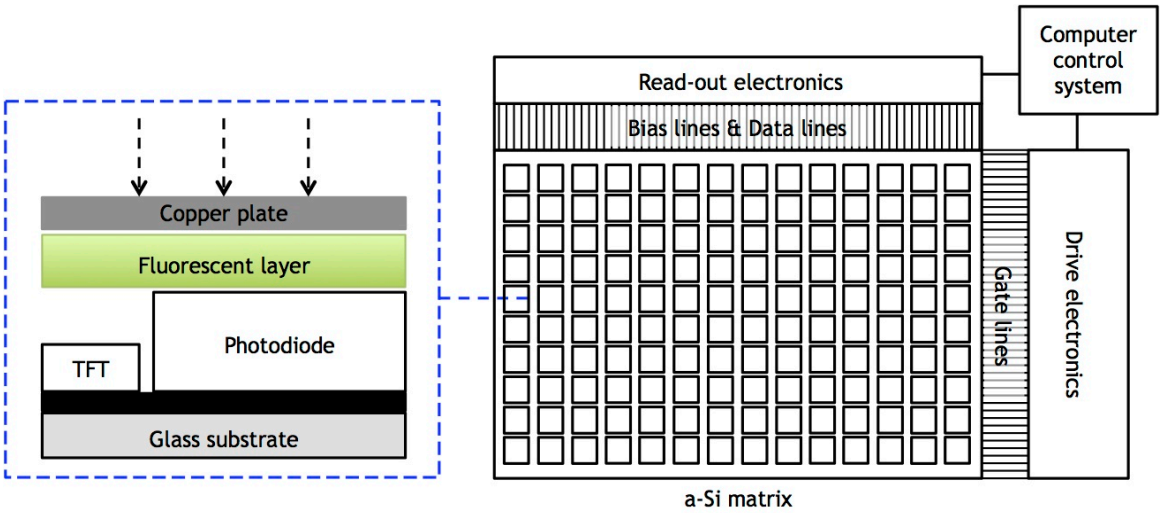

Figure 1-3 A simplified illustration of an amorphous-silicon (a-Si) EPID. A-Si EPID (right) and a cross-sectional view of a detector pixel (left).

Characteristics

The a-Si EPID has the advantage of being compact in size, superior in detector resolution (as small as 0.04 cm) and is capable of fast image acquisition (typically about 0.3 s/frame). Also, the response of a-Si EPID is found to be stable over time, implying that the detector does not require frequent re-calibration for dosimetry purpose. In general, the response of a-Si EPIDs varied by less than 1% to 2% over a 12 months period (Van Esch et al., 2004, Winkler & Georg, 2006) and did not show any dependence on gantry angle (Kavuma et al., 2008).

Furthermore, the dose-response relationship of a-Si EPID is fairly linear which simplifies the conversion of EPID signal (or pixel value) to dose. The linearity of dose response was within 2% from 30 MU to 1000 MU (Winkler et al., 2005, Kavuma et al., 2008) but under-response ranging from 5% to 7% was detected at lower MU (McDermott et al., 2004, Winkler et al., 2005, Kavuma et al., 2008). The trend of under-response at low MU is common to most commercial a-Si EPIDs (McDermott et al., 2006a) and is due to lower sensitivity at the beginning of acquisition. The effect is more pronounced for low MU irradiation because of larger relative contribution of deficit in the early acquisition and becomes less prominent as the total dose increases. The lower response at the start of acquisition can mainly be attributed to charge trapping in the photodiodes that causes delay in charge read-out and also an alteration in the electric field strength that changes the detectors sensitivity (McDermott et al., 2004, McDermott et al., 2006a).

Besides that, the slow release of trapped charges also increases the reading for subsequent frames and can be observed as a persistent image post-irradiation, commonly known as ghosting (Siewerdsen & Jaffray, 1999). Another less dominant source of ghosting is the afterglow of visible light from the phosphor layer (Siewerdsen & Jaffray, 1999). While the ghosting phenomenon was found to be negligible for Varian aS500 EPIDs (Greer & Popescu, 2003, Van Esch et al., 2004, Kavuma et al., 2008), it was more pronounced for Elekta iViewGT EPIDs (Winkler et al., 2005). Variation in ghosting between EPIDs from different manufacturers could be due to differences in the a-Si layer, photodiodes, read-out electronics and image acquisition software settings. Although the signal

enhancement from ghosting was reported to be as much as 9% (Winkler et al., 2005), the experimental setting of 50 MU pre-irradiation followed by a 2.5 MU test field was to simulate an extreme condition that is rare even in a segmented IMRT delivery. Moreover, the 9% increase in response for a 2.5 MU field may not be substantial when evaluated as a complete IMRT delivery with total MU in the order of hundreds. In a more common situation, for example a 5 MU pre-irradiation followed by a 2.5 MU field, the increase in response was generally less than 1.5% for Elekta iViewGT (Winkler et al., 2005). To understand how these two characteristics, non-linearity at low MU and ghosting, would affect an IMRT delivery where multiple low MU segments are integrated, Kavuma et al. (2008) compared the Varian aS500 EPID signal for a single 20 MU delivery with different combinations of low MU segments totalling to 20 MU. Without any correction, the percentage difference between a single 20 MU delivery with 1 MU x 20 segments (most extreme condition) and 5 MU x 4 segments (a more realistic situation) was 2.9% and 1.6% respectively. No comparable experiment can be found for other commercial a-Si EPIDs.

Another dosimetric characteristic that should be evaluated, especially when used for VMAT verification, is the constancy of a-Si EPID response with linac repetition rate (MU/min) setting. Winkler & Georg (2006) investigated 11 Elekta iViewGT EPIDs and reported a 1.4% to 2.8% increase in pixel value when linac repetition rate was doubled. The relative response of EPID deviated by up to 7% when the repetition rate was changed from 12 MU/min to 400 MU/min (Winkler et al., 2005). Meanwhile, a smaller deviation, within 1.8%, was reported for Varian aS500 EPIDs when repetition rate was changed from 100 MU/min to 600 MU/min (Kavuma et al., 2008). The variation in response with repetition rate was related to dose per frame effect (non-linearity of EPID signal and delivered dose in one frame) (Winkler et al., 2005) and may be affected by the EPID acquisition settings (Kavuma et al., 2008).

Perhaps the major hindrance in using a-Si EPID for dose measurement is its energy dependence. Because of the increased probability of photoelectric interaction with high Z material (Gd_2O_2S, z = 64) in the phosphor layer, the a-Si EPID showed an over-response to low energy photons below 1 MeV (Kirkby & Sloboda, 2005). Therefore, the EPID response is expected to vary as the beam

energy spectrum changes with: (1) off-axis position, (2) field size and (3) the presence of an attenuator (either phantom or patient) in the beam.

Firstly, the change in mean energy at off-axis position is a consequence of differential beam hardening by the cone-shaped flattening filter. Because the mean energy is lower at off-axis positions, the response of a-Si EPID was found to be higher than the central axis by up to 29% (Parent et al., 2006). In comparison with IC measurement in water, the a-Si EPID over-responded by 13% at 15 cm off-axis (Greer, 2005).

Secondly, the variation in beam spectrum with field size is due to increased contribution of low energy scattered photons for larger fields. Because of a-Si EPID over-sensitivity to low energy photons, the output factor (output for a field normalised to a 10 x 10 cm^2 reference field) for EPID and IC measurement in water was found to vary by as much as 2.5% for a 6 MV beam (Greer & Popescu, 2003) and 9% for an 18 MV beam (Van Esch et al., 2004). The difference in output factor between EPID and water measurement can also be attributed to the presence of non-water equivalent components in the EPID that increases scattering within the detector itself.

Thirdly, in the presence of an attenuator, the transmitted beam spectrum changes due to attenuation of low energy photons. Kirkby & Sloboda (2005) found that, for a 6 MV beam, the a-Si EPID calibration curves (relative response of EPID versus IC at the same level) measured without and with an attenuator differed by up to 8%. The EPID response was found to be lower for attenuated beams and this effect was attributed to less low energy photons in the transmitted beam that reduces the over-response of EPID. If an attenuator is present in the beam, the effect of additional scatter from the object reaching the EPID must also be considered. The amount of scatter reaching the phosphor layer is inversely proportional to the distance (or air gap) between the object and the EPID. The response of EPID was 14% higher with 10 cm air gap relative to 60 cm air gap for a 6MV beam (McDermott et al., 2004). Grein et al. (2002) reported that the difference in relative transmission between EPID and IC measured dose for a 6 MV beam transmitted through a 21 cm thick polystyrene

phantom was 6% when the air gap was 30 cm and increased to 8% when the air gap was reduced to 16.5 cm.

One possible way to reduce the over-response of a-Si EPID due to beam spectral change is by placing an additional copper plate above the detector to absorb the low energy photons. McDermott et al. (2004) showed that by placing a 2.5 mm copper plate on top of the EPID, the variation in response due to different air gap distance could be minimised to within 1%. However, the additional weight of the copper plate may activate the touch guard of the EPID. Moreover, the placement of copper plate on top of the EPID cover only allows measurement at gantry zero degree. Although technically the copper plate can be permanently fixed inside the EPID, it requires modification of the panel that may not be desirable in most clinical departments. Kirkby & Sloboda (2005) recommended the use of 7 mm copper plate in an elevated position, 15 cm above the EPID, but again this experimental set-up is not practical as it creates mechanical limitation and was found to degrade the image quality.

1.6 Advantages of a-Si EPID over other detectors

Despite the dosimetric challenges described in the above paragraphs, the a-Si EPID has many inherent advantages over other types of detectors. For instance, the a-Si EPID is a 2D detector with much higher spatial resolution compared to 2D array devices. The spatial resolution for a-Si EPID is less than 0.08 cm while the spatial resolution for 2D array devices are typically in the range of 0.5 cm to 1 cm. Although the spatial resolution for film is also excellent, the a-Si EPID has the advantage of not requiring any manual processing and the image is available immediately in digital format. Since the EPID comes as an attachment on most linacs, the cost of using EPID for treatment verification is relatively low because there is no need to purchase additional hardware or consumable items. Moreover, unlike any of the other detectors, the a-Si EPID can be positioned automatically and thus, very convenient to set-up. Most importantly, the a-Si EPID can be used for both pre-treatment and actual treatment verification. The position of EPID panel perpendicular to the radiation source and behind the patient allows passive measurement of radiation without interfering with the delivery of treatment.

These advantages have led to the search for solutions to overcome the dosimetric challenges associated with a-Si EPID. A literature review on the different approaches to a-Si EPID dosimetry are summarised in the next chapter. The gap in knowledge and the aim of this research will also be discussed.

Table 1-1 Characteristics of different detectors used for patient-specific treatment verification.

	IC	Diode	MOSFET	TLD	OSLD	Radiographic film	Radiochromic film	a-Si EPID[a]
Measurement dimension	Point or 2D[c]	Point or 2D[c]	Point	Point	Point	2D	2D	2D
Application	Pre-treatment	Actual treatment or Pre-treatment[c]	Actual treatment	Actual treatment	Actual treatment	Pre-treatment	Pre-treatment	Actual treatment or/and Pre-treatment
Reproducibility	Good	Good	Moderate	Moderate[d]	Moderate[d]	Moderate[d]	Moderate[d]	Good
Dose linearity	Good	Good	Good	Moderate[e]	Moderate	Moderate[e]	Moderate[e]	Good
Energy independence[b]	Good	Poor	Poor	Good	Poor	Poor	Good	Poor
Temperature independence	Poor	Poor	Good[e]	Good	Good	Poor	Moderate	Moderate[g]
Angular independence	Good[f]	Poor	Good[e]	Good	Good	Poor	Good	Good
Spatial resolution	Poor	Good	Good	Good	Good	Good	Good	Good
Read-out convenience	Good	Good	Good	Poor	Moderate	Poor	Moderate	Good
Lifespan	Good	Moderate	Poor	Poor	Poor	Not applicable	Not applicable	Good
Other advantages	• Gold standard • Traceable to PSDL • Well established correction factors	• Rugged	• Less dose perturbation compared to diode	• Available in different forms and shapes (very adaptable) • No cables	• Signals can be re-read • No cables	• Permanent record	• Not sensitive to visible light • Self-develop	• Minimal set-up • Digital record • Hardware readily available as part of the linac
Other disadvantages	• Risk of charge particle disequilibrium for small field • Risk of fluence-averaging perturbation effect for high gradient field	• Dose perturbation due to the presence of build-up cap • Requires many correction factors • Requires re-calibration due to radiation damage	• High cost considering the short lifespan	• Tedious post-processing • Delayed results	• Change in sensitivity and reproducibility with accumulated dose	• Inter-batch response variation • Sensitive to light and processing conditions	• Inter-batch response variation • Continuous polymerisation • Requires strict scanning protocol • Much more expensive than radiographic film	• Requires a dosimetric model to convert EPID signal to dose distribution

Note: Performance are categorised into three groups – 'Good', 'Moderate' and 'Poor'. Numerical values are given in text with the respective references.

[a] Only a-Si EPID is included since it is currently the most common type of EPID

[b] Energy independence to low energy photons

[c] Commercial 2D array detectors in a phantom

[d] Assumes strict adherence to standardised protocols

[e] Dependent on detector type/model

[f] Cylindrical IC

[g] Warm up effect: Detector sensitivity lower by 2.5% after an extended period in the standby mode (Winkler et al., 2005)

Chapter 2: Literature review and aim of research

2.1 Literature review

The main challenge with a-Si EPID dosimetry is the presence of high Z material in the phosphor layer, which causes deviation from water-equivalent behaviour. Various investigators have proposed different methods to workaround the dosimetric problem inherent to a-Si EPID. The focus of this literature review is on the different approaches to a-Si EPID dosimetry.

Only a-Si EPID is included in this review as it is currently the most widely available EPID model. Methods that involved a-Si EPID in direct configuration mode (without the phosphor layer) are excluded because the direct detection a-Si EPID is not commercially available and requires in-house modification of the EPID panel. From here onwards, the 'a-Si EPID' will be referred to as 'EPID' for brevity.

2.1.1 Search strategy

Literature searches were carried out on the Embase, Ovid Medline, Scopus and Web of Science databases. The terms used for search were 'EPID dosimetry', 'portal dosimetry' and 'treatment verification'. Primary studies included were published from January 1995 until April 2015 with the language of report in English. Relevant references cited in the primary studies were also included regardless of publication year. Conference abstracts without full papers were excluded.

2.1.2 Definition of common terminology

Different terms are used in the literature when describing EPID dosimetry techniques. For clarity, a common set of terminology, defined in the following sub-sections, will be used in this literature review.

2.1.2.1 Measurement arrangement: Non-transit & transit dosimetry

Depending on the measurement arrangement, EPID dosimetry model can be referred to as non-transit or transit dosimetry.

- ***Non-transit dosimetry***: refers to EPID measurements without attenuator between the source and EPID detector. The EPID measures radiation through air and without transiting any object.
- ***Transit dosimetry***: refers to EPID measurements with an attenuator, either a phantom or patient, between the source and EPID detector. The EPID measures radiation that transits through the attenuator.

Figure 2-1 shows the measurement arrangement for non-transit and transit dosimetry. Since no attenuator can be present for non-transit dosimetry, the technique is limited to only pre-treatment verification. On the other hand, transit dosimetry can be used for both pre-treatment and actual treatment verification with phantom and patient in the beam respectively.

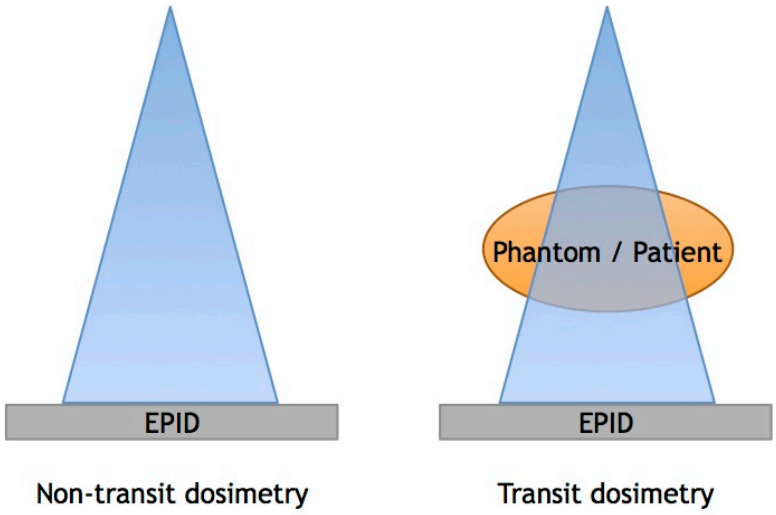

Figure 2-1 Arrangement for EPID dosimetry measurement. Non-transit dosimetry (left) and transit dosimetry (right).

2.1.2.2 Comparison location: EPID plane & in-phantom/in-vivo

EPID dosimetry models can be differentiated based on where the dose is predicted (or reconstructed) and compared.

- ***Comparison at EPID plane***: refers to a dosimetry model that predicts dose at the EPID detector. The predicted dose is compared directly to the EPID measured dose plane.
- ***Comparison in-phantom/in-vivo***: refers to a dosimetry model that reconstructs dose inside a phantom (in-phantom) or patient (in-vivo) from EPID images. The reconstructed dose is usually, but not always, compared to the TPS dose computed for the phantom/patient.

Comparison at the EPID plane has the advantage of being more efficient because the dose at the EPID is only predicted once and repeatedly used for comparisons with EPID images measured on different treatment days. On the other hand, comparison in-phantom/in-vivo uses EPID images captured during different treatment days as an input and therefore, requires dose to be reconstructed each time. However, comparison in-phantom/in-vivo is verified in a more clinically relevant location and usually in centigray (cGy) units. Discrepancies seen at the EPID plane are less meaningful, especially when the unit of comparison is expressed in pixel values. Furthermore, the dose comparison in-phantom/in-vivo can be extended to a 3D volume. In the case of in-vivo dose comparison, patient computed tomography (CT) images can be used to reconstruct 3D dose to different organs or regions of interest and comparison can be done in terms of DVHs.

2.1.3 EPID dosimetry model

In general, different EPID dosimetry models reported in the literature can be classified into three broad categories based on the methods used for dose prediction/reconstruction: Monte Carlo (MC)-based model, convolution-based model and empirical-based model.

2.1.3.1 Monte Carlo (MC)-based model

MC-based EPID dosimetry model uses MC simulation in the dose prediction/reconstruction process, which requires detailed modelling of the linac's radiation source, components in the treatment head, phantom/patient if present in the beam and the EPID panel. During the simulation process, a phase space file is created that specifies energy, position, direction and statistical weight of each photon and electron transport. This phase space file is then used to score the energy deposition in phantom/patient or EPID detector for absorbed dose computation. Because MC is capable of simulating to a high accuracy the physical principles of photons and electrons interactions, it is the most accurate form of prediction model.

For non-transit dosimetry, EPID response can be simulated and compared directly to EPID measured image. This is the simplest form of MC-based EPID

dosimetry model and was demonstrated by Parent et al. (2006) and Siebers et al. (2004). In both studies, the MC simulated EPID response showed excellent agreement with EPID measurement for a small number of IMRT fields. The gamma pass rates were above 98% for gamma criterion 3%/2mm and 2%/2mm used by Parent et al. (2006) and Siebers et al. (2004) respectively.

As for transit dosimetry, various authors have proposed different MC simulation methods. For comparison at the EPID plane, Kairn et al. (2011) used a MC code to combine the phantom and EPID model for simulation of EPID response in a transit arrangement. The simulated EPID response was compared directly with EPID transit measurement. Instead of a single simulation, Lin et al. (2009) proposed a two-stage MC simulation that first simulates dose within the phantom and then at the EPID plane. For the first stage, EPID images acquired through air was needed to simulate the in-phantom dose and comparison with TPS served as a pre-treatment verification. For the second stage, the simulated EPID transit dose was compared with EPID image measured during treatment for actual treatment verification. Excellent gamma agreement (>98.6%, using 3%/3mm criterion) for both types of comparisons was reported for three IMRT fields tested on homogeneous slab phantom.

Jarry & Verhaegen (2007) described a MC simulation method that used the EPID transit image measured during treatment to reconstruct in-phantom dose for comparison with a full MC dose calculation engine in place of a commercial TPS. The measured EPID image was separated into primary and scattered components and the former was back-projected for in-phantom dose reconstruction using MC simulation. For an anthropomorphic phantom irradiated with a 10 x 10 cm^2 open field, the gamma comparisons with 5%/3mm criterion showed 87% agreement between in-phantom mid-sagittal dose reconstructed from measured EPID image and the reference dose from MC dose calculation engine without measurement input. The author attributed the inferior results to uncertainty in phantom alignment and EPID position. Despite the inferior results, the study served to show that a verification method completely independent of TPS was possible.

An interesting observation from this literature review on MC-based EPID dosimetry was that all the studies reported their results based on a very small

number of test fields (ranging from one to four fields only). This is probably due to the time consuming nature of MC simulation. To speed up the MC simulation, Lin et al. (2009) incorporated measurement and convolution in the MC model but even so, the time required to simulate one case was almost 6.4 h on a 10 PC cluster, each with a 2.8 GHz CPU. Because of the intensive computation requirement, the routine application of MC-based EPID dosimetry may not be currently possible especially in clinical departments with a large number of linacs and limited resources.

2.1.3.2 Convolution-based model

Convolution-based EPID dosimetry models employ kernels that describe scatter or dose deposition properties in EPID or phantom/patient. Convolution and de-convolution of different kernels are used in various stages of the dosimetry model to give a desired parameter. For example, de-convolution of the scatter kernel from the EPID measured dose distribution gives the primary fluence while convolution of the primary fluence with the dose deposition kernel results in absorbed dose distribution. Kernels can be generated either by measurements or MC simulations.

Non-transit EPID images can be used to reconstruct in-phantom or in-vivo dose, by means of convolution, for comparison with the intended dose. In the model described by Ansbacher (2006), the EPID response for non-transit arrangement was first calibrated to the equivalent dose at the mid-plane of a cylindrical water phantom before the EPID dose distribution was convolved with a scatter kernel to account for differences in EPID and cylindrical phantom scattering. The reconstructed in-phantom dose was compared to the TPS dose computed for a similar virtual cylindrical water phantom. Because the EPID was calibrated to a fixed depth in a phantom, the model was limited to dose prediction for that particular phantom only. For a wider scope of application, most EPID dosimetry models aimed to retrieve the primary fluence incident on EPID detectors. In a non-transit arrangement, the primary fluence can be retrieved by de-convolution of EPID measurement with EPID scatter kernel. Subsequently, the primary fluence can be used in different ways to reconstruct dose. Warkentin et al. (2003) convolved the primary fluence with a water phantom dose deposition kernel to reconstruct in-phantom dose. Meanwhile, Steciw et al. (2005) used the

primary fluence as an input to the TPS. Together with patient CT images, 3D in-vivo dose was recalculated by the TPS using the EPID measured fluence. However, the method was not clinically feasible because of the excessive time required to convert measurement files into a format recognisable by the TPS. Furthermore, the use of TPS for dose reconstruction may mask certain inaccuracies in the TPS algorithm. Rather than using the TPS, Renner et al. (2005) entered the primary fluence into an independent commercial dose calculation algorithm, Dosimetry Check (Math Resolutions, Columbia, MD, US), for 3D in-vivo dose calculation. Zhu et al. (2015) used a rather similar approach but with an in-house collapsed-cone convolution/superposition calculation algorithm implemented on a graphic processing unit (GPU) to achieve fast computation speed. Alternatively, Van Elmpt et al. (2006) used the primary fluence as input to an in-house MC dose engine to reconstruct 3D in-phantom dose distribution. By using a method independent of the TPS for dose reconstruction, Van Elmpt et al. (2007) proved that inaccuracies in TPS algorithms could be detected, as confirmed by results from film measurements. The developed EPID dosimetry model was used as a pre-treatment verification tool for 3D conformal as well as IMRT plans, and dose agreement with TPS was evaluated in terms of DVHs (Van Elmpt et al., 2008b).

For transit dosimetry, the fluence incident on the EPID consists of both primary and scattered radiation from phantom/patient. In the model proposed by McCurdy & Pistorius (2000), McCurdy et al. (2001) and Chytyk & McCurdy (2009), the primary and scattered fluence incident on the EPID were predicted separately using patient CT data and libraries of MC generated scatter kernels. Subsequently, the incident fluence was convolved with the EPID dose deposition kernel to predict the EPID transit dose for direct comparison with EPID measurement. Instead of predicting EPID transit dose, Chen et al. (2006) and Nijsten et al. (2007) converted the measured EPID transit image to water-equivalent dose distribution, for comparison with IC measurement in water at the EPID distance. Correction factors and kernels derived from measurements with different field sizes and attenuator thicknesses were used in the conversion process. The correction factors and kernels served to correct for differences in scatter within the EPID and water as well as variation in response as the beam energy spectrum changes with attenuator thickness, field size, off-axis position

and scatter from the phantom. Although both authors reported good agreement between EPID converted and IC measured dose distributions, the need to set-up the scanning water tank and perform IC measurements in water for each test field was too cumbersome for routine clinical implementation.

Another option for EPID transit dosimetry was to use the convolution method to reconstruct dose in-phantom/in-vivo from the EPID measured transit image, as reported by the group of researchers from The Netherlands Cancer Institute. Briefly, as described by Wendling et al. (2006), the EPID measured dose distribution was de-convolved with the EPID scatter kernel and subtracted with radiation scattered from phantom to EPID, to retrieve the primary fluence. Then, the primary fluence was back-projected to reconstruct 2D dose at the mid-plane of a homogeneous phantom using an inverse square law (ISQL) correction, attenuation correction from mid-plane to exit surface and correction for scattered radiation within the phantom. Pre-treatment verification with a slab phantom for 50 IMRT prostate fields showed good agreement with film measurement (99.1% pass rate using 2%/2mm criterion) and comparison with TPS dose revealed a systematic error that was subsequently traced to an incorrect MLC setting in the TPS (McDermott et al., 2006b). The model was also proven to be useful for 2D in-vivo actual treatment verification of prostate IMRT treatment by comparing reconstructed dose with TPS planned dose at the isocentre level (McDermott et al., 2007). Wendling et al. (2009) further extended the model to reconstruct 3D in-vivo dose, where multiple 2D planes parallel to the EPID were reconstructed for each gantry angle, summed in a 3D grid and overlaid on patient CT data. The attenuation at different reconstruction planes was estimated from ratio of geometrical path length, from plane of interest to exit surface, derived from patient external body contour. Comparison of 3D in-vivo reconstructed dose and TPS computed dose showed excellent agreement for nine patients undergoing prostate IMRT treatment (99% pass rate using 3%/3mm criterion) (McDermott et al., 2008) and the same model was also proven to be feasible for VMAT treatments (Mans et al., 2010a).

The only major limitation with the proposed model was the assumption of homogeneous condition that caused large deviation in the presence of inhomogeneity, such as in the lung region. Wendling et al. (2012) presented a

workaround, which involved modification of the measured EPID transit image to mimic transmission through a homogeneous patient. The reconstructed dose was compared to the TPS computed dose with homogeneity correction turned off. Using the modified model for 10 lung cases, the results for 3%/3mm gamma evaluations improved from an average of 66.2% to 93.1% for IMRT plans and 43.6% to 97.5% for VMAT plans (Wendling et al., 2012). Despite the considerable improvement in results, the method was not ideal because the comparison was not made in a true situation and TPS accuracy in the presence of inhomogeneity could not be checked. But overall, the proposed convolution-based model was proven to be suitable for large-scale implementation. Since January 2008, the EPID transit dosimetry model has been routinely used for verification of almost all IMRT and VMAT treatments in The Netherlands Cancer Institute (Mijnheer et al., 2010). The analysis and reporting of results has since been automated to improve efficiency and further streamline the clinical workflow of EPID in-vivo verification (Olaciregui-Ruiz et al., 2013).

In general, compared to MC-based models, convolution-based models are less accurate in the presence of inhomogeneity, especially if the kernels and correction factors were derived in homogenous medium. However, convolution-based EPID dosimetry models are less computationally intensive and the use of pre-generated kernels saves calculation time. The shorter calculation time for convolution-based models made it practical for clinical implementation, as demonstrated by The Netherlands Cancer Institute. But convolution-based models still require appropriate expertise, software and hardware for mathematical modelling and therefore, are mostly contained in the research department where the model was developed.

2.1.3.3 Empirical-based model

An empirical-based model uses only experimental measurements in the calibration and dose prediction/reconstruction process. Due to the limited number of measurements that can be carried out, assumptions are usually made that may affect the accuracy of results. However, models with only physical measurements are the most practical and can be adopted in all centres. Different approaches have been described in the literature for empirical-based EPID dosimetry model. They include: (1) measuring EPID beam model to replace

the usual water-based beam model in the TPS; (2) measuring at a reference condition where EPID response can be considered identical to water; or (3) measuring coefficients and corrections factors to account for differences between EPID and water phantom.

The first type of approach used output factors and profiles measured with the EPID, rather than an ionisation chamber in water, to create a dedicated EPID beam model in a commercial TPS. While maintaining the original water dose deposition kernel in the TPS, Khan et al. (2008) iteratively optimised various TPS parameters such as energy spectrum, source size, jaw transmission, MLC transmission and electron contamination until a best fit was achieved between TPS computed and EPID measured profiles and output factors. The optimised EPID beam model in the TPS was then used to compute EPID dose for direct comparison with the EPID dose measured in a non-transit arrangement. Evaluation of a nine-field IMRT plan resulted in more than 95% of evaluated points passing the 3%/3mm gamma criterion. Van Esch et al. (2004) and Rosca & Zygmanski (2008) also proposed models that involved modification of a water beam model in commercial TPS for EPID dose prediction. But rather than adjusting various parameters without any physical meaning, the original water dose deposition kernel in the TPS was replaced by the EPID dose deposition kernel. The EPID kernel was derived from fitting the computed and measured EPID dose distribution for a single dynamic MLC test field (Van Esch et al., 2004) or for a set of MLC test fields (Rosca & Zygmanski, 2008). Since all the above-mentioned models were for non-transit dosimetry, Berry et al. (2012) extended the model by Van Esch et al. (2004) to allow EPID dose prediction in a transit arrangement. The model used MC simulation to quantify the decrease in primary fluence as a function of attenuator thickness and a set of EPID measurements to account for variation in EPID response as the beam spectrum changed with field size and thickness. The two components were added to the initial TPS prediction of EPID dose. Verification with an anthropomorphic phantom for 33 IMRT fields showed that an average of 98.1% pixels passed the 3%/3mm gamma evaluation. Apart from the model by Khan et al. (2008), all the other models were not strictly empirical-based models but were included in this section since the basic concept, of replacing TPS water-based beam model with an EPID beam model, was the same. The main disadvantage of this approach was the inability to verify

the accuracy of actual clinical beam model since the EPID beam model was used for the TPS calculation.

The second type of empirical-based EPID dosimetry model involved determining a reference condition, where the EPID showed similar dosimetric behaviour as water measurements. EPID measurement under this condition can be calibrated to dose and compared directly to TPS calculated dose in water. To find this reference condition, Talamonti et al. (2006) evaluated the EPID response for different combinations of field size, phantom thickness, air gap and Copper filter. The authors established that for a 6 MV beam, the variation of EPID response with field size (from 3 x 3 cm^2 to 20 x 20 cm^2) could be minimised to within 3% if measured with a 20 cm water phantom, 56 cm air gap and a 3 mm Copper filter. By measuring at this reference condition, a universal calibration factor independent of field size could be used for straightforward conversion of EPID signal to equivalent dose in water. Comparison between EPID measured dose and TPS calculated dose in a water phantom showed a mean gamma agreement of 97.6% for 15 IMRT fields investigated. Meanwhile, Lee et al. (2009) found that the same could be achieved with a simpler set-up with no attenuator (non-transit arrangement). The EPID measured profiles and output factors for field size 2 x 2 cm^2 to 15 x 15 cm^2 were similar to measurements in water at a reference depth of 5 cm and 3 cm for 6 MV and 18 MV beam respectively. Using a universal calibration factor independent of field size, the EPID signal was converted to dose and compared with TPS computed dose in water at the reference depth. The gamma pass rate for 14 6 MV IMRT fields ranged from 93.6% to 99% when the analysis criteria was set at 3%/3mm. Results for comparison with TPS were not presented for 18 MV IMRT fields. Although relatively simple and straightforward, both non-transit and transit EPID dosimetry models based on this approach were restricted to pre-treatment verification because of the fixed measurement set-up.

The third, and most common, type of empirical-based EPID dosimetry model involved performing a series of measurements to derive correction factors and coefficients to account for differences between EPID and water measurements. For non-transit dosimetry, the EPID response is dependent on field size and different from water measurement. Instead of using a pre-generated table of

correction factors, Nicolini et al. (2006) proposed the use of general coefficients to calculate correction factors based on field size (General Linear calibration Algorithm, GLAaS). The general coefficients were derived separately for primary and MLC transmission radiation by fitting a limited number of open and MLC-closed fields respectively. With these coefficients and field size extracted from MLC file, the appropriate correction factor could be determined for every segment in an IMRT delivery for the conversion of EPID signal to dose. The sum of converted EPID dose was compared to TPS computed dose in water. To avoid dose comparison at surface (the inherent build up of EPID was only 0.8 cm), slabs of water phantom were placed on the EPID for all measurements and the TPS dose was computed for the same depth. The mean gamma agreement between EPID measured and TPS computed dose for 34 IMRT fields evaluated using 4%/3mm criterion was 97.7% and 96.9% for build up 1.5 cm and 3.8 cm respectively, comparable with film verification of the same fields (97.6%).

For a transit arrangement, the EPID signal to dose in water correction factor is dependent not only on field size, but also attenuator thickness and air gap. With the additional variables, it is impractical to physically measure the correction factor for all possible combinations of parameters. Francois et al. (2011) and Piermattei et al. (2006) have described different ways to reconstruct in-vivo point dose at the central axis from EPID transit signal. The model by Francois et al. (2011) first converted the EPID transit signal to transit dose in water at maximum depth (d_{max}) via a correction factor. Then, dose in water at d_{max} without attenuator was derived using the Transit Tissue Maximum Ratio (TMR^t), defined as the ratio of dose in water at d_{max} measured with and without attenuator. Because TMR^t was dependent on field size, thickness and air gap, fitting coefficients were derived to reduce the number of measurements required. Finally, in-vivo dose at the isocentre was reconstructed by applying ISQL correction and conventional Tissue Maximum Ratio (TMR). Comparison between reconstructed and TPS computed point dose for 145 patients undergoing pelvis treatment showed a mean deviation of -1.0±2.2% (1SD) and -0.3±2.6% (1SD) for 3D conformal and IMRT treatment respectively (Camilleri et al., 2014) . As for the model by Piermattei et al. (2006) and Piermattei et al. (2007), a set of correlation functions, defined as the ratio of EPID transit signal to IC dose at the mid-plane of a homogeneous phantom, was measured at the

central axis for a limited number of square fields and phantom thicknesses. Fitting coefficients were derived so that correlation function and consequently, the in-vivo mid-plane dose could be reconstructed if the field size, phantom thickness and EPID transit signal were known. The same group of researchers later published generalised correlation functions for Elekta (Cilla et al., 2011), Varian (Fidanzio et al., 2011a) and Siemens (Fidanzio et al., 2011b) linacs to allow easier implementation by other users without having to repeat the calibration measurements. Piermattei et al. (2012) reported the first results of using the generalised procedure in three centres with different linacs for 3D conformal pelvis treatments. Out of the 480 fields analysed, 45 fields deviated from the TPS dose by more than 5% and the discrepancies were attributed to the presence of bowel gas, incorrect set-up and error in TPS wedge parameter. A later report by Fidanzio et al. (2015) included results for other 3D conformal treatment sites (pelvis, breast, lung and head and neck) over three years in a centre with three linacs (n = 1287) and again showed that the in-vivo dose verification was effective in detecting errors, which led to intervention in 19 cases. The model has since been extended for point dose verification of IMRT (Greco et al., 2013) and VMAT delivery (Fidanzio et al., 2014). The use of generalised factors is an advantage as it saves measurement time and is, therefore, more likely to be accepted by users. The main shortcoming of both methods was the point comparison at central axis, which was not ideal because treatment accuracy could not be verified elsewhere in the field.

Instead of reconstructing dose to a point, Peca & Brown (2014) adapted the model by Piermattei et al. (2006) for 2D in-vivo dose reconstruction from EPID transit signal. In the original model, the correlation functions were defined only at the central axis. To quantify the variability of these correlation functions at off-axis positions, 2D EPID image was divided by TPS computed 2D dose (instead of IC measured point dose) at the mid-plane of water phantom and then, normalised to the central axis. From this 2D relative matrix, 1D in- and cross-plane correction profiles were extracted and multiplied to the original correlation function derived at the central axis. Also, a 2D map of radiological path length was derived from CT data to account for tissue inhomogeneity. Validation with 3D conformal fields on an anthropomorphic phantom showed good agreement in the head region (≥96.5% with 3%/3mm criterion) but over-

estimation of dose up to 9% was observed in the lung region. The authors attributed the dose discrepancies to inadequate in-phantom scatter correction and failure of the 1D correction profiles to properly account for off-axis variation for highly irregular fields. The model was not validated for delivery of IMRT fields.

Alternatively, Kairn et al. (2008) proposed the use of a quadratic equation to convert EPID transit signal to 2D radiological or equivalent path length (EPL) as a form of treatment verification. The quadratic equation, established by Swindell (1983), relates the reduction in radiation intensity due to the presence of an attenuator to the thickness of the attenuator. The coefficients in the quadratic equation were generated in 2D to include off-axis variations by fitting, pixel-by-pixel, a set of EPID transit signal measured for homogeneous phantoms of different thicknesses (Morton 1991). Since dose, and not EPL, is the preferred metric for treatment verification, Kavuma et al. (2010) used the EPL calculated from EPID transit signal to reconstruct 2D entrance and exit in-phantom doses. The conversion of EPL to dose required a pre-generated look-up table of percentage exit thickness dose (PETD) values given as a function of field size and thickness. The PETD values were derived from Tissue Phantom Ratio (TPR) and theoretically justified by the authors. Envelope and boundary profiles generated from the Pencil Beam Convolution algorithm in Eclipse TPS (Varian, Palo Alto, CA, USA) were also required for off-axis dose calculations. The model was evaluated with 3D conformal fields on anthropomorphic phantom. Comparison between reconstructed and TPS computed in-phantom dose resulted in 90% of points passing 3%/3mm gamma criterion, with discrepancies observed at the penumbra region (Kavuma et al., 2011). Despite the advantage of being a 2D empirical-based EPID transit dosimetry model, the method was also not validated for IMRT fields, which is the main focus of treatment verification.

Sabet et al. (2014) reported a 2D empirical-based EPID transit dosimetry model that could be used to verify IMRT fields. However, the model only aimed to convert measured EPID transit signal to equivalent dose in water. The converted EPID transit dose was then compared to another transit dose measured by a commercial 2D IC-array, MatriXX (IBA Dosimetry, Schwarzenbruck, Germany), positioned at the EPID level. This strategy cannot be used for actual treatment

verification since it is not possible to perform two deliveries in a single treatment fraction for a patient. In fact, there is little value in comparing two consecutive measurements, albeit using different devices, with no information on the agreement with the intended or planned dose. Therefore, despite the transit arrangement and validation with IMRT fields, the usefulness of the model is limited.

Overall, empirical-based EPID dosimetry model is possibly the most practical model for clinical centres with limited resources for computationally intensive MC simulations or mathematical modelling. In addition, most methods in empirical-based models involved general measurements that can be accomplished by a clinical physicist without requiring special expertise. Also, general measurements can be performed on all linacs and EPIDs regardless of manufacturer. However, there is a lack of publication on empirical-based EPID transit dosimetry for 2D or 3D verification of modulated IMRT or VMAT fields.

2.1.3.4 Others

Baek et al. (2014) used the EPID to measure transit radiation and compare it with TPS computed dose at the EPID level. The described method does not fall into any of the categories above because, aside from a simple calibration curve to convert EPID pixel value to dose in cGy, no other considerations were given to account for the dosimetric differences between EPID and a water-equivalent detector. In the TPS, an over-simplified virtual EPID was created at 130 cm from source and contoured as part of the body for dose computation. Relative gamma comparisons (using 3%/3mm criterion) between TPS-computed and EPID-measured dose for 24 IMRT fields with an anthropomorphic phantom resulted in average pass rate of 86.8%. The author suggested that the method could potentially be used as a crude way to detect delivery of a wrong treatment field or treating a wrong patient.

2.2 Commercial software

2.2.1 Non-transit EPID dosimetry software

The majority of commercial software packages are for non-transit measurement and can only be used for pre-treatment verification. Non-transit EPID dosimetry software that are currently commercially available are:

- Portal Dosimetry by Varian (Palo Alto, CA, USA)
- EPIDose by Sun Nuclear (Melbourne, FL, USA)
- Epiqa by EPIdos (Danube, Slovakia)

2.2.1.1 Portal Dosimetry (Varian, Palo Alto, CA, USA)

The Portal Dosimetry software is based on the method described by Van Esch et al. (2004) (see Section 2.1.3.3). The software predicts the 2D EPID dose plane for comparison with EPID measurements in a non-transit arrangement. The Portal Dosimetry Image Prediction (PDIP) algorithm, a module in the Eclipse TPS, uses a dedicated EPID beam model instead of the clinical water-based beam model to predict the EPID dose plane. In the Portal Dosimetry mode, both the PDIP and EPID are calibrated to produce dose plane values in Calibrated Units (CU). The Portal Dosimetry solution has a unique advantage of being completely integrated with the clinical workflow. The EPID image acquisitions, TPS prediction and dose plane comparisons, are seamlessly integrated and stored as part of the clinical database. As a consequence, the Portal Dosimetry treatment verification does not require any import/export and the analysis of results can be easily reviewed and managed in modules built into the TPS and oncology information system. On the other hand, integration of Portal Dosimetry into TPS and oncology information system limits its availability to only Varian users. Also because of this integration, the Portal Dosimetry cannot be considered as an independent verification system. Another inherent weakness of Portal Dosimetry software is that the use of a separate EPID beam model does not check the accuracy of actual clinical dose calculation.

2.2.1.2 EPIDose (Sun Nuclear, Melbourne, FL, USA)

EPIDose uses an algorithm to convert a non-transit EPID image to equivalent 2D dose at depth in a homogenous water phantom for comparison with TPS calculated dose and a description of the reconstruction algorithm can be found

in Nelms et al. (2010). Briefly, the conversion process from pixel value to dose in water involves: (1) per segment field size output correction, weighted according to primary and transmitted radiation exposure, (2) convolution with a kernel that accounts for scatter difference between EPID and water and finally (3) absolute dose calibration by comparing EPID signal with dose measured with diode array (MapCHECK, Sun Nuclear, Melbourne, FL, USA), for open fields of different MUs. The EPIDose, when used in conjunction with 3DVH (Sun Nuclear, Melbourne, FL, USA), allowed reconstruction of 3D dose on patient CT data for DVH analysis. The 3DVH is based on the concept of applying dose perturbation (quantified from difference between measured and expected dose) to the 3D dose originally computed by the TPS algorithm. It provides an estimate of the effect of dose discrepancies on organs of interest but does not check the accuracy of TPS algorithm. Although comparisons can be made in-vivo using the additional 3DVH software, it should not be confused with actual treatment verification since the EPID measurement is done prior to treatment and without the patient.

2.2.1.3 Epiqa (EPIdos, Danube, Slovakia)

Epiqa is based on the GLAaS algorithm detailed by Nicolini et al. (2006) (see Section 2.1.3.3). The aim of Epiqa is also to convert the EPID image measured in a non-transit arrangement to dose in water for comparison with the TPS computed dose in a water phantom. Similar to EPIDose, the GLAaS algorithm applies per segment field size output correction weighted according to fractional contribution of primary and transmitted radiation. The field size correction factor was calculated using general coefficients derived from a limited number of measured data. But unlike EPIDose, the algorithm does not include a scatter kernel. Also, build-up in the form of solid water phantom slabs must be placed atop the EPID panel during measurement. This requirement limits the irradiation to a fixed gantry angle.

2.2.2 Transit EPID dosimetry software

Transit EPID dosimetry software can be used for both pre-treatment and actual treatment verification. At present, there are only two commercial transit EPID dosimetry software systems:

- EPIgray by DOSIsoft (Cachan, France)

- Dosimetry Check by Math Resolutions (Columbia, MD, USA)

Of the two, only the Dosimetry Check software is capable of verifying dose in 2D/3D. With IMRT and VMAT, it is warranted that dose is verified in at least 2D.

PerFRACTION by Sun Nuclear (Melbourne, FL, USA) is excluded from the list above because it is not a dosimetry package, although it uses the EPID to capture radiation exiting the patient during treatment. The software only performs relative comparison between the EPID image captured daily with the EPID image captured on the first treatment fraction, to check for inter-fraction variation of treatment delivery. It does not verify the accuracy of delivered treatment with the intended prescription.

2.2.2.1 EPIgray (DOSIsoft, Cachan, France)

The EPIgray software is based on the method described by Francois et al. (2011) (see Section 2.1.3.3). The algorithm converts the EPID transit signal, captured during treatment, to in-vivo point dose using TMR and other correction factors. The reconstructed point dose is compared to the TPS computed point dose to verify the accuracy of treatment delivery. An additional module, the InVivo Manager (DOSIsoft, Cachan, France), provides a useful tool that manages the automatic analysis and notification of EPIgray results. This is a very attractive feature as it allows in-vivo EPID dosimetry to be implemented almost effortlessly with minimal staff involvement. The major shortcoming of the EPIgray solution is the single point comparison, which is not ideal for IMRT/VMAT treatment since it does not check the accuracy at other parts of the treatment field. Furthermore, it is often difficult to identify an optimal comparison point for highly modulated fields.

2.2.2.2 Dosimetry Check (Math Resolutions, Columbia, MD, USA)

At the time of writing (December 2014), Dosimetry Check is the only commercial software package that offers EPID transit dose verification in 3D. The software is based on a convolution-based model described by Renner et al. (2005) for non-transit dosimetry (see Section 2.1.3.2) that has since been extended for transit application. The method involves retrieving primary fluence incident on the EPID by de-convolution of the EPID transit image with a kernel. Subsequently, the primary fluence is used as an input for 3D dose reconstruction with a pencil

beam algorithm. The reconstructed volume dose is compared with TPS computed dose for treatment verification. Volumetric in-vivo dose verification is advantageous as it provides a complete evaluation of the treatment delivery and allows better clinical judgement. Despite promise, the accuracy of Dosimetry Check software still requires further validation. In a recent technical note by Gimeno et al. (2014), it was found that in the presence of heterogeneity, the isocentre point dose from Dosimetry Check software deviated by up to 15% compared to TPS dose computed by AcurosXB algorithm (Varian, Palo Alto, CA, USA). 3D gamma evaluation using 3%/3mm criterion revealed that only 11.7% of points passed the comparison (Dosimetry Check versus AcurosXB) for a VMAT delivery on a thorax anthropomorphic phantom. The gamma pass rate was also unsatisfactory, at only 77.4%, for a simple 10 x 10 cm^2 field delivered to a homogeneous cylindrical phantom. The authors concluded that improvements are required in the software calculation algorithm. Besides dosimetric accuracy, the authors also highlighted practical issues such as laborious process because of poor integration and long calculation time that could take up to an hour to calculate a case.

2.3 Summary

From the literature reviews and evaluations of commercial software, the gap in knowledge on EPID dosimetry, which serves as the motivation of this research, can be summarised as below:

- The MC-based EPID dosimetry model requires long calculation time and thus, is impractical for routine clinical application. Furthermore, accurate MC simulation requires detailed information of different components in the linac and EPID, which may not be easily available to all.
- Convolution-based EPID dosimetry models are suitable for routine clinical application due to the shorter calculation time. But the method is not easy to replicate outside the research centre because it requires a level of expertise and software that is not usually available in clinical centres.
- Empirical-based EPID dosimetry models can gain wider acceptance, as the method is easier to replicate with only general measurements and can be performed on all linacs and EPIDs regardless of manufacturer. However, there were only two publications on 2D empirical-based EPID transit

dosimetry that were suitable for actual treatment verification (Kavuma et al., 2010, Peca & Brown, 2014) and both were not tested for IMRT (or VMAT) application.

- The majority of commercial EPID dosimetry software packages are for non-transit application. Non-transit EPID commercial software merely provides an alternative method to perform patient-specific pre-treatment verification. Although EPID is better than the widely used 2D array devices in terms of convenience and superior detector resolution, non-transit EPID commercial software does not fulfil the need for an effective way to perform actual treatment verification.
- At present, there are only two options for commercial EPID transit dosimetry software, the EPIgray and Dosimetry Check. Although the software can be used for in-vivo actual treatment verification, the EPIgray only verifies dose to a point and the accuracy of Dosimetry Check software requires further validation.

2.4 Aim of this research

The aim of this research is to build an EPID dosimetry model that addresses the above problems and:

- Is completely based on empirical approach and generic to allow broad-scale implementation
- Is relatively simple for practical implementation in the routine clinical workflow
- Is applicable for transit measurement to allow both pre-treatment and actual treatment verification
- Can predict/reconstruct dose in 2D for a more complete verification of treatment accuracy
- Can offer user the flexibility to choose either to predict dose at the EPID level or reconstruct dose in-vivo
- Is applicable for both 3D conformal and modulated IMRT fields

Chapter 3: Evaluation of six TPS algorithms in computing entrance and exit doses

3.1 Publication/presentation arising from work in this chapter

- **Evaluation of six TPS algorithms in computing entrance and exit doses**, Tan, Y., Metwaly, M., Glegg, M., Baggarley, S. & Elliott, A., 2014, *Journal of Applied Clinical Medical Physics*, 15 (3), 229-240.
- **Accuracy of six commercial TPS algorithms in computing entrance and exit doses**, Tan, Y., Metwaly, M., Glegg, M., Baggarley, S. & Elliott, A., 2013, Oral presentation (Best Oral Presentation award), *13th Asia-Oceania Congress of Medical Physics, 11th South-East Asian Congress of Medical Physics*, Singapore.

3.2 Introduction

Patient-specific treatment verification, especially in-vivo dosimetry, is recommended to prevent major errors in radiotherapy (Garavaglia et al., 1993, Essers & Mijnheer, 1999, Derreumaux et al., 2008, Williams & McKenzie, 2008, Mans et al., 2010b). As described in Chapter 1, in-vivo dosimetry can be performed in various ways using different types of detectors. Ideally, detectors should be placed close to the organ of interest but most in-vivo measurements are done at the beam entrance, exit or both to avoid invasive application. In the case where an EPID is used as the detector, the measured transit dose can be used to reconstruct dose at the entrance or exit level of the patient (Kavuma et al., 2010, Kavuma et al., 2011). To verify the accuracy of treatment delivery, the measured or reconstructed dose at the entrance or exit level is compared to an expected range, usually generated by the TPS. When using the TPS as a reference for dose verification, it is essential that the TPS calculates the dose to a high degree of accuracy for all conditions in the clinical setting. However, due to the limited build up and backscatter at the entrance and exit level respectively, the accuracy of the TPS dose computation must be validated. Although the accuracy of different TPS algorithms has been extensively reported, they mainly focused on dose nearer to the isocentre and with the

presence of inhomogeneity. Examples of such studies were published by Knoos et al. (2006), Van Esch et al. (2006), Fogliata et al. (2007), Bush et al. (2011), Fogliata et al. (2011), Han et al. (2011), Alhakeem et al. (2012), Fogliata et al. (2012) and Han et al. (2012).

The primary aim of this study was to perform a fundamental evaluation of the accuracy of TPS algorithms in computing entrance and exit doses. This subject was of general interest because a better understanding of TPS performance at the entrance and exit level would help in the interpretation of in-vivo dosimetry results when using the TPS as a reference. More importantly, this study was necessary because entrance and exit doses were extensively used in the EPID dosimetry model developed in this research and hence, any inaccuracies in the TPS algorithms must first be identified and quantified. The secondary aim of this study was to experimentally quantify the backscatter correction factor (BCF) as a function of field size, depth and backscatter thickness. The BCF values served as a useful gauge of the backscatter effect under different conditions.

In this study, a total of six commercial TPS algorithms were evaluated. Ionization chamber (IC) measurements were used as a reference. Entrance and exit doses were defined as doses at depth of 1.5 cm from the beam entry and exit surfaces respectively, this depth being chosen to provide reasonable electronic equilibrium condition for the 6 MV photon beam investigated. Dose uncertainties in the build up region were beyond the scope of this study. The same depth for exit dose was chosen for a symmetric geometry. Central axis point dose, 1D relative profiles and 2D absolute dose comparisons were investigated for a range of clinically relevant field sizes and thicknesses in homogeneous water phantoms.

3.3 Materials and methods

3.3.1 Central axis point dose analysis

3.3.1.1 TPS virtual simulation

Virtual water phantoms with dimensions of 30 cm x 30 cm x ‘1.5+Th+1.5’ cm (where thickness, Th, ranged from 0 cm to 30 cm) were created in Eclipse, XiO and Monaco TPSs (Figure 3-1). The range of Th was chosen to include all

clinically relevant thicknesses. Entrance and exit doses, defined as doses at 1.5 cm from the beam entry and exit surface, were computed for a 6MV beam, source to surface distance (SSD) 100 cm, at a gantry angle of zero degrees and field sizes ranging from 5 x 5 cm^2 to 20 x 20 cm^2 using six different algorithms on three TPSs:

- Eclipse TPS (version 10.0.28, Varian, Palo Alto, CA, USA)
  - Pencil Beam Convolution (Eclipse PBC)
  - Analytical Anisotropic Algorithm (Eclipse AAA)
  - AcurosXB (Eclipse AXB)
- XiO TPS (version 4.70, Elekta, Stockholm, Sweden)
  - FFT Convolution (XiO Convolution)
  - Multigrid Superposition (XiO Superposition)
- Monaco TPS (version 3.20.02, Elekta, Stockholm, Sweden)
  - Monte Carlo Photon (Monaco MC)

The different algorithms can be categorised into three broad groups: (a) correction-based algorithms, (b) model-based algorithms and (c) Monte Carlo-based algorithms. Correction-based algorithms, such as Eclipse PBC and XiO Convolution, use data measured in water with additional correction factors or analytic functions to calculate dose in patients. The corrections are used to account for deviation between water measurements and patients, for examples, contour irregularity, distance from source and change in attenuation due to tissue inhomogeneity based on equivalent path lengths. Scattered photons and electrons from primary interaction are not considered when calculating dose to a point. Model-based algorithms, such as Eclipse AAA and XiO Superposition, simulate the incident primary photon energy fluence and energy spectrum with a physical model. Scattered photons and electrons from the primary interaction are considered when calculating dose to a point. A convolution kernel, derived from measurement or Monte Carlo simulation, is used in the dose calculation. Monte-Carlo based algorithms, such as Monaco MC, simulate photons and particles transport and use fundamental physics to determine the probability of interactions. Dose is determined by scoring interaction and energy deposition in each voxel. Instead of Monte Carlo method, the Eclipse AXB algorithm uses numerical method to explicitly solve the linear Boltzmann transport equation, which describes the interactions of radiation particles with matter. The method

involves discretization of photon and electron fluences in space, angle and energy and is an alternative solution to the time consuming Monte Carlo simulation.

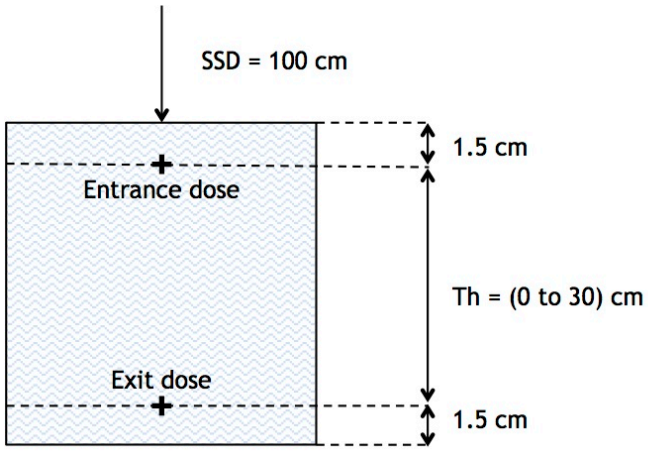

Figure 3-1 Set-up for TPS dose computation. The entrance and exit doses were defined as doses at 1.5 cm from the beam entry and exit surface respectively. Doses were computed for virtual water phantoms with total thickness (1.5+Th+1.5) cm, where Th ranged from 0 cm to 30 cm.

Doses on all TPSs, except for Monaco MC, were calculated using 0.1 cm grid size with the calculation box enclosing the outer border of the virtual phantoms. The Monaco MC calculation grid was set to 0.2 cm with 1% standard deviation per plan criteria because of hardware limitations.

The TPSs were located in two separate and independent institutions; Institution A (Inst. A) is equipped with the Eclipse TPS commissioned for the Varian Clinac 21EX (Palo Alto, CA, USA) linac while Institution B (Inst. B) is equipped with XiO and Monaco TPSs commissioned for the Elekta Synergy (Stockholm, Sweden) linac. All comparisons described in this study were performed between TPS and the corresponding linac for which the TPS was commissioned.

3.3.1.2 Experimental measurement

Using a 0.6 cc Farmer IC (Inst. A: NE2581, Nuclear Enterprises, Fairfield, NJ, USA and; Inst. B: PTW30001, Freiburg, Germany) in water-equivalent solid phantoms of dimension 30 x 30 cm^2 (Inst. A: Solid Water with density 1.04 g/cm^3, Gammex Inc., Middleton, WI, USA and; Inst. B: Plastic Water with density 1.03 g/cm^3, CIRS Inc., Norfolk, VA, USA) set-up at SSD 100 cm, entrance and exit central axis point doses were measured for a 6 MV beam on the Clinac 21EX and Synergy

linacs. Entrance doses were measured at depth 1.5 cm with backscatter thickness ranging from 1.5 cm to 31.5 cm while exit doses were measured at depths 1.5 cm to 31.5 cm with backscatter thickness of 1.5 cm. Doses were measured at a gantry angle of zero degrees for field sizes 5 x 5 cm^2 to 20 x 20 cm^2. This experimental set-up, illustrated in Figure 3-2, replicates the condition for TPS dose computations described in Section 3.3.1.1.

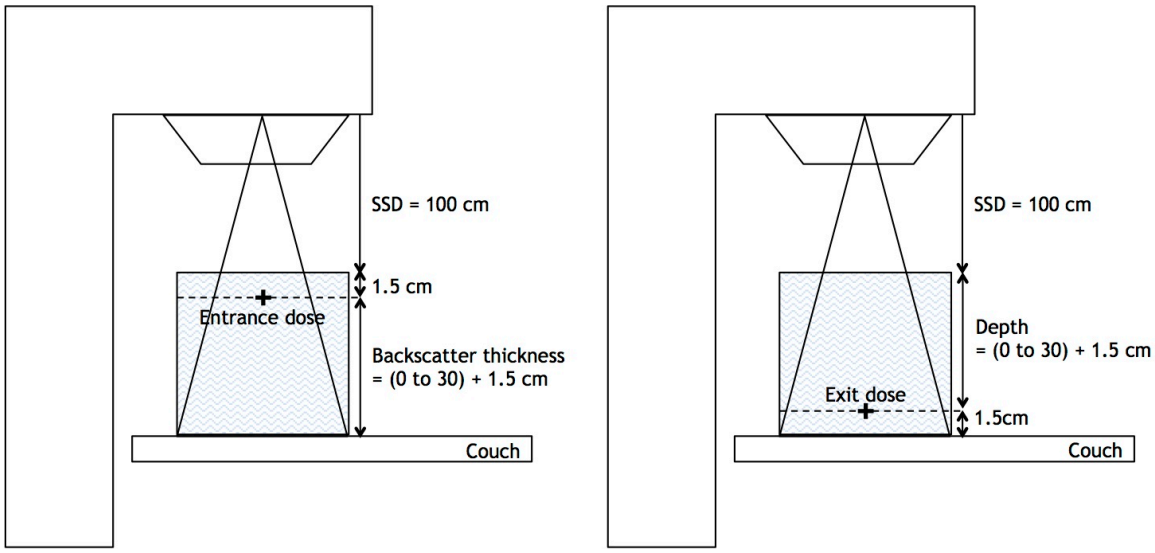

Figure 3-2 Set-up for experimental measurement with IC and water-equivalent solid phantoms. Entrance doses were measured at depth 1.5 cm with backscatter thickness ranging from 1.5 cm to 31.5 cm while exit doses were measured at depths 1.5 cm to 31.5 cm with backscatter thickness of 1.5 cm. Measured doses were used as reference for comparison with TPS computed doses.

To avoid uncertainties related to differences in chambers, electrometers and water-equivalent solid phantoms in the two institutions, a 'relative' approach was taken. As outputs for linacs at both institutions were calibrated in water to 1 cGy/MU at calibration condition, readings were first taken in charge mode at calibration condition to obtain the charge to dose conversion factor. Subsequent measurements were performed in charge and converted to dose using this factor. This method also allowed variation in daily output to be corrected. In addition, measurements were repeated with a CC04 IC (IBA Dosimetry, Schwarzenbruck, Germany) to provide a crosscheck on the accuracy of the data measured with the 0.6 cc Farmer IC, especially for the smallest field size of 5 x 5 cm^2. To maintain consistency, the same investigator performed all measurements in both institutions. Finally, the measured doses were used as a

reference for comparison with TPS computed doses to evaluate the accuracy of different algorithms.

3.3.1.3 Deriving Backscatter Correction Factor (BCF)

BCF was defined as the ratio of dose without full backscatter to dose with full backscatter (Equation 3-1).

$$\text{Backscatter Correction Factor, BCF} = \frac{\text{Dose without Full Backscatter}}{\text{Dose with Full Backscatter}}, \text{ where BCF is} \leq 1 \quad (3\text{-}1)$$

Doses without full backscatter were the doses measured using methods described in Section 3.3.1.2. Doses with full backscatter were calculated using percentage depth dose (PDD) and field size output factor (OF) according to Equation 3-2. PDD and OF were measured with CC13 IC (IBA Dosimetry, Schwarzenbruck, Germany) in a scanning water tank (IBA Dosimetry, Schwarzenbruck, Germany).

$$\text{Dose}_{fs}^{d} = D_{dmax} \times \text{PDD}_{fs}^{d} \times \text{OF}_{fs} \quad (3\text{-}2)$$

where 'd' is the depth where dose is calculated, 'fs' is the field size at distance 100 cm, 'D_{dmax}' is the dose at depth of maximum for reference field size (usually 10 x 10 cm^2), 'PDD_{fs}^{d}' is the percentage depth dose and 'OF_{fs}' is the field size output factor.

3.3.2 1D relative profile analysis

To check the accuracies of the TPS algorithms in computing off-axis doses, TPS profiles were compared with profiles measured with IC (Inst. A: CC04 and Inst. B: CC13, IBA Dosimetry, Schwarzenbruck, Germany) in the scanning water tank. The 1D TPS profiles were extracted from 2D entrance and exit dose planes computed by the six TPS algorithms for a 6 MV beam with different field sizes (5 x 5 cm^2 to 20 x 20 cm^2) and depths (1.5 cm to 31.5 cm) in virtual water phantoms. The IC profiles could not be measured at the exit plane because of limitations in measuring with 1.5 cm backscatter using the scanning water tank, but the differences in set-up between TPS and IC profiles were not critical as backscatter thickness affects the relative profiles only minimally (Vial et al., 2009).

However, since the IC measured profiles were used as a reference, they were independently checked against exit measurements performed with commercial 2D array devices, MapCHECK2 (Sun Nuclear, Melbourne, FL, USA) in Inst. A and MatriXX^{Evolution} (IBA Dosimetry, Schwarzenbruck, Germany) in Inst. B. Water-equivalent solid phantoms of appropriate thicknesses were placed on top of the devices to measure 2D exit dose planes at various depths (the inherent thickness of material behind the detectors, less than 3.5 cm, were ignored). Profiles were extracted from the 2D array measured dose planes for comparison with the IC measured profiles.

All profiles were normalized to the central axis for relative comparisons. Image processing and analysis were performed using MATLAB (R2011a_Student, The Mathworks, Natick, MA, USA) software.

3.3.3 2D absolute dose analysis

The 1D relative profiles measured with IC in the scanning water tank, either in the in-line or cross-line direction, were used to generate 2D dose planes. For each depth and field size, the measured 1D relative profile was duplicated to fill a 2D matrix. Assuming that the in-line and cross-line profiles were identical in shape, the same 1D relative profile was used to fill another 2D matrix but in a direction perpendicular to the previous matrix. Then, the two matrices, representing the in-plane and cross-plane, were multiplied to generate a 2D relative dose plane. Finally, the 2D relative dose plane was converted to a 2D absolute dose plane by multiplication with the measured central axis point dose.

The 2D absolute dose planes derived from IC measurements were compared to TPS computed dose planes using 2D global gamma evaluations. Results were given as percentage points that passed the gamma criterion of 3%/3mm.

3.4 Results

3.4.1 Central axis point doses: TPS versus IC

Repeated entrance and exit central axis point measurements using two different chambers, 0.6 cc Farmer and CC04 ICs, showed excellent agreement with

difference less than 0.7% for the whole range of field sizes (5 x 5 cm^2 to 20 x 20 cm^2) and backscatter thicknesses or depths (1.5 cm to 31.5 cm) measured in this study. To account for set-up uncertainties, repeated measurements with the same chamber on different occasions showed a maximum disagreement of less than 0.5%. The consistency in these results gave confidence to the measured data.

Comparison of central axis entrance doses between TPS computed and IC measured for different field sizes (5 x 5 cm^2 to 20 x 20 cm^2) and backscatter thicknesses (1.5 cm to 31.5 cm) showed good agreement to within 2%. All six TPS algorithms accurately computed the entrance doses at depth 1.5 cm for the 6 MV beam.

Central axis point dose comparisons at the exit level, where the thickness of underlying material was 1.5 cm, showed a variable degree of accuracy among the different algorithms. Figure 3-3 shows the percentage difference in TPS computed and IC measured exit doses as a function of depth (for clarity of presentation, only field size 20 x 20 cm^2 results are shown in the figure). Exit doses computed with XiO Convolution, XiO Superposition and Monaco MC agreed with the IC measured doses to within 2.3%. Eclipse AXB showed similar results except for the smallest field size (5 x 5 cm^2) where deviation was 3.3%. Poorer results were seen with Eclipse PBC and Eclipse AAA where the computed exit doses deviated from IC measured doses by up to 5.3% and 4.8% respectively. In the case of Eclipse PBC and Eclipse AAA, deviations of exit doses increased with increasing field size and depth. Figure 3-4 shows the percentage exit dose difference between Eclipse AAA and IC measured doses for different field sizes as a function of depth. For clearer illustration, only Eclipse AAA results are shown in the figure.

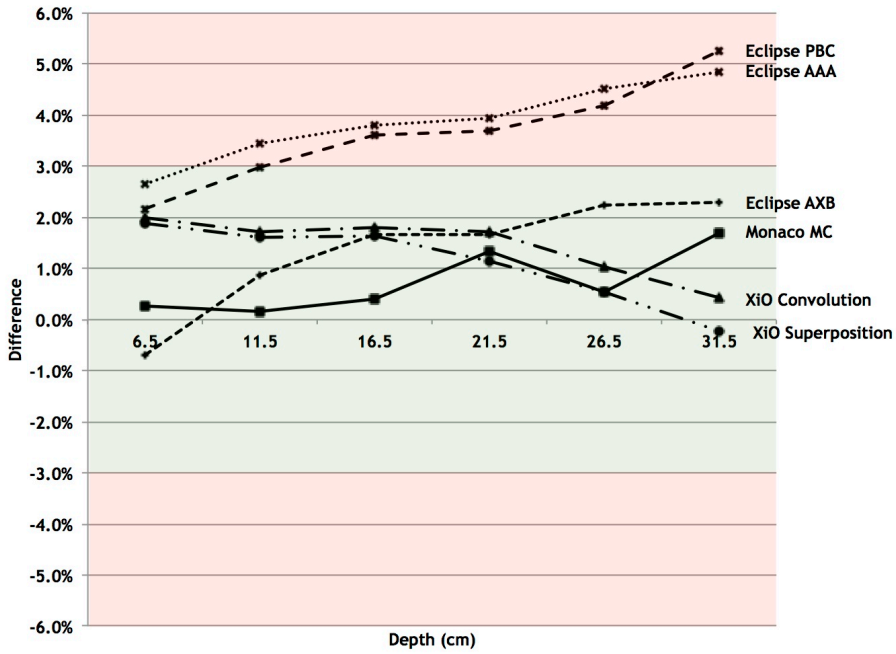

Figure 3-3 Percentage difference in central axis exit doses between computed by different TPS algorithms and measured by IC. For clarity, only field size 20 x 20 cm^2 results are plotted.
(Note: Percentage difference was calculated as [(TPS/IC)-1]*100).

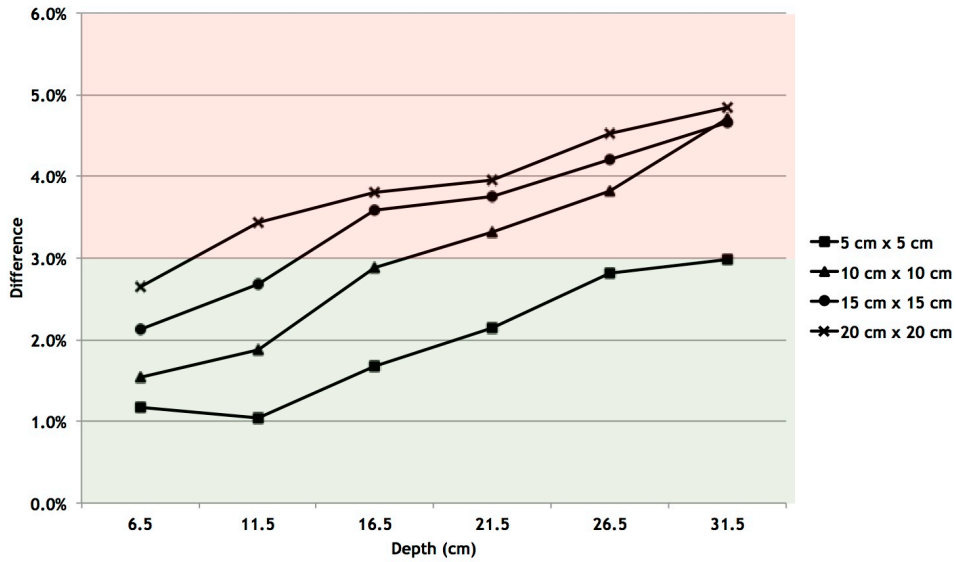

Figure 3-4 Percentage difference in central axis exit doses between Eclipse AAA and IC measured as a function of depth for different field sizes, 5 x 5 cm^2 to 20 x 20 cm^2. Eclipse AAA computed exit doses were all higher than IC measured exit doses. The discrepancies increased with increasing field size and depth. For clarity, only Eclipse AAA results are plotted.
(Note: Percentage difference was calculated as [(TPS/IC)-1]*100).

3.4.2 Backscatter Correction Factor (BCF) values

To quantify the effect of backscatter on the entrance and exit doses, BCF values were experimentally derived and are presented in Table 3-1 for the 6 MV beam

from Clinac 21EX and Elekta Synergy linacs. The BCF tables were separated into entrance BCF and exit BCF. Entrance BCF was derived at a fixed depth of 1.5 cm with underlying material thickness ranging from 1.5 cm to 31.5 cm. Exit BCF was derived at depths ranging from 6.5 cm to 31.5 cm with the thickness of underlying material being kept constant at 1.5 cm. The BCF values are presented for field size ranging from 5 x 5 cm^2 to 20 x 20 cm^2.

BCF values were found to be very similar for both beams as the beam quality was almost identical for the 6MV beam from Clinac ($TPR_{20,10}$ = 0.669) and Synergy ($TPR_{20,10}$ = 0.687). The average differences in BCF values between the two linacs were 0.1%±0.07% (1 SD) and 0.5%±0.47% (1 SD) for the entrance and exit BCF respectively. Entrance BCF initially increased before it reached unity as the thickness of underlying material and field size increased. The minimum entrance BCF occurred when the underlying material was the smallest, 1.5 cm, and the field size largest, 20 x 20 cm^2. The values were 0.972 for Clinac and 0.978 for Synergy beams. The dose reduction became negligible (less than 0.5% dose reduction) when the thickness of underlying material was equal to or more than 11.5 cm. Meanwhile, the exit BCF ranged from 0.995 to 0.963 and 1.000 to 0.960 for the Clinac and Synergy beam respectively. The largest correction occurred at the largest depth, 31.5 cm, and field size, 20 x 20 cm^2.

As most clinical treatments are isocentric with variable SSD, BCF values were also derived for phantoms set-up at 100 cm to the centre. Comparison of BCF values between fixed SSD 100 cm and variable SSD showed very similar results with a maximum difference of 0.8% and standard deviation of 0.15% (1 SD) for the whole range of depths and field sizes tested.

Table 3-1 Entrance and exit backscatter correction factor (BCF) for 6 MV photon beams from Clinac and Synergy linacs. BCF values were tabulated as a function of field size and thickness of underlying material (backscatter thickness) for the entrance BCF and thickness of overlying material (depth) for the exit BCF.

Entrance BCF (Depth 1.5 cm)

	Backscatter thickness (cm)						
Field size (cm^2)	**1.5[a]**	**6.5**	**11.5**	**16.5**	**21.5**	**26.5**	**31.5**
Clinac 21EX ($TPR_{20,10}$ = 0.669)							
5 x 5	0.991	0.995	0.998	0.998	0.999	0.999	1.000
10 x 10	0.985	0.994	0.998	0.999	0.999	1.000	1.000
15 x 15	0.978	0.991	0.997	0.999	0.999	1.000	1.000
20 x 20	0.972	0.990	0.996	0.999	0.999	1.001	1.000
Synergy ($TPR_{20,10}$ = 0.687)							
5 x 5	0.993	0.996	0.997	0.997	0.998	0.998	1.000
10 x 10	0.987	0.995	0.997	0.998	0.999	0.999	1.000
15 x 15	0.981	0.993	0.996	0.998	0.999	0.998	1.000
20 x 20	0.978	0.992	0.996	0.999	1.000	1.000	1.000

Exit BCF (Backscatter thickness 1.5 cm)

	Depth (cm)						
Field size (cm^2)	**1.5[a]**	**6.5**	**11.5**	**16.5**	**21.5**	**26.5**	**31.5**
Clinac 21EX ($TPR_{20,10}$ = 0.669)							
5 x 5	0.991	0.995	0.991	0.984	0.976	0.970	0.972
10 x 10	0.985	0.987	0.983	0.980	0.973	0.970	0.960
15 x 15	0.978	0.983	0.978	0.974	0.972	0.968	0.965
20 x 20	0.972	0.981	0.972	0.973	0.969	0.965	0.963
Synergy ($TPR_{20,10}$ = 0.687)							
5 x 5	0.993	1.000	0.993	0.987	0.984	0.977	0.975
10 x 10	0.987	0.988	0.987	0.986	0.985	0.982	0.983
15 x 15	0.981	0.978	0.978	0.976	0.971	0.972	0.971
20 x 20	0.978	0.971	0.968	0.966	0.965	0.962	0.960

[a] Exit BCF for depth 1.5 cm was equivalent to entrance BCF with backscatter thickness 1.5 cm.

3.4.3 1D relative profiles: TPS versus IC

Comparisons between TPS and IC relative profiles at depths 1.5 cm to 31.5 cm are presented in Figure 3-5. Only the maximum field size, 20 x 20 cm^2, is shown for brevity. The profiles are compared in the diagonal direction, rather than in-line or cross-line, to maximise the area of analysis.

From the figure, it can be observed that the relative profiles from Eclipse PBC, XiO Convolution and XiO Superposition algorithms matched well with IC measured relative profiles at all depths. As for Eclipse AAA, slight mismatches with IC measured relative profiles were seen at depth 1.5 cm and 11.5 cm. Mismatches were also observed between Eclipse AXB and IC measured relative profiles at depths 21.5 cm and 31.5 cm. The Eclipse AXB profiles were found to be higher than IC measured profiles at the shoulder regions. The discrepancies worsened as depth increased from 21.5 cm to 31.5 cm. Similarly, mismatches were observed between Monaco MC and IC measured relative profiles at depths 21.5 cm and 31.5 cm. But unlike Eclipse AXB, the Monaco MC profiles were lower than the IC measured profiles and the disagreements were seen nearer to the centre. The arrows in Figure 3-5 indicate the different areas of mismatch.

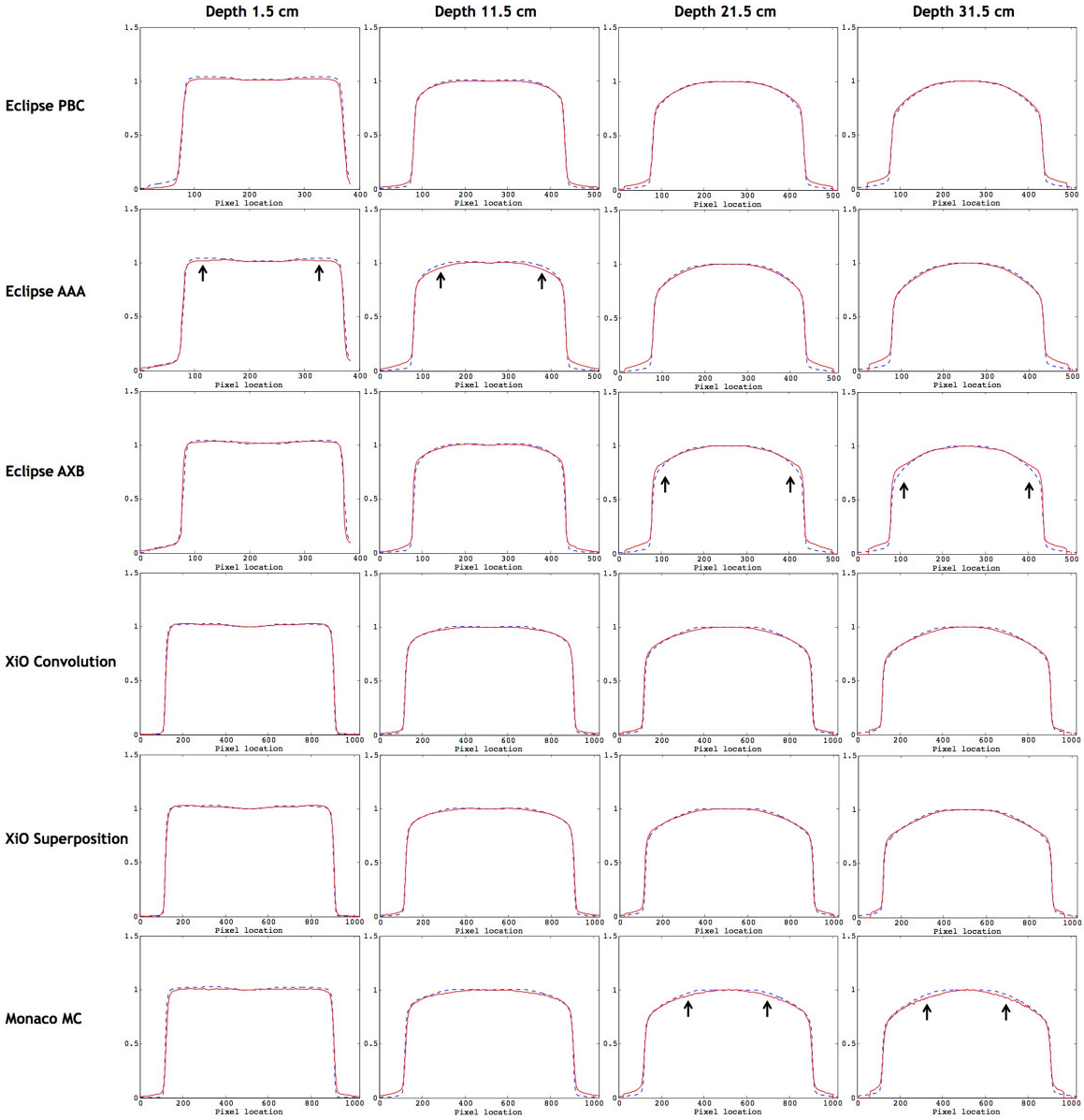

Figure 3-5 Comparisons between TPS computed and IC measured relative profiles. TPS (red solid line) and IC (blue dashed line) relative profiles for 20 x 20 cm^2 open field at depths 1.5 cm to 31.5 cm. The profiles were extracted in the diagonal direction from TPS computed dose planes and IC measured dose planes and normalised to the central axis. The arrows show areas of mismatch.

3.4.4 Validation of IC dose planes: IC versus 2D array

The IC dose planes were derived from simple cross-multiplication of in-line and cross-line profiles measured in a scanning water tank. Since the IC dose planes were used as a reference, they were independently verified with a commercial 2D array device. Figure 3-6 shows the comparisons of relative profiles extracted from IC dose planes derived in this study and from 2D array measured dose planes. Good agreements were seen for all depths, confirming the validity of

the method used to create the IC dose planes and thereby, justifying the use of the IC dose planes as a reference for evaluating the accuracy of TPS algorithms.

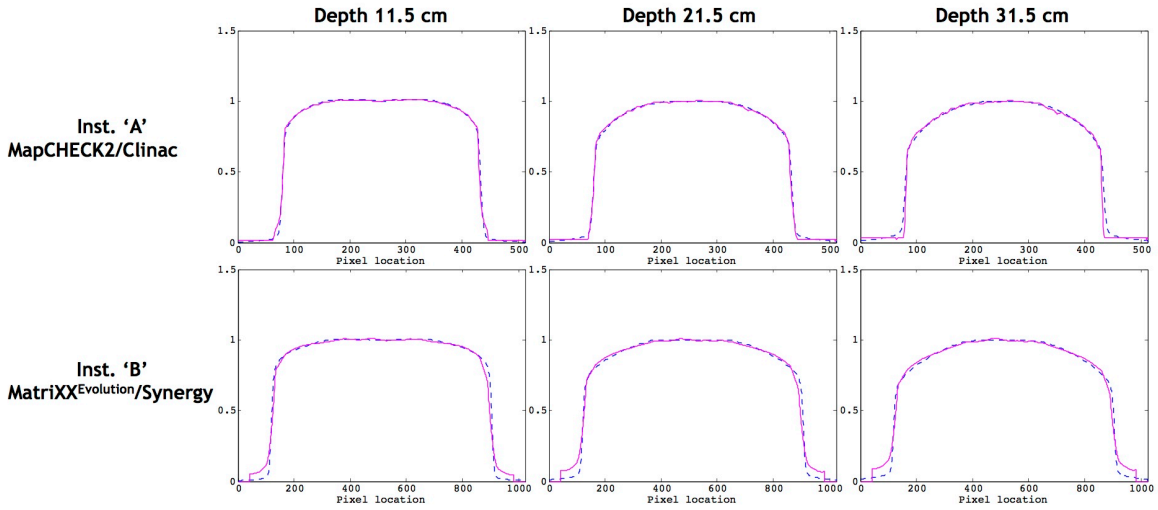

Figure 3-6 Comparisons between IC and 2D array measured relative profiles. IC (blue dashed line) and 2D array (magenta solid line) relative profiles for 20 x 20 cm^2 open field at depths 11.5 cm to 31.5 cm. The profiles were extracted in the diagonal direction from IC derived dose planes and 2D array measured dose planes and normalised to the central axis. Good agreements were observed for all comparisons, confirming the validity of IC dose planes for use as reference.

3.4.5 2D absolute gamma: TPS versus IC

Figure 3-7 shows the results for the 2D absolute gamma comparison between TPS computed dose planes and IC measured dose planes. The percentage of points that passed the global gamma criterion of 3%/3mm in the whole field and at the centre 80% of the fields are given in Table 3-2. The boundaries of region for analysis (whole field and centre 80% of the fields) are defined manually without applying automatic threshold. The 2D absolute gamma analysis could not be performed for Eclipse PBC and Eclipse AAA because of the large deviation in dose, of more than 3%, up to about 5%, as reported in Section 3.4.1.

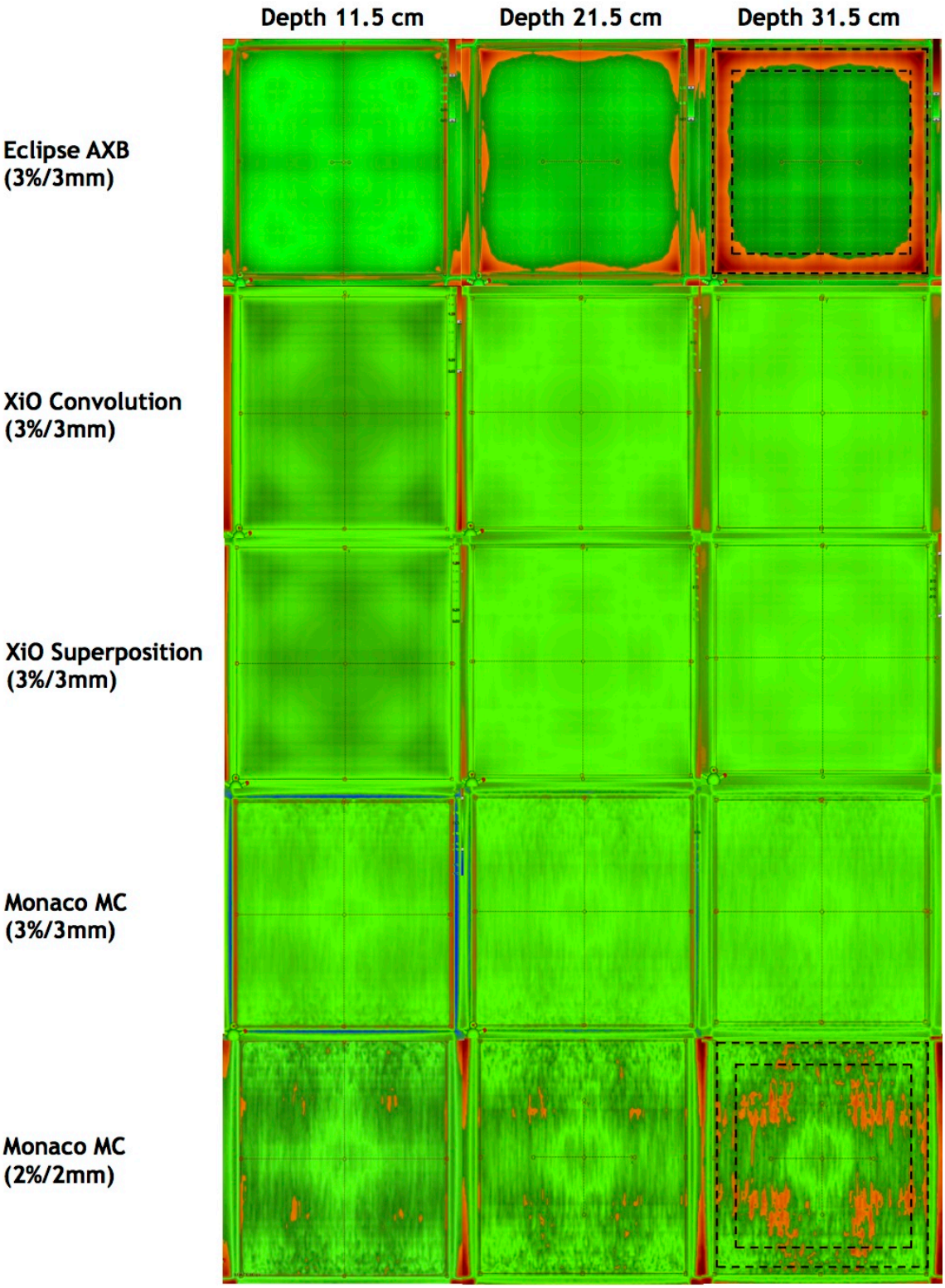

Figure 3-7 2D absolute gamma comparisons between TPS computed and IC measured dose planes for 20 x 20 cm^2 open field. Areas that passed the gamma criterion of 3%/3mm are indicated in green and areas that failed are indicated in red. The outer dashed box and the inner dashed box mark the 100% and 80% field areas used for analysis respectively. 2D absolute gamma comparisons could not be performed for Eclipse PBC and Eclipse AAA because of the large deviation in dose. Additional comparisons for Monaco MC using a 2%/2mm criterion (last row) are included to show the effect of relative profile mismatches seen in Figure 3-5.

Table 3-2 2D absolute gamma comparisons between TPS computed dose planes and IC measured dose planes for 20 x 20 cm^2 open field. The gamma comparison results were given as percentage of points that passed the gamma criterion of 3%/3mm. 2D absolute gamma comparisons could not be performed for Eclipse PBC and Eclipse AAA because of the large deviation in dose.

	Depth (cm)	[b]Central axis point dose difference	Gamma criterion (3%/3mm)	
			100% of field area	80% of field area
Eclipse AXB	**11.5**	0.9%	99.8%	100.0%
	21.5	1.7%	89.2%	100.0%
	31.5	2.3%	73.7%	98.1%
XiO Convolution	**11.5**	1.7%	100.0%	100.0%
	21.5	1.7%	100.0%	100.0%
	31.5	0.4%	100.0%	100.0%
XiO Superposition	**11.5**	1.6%	100.0%	100.0%
	21.5	1.1%	100.0%	100.0%
	31.5	-0.2%	100.0%	100.0%
Monaco MC	**11.5**	0.2%	100.0%	100.0%
	21.5	1.3%	100.0%	100.0%
	31.5	1.7%	100.0%	100.0%

[b] The central axis point dose difference was calculated as [(TPS/IC)-1]*100

XiO Convolution, XiO Superposition and Monaco MC absolute dose planes showed excellent agreement with IC measured dose planes. The gamma pass rates with 3%/3mm criterion were 100% for these three algorithms. Meanwhile, the gamma pass rates for Eclipse AXB ranged from 73.7% to 99.8% with poorer pass rates as depth increased. When only the centre 80% of the field was analysed, the Eclipse AXB gamma pass rates improved to above 98.1%.

3.5 Discussion

3.5.1 Consistency of data from different institutions

This study compared TPS computed doses with IC measured doses in two different institutions with TPS, linac and dosimetry equipment of different models. To ensure that the results in this study were not affected by these

differences, the quality of TPS beam models and the methods used to collect data for this study must remain consistent in both institutions.

Commissioning data for all TPSs in both institutions were measured according to manufacturers' requirements. Similarly, beams were modelled according to manufacturers' methods, with no additional users' intervention for the Eclipse and Monaco TPSs. Although XiO TPS beams were modelled in-house, the procedures were also consistent with manufacturer's requirements. Therefore, any variation would be TPS/manufacturer specific and not due to differences introduced by users. In general, the manufacturers state an accuracy of better than 3% for the beam models. This specification was independently verified for each of the beam models by comparing the measured and modelled PDD curves for all the field sizes investigated in this study (5 x 5 cm^2 to 20 x 20 cm^2). The measured PDD curves referred to the PDD values measured with an IC in a scanning water tank. The modelled PDD curves were represented by normalised doses computed with the beam models at different depths in a virtual water tank (dimension 65 cm x 65 cm x 50 cm). By comparing the two curves, accuracy of the beam models can be quantified. Comparisons of values at different points along the PDD curves, up to depth 31.5 cm, showed an accuracy of better than 2% for all the beam models tested in this study. The mean percentage differences (±1SD) were 0.4%±0.44% (Eclipse PBC), 0.6%±0.57% (Eclipse AAA), 0.8%±0.75% (Eclipse AXB), -0.4%±0.41% (XiO Convolution), -0.4%±0.67% (XiO Superposition) and 0.2%±0.50% (Monaco MC). This validation was important to ensure that baseline differences in beam models were not large enough to affect the outcome of this study.

As for the consistency in TPS dose calculations on virtual phantoms, the same settings, as far as possible, were used for all calculations. The same investigator created the virtual phantoms in all TPSs to avoid inter-personal variation. As these virtual phantoms were simple cubes with assigned uniform water density, the uncertainties related to inaccuracies in creation of the virtual phantoms were negligible. Lastly, the differences in dosimetry equipment in the two institutions were mitigated by using a 'relative' measurement technique. Readings were first taken in charge mode and later converted to dose using factors derived from measurements under calibration condition.

3.5.2 Central axis point dose deviation

Exit doses computed by Eclipse PBC and Eclipse AAA were found to be higher than IC measured doses by up to 5% (Figure 3-3 and Figure 3-4). To further investigate the large deviation seen with Eclipse PBC and Eclipse AAA, an additional virtual water phantom with dimension 65 cm x 65 cm x 50 cm was created to simulate full scatter condition. Using the same beam settings, doses to this phantom were computed with full scatter condition (Figure 3-8, right) as well as to another phantom with only 1.5 cm backscatter (Figure 3-8, left). The dose to point 'P' for both phantoms was compared for a wide range of field sizes (5 x 5 cm^2 to 20 x 20 cm^2) and depths (1.5 cm to 31.5 cm). In theory, the dose at the exit, where the backscatter thickness was 1.5 cm, should be lower because of reduced backscattered photon. However, results from Eclipse PBC and Eclipse AAA showed similar doses for both phantoms, with and without full backscatter. The average percentage dose difference was 0.4%±0.29% and 0.2%±0.20% for Eclipse PBC and Eclipse AAA respectively.

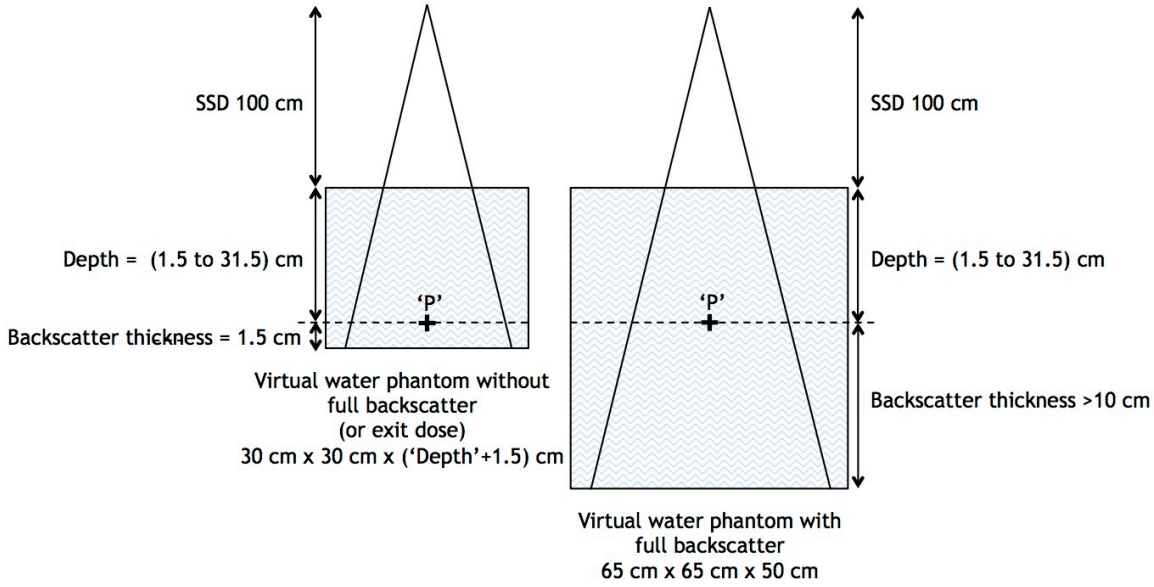

Figure 3-8 TPS virtual water phantoms without and with full backscatter. Virtual water phantoms, created in the TPS, to represent conditions without full backscatter (or exit dose) (left) and with full backscatter (right). The dose to point 'P' was computed for the same beam settings (6 MV, field size 5 x 5 cm^2 to 20 x 20 cm^2, SSD 100 cm) on both phantoms and compared. Results from Eclipse PBC and Eclipse AAA showed that the algorithms computed similar dose to point 'P' for both conditions, with and without full backscatter, implying that the effect of backscatter thickness was not taken into account by the algorithms.

Furthermore, comparisons between Eclipse PBC and Eclipse AAA exit doses with doses calculated from PDD using Equation 3-2, where full backscatter existed, again showed very similar values with an average difference of 0.5%±0.41% and 0.4%±0.44% for Eclipse PBC and Eclipse AAA respectively. This suggested that both algorithms do not consider the lack of backscatter and assume that full backscatter exists even at the exit level. This omission caused the dose at the exit level to be over-estimated by the TPS as indicated in the comparison with IC measured dose in Section 3.4.1. In clinical treatment planning, an error of 5% in the computed exit dose, where the dose is originally low, would be of limited implication. However, this shortcoming in the TPS algorithms must be taken into account especially in the case where in-vivo exit dose measurements were directly compared to the TPS computed values to avoid wrong interpretation of in-vivo dosimetry results. To facilitate the estimation of backscatter effect for different conditions, the BCF values were provided in Table 3-1.

3.5.3 BCF values

BCF values were almost identical for the two 6 MV beams with very similar beam quality investigated in this study. BCF is influenced by beam energy because the probability of Compton interaction and the direction of scatter are energy dependent. The effect of backscatter is less for higher energy beams due to more forward scatter and less large-angle scatter photons.

For the entrance BCF, the effect of backscatter contribution was as much as 2% to 3% (for backscatter thickness 1.5 cm and field size 20 x 20 cm^2). However, the extremely small vertical thickness is not common in clinical practice. In this study, the dose reduction became negligible when the thickness of underlying material was equal to or more than 11.5 cm. For a 6 MV beam with the same field size and depth, Hu & Zhu (2011) reported a smaller thickness, 5 cm, to reach full backscatter condition. As for the field size influence on BCF, the backscatter effect is more prominent for bigger field sizes due to the larger area of scattering.

For the exit BCF, the lack of backscattered photons at the exit level resulted in an approximately 4% reduction in dose at depth 31.5 cm and field size 20 x 20 cm^2. This value was within the ICRU recommendation of less than 5% (ICRU

Report No. 24, 1976) and agreed favourably with published data. For example, at depth 20 cm and field size 20 x 20 cm^2, Kappas & Rosenwald (1991) reported a value of 0.967 compared to our values of 0.969 (Clinac) and 0.965 (Synergy). The backscattering effect was more obvious at larger depths because, as the beam traverses the medium, the change in the beam spectrum results in higher relative contributions of backscattered photons.

Finally, BCF values were found to be very similar between fixed SSD 100 cm and variable SSD. Since the fractional scatter contribution to depth dose is independent of the beam divergence (Johns et al., 1958), the backscatter effect would be expected to be independent as well. The results shown above confirm that the BCF table was independent of SSD and the same was reported by Lambert et al. (1983) and Kappas & Rosenwald (1991).

3.5.4 1D relative profile and 2D absolute dose analysis

Mismatches in the relative profiles from TPS and IC measured were observed for Eclipse AAA, Eclipse AXB and Monaco MC (Figure 3-5). While the Eclipse AAA dose planes could not be evaluated using absolute gamma comparisons because of the large deviation in dose, the profile mismatches seen with Eclipse AXB and Monaco MC could be seen in the absolute gamma comparison results presented in Figure 3-7. The Eclipse AXB profiles mismatched at the shoulders causing gamma failure at the field borders, which explained the improvement in gamma pass rate when only the central 80% of the field area was analysed. Meanwhile, mismatches for Monaco MC profiles, which were lower than IC profiles near the centre of the fields, were cancelled off by the higher central axis point dose calculated by Monaco MC and this resulted in good gamma agreement using the 3%/3mm gamma criteria. The effect of the profile mismatches, which was nearer to the centre, became noticeable when the gamma evaluation criterion was set to 2%/2mm, as shown in Figure 3-7.

3.6 Conclusions

In conclusion, all six TPS algorithms accurately computed the central axis entrance doses to within 2%. However, for the exit doses, Eclipse PBC and Eclipse AAA algorithms failed to account for the lack of backscatter, which

resulted in central axis dose errors of up to 5%. Since the tolerance level for in-vivo dosimetry is commonly set at 5%, the dose error for Eclipse PBC and Eclipse AAA must be considered to avoid misinterpretation of results. The correction factors to account for the effect of reduced backscatter under different conditions were presented in the result section as BCF values.

Away from the central axis, slight mismatches were observed between IC and TPS relative profiles computed with Eclipse AAA, Eclipse AXB and Monaco MC algorithms at certain depths. Comparisons of two-dimensional dose planes in absolute term, using gamma analysis with 3%/3mm criterion, showed good agreement between IC and TPS dose planes computed by XiO Convolution, XiO Superposition and Monaco MC. Meanwhile, the Eclipse AXB dose planes disagreed with IC measured dose planes mostly at the outer 20% of the field area. The 2D absolute gamma evaluation was not performed for Eclipse PBC and Eclipse AAA dose planes because of large deviation in absolute dose of more than 3%.

Accurate computation of entrance and exit dose is essential if a TPS is to be used for reference dose comparisons in in-vivo dosimetry. The findings of this study, therefore, serve as a useful baseline for the implementation of entrance and exit in-vivo dosimetry in clinical departments utilizing any of these six common TPS algorithms for reference comparison. Also, this study was necessary as a preliminary assessment on the accuracy of TPS computed entrance and exit dose planes before the dose planes were used in the EPID dosimetry model developed in this research, as described in the following chapters.

Chapter 4: Relating EPID and TPS – Proof of concept

4.1 Publication/presentation arising from work in this chapter

- **EPID and TPS: Connecting the dots**, Tan, Y., Metwaly, M., Glegg, M. & Elliott, A., 2012, Oral presentation, *Scottish Plus Radiotherapy Physics Meeting*, Glasgow, Scotland, UK.
- **A simple method to predict 2D EPID transit dose**, Tan, Y., Metwaly, M., Glegg, M., Baggarley, S. & Elliott, A., 2013, Oral presentation, *Engineering and Physical Sciences in Medicine Conference*, Perth, Australia.

4.2 Introduction

EPID and TPS are markedly different in their response and scatter characteristics. While the TPS is based on water measurements, the presence of high Z material in the a-Si EPID detectors causes deviation from water-equivalent behaviour. Because of this reason, the comparison between EPID measured dose and TPS computed dose is not straightforward.

In this chapter, a novel method that uses radiological thickness or water equivalent path length (EPL) to relate two different dosimetry systems, EPID and TPS, is presented. The rationale for using EPL to link two different dosimetry systems is based on the premise that the EPL is a property of the attenuator and hence, a common parameter for both systems.

The EPL was calculated using a quadratic equation that was established by Swindell (1983), which relates transmitted radiation to attenuator thickness. Earlier description of the calibration method to derive coefficients in the quadratic equation can also be found in the publication by Morton et al. (1991). Historically, the quadratic calibration method was intended for use in image reconstruction and restoration. Swindell (1983) established the quadratic equation to calculate integral linear attenuation coefficients for CT image reconstruction, in an attempt to modify a megavoltage (MV) accelerator for

concurrent use as a CT scanner. Separately, Morton et al. (1991) used the quadratic calibration method to remove artefacts from raw MV images acquired with a prototype imaging panel during radiotherapy treatment. The image processing was necessary to improve the quality of MV images, which were inherently low in contrast because of the predominant Compton interaction with high scatter contribution and low differential attenuation between materials of different Z. Also for image processing, Fielding et al. (2002) investigated the use of the quadratic calibration method to remove intensity modulations from EPID images captured during IMRT treatment delivery, in order to view the outline of bony anatomy for positional verification.

Apart from image processing, the quadratic calibration method could also be extended for dosimetric application, as reported by several investigators and also the intention of this research. For example, Evans et al. (1995) and Symonds-Tayler et al. (1997) calibrated an in-house imaging panel for the conversion of the patient transit image to an EPL map, which was subsequently used to design compensators for breast treatment. Rather than actual CT scans, the EPL map was used to estimate a 'pseudo-CT' slice for the calculation of compensated beams to achieve a desired dose distribution. The method was later applied to a commercial SLIC EPID for the same purpose (Evans et al., 1999). More recent studies had suggested that the quadratic calibration method was also applicable to the newer a-Si EPID (Kairn et al., 2008). Kairn et al. (2008) proposed the use of a 2D EPL map calculated from the measured EPID transit signal as a form of treatment verification. Although, in theory, any deviation in EPL from the expected value could be indicative of inaccuracy in treatment delivery, the comparison in unit length was undesirable since the dosimetric impact could not be immediately quantified. Instead of using EPL to verify the accuracy of treatment delivery, Kavuma et al. (2010) extended the application of EPL to reconstruct in-phantom entrance and exit doses for comparison with TPS computed doses. In the EPID transit dosimetry model described by Kavuma et al. (2010), the conversion of EPL to 2D in-phantom doses required additional parameters such as TPR values and envelope and boundary profiles generated by the Eclipse TPS (Varian, Palo Alto, CA, USA). For dose reconstruction of enhanced dynamic wedge fields, the golden segmented treatment table (GSTT) implemented by Varian was also required (Kavuma et

al., 2011). The need for parameters specific to Varian in the dose reconstruction process was a major drawback, as it disallowed the application of the dosimetry model in centres with models of linac and TPS from other manufacturers.

The focus of this chapter is to describe a concept, capable of converting EPL to dose without requiring input parameters specific to any manufacturer. The method involves calibrating the quadratic equation and deriving the coefficients for TPS as well as EPID. Consequently, with two sets of coefficients, EPL of any attenuator can be calculated using either EPID measured dose planes or TPS computed dose planes. The EPL, together with the sets of coefficients, are then used to provide a two-way relationship for the:

1. Reconstruction of in-phantom exit dose from EPID measured dose planes, for comparison with TPS planned dose. (The in-phantom exit dose was defined as dose at 1.5 cm upstream from the beam exit surface of the phantom); and

2. Prediction of EPID transit dose from TPS computed dose planes, for comparison with EPID measurement during treatment.

As a preliminary study to prove the validity of this concept, the method was tested with open fields of different field sizes on homogeneous water-equivalent phantoms of different thicknesses. To demonstrate that the method was generic and non-manufacturer specific, the study was performed in two separate and independent institutions with different models of linac, EPID and TPS.

4.3 Materials and methods

4.3.1 Photon beam attenuation and quadratic formalism

For a very narrow mono-energetic photon beam that traverses an attenuator, the reduction in radiation intensity is proportional to the thickness of the attenuator and can be described with a linear exponential function, given in Equation 4-1 (Podgorsak, 2005, Khan, 2010b).

$$\frac{I}{I_0} = e^{-\mu t} \qquad (4\text{-}1)$$

where 'I_0' is the intensity of incident photons, 'I' is the intensity of photons after the beam traverses an attenuator with thickness 't' and 'μ' is the linear attenuation coefficient. The linear attenuation coefficient represents the attenuation per unit length and is dependent on the beam energy and the attenuator material (Khan, 2010b). If the attenuator thickness were given in centimetres, then the unit of the linear attenuation coefficient would be cm^{-1}.

In practice, clinical photon beams are not mono-energetic nor are they very narrow and, therefore, may not strictly follow the linear exponential function. Through experimental measurements, Swindell (1983) showed that, for a broad poly-energetic beam, the relationship between amount of attenuation and attenuator thickness could be described accurately with a quadratic equation.

$$\frac{I}{I_0} = e^{-(At + Bt^2)} \tag{4-2}$$

where 'A' is the linear coefficient analogous to μ in Equation 4-1 and 'B' is the coefficient for the quadratic term that describes the non-linear relationship mainly due to spectral variation in a photon beam, with minimal contribution from scatter. By taking the logarithm on both sides of Equation 4-2, a variation to the quadratic equation could also be expressed as follows (Equation 4-3):

$$-\ln\left[\frac{I}{I_0}\right] = At + Bt^2 \tag{4-3}$$

4.3.2 Quadratic formalism in this model

For the purpose of this study, the terms in quadratic Equation 4-3 were re-designated as:

$$-\ln\left[\frac{M(i,j)}{M0(i,j)}\right] = A(i,j) \times EPL(i,j) + B(i,j) \times EPL^2(i,j) \tag{4-4}$$

where 'M0' is the entrance dose plane before a beam traverses an attenuator, 'M' is the exit (or transit) dose plane after a beam traverses an attenuator and 'EPL' is the water-equivalent path length of the attenuator. The 'i' and 'j' denote the Cartesian coordinate of pixels in a 2D plane.

The A and B coefficients were derived separately for EPID and TPS, $(A \text{ and } B)_{EPID}$ and $(A \text{ and } B)_{TPS}$, using sets of calibration M and M0 dose planes from EPID measurements and TPS computations respectively. The calibration dose planes were acquired for both EPID and TPS using the same reference beam (6 MV, 100 MU, and field size 20 x 20 cm^2) and the same set of water-equivalent phantoms thicknesses (0 cm to 35 cm, in 5 cm increment). Detailed descriptions of the EPID and TPS calibration dose planes acquisition are provided in sub-Sections 4.3.3.1 and 4.3.3.2.

Following Equation 4-4, the A and B coefficients could be derived by applying a second-order polynomial fit to the negative logarithm of transmission, -ln(M/M0), against the phantom thickness, PT, for the whole set of calibration dose planes. Since the density of phantoms used in the calibration process was equivalent to water, the PT could be used to represent EPL. The fitting process was repeated pixel-by-pixel to derive A and B coefficients in 2D. To account for the slight variation in phantom thickness due to beam divergence away from the central axis, the PT was calculated for each pixel according to Equation 4-5. This equation was briefly mentioned in Kairn et al. (2008) and a detailed mathematical derivation is provided in Appendix A of this thesis.

$$PT(i,j) = \frac{PT(0,0) \times \sqrt{i^2+j^2}}{SDD(0,0) \times \sin\theta} \quad , \text{ where } \quad \theta = \tan^{-1}\left[\frac{\sqrt{i^2+j^2}}{SDD(0,0)}\right] \tag{4-5}$$

where 'PT(i,j)' is the phantom thickness corrected for beam divergence, 'PT(0,0)' is the phantom thickness at the central axis and 'SDD' is the source to detector distance defined at the central axis. 'Θ' is the angle between the central axis ray and the divergent ray.

With the availability of A and B coefficients, EPL of any attenuator could be calculated from Equation 4-6 (inversion of Equation 4-4) if the value of M/M0 were known.

$$EPL(i,j) = \frac{-A(i,j) \pm \sqrt{A^2(i,j) - 4B(i,j) \times \ln\left[M(i,j)/M0(i,j)\right]}}{2B(i,j)} \tag{4-6}$$

Although mathematically, the quadratic equation should be solved with both plus and minus sign, the negative answer was excluded since the EPL must be a positive value. Also, depending on whether the M and M0 were measured with EPID or computed with TPS, the coefficients must be chosen accordingly when calculating the EPL. For example, to calculate EPL from EPID measured M and M0 dose planes, the $(A \text{ and } B)_{EPID}$ coefficients must be used.

Another important point to note was that the calibration process to derive A and B coefficients was carried out under a fixed reference condition. Therefore, Equation 4-6 could only calculate the EPL correctly if the same reference condition was observed. Deviation from the reference condition must be addressed using additional correction factors. One such correction was the field size correction factor (FSF), defined as the ratio of dose for the reference field size to dose for other field sizes of interest. The FSF was experimentally measured and tabulated for a range of field sizes (3 x 3 cm^2 to 20 x 20 cm^2) and attenuator thicknesses (0 cm to 35 cm) for both EPID and TPS. The FSF was necessary to account for changes in head scatter as well as changes in the amount of phantom scatter to detector, when the field size deviated from the reference field size of 20 x 20 cm^2. This correction factor was included as a coefficient to the M/M0 term to become:

$$EPL(i,j) = \frac{-A(i,j) \pm \sqrt{A^2(i,j) - 4B(i,j) \times \ln\{FSF(i,j) \times [M(i,j)/M0(i,j)]\}}}{2B(i,j)} \quad (4\text{-}7)$$

Lastly, the EPL was calculated using an iterative numerical method similar to that described by Kavuma et al. (2010). The iteration method was required since the FSF was a function of attenuator thickness. Using the value from Equation 4-6 as an initial approximation (EPL_n), the calculation was set to repeat itself five times until a converged solution was reached (EPL_{n+1}). The equation used for the iterative calculation is given in Equation 4-8 and the derivation of this iterative equation is presented in Appendix B.

$$EPL_{n+1}(i,j) = \frac{B(i,j) \times EPL_n^2(i,j) - \ln\{FSF(i,j) \times [M(i,j)/M0(i,j)]\}}{A(i,j) + 2B(i,j) \times EPL_n(i,j)} \quad (4\text{-}8)$$

4.3.3 Commissioning process: Calibration dose planes for A and B derivation

The calibration dose planes were acquired separately for EPID and TPS using the same reference beam (6 MV, 100 MU and field size 20 x 20 cm^2) and the same set of thicknesses (0 cm to 35 cm, in 5 cm increment). The EPID measurements and TPS computations were performed in two institutions, 'Inst. A' and 'Inst. B', equipped with linac, EPID and TPS from different manufacturers as shown in Table 4-1.

Table 4-1 Linac, EPID and TPS models used in this study.

	Institution A (Inst. A)	**Institution B (Inst. B)**
Manufacturer	Varian (Palo Alto, CA, USA)	Elekta (Stockholm, Sweden)
Linac	Clinac	Synergy
EPID panel	aS500 (Pixels: 384 x 512, Active area: 30 x 40 cm^2)	iViewGT (Pixels: 1024 x 1024, Active area: 41 x 41 cm^2)
EPID software	IAS3	Revision 3.4
TPS (Algorithm)	Eclipse (AAA), version 10.0.28	XiO (Superposition), version 4.70

4.3.3.1 Measurements of EPID calibration dose planes to derive $(A \text{ and } B)_{EPID}$

The experimental set-up to measure EPID calibration dose planes is shown in Figure 4-1. The same experimental set-up was used in both institutions except for the source to EPID distance. The source to EPID distance was fixed at 140 cm in 'Inst. A' and 160 cm in 'Inst. B'. The shorter 140 cm distance was selected in 'Inst. A' because the aS500 panel has a smaller active area (30 x 40 cm^2) that limits the maximum irradiation field size to approximately 20 cm at the isocentre. Meanwhile, the iViewGT panel in 'Inst. B' was by default fixed at 160 cm distance and not adjustable in the vertical direction. No filter was added and no modification was done to the EPID panels for practical implementation.

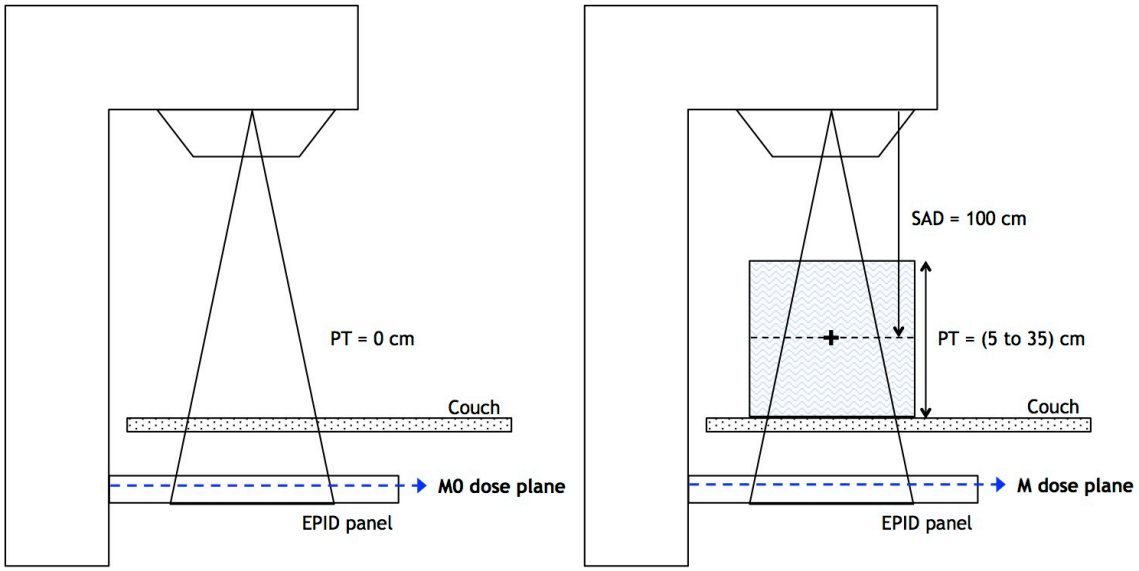

Figure 4-1 Experimental set-up for EPID calibration dose planes measurements. Using a reference beam (6 MV, 100 MU, field size 20 x 20 cm^2) at zero gantry angle, the entrance (M0) calibration dose planes were measured without any phantom in the beam, while the exit (M) calibration dose planes were measured with water-equivalent solid phantoms of different thicknesses (PT = 5 to 35 cm, in 5 cm increment) positioned isocentrically at source to axis distance (SAD) 100 cm.

As can be seen from Figure 4-1, the M0 dose planes were measured without a phantom in the beam (PT = 0 cm) while M dose planes were measured with slabs of water-equivalent solid phantoms of different thicknesses (PT = 5 cm to 35 cm, in 5 cm increment) positioned isocentrically at source to axis distance (SAD) of 100 cm. The couch was placed in the beam for both M0 and M measurements. All measurements were done at a gantry angle of zero degrees. The phantoms used for measurements in the two institutions were: 'Inst. A' - Solid Water with density 1.04 g/cm^3 (Gammex Inc., Middleton, WI, USA); and 'Inst. B' - Plastic Water with density 1.03 g/cm^3 (CIRS Inc., Norfolk, VA, USA).

All the EPID images in this study were acquired using default manufacturer's settings that automatically perform dark field, flood field and defect pixel corrections as part of the standard image processing procedure.

$$\text{EPID image} = \frac{\text{Raw image - DF}}{\text{FF - DF}} \tag{4-9}$$

where 'DF' is the dark field (or offset correction) used to remove background signal detected when no radiation is present and 'FF' is the flood field (or gain

correction) used to correct for non-uniform response of each pixel caused by intrinsic differences of the photodiodes. After the DF and FF corrections, any bad pixels were automatically identified and replaced with an average value based on the neighbouring pixels. Although the DF and FF corrections may change due to routine EPID re-calibration, the calibration dose planes need not be re-measured because the A and B coefficients were derived based on ratios (M/M0) and any signal differences would be cancelled out. In the case of iViewGT, the EPID images were by default stored after multiplication with a scaling factor. Therefore, the pixel value readout from the iViewGT EPID image must be divided by the scaling factor, which could be retrieved from the image log file.

Since the EPID was not absolutely calibrated to dose, the more appropriate term to describe the EPID measurements should be 'EPID image' or 'EPID signal'. However, the term 'EPID dose plane' is used in this thesis for consistency with the TPS computed dose planes.

4.3.3.2 Computations of TPS calibration dose planes to derive $(A \text{ and } B)_{TPS}$

Virtual water phantoms of dimensions 30 cm x 30 cm x '1.5+PT+1.5' cm (where PT = 0 cm to 35 cm, in 5 cm increment) were created in the Eclipse TPS in 'Inst. A' and the XiO TPS in 'Inst. B'. With the virtual water phantoms set isocentrically at SAD 100 cm, doses were computed for the reference beam (6 MV, 100 MU, field size 20 x 20 cm^2) at gantry angle zero degrees. The algorithm used for the dose computation was AAA (Eclipse, version 10.0.28, Varian, Palo Alto, CA, USA) in 'Inst. A' and Multigrid Superposition (XiO, version 4.70, Elekta, Stockholm, Sweden) in 'Inst. B'. Doses were computed with 0.1 cm grid size with the calculation box enclosing the outer borders of the virtual phantoms. The set-up dimension for TPS dose computation is illustrated in Figure 4-2.

The M0 and M, defined as dose at 1.5 cm from the beam entry and exit surface respectively, were exported as the TPS calibration dose planes. The 1.5 cm depth was chosen to provide reasonable electronic equilibrium conditions for the 6 MV photon beam used in this study. Before the exported dose planes were used to derive the A_{TPS} and B_{TPS} coefficients, all the M0 and M dose planes were scaled to the same reference level using inverse square distance correction. In this

study, the isocentre (100 cm from source), which was also the mid-plane of the phantom, was chosen as the reference level. The inverse square distance scaling was done so that the ratio of M and M0 will reflect the reduction of dose due to object attenuation entirely without the effect of distance.

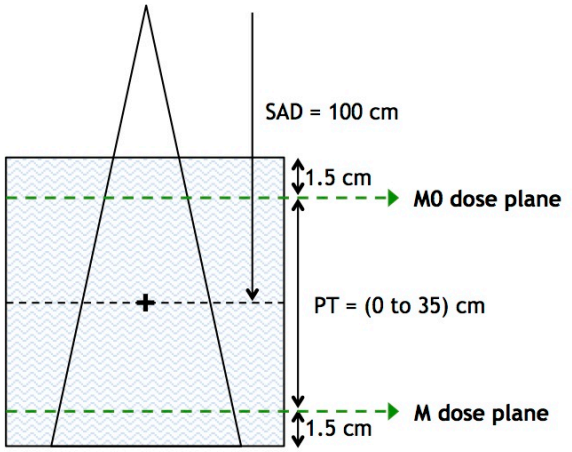

Figure 4-2 Set-up for TPS calibration dose planes computations. Doses were computed for the reference beam (6 MV, 100 MU, field size 20 x 20 cm^2) on virtual water phantoms with dimension 30 cm x 30 cm x '1.5+PT+1.5' cm (where PT = 0 cm to 35 cm, in 5 cm increment) positioned isocentrically at SAD 100 cm. The M0 and M calibration dose planes were exported at depth 1.5 cm from the beam entry and exit surface respectively.

4.3.4 Relating EPID and TPS based on quadratic formalism

The principle of the quadratic formalism, including the derivation of A and B coefficients and the calculation of EPL of attenuator, was explicitly described in previous paragraphs. Figure 4-3 illustrates the function of these A and B coefficients and EPL in relating the two different dosimetry systems, EPID and TPS.

The two areas framed in Figure 4-3 were used to visually distinguish the EPID dosimetry system (on the left) from the TPS dosimetry system (on the right). From the figure, it can be observed that the EPL plays a central role in linking the EPID and TPS. The EPL could be used for this purpose because it is a property of the attenuator and, thus, common to both dosimetry systems. On the other hand, it was necessary to derive $(A \text{ and } B)_{EPID}$ and $(A \text{ and } B)_{TPS}$ separately and use the correct coefficients in the calculations since the dose response and scatter characteristics of the EPID are different from the water-based TPS.

Also as can be seen from the figure, the two-way prediction model allows users to either: (Path 1) predict in-phantom TPS dose ratio from EPID measured dose planes (Figure 4-3, blue arrows from left to right) or; (Path 2) predict EPID dose ratio from TPS computed dose planes (Figure 4-3, green arrows from right to left). From the predicted dose ratios, the final reconstruction of in-phantom exit dose and prediction of EPID transit dose are provided in sub-Sections 4.3.5 and 4.3.6 respectively.

In this study, all image processing and calculations were performed using MATLAB software (R2011a Student version, The MathWorks, Natick, MA).

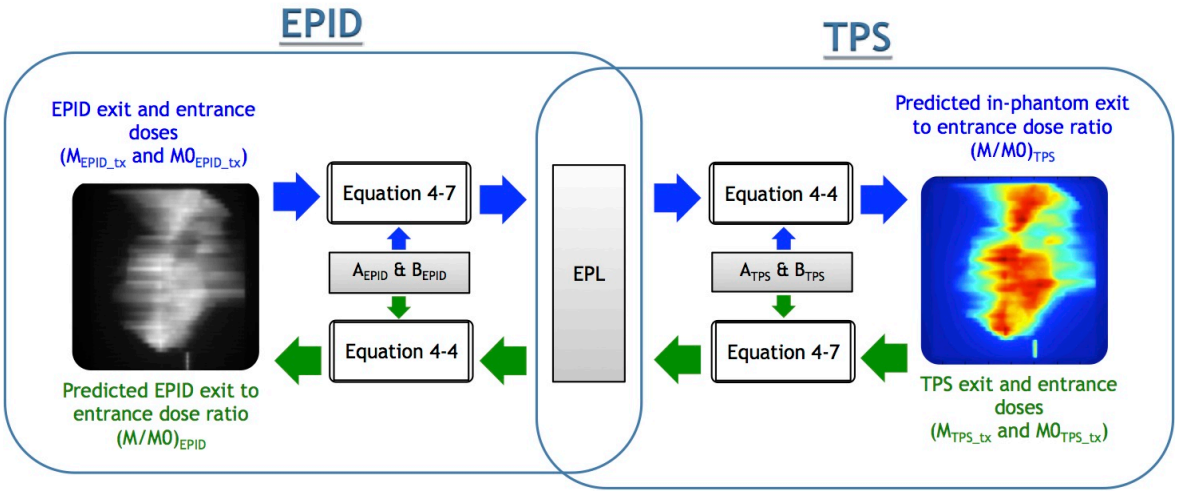

Figure 4-3 The role of (A and B)$_{EPID}$, (A and B)$_{TPS}$ and EPL in relating the two different dosimetry systems, EPID and TPS. Equations 4-4 and 4-7 are the different forms of quadratic equation, as given in the text. From left to right is the path to predict in-phantom dose ratio $(M/M0)_{TPS}$ from EPID measured dose planes (Path 1). From right to left is the path to predict EPID dose ratio $(M/M0)_{EPID}$ from TPS computed dose planes (Path 2). Depending on the path chosen by the user, the predicted $(M/M0)_{TPS}$ or $(M/M0)_{EPID}$ were subsequently used to either reconstruct in-phantom exit dose or predict EPID transit dose respectively. Descriptions of the final dose re-construction/prediction process are given in sub-Sections 4.3.5 and 4.3.6.

4.3.5 Path 1: Reconstruction of in-phantom exit dose

Figure 4-3, from left to right, shows the pathway to predict in-phantom exit to entrance dose ratio $(M/M0)_{TPS}$ from EPID measured dose planes (Path 1). Besides the EPID transit dose plane captured during treatment delivery (M_{EPID_tx}), an additional measurement of the same treatment field without attenuator in the beam was also required ($M0_{EPID\_tx}$). The $M0_{EPID\_tx}$ can either be measured once for repeated use in the subsequent dose prediction or a new dose plane can be

captured each time on the day of verification. By using the latter, machine output variation for the day was taken into account and would not be reflected in the results. In this study, the $M0_{EPID\_tx}$ was measured on the same day as the M_{EPID_tx}. Then, the ratio of M_{EPID_tx} to $M0_{EPID\_tx}$ together with the (A and B)$_{EPID}$ coefficients were used as input to Equation 4-7 for the calculation of EPL of the attenuator. The FSF_{EPID}, tabulated for EPID measured dose planes as a function of field sizes (3 x 3 cm^2 to 20 x 20 cm^2) and attenuator thicknesses (0 cm to 35 cm), was used in Equation 4-7 to correct for non-reference treatment field size. Moving from the EPID environment to the TPS environment, the calculated EPL was used in combination with (A and B)$_{TPS}$ coefficients to derive the equivalent TPS ratio $(M/M0)_{TPS}$ based on Equation 4-4.

Once the equivalent TPS ratio was derived, the in-phantom exit dose could be reconstructed by multiplying this equivalent TPS ratio with a TPS entrance dose plane ($M0_{TPS\ ref}$) (reference field size 20 x 20 cm^2) that was previously computed as the calibration dose plane. An inverse square correction was also added to scale dose from the reference level (100 cm) to the exit level. The mathematical expression to calculate in-phantom exit dose from the TPS ratio is given in Equation 4-10.

$$M_{TPS\ pred} = \left(\frac{M}{M0}\right)_{TPS} \times M0_{TPS\ ref} \div FSF_{TPS} \times \left(\frac{100}{SDD}\right)^2 \qquad (4\text{-}10)$$

where '$M_{TPS\ pred}$' is the reconstructed in-phantom exit dose plane, '$(M/M0)_{TPS}$' is the equivalent TPS ratio predicted from EPID measured dose planes as shown in Figure 4-3, '$M0_{TPS\ ref}$' is the TPS entrance calibration dose plane computed for the reference beam and 'SDD' is the source to detector distance (or source to exit distance in this case). The FSF_{TPS} is the field size correction factor, defined as the ratio of dose for the reference field size to dose for other field sizes of interest, tabulated for TPS computed doses as a function of field sizes (3 x 3 cm^2 to 20 x 20 cm^2) and attenuator thicknesses (0 cm to 35 cm).

Finally, the 2D in-phantom exit dose reconstructed from EPID dose planes was compared to TPS computed dose to verify the accuracy of treatment delivery.

4.3.6 Path 2: Prediction of EPID transit dose

Figure 4-3, from right to left, shows the pathway to predict EPID exit to entrance dose ratio from TPS exported dose planes (Path 2). The TPS exported entrance ($M0_{TPS\_tx}$) and exit (M_{TPS_tx}) planned doses, along with the (A and B)$_{TPS}$ coefficients were used to calculate the EPL matrix of the attenuator from Equation 4-7. The FSF_{TPS} was used in Equation 4-7 to correct for non-reference treatment field size. The calculated EPL was used to move from the TPS environment to the EPID environment. Using the calculated EPL together with the (A and B)$_{EPID}$ coefficients, the equivalent EPID ratio (M/M0)$_{EPID}$ was calculated from Equation 4-4.

With this equivalent EPID ratio, the EPID transit dose ($M_{EPID\ pred}$) can be predicted by multiplying the EPID ratio with an EPID dose plane captured for the reference beam without any phantom in the beam ($M0_{EPID\ ref}$). The $M0_{EPID\ ref}$ can be either the original EPID commissioning dose plane or a newly captured dose plane on the day of verification as noted above. Equation 4-11 below shows the mathematical expression to predict EPID transit dose using the EPID ratio derived from TPS computed dose planes.

$$M_{EPID\ pred} = \left(\frac{M}{M0}\right)_{EPID} \times M0_{EPID\ ref} \div FSF_{EPID} \qquad (4\text{-}11)$$

where '$M_{EPID\ pred}$' is the predicted EPID transit dose plane, '(M/M0)$_{EPID}$' is the equivalent EPID ratio derived from TPS exported dose planes as shown in Figure 4-3 and '$M0_{EPID\ ref}$' is the EPID entrance calibration dose plane measured for the reference beam. The FSF_{EPID} is the field size correction factor, defined as the ratio of dose for the reference field size to dose for other field sizes of interest, tabulated for EPID measured dose planes as a function of field sizes (3 x 3 cm^2 to 20 x 20 cm^2) and attenuator thicknesses (0 cm to 35 cm).

Finally, the 2D EPID transit dose predicted from TPS dose planes was compared to EPID measured dose plane to verify the accuracy of treatment delivery.

4.4 Results

4.4.1 Quadratic equation coefficients for EPID and TPS

Figure 4-4 shows the plots of negative logarithm of transmission, -ln(M/M0), against the phantom thickness for both EPID and TPS calibration dose planes. Data in the graphs represent the mean value of 12 x 12 pixels in the central region of a 2D dose plane (equivalent to a 1.0 cm^2 region for Varian and a 0.5 x 0.5 cm^2 region for Elekta). All data points, from both EPID and TPS, could be fitted very well with a second-order polynomial (also known as the quadratic function), $y = Bx^2 + Ax$. The goodness of fit of the trend lines to the data, as indicated by the R-squared values, were very close to unity, ranging from 0.9988 to 0.9999. In general, it can be seen that the linear term (A coefficient = 10^{-2}) dominates over the quadratic term (B coefficient = 10^{-4}). Nevertheless, the quadratic term should be included for better accuracy especially with thicker attenuators where the non-linear component becomes more important.

It can also be observed from Figure 4-4 that the values of A and B coefficients for EPID and TPS were different, for the same photon beam. The value of A coefficient was higher for the EPID (Varian = 0.043 cm^{-1}; Elekta = 0.046 cm^{-1}) compared to the TPS (Varian = 0.023 cm^{-1}; Elekta = 0.022 cm^{-1}). The value of B coefficient, observed as deviation from the arbitrary straight line in the graphs, highlights the difference between EPID and TPS in the pattern of deviation from linearity. As thickness increases, the amount of attenuation was less compared to a linear relationship for EPID measured doses (Varian = -0.0001 cm^{-2}; Elekta = -0.0002 cm^{-2}), but more compared to a linear relationship for TPS computed doses (Varian = 0.0003 cm^{-2}; Elekta = 0.0003 cm^{-2}). As noted from the values, the variation between EPID and TPS was consistent for both manufacturers.

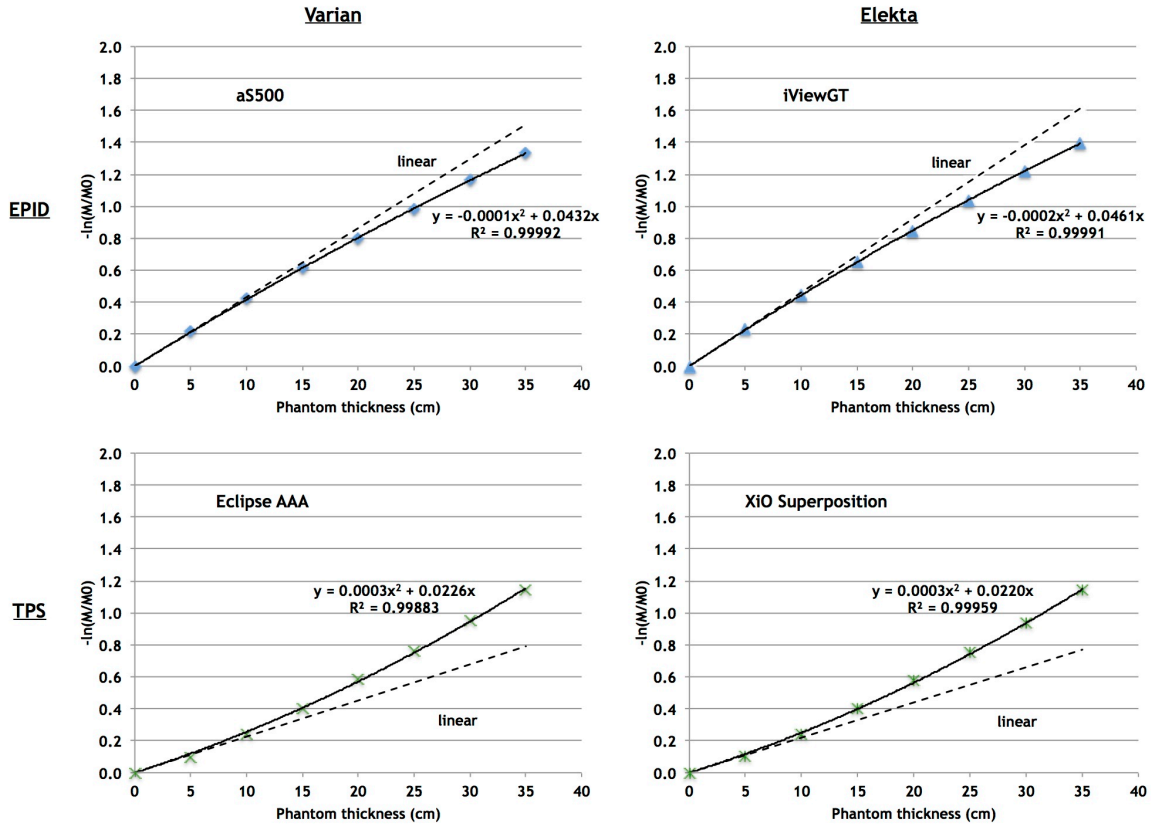

Figure 4-4 Plot of negative logarithm of transmission, -ln(M/M0), versus phantom thickness, PT. Data from EPID calibration dose planes and TPS calibration dose planes are shown in the top and bottom row respectively. Data represent the mean value of 12 x 12 central pixels in a 2D dose planes. The data were fitted with a second-order polynomial, $y = Bx^2 + Ax$, (solid line) and compared with an arbitrary linear trend line (dashed line). The values of A and B coefficients were found to be different for EPID (top row) and TPS (bottom row), but fairly consistent between the two manufacturers, Varian (left column) and Elekta (right column).

The fitting of data to a second-order polynomial was performed for each pixel, resulting in a 2D matrix of A and B coefficients. Figure 4-5 shows the cross-line profiles extracted from 2D A and B coefficients for EPID and TPS. From the plots, it can be observed that the A and B coefficients vary in a symmetrical manner with off-axis positions. Discontinuity of profile at the sides of B coefficient derived from iViewGT EPID images could be due to slight misalignment of the set of calibration dose planes caused by jaw position inaccuracy. Although the absolute values of the coefficients were different between the EPID and TPS, the patterns of variation across the fields were similar. For the A coefficient of the linear term, the minimum value occurred at the centre of the field and increases with increasing distance from the central axis. On the contrary, the maximum value of the B coefficient for the quadratic term was at the centre of the field

and decreases with increasing distance from the central axis. The same observation was true for both Varian and Elekta.

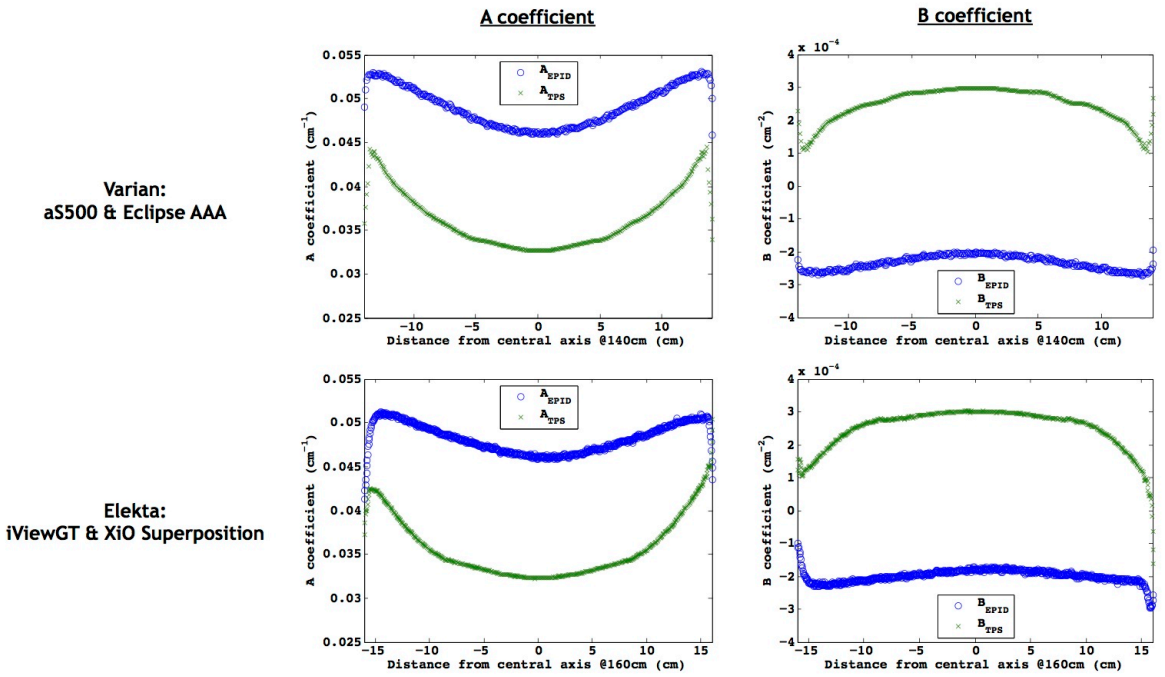

Figure 4-5 Cross-line profiles extracted from 2D A and B coefficients. Profiles for Varian and Elekta are shown in the top and bottom row respectively. Blue data points indicate the (A and B)$_{EPID}$ while green data points indicate the (A and B)$_{TPS}$.

4.4.2 Accuracy of EPL calculated from EPID and TPS dose planes

The accuracy of EPLs calculated from the quadratic equation (Equation 4-7 and 4-8) and the derived coefficients were verified using slabs of homogeneous water-equivalent phantoms with thickness ranging from 5 cm to 35 cm. The reference beam (6 MV, 100 MU, field size 20 x 20 cm^2) was used in this evaluation. The EPLs were calculated from EPID measured dose planes and (A and B)$_{EPID}$ as well as TPS computed dose planes and (A and B)$_{TPS}$. Both sets of calculated EPLs were compared to the expected values. Since the phantoms are of the same density as water, the expected EPL values were equivalent to the physical thickness of the phantoms. Table 4-2 summarises the accuracy of EPL values calculated from EPID and TPS dose planes for both Varian and Elekta. Although all EPLs were calculated as 2D matrices, for clarity the EPL comparisons are presented as the mean value of 12 x 12 pixels in the central region.

Table 4-2 Comparisons of calculated versus expected EPL of attenuators. The EPLs calculated from EPID measured dose planes and (A and B)$_{EPID}$ are listed in the 'EPID' column, while the EPLs calculated from TPS computed dose planes and (A and B)$_{TPS}$ are listed in the 'TPS' column.

		EPID		TPS	
	Expected EPL (cm)	[a]Calculated EPL (cm)	Difference (cm)	[a]Calculated EPL (cm)	Difference (cm)
Varian	5	5.36	0.36	4.65	-0.35
	10	10.14	0.14	9.88	-0.12
	15	14.93	-0.07	15.04	0.04
	20	19.90	-0.10	20.22	0.22
	25	24.84	-0.16	25.13	0.13
	30	29.91	-0.09	29.79	-0.21
	35	35.19	0.19	35.04	0.04
Elekta	5	5.19	0.19	4.71	-0.29
	10	10.09	0.09	9.79	-0.21
	15	15.02	0.02	14.96	-0.04
	20	19.90	-0.10	20.17	0.17
	25	24.88	-0.12	25.17	0.17
	30	29.95	-0.05	30.00	0.00
	35	35.12	0.12	34.90	-0.10

[a] Mean values of 12 x 12 pixels in the central region of the calculated 2D EPL matrix.

The maximum difference between calculated and expected EPL values was ±0.36 cm. The difference in EPL calculated from EPID dose planes and its coefficients ranged from -0.16 cm to 0.36 cm for Varian and -0.12 cm to 0.19 cm for Elekta. Meanwhile, the accuracy of EPL calculated from TPS dose planes and its coefficients ranged from -0.35 cm to 0.22 cm for Varian and -0.29 cm to 0.17 cm for Elekta.

4.4.3 Comparisons of in-phantom exit dose: Reconstructed versus TPS

Figure 4-6 shows the in-phantom exit dose profiles comparisons between those reconstructed from EPID dose planes and TPS computed. The accuracy of dose reconstruction was initially tested with the reference beam of field size 20 x 20 cm^2 and slabs of homogeneous water-equivalent phantoms placed at the isocentre. The thickness of homogeneous phantoms used in this test was: 5 cm, 10 cm, 15 cm, 20 cm, 25 cm, 30 cm and 35 cm. Differences in in-phantom exit

doses at the central region between the reconstructed and TPS computed are listed in Table 4-3.

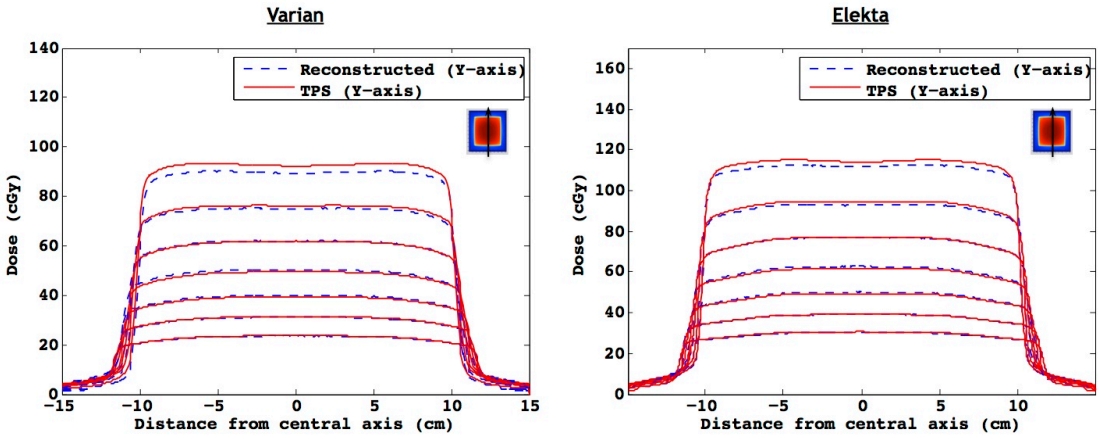

Figure 4-6 In-phantom exit dose profiles comparisons between reconstructed versus TPS computed for a 6 MV, 100 MU beam with field size 20 x 20 cm^2 irradiated at gantry angle zero degrees. The reconstructed (blue dashed line) and TPS (red solid line) profiles were extracted in the in-line direction from 2D dose planes. Profiles, from top to bottom, were the in-phantom exit doses for homogeneous water-equivalent phantoms with thickness 5 cm, 10 cm, 15 cm, 20 cm, 25 cm, 30 cm and 35 cm positioned at the isocentre. The tests were done on both Varian (left) and Elekta (right) systems. Dose values in the central region are given in Table 4-3.

Table 4-3 Comparisons of in-phantom exit dose values between reconstructed and TPS computed (various phantom thicknesses, field size 20 x 20 cm^2). Doses (represented by the mean values of 12 x 12 pixels in the central region) were compared for homogeneous water-equivalent phantoms with different thicknesses ranging from 5 cm to 35 cm and a 6 MV reference beam with field size 20 x 20 cm^2.

Homogeneous phantom thickness (cm)	Varian			Elekta		
	TPS computed (cGy)	Reconstructed (cGy)	[a]Difference (%)	TPS computed (cGy)	Reconstructed (cGy)	[a]Difference (%)
5	92.2	89.2	-3.3%	114.2	111.7	-2.2%
10	76.1	74.9	-1.5%	94.4	93.0	-1.5%
15	61.7	61.9	0.4%	77.1	76.8	-0.4%
20	49.5	50.2	1.6%	61.9	62.8	1.5%
25	39.3	40.0	1.7%	49.4	50.2	1.6%
30	31.3	31.1	-0.7%	39.3	39.3	0.0%
35	23.7	23.5	-0.7%	30.7	30.4	-1.0%

[a] Percentage dose difference was calculated as [(Reconstructed/TPS computed)-1]*100

Comparisons of in-phantom exit dose profiles, between reconstructed from EPID dose planes and TPS computed, showed good matching even at the penumbra region. All reconstructed in-phantom exit doses, represented by the mean of 12

x 12 pixels in the central region, deviated by less than 1.7% from the TPS computed doses except for the smallest phantom with thickness 5 cm. The reconstructed exit dose for the 5 cm thick phantom was lower than the TPS computed dose by 3.3% and 2.2% for Varian and Elekta system respectively.

Comparisons of in-phantom exit doses were also performed for open fields of different sizes: 3 x 3 cm^2, 5 x 5 cm^2, 10 x 10 cm^2 and 15 x 15 cm^2. The results are presented for homogeneous phantoms with thickness 10 cm, 15 cm, 20 cm and 30 cm. The in-phantom exit dose profiles comparisons are shown in Figure 4-7 while dose differences in the central region are given in Table 4-4.

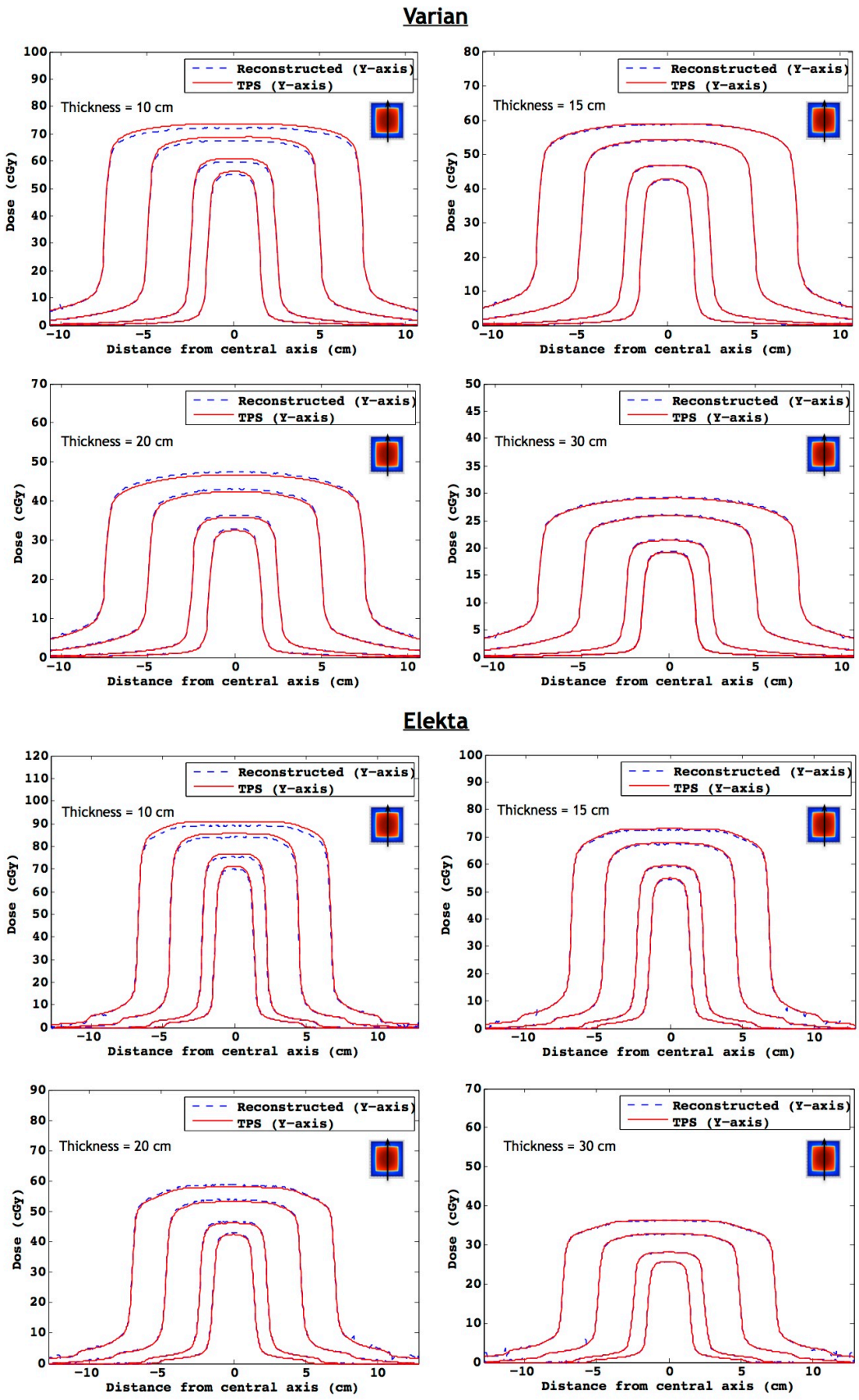

Figure 4-7 In-phantom exit dose profiles comparisons between reconstructed versus TPS computed for a 6 MV, 100 MU beam with field sizes 3 x 3 cm^2, 5 x 5 cm^2, 10 x 10 cm^2 and 15 x 15 cm^2. Blue dashed lines and red solid lines represent the reconstructed and TPS profiles respectively. The thicknesses of homogeneous water-equivalent phantoms used were 10 cm, 15 cm, 20 cm and 30 cm. Dose values in the central region are given in Table 4-4.

Table 4-4 Comparisons of reconstructed and TPS computed in-phantom exit dose values for beams with different field sizes (3 x 3 cm^2 to 15 x 15 cm^2). Doses are represented by the mean values of 12 x 12 pixels in the central region.

Homogeneous phantom thickness (cm)	Field size (cm^2)	Varian			Elekta		
		TPS computed (cGy)	Reconstructed (cGy)	[b]Difference (%)	TPS computed (cGy)	Reconstructed (cGy)	[b]Difference (%)
10	**3 x 3**	56.1	55.0	-2.0%	71.2	69.8	-2.0%
	5 x 5	60.9	59.7	-2.0%	76.7	75.2	-2.0%
	10 x 10	68.8	67.4	-2.0%	85.7	84.1	-1.9%
	15 x 15	73.5	72.0	-2.0%	90.8	89.1	-1.9%
15	**3 x 3**	42.6	42.5	-0.4%	54.9	54.5	-0.7%
	5 x 5	46.8	46.7	-0.4%	59.6	59.2	-0.7%
	10 x 10	54.3	54.1	-0.4%	67.9	67.4	-0.7%
	15 x 15	59.0	58.7	-0.4%	73.1	72.6	-0.7%
20	**3 x 3**	32.4	32.9	1.6%	42.4	42.8	0.9%
	5 x 5	35.8	36.4	1.6%	46.2	46.7	1.1%
	10 x 10	42.4	43.0	1.5%	53.3	53.8	0.9%
	15 x 15	46.6	47.4	1.6%	58.2	58.8	1.0%
30	**3 x 3**	19.1	19.3	0.9%	25.7	25.7	0.0%
	5 x 5	21.3	21.5	0.8%	28.2	28.2	0.0%
	10 x 10	25.9	26.0	0.5%	32.9	32.9	0.0%
	15 x 15	29.1	29.2	0.5%	36.4	36.4	0.0%

[b] Percentage dose difference was calculated as [(Reconstructed/TPS computed)-1]*100

It can be observed from Figure 4-7 and Table 4-4 that the method proposed in this study can accurately reconstruct in-phantom exit doses from EPID measured dose planes even when the field size differed from the reference condition. Good matching between reconstructed in-phantom exit dose and TPS computed dose profiles can be seen for all field sizes including the smallest field of 3 x 3 cm^2. Although the difference between reconstructed dose profiles and TPS dose profiles seems to be more prominent for the phantom with thickness 10 cm, the dose differences were 2% or less. From Table 4-4, it can also be noticed that the percentage dose deviations were fairly consistent for different field sizes for the same phantom thickness, indicating that the method of FSF correction was accurate.

In general, the in-phantom exit dose could be reconstructed from EPID measured dose planes with an accuracy of approximately 2% for open fields of different sizes (3 x 3 cm^2 to 20 x 20 cm^2) tested on homogeneous water-equivalent phantoms of different thicknesses (5 cm to 35 cm). The only exception was the

3.3% dose deviation for the 5 cm thick phantom tested with a 20 x 20 cm^2 field on the Varian system.

4.4.4 Comparisons of EPID transit dose: Predicted versus measured

Instead of comparing doses in-phantom at the exit level, doses can also be compared at the EPID level. Figure 4-8 shows the profiles comparisons between EPID transit doses predicted from TPS dose planes and EPID transit doses measured during treatment delivery, with dose differences in the central region listed in Table 4-5.

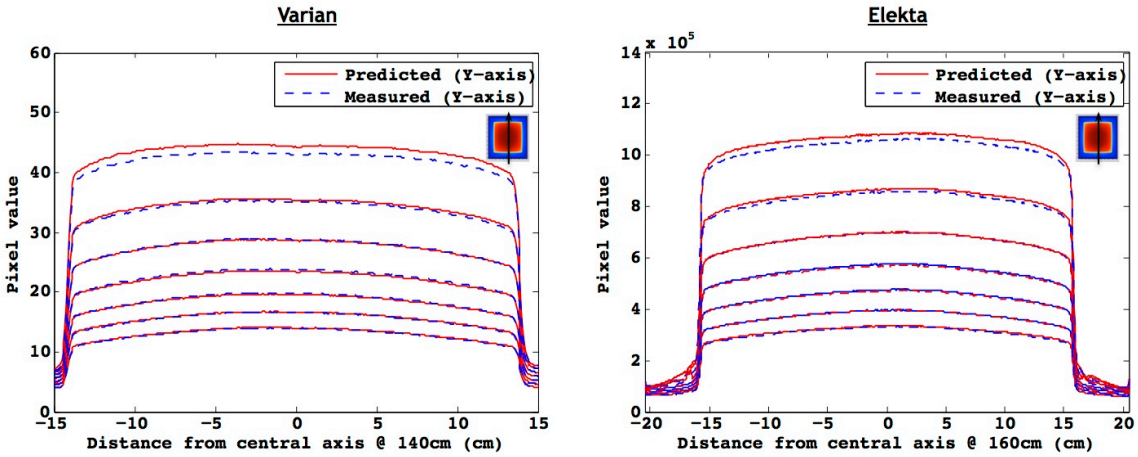

Figure 4-8 EPID transit dose profiles comparisons between predictions from TPS dose planes and measured with EPID for a 6 MV, 100 MU, field size 20 x 20 cm^2 beam irradiated at gantry angle of zero degrees. The TPS predicted (red solid line) and EPID measured (blue dashed line) profiles were extracted in the in-line direction from 2D dose planes. Profiles, from top to bottom, were the EPID transit doses for homogeneous water-equivalent phantoms with thickness 5 cm, 10 cm, 15 cm, 20 cm, 25 cm, 30 cm and 35 cm positioned at the isocentre. The tests were done on both Varian (left) and Elekta (right) systems. Dose values in the central region are listed in Table 4-5.

Table 4-5 Comparisons of predicted and measured EPID transit pixel values (various phantom thicknesses, field size 20 x 20 cm^2). Doses (represented by the mean values of 12 x 12 pixels in the central region) were compared for homogeneous water-equivalent phantoms with different thicknesses ranging from 5 cm to 35 cm and a reference beam with field size 20 x 20 cm^2.

Homogeneous phantom thickness (cm)	Varian			Elekta		
	EPID measured (pixel value)	Predicted (pixel value)	[c]Difference (%)	EPID measured (pixel value)	Predicted (pixel value)	[c]Difference (%)
5	43.0	44.3	3.1%	1.1E+06	1.1E+06	1.9%
10	35.0	35.4	1.1%	8.6E+05	8.7E+05	1.2%
15	28.8	28.6	-0.5%	7.0E+05	7.0E+05	0.1%
20	23.7	23.4	-1.2%	5.8E+05	5.7E+05	-1.0%
25	19.8	19.6	-1.0%	4.8E+05	4.7E+05	-1.1%
30	16.6	16.6	0.4%	4.0E+05	4.0E+05	0.0%
35	13.9	14.0	0.6%	3.3E+05	3.4E+05	0.9%

[c] Percentage difference was calculated as [(Predicted/EPID measured)-1]*100

Figure 4-8 shows very good matching of profiles, across the whole field area, between predictions from TPS dose planes and planes directly measured with the EPID. Comparisons of doses in the central region revealed that most of the doses agreed to within 2% except for the smallest phantom thickness of 5 cm tested on the Varian system, where the predicted dose was higher than the measured by 3.1%. Overall, the difference between predicted and measured EPID transit dose ranged from -1.2% to 3.1% for the Varian system and -1.1% to 1.9% for the Elekta system.

In addition to the reference beam with field size 20 x 20 cm^2, results for EPID transit dose comparisons for other field sizes are presented in Figure 4-9 (for profiles comparisons) and Table 4-6 (for central region dose comparisons). Beams with different field sizes (3 x 3 cm^2, 5 x 5 cm^2, 10 x 10 cm^2 and 15 x 15 cm^2) were selectively tested on homogeneous water-equivalent phantoms with thickness 10 cm, 15 cm, 20 cm and 30 cm on both the Varian and Elekta systems.

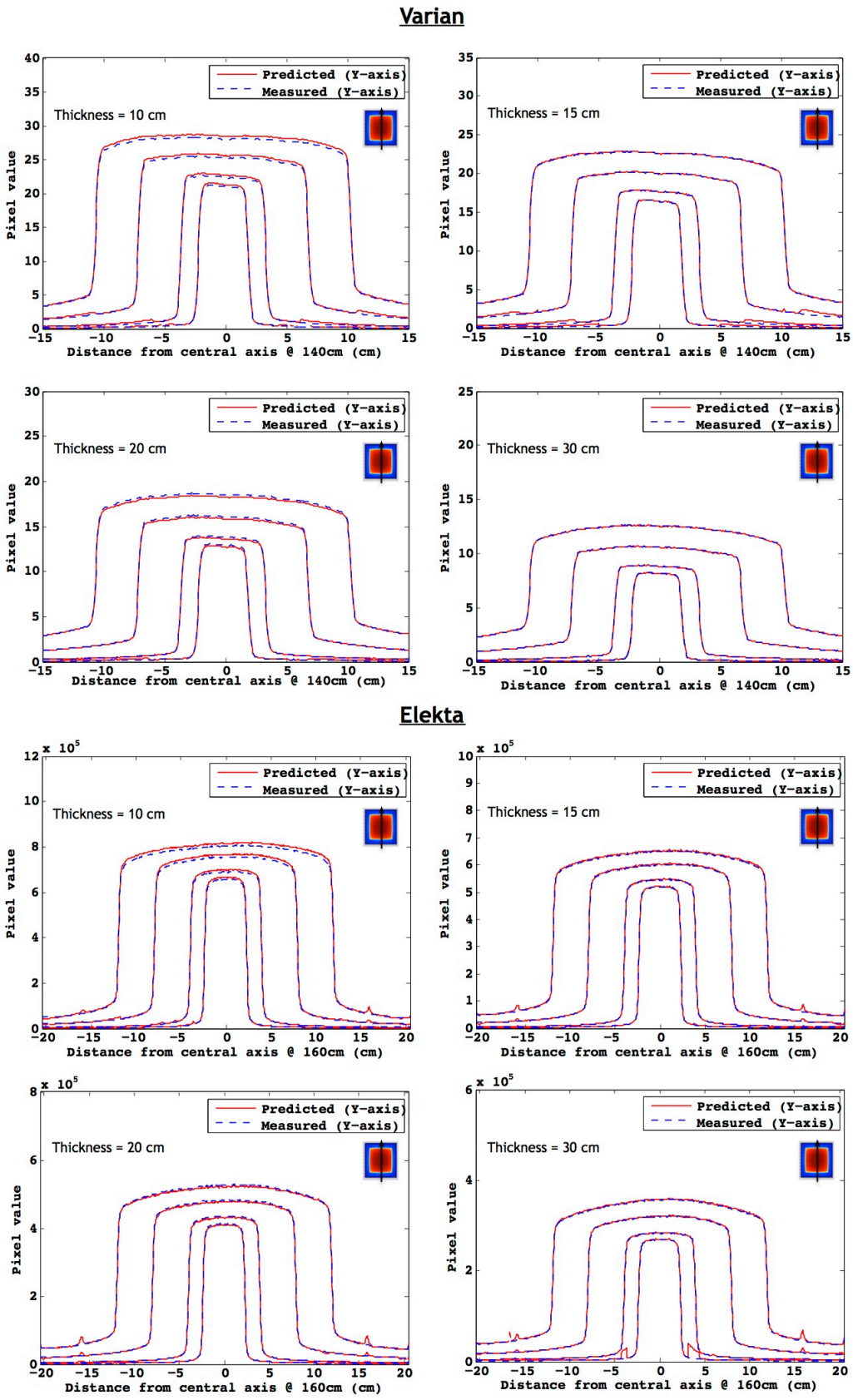

Figure 4-9 EPID transit dose profiles comparisons between predictions from TPS dose planes versus measured with EPID for a 6 MV, 100 MU beam with field sizes 3 x 3 cm^2, 5 x 5 cm^2, 10 x 10 cm^2 and 15 x 15 cm^2. Red solid lines and blue dashed lines represent the TPS predicted and EPID measured profiles respectively. The thicknesses of water-equivalent phantoms used were 10 cm, 15 cm, 20 cm and 30 cm. Differences in pixel values at the central region are given in Table 4-6.

Table 4-6 Comparisons of predicted and measured EPID transit pixel values for beams with different field sizes (3 x 3 cm^2 to 15 x 15 cm^2). Doses are represented by the mean values of 12 x 12 pixels in the central region.

Homogeneous phantom thickness (cm)	Field size (cm^2)	Varian			Elekta		
		EPID measured (pixel value)	Predicted (pixel value)	[d]Difference (%)	EPID measured (pixel value)	Predicted (pixel value)	[d]Difference (%)
10	**3 x 3**	21.0	21.4	1.5%	6.6E+05	6.7E+05	1.4%
	5 x 5	22.4	22.8	1.5%	6.9E+05	7.0E+05	1.4%
	10 x 10	25.3	25.7	1.5%	7.6E+05	7.7E+05	1.6%
	15 x 15	28.1	28.5	1.5%	8.0E+05	8.2E+05	1.6%
15	**3 x 3**	16.4	16.5	0.1%	5.2E+05	5.2E+05	0.4%
	5 x 5	17.7	17.7	0.1%	5.5E+05	5.5E+05	0.4%
	10 x 10	20.0	20.0	0.1%	6.0E+05	6.0E+05	0.5%
	15 x 15	22.6	22.7	0.1%	6.5E+05	6.5E+05	0.5%
20	**3 x 3**	12.9	12.8	-1.3%	4.1E+05	4.1E+05	-0.7%
	5 x 5	13.8	13.6	-1.3%	4.4E+05	4.3E+05	-0.9%
	10 x 10	16.1	15.9	-1.3%	4.8E+05	4.8E+05	-1.0%
	15 x 15	18.5	18.3	-1.3%	5.3E+05	5.2E+05	-0.9%
30	**3 x 3**	8.2	8.2	-0.2%	2.7E+05	2.7E+05	0.0%
	5 x 5	8.9	8.8	-0.2%	2.8E+05	2.8E+05	0.0%
	10 x 10	10.2	10.2	-0.2%	3.2E+05	3.2E+05	0.3%
	15 x 15	12.6	12.5	-0.2%	3.6E+05	3.6E+05	0.3%

[d] Percentage difference was calculated as [(Predicted/EPID measured)-1]*100

Similar to field size 20 x 20 cm^2, tests with other field sizes showed very good profiles matching between predictions from TPS dose planes and measured with EPID. The results show that the proposed model is capable of predicting EPID transit dose for field sizes other than the reference, including the very small 3 x 3 cm^2 field. Differences in pixel values in the central region ranged from -1.3% to 1.6% for all the phantom thicknesses and field sizes tested. For the same phantom thickness, the dose differences were fairly consistent for test fields with different sizes.

From these results, it can be summarised that the EPID transit doses can generally be predicted to within 2% of direct measurements for open fields of various sizes and homogeneous phantoms of various thicknesses. The only exception was for the reference beam tested on the smallest phantom with thickness 5 cm for the Varian system, where the dose deviation between predicted and measured amounted to 3.1%.

4.5 Discussion

In a photon beam produced by a conventional linac, the beam energy spectrum varies with off-axis position because of differential beam hardening by the cone-shaped flattening filter. Since the amount of beam attenuation is dependent on the beam energy (Khan, 2010b), the A and B coefficients are expected to vary at off-axis positions as well. This effect is obvious in Figure 4-5, where the coefficients varied symmetrically away from the central axis. The same trend could be observed for both EPID and TPS. Several authors have reported the same finding with EPID measurements (Swindell, 1983, Symonds-Tayler et al., 1997, Kairn et al., 2008, Kavuma et al., 2010) and MC simulation of EPID response (Kairn et al., 2008) but no publications could be found for TPS or IC measurements. Nevertheless, the relative variation of A and B coefficients at off-axis positions highlights the importance of deriving the coefficients for each point in the 2D plane.

Although both the EPID and TPS showed the same pattern of relative off-axis variations, the absolute values of the A and B coefficients were distinctly different (Figure 4-5). This was because the amount of attenuation quantified from EPID measured and TPS computed dose planes was different for the same reference beam and phantom thickness, as can be seen from Figure 4-4. In this study, the A coefficient (analogous to linear attenuation coefficient) was found to be higher for the EPID compared to the TPS. This was consistent with the observation by Kirkby & Sloboda (2005) where the response to an attenuated beam, relative to a non-attenuated beam, was lower (or more attenuation) for the EPID compared to IC measurements at the same level. The effect was attributed to reduced over-response of the EPID due to removal of low energy photons from the attenuated beam. As for the B coefficient, the EPID measurements reflected less attenuation than would be expected for a linear relationship with increasing attenuator thickness. This less than linear trend for EPID measurements also concurred with those reported by other researchers (Swindell, 1983, Kairn et al., 2008) and may be an effect of beam hardening with increasing attenuator thickness (Kirkby & Sloboda, 2005). However, in contrast to the EPID, the TPS graphs indicated more attenuation with increasing thickness, compared to a linear relationship. This might be because the TPS M0

and M were defined differently in this study, as dose inside the phantom at 1.5 cm from the beam entrance and exit surface of the attenuator respectively. The TPS set-up to compute M0 and M was not designed to satisfy the narrow beam geometry for transmission measurements and could have resulted in the impression of a beam softening effect. The different deviation from linearity was not further investigated as beam spectrum quantification was beyond the scope of this study. What was more important for the purpose of this study was that both the EPID and TPS transmission data could be fitted very well with a quadratic function (Figure 4-4). But recognising the difference, it was imperative that the A and B coefficients must be derived separately for EPID and TPS.

By using the respective A and B coefficients, EPL of the attenuator could be derived accurately from either EPID measured dose planes or TPS computed dose planes (Table 4-2). For both instances, accuracy of the calculated EPLs was found to be better than ±0.36 cm. The EPL results from this study compared favourably with those reported by previous researchers. Employing the same quadratic calibration method for EPID measurements, Kavuma et al. (2010) reported that the calculated EPLs deviated by less than ±0.30 cm from the expected values, while Kairn et al. (2008) reported that the EPLs calculated from EPID measured dose planes and MC simulated EPID dose planes deviated by less than ±0.25 cm and ±0.50 cm respectively from the expected values. No literature could be found for EPL calculation with TPS computed dose planes based on the quadratic calibration method.

In this study, an iterative numerical method was used to calculate all the EPLs, where the value from Equation 4-6 served as an initial approximation and the calculation repeated itself five times to obtain a converged solution. The choice of five iterations was based on the results in Table 4-7. Results from the randomly chosen sample showed that convergence could be achieved in five iterations for most conditions. Kairn et al. (2008) and Kavuma et al. (2010) also reported the same number of iterations for convergence.

Table 4-7 Calculated EPL values according to the number of iterations. The EPL values were represented by the mean of 12 x 12 pixels in the central region. For brevity, results are only presented for a few randomly chosen experimental conditions but were representative of all other conditions. In general, convergence was observed after five iterations.

Number of iteration	Elekta							
	EPL calculated from EPID dose planes (cm)				EPL calculated from TPS dose planes (cm)			
	Field size: 3x3cm^2; Phantom thickness: 10 cm	Field size: 5x5cm^2; Phantom thickness: 15 cm	Field size: 15x15cm^2; Phantom thickness: 30 cm	Field size: 20x20cm^2; Phantom thickness: 35 cm	Field size: 3x3cm^2; Phantom thickness: 10 cm	Field size: 5x5cm^2; Phantom thickness: 15 cm	Field size: 15x15cm^2; Phantom thickness: 30 cm	Field size: 20x20cm^2; Phantom thickness: 35 cm
1	9.885	14.645	29.851	35.204	9.264	14.651	30.044	34.902
2	10.119	15.087	29.968	35.204	9.981	15.034	30.042	34.902
3	10.084	15.021	29.962	35.204	9.803	14.963	30.042	34.902
4	10.089	15.031	29.963	35.204	9.846	14.974	30.042	34.902
5	10.088	15.030	29.962	35.204	9.836	14.972	30.042	34.902
6	10.088	15.030	29.962	35.204	9.838	14.972	30.042	34.902
7	10.088	15.030	29.962	35.204	9.838	14.972	30.042	34.902
8	10.088	15.030	29.962	35.204	9.838	14.972	30.042	34.902
9	10.088	15.030	29.962	35.204	9.838	14.972	30.042	34.902
10	10.088	15.030	29.962	35.204	9.838	14.972	30.042	34.902

In this EPID dosimetry model, the calculated EPL was used to relate the EPID and the TPS (Figure 4-3). Depending on the path chosen by the users, either the in-phantom exit dose could be reconstructed (Section 4.3.5) or the EPID transit dose could be predicted (Section 4.3.6). In either case, a field size correction factor, FSF, was required to account for deviation from the reference field size that was used to derive the A and B coefficients. Since the EPID and water-based TPS were known to respond differently with field size (Greer & Popescu, 2003, Van Esch et al., 2004), the FSFs were separately tabulated from dose planes measured with the EPID (FSF_{EPID}) and computed with the TPS (FSF_{TPS}) for a range of field sizes and phantom thicknesses. Figure 4-10 shows the plot of central axis FSF_{EPID} and FSF_{TPS} for the Varian and Elekta system. From the figure, it can be noted that the FSF values are dependent on phantom thickness and different between EPID and TPS.

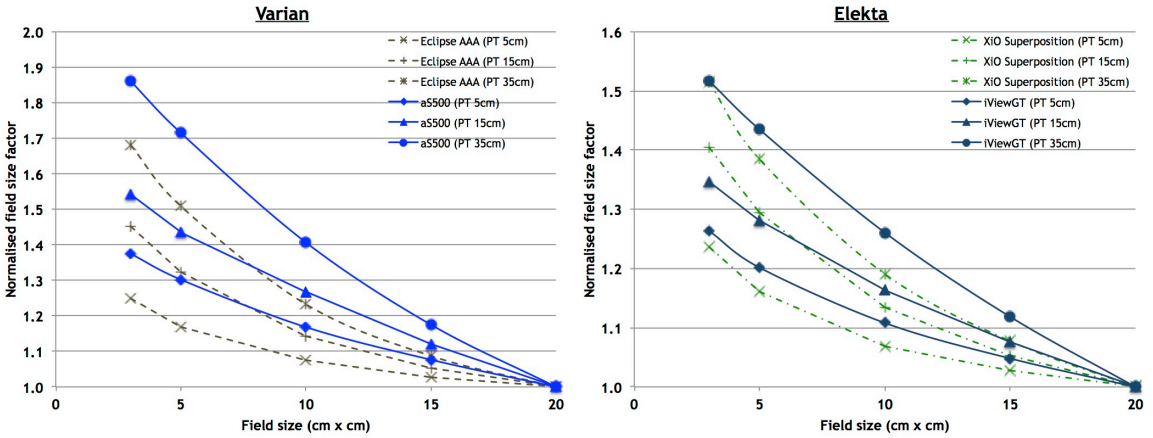

Figure 4-10 Field size correction factor (FSF) for EPID and TPS. The FSF_{EPID} (solid line) and FSF_{TPS} (dashed line) for field size ranging from 3 x 3 cm^2 to 20 x 20 cm^2 are shown in the graphs. By definition, FSF values are normalised to the reference field size of 20 x 20 cm^2. Data plotted represent the central axis value. For clarity, only FSF for water-equivalent phantom thickness (PT) 5 cm, 15 cm and 35 cm were shown in the graphs.

Rather than tabulating the correction factor from a single FSF value taken at the central axis, the FSF was tabulated in 2D and the correction was applied based on the individual pixel location. The use of 2D FSF correction improved the accuracy of off-axis dose reconstruction or prediction considerably, as shown in Figure 4-11.

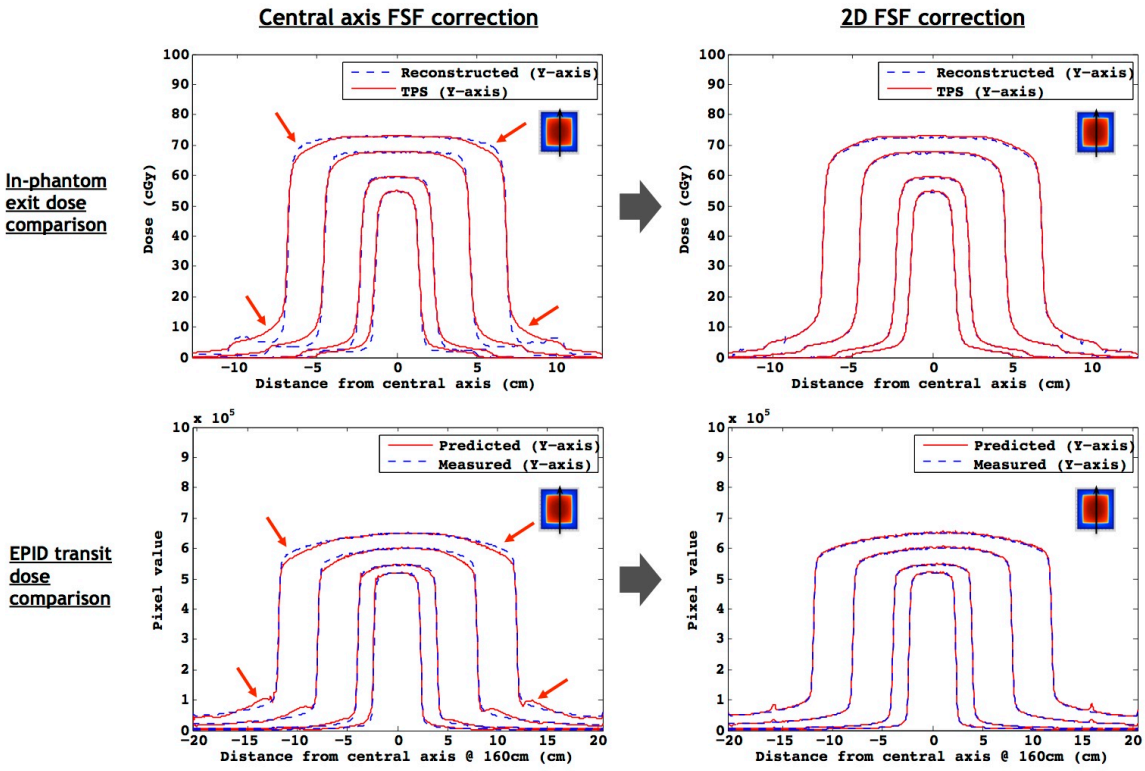

Figure 4-11 Field size correction using central axis FSF values versus position dependent 2D FSF values. Results on the left column were corrected using central axis FSF values while results on the right column were corrected using 2D FSF. Doses at off-axis positions were reconstructed/predicted more accurately with the 2D FSF correction method. Areas of mismatch (indicated by red arrows) seen with doses reconstructed/predicted using central axis FSF value were no longer apparent when the 2D FSF method was used. The improvements were obvious for both in-phantom exit dose comparisons (top row) as well as EPID transit dose comparisons (bottom row). Profiles in this figure were for a 6MV, 100MU beam with field sizes 3 x 3 cm^2, 5 x 5 cm^2, 10 x 10 cm^2 and 15 x 15 cm^2, tested on 15 cm thick homogeneous water-equivalent phantom for the Elekta system.

One of the advantages of the EPID dosimetry model described in this study is its simplicity and practicality. Besides field size correction, the model does not require any other complex correction, such as those associated with the standard flood field correction. As part of the manufacturer's standard procedure, all a-Si EPID panels are corrected with a flood field to eliminate pixel sensitivity variations for better imaging quality. However, this standard flood field correction removes the characteristic horns of a photon beam from the resultant image ("washed-out" effect) and caused dose error up to 8% for fields larger than 10 x 10 cm^2 (Parent et al., 2007). Different approaches had been proposed to overcome the washed-out effect due to standard flood field correction. These methods either: (1) create a near uniform beam to be the

flood field or (2) restore the lost profile after a standard flood field calibration. In the first approach, a near uniform flood field was created by placing an appropriate amount of attenuating material in the path of the beam (Greer & Popescu, 2003, Siebers et al., 2004) or by systematically irradiating different parts of the EPID with multiple small fields, where the beam could be considered as flat (Greer, 2005, Parent et al., 2006). As for the second approach, the lost profile could be restored based on additional correction derived from IC measurement (Renner et al., 2005, Chen et al., 2006), film measurement (Van Esch et al., 2004), Monte Carlo simulation (Siebers et al., 2004, Parent et al., 2007) or TPS generated profiles (Talamonti et al., 2006, Kavuma et al., 2010). Although these methods could overcome the washed-out effect of EPID images, they were often very cumbersome, with some of the methods requiring a dedicated flood field correction procedure that differed from manufacturer's default setting. Deviating from the standard manufacturer's recommendation is often not desirable, and sometimes not possible, in a clinical department.

The washed-out effect due to standard flood field calibration was not an issue in this dosimetry model because the $(A \text{ and } B)_{EPID}$ coefficients were derived from EPID dose planes measured with standard flood field calibration and therefore, the washed-out effect was inherent in the coefficients. Consequently, for Path 1, the EPL of the attenuating object could still be calculated correctly from EPID dose planes that contained the washed-out effect using the $(A \text{ and } B)_{EPID}$ coefficients. Once the EPL was correctly calculated, the subsequent in-phantom dose prediction would not be a problem because the washed-out effect only affects EPID measurements. As for Path 2, the calculation of EPL from TPS exported dose planes did not involve any EPID images and is, therefore, unaffected by the washed-out effect. Although the subsequent prediction of EPID transit dose plane from EPL and $(A \text{ and } B)_{EPID}$ coefficients would reflect the washed-out effect, this was not an issue because the predicted dose plane would be directly compared with an EPID measured transit dose plane that had the same feature. The ability to use EPID images captured under standard flood field calibration in the clinical mode and without additional correction simplifies the EPID dosimetry model and makes it practical for other clinical departments to adopt the model.

In addition, artefacts due to non-uniform backscatter from the metallic component of the aS500 support arm were also not an issue in this EPID dosimetry model. Several authors had reported that the additional backscatter from the support arm could cause the EPID response to increase by approximately 4% to 6%, particularly in the in-plane direction (Ko et al., 2004, Greer et al., 2009, Berry et al., 2010, Rowshanfarzad et al., 2010). To reduce the arm backscatter effect, Ko et al. (2004) suggested that a 0.5 cm lead sheet should be placed in between the detector and the support arm. Instead of adding a filter to the EPID panel, Greer et al. (2009) incorporated the backscatter component in the pixel sensitivity correction matrix by measuring the flood field with and without the support arm (by physically detaching the EPID from the support structure). Alternatively, Rowshanfarzad et al. (2010) derived a backscatter kernel from 1 cm^2 pencil beam measured at different positions on the EPID panel with and without the support arm. Since the backscatter effect is dependent on field size and position, Berry et al. (2010) suggested the use of either a series of field size specific 2D correction matrices or a generalised correction equation to eliminate the backscatter effect. Again, all these methods would add to the complexity of the EPID dosimetry model. Furthermore, the methods by Ko et al. (2004), Greer et al. (2009) and Rowshanfarzad et al. (2010) involved physical modification of the EPID panel and would be impractical in most clinical departments. In this EPID dosimetry model, no additional correction was required to account for backscatter from the aS500 support arm. The correction was not necessary because the use of exit to entrance ratio in the dosimetry model would have cancelled off the arm backscatter effect, as long as the imager was positioned at the same location for the two measurements. As can be seen from the Varian profiles comparisons in Figure 4-8 and 4-9, without any additional correction, discrepancies due to the arm backscatter effect were not present even for large open fields in the in-line direction where the effect was thought to be most prominent.

Besides being simple and practical, this EPID dosimetry model also has the advantage of being generic and flexible. The results presented above for EPID and TPS from both Varian and Elekta demonstrate that the model is not manufacturer-specific. The proposed model is applicable as long as the calibration dose planes were computed and measured for the TPS and EPID of

interest. To accommodate the preference of different users, the model also offers the flexibility to choose between comparing doses in-phantom or at the EPID level. It has been shown that both the comparison of 'reconstructed versus TPS computed in-phantom exit dose' as well as 'predicted versus EPID measured transit dose' are feasible and accurate.

However, there are a few weaknesses in the proposed EPID dosimetry model. One obvious and general disadvantage that affects all EPID-based dosimetry model is related to the relatively small active area, which limits the maximum field size that could be analysed. Because a reference field size of 20 x 20 cm^2 was used to derive the A and B coefficients in this study, the quadratic equation could only calculate EPL correctly for measurements within this field area. Beyond the 20 x 20 cm^2 area, the EPL calculation would be inaccurate because no proper coefficients were available. The 20 x 20 cm^2 field size was selected considering that the aS500 EPID has an active area of 30 x 40 cm^2 and at 140 cm source to detector distance, the maximum field size at 100 cm must be less than 21 x 28 cm^2 to avoid irradiation of EPID electronics. Although the detector distance could be reduced to maximise the irradiation field size, the 140 cm source to detector distance was chosen to allow for more clearance, since the ultimate aim of this study was to extend the application to actual patient treatment verification with different gantry angles. As for the iViewGT EPID, which has a fixed source to detector distance of 160 cm but a larger active area (41 x 41 cm^2), the maximum field size that could be used is 25 x 25 cm^2. However, the same 20 x 20 cm^2 reference field size was chosen for both the aS500 and iViewGT EPIDs in this study for consistency.

The other disadvantage that was more specific to this study was the use of TPS computed dose planes in the calibration process. Although the calibration dose planes were simple and could be computed easily with any TPS models, this requirement is undesirable because any inaccuracies in the calibration dose planes will become an integral part of the EPID dosimetry model. This factor is even more critical in the context of this study because the calibration dose planes were taken at the entrance and exit level, where inaccuracies in the TPS computed doses could be as much as 5% (Tan et al., 2014). Errors in the calibration data would propagate to the end results and may mask real

inaccuracies in the treatment delivery. For example, as shown in the experiment described in Chapter 3, the Eclipse AAA computed dose was 3.8% higher than IC measured dose at the exit level of a water-equivalent phantom with thickness 15 cm, for a 6 MV beam with 20 x 20 cm^2 field size. However, this error in the TPS algorithm would not be detected in this EPID dosimetry model. The difference between reconstructed and TPS computed in-phantom exit dose for the same beam and phantom thickness was only 0.4% (Table 4-3). Ideally, the calibration data should be as accurate as possible so that real differences between planned and delivered dose would be reflected as discrepancies in the EPID dosimetry results.

4.6 Conclusions

A novel empirical-based EPID transit dosimetry model that used EPL to relate EPID and TPS has been described and proven to be valid. The methods used in the dosimetry model were relatively simple and practical without requiring modification of the EPID panel or measurements out of clinical mode. The described dosimetry model is also generic and has been shown to work with linac, EPID and TPS from different manufacturers. In addition, the model is flexible and allows users to choose their preferred location for dose comparisons, either in-phantom (at 1.5 cm from the exit surface of the phantom) or at the EPID level.

In this preliminary study with homogeneous phantoms and open fields, the overall discrepancies (taken at the central region) between 'reconstructed versus TPS computed in-phantom exit dose' and 'predicted versus EPID measured transit dose' were less than 2%, except for the smallest phantom with thickness 5 cm where a maximum dose difference of 3.3% was observed. Profiles matching across the field were also found to be excellent including the penumbra region.

The issue of reliance on the TPS computed dose planes in the calibration process will be discussed and addressed in the next chapter.

Chapter 5: A dual 2D EPID transit dosimetry model based on an empirical quadratic formalism

5.1 Publication/presentation arising from work in this chapter

- **A 2D EPID transit dosimetry model based on an empirical quadratic formalism**, Tan, Y., Metwaly, M., Glegg, M., Baggarley, S. & Elliott, A., 2014, Poster presentation, *56th Annual Meeting and Exhibition, American Association of Physicists in Medicine (AAPM)*, Austin, Texas, USA.
- **A dual two dimensional electronic portal imaging device transit dosimetry model based on an empirical quadratic formalism**, Tan, Y., Metwaly, M., Glegg, M., Baggarley, S. & Elliott, A., 2015, *British Journal of Radiology*, 88 (1051), 20140645: 1-15.

5.2 Introduction

A novel method was described in Chapter 4 that used the EPL of the attenuator to relate the EPID and TPS. Based on this relationship, an empirical 2D EPID transit dosimetry model was developed for treatment verification. The dosimetry model has the advantage of being simple, practical and generic. Another unique advantage of the dosimetry model is the dual nature that can either:

- Reconstruct in-phantom exit dose from EPID measured dose planes. (The in-phantom exit dose was defined as dose at 1.5 cm upstream from the beam exit surface of a phantom); or
- Predict EPID transit dose from TPS exported dose planes.

Initial investigation of the dosimetry model using simple square fields of different field sizes on homogeneous slab phantoms of various thicknesses proved that the model was valid. The overall discrepancies at the central region between ‘reconstructed versus TPS computed in-phantom exit dose’ and ‘predicted versus EPID measured transit dose’ were less than 2%, except for the smallest phantom with thickness 5 cm where a maximum difference of 3.3% was observed. Comparison of measured and predicted profiles across the field,

including the penumbra region, showed excellent agreement for all fields investigated.

However, the EPID transit dosimetry model proposed in Chapter 4 required TPS calibration dose planes, computed for a reference beam and exported at 1.5 cm from the beam entry and exit surface of a water-equivalent phantom, in the commissioning process. The accuracy of TPS computed dose at these levels, where the amount of build up and backscatter is limited, had been found to vary with different TPS algorithms, as detailed in Chapter 3. Comparisons between IC measured and TPS computed doses revealed that, while most TPS algorithms could accurately compute doses at the entrance level to within 2%, the accuracy of TPS computed doses at the exit level were generally poorer with discrepancies of up to about 5% (Tan et al., 2014). By using TPS computed entrance and exit doses as the calibration dose planes in the commissioning process, any inaccuracies from the TPS algorithm would become inherent in the EPID dosimetry model. Ideally, the commissioning data for the EPID dosimetry model should be as accurate as possible to prevent systematic errors from propagating to the end results and affecting the reconstructed/predicted doses.

Therefore, the first objective of this chapter was to replace the TPS calibration dose planes, used to derive the quadratic equation coefficients, with calibration dose planes measured with IC in water. By using the IC measured calibration dose planes rather than TPS computed calibration dose planes, the EPID dosimetry model would not be reliant on the TPS computed doses that may contain inaccuracy. Also, by using a commissioning method that is independent of the TPS, the EPID dosimetry model should be better able to reveal actual discrepancies between measured and TPS planned doses.

The second objective of this chapter was to expand the EPID transit dosimetry model to allow analysis of modulated fields. The ability of a dosimetry model to perform verification of modulated treatment is crucial and more relevant in today's context of radiotherapy practice. This is because modulated treatment fields, such as the IMRT, are more complex and place greater demands on the treatment planning and delivery systems. As modulated treatments become more commonplace, it is imperative that the EPID dosimetry model be capable

of verifying modulated fields to reduce the probability of major errors in treatment delivery.

The third objective of this chapter was to test the dosimetry model not only on homogeneous phantoms but also heterogeneous phantoms. The ability of an EPID transit dosimetry model to deal with heterogeneity is another important aspect that must be evaluated before the model can be applied for actual patient treatment verification, which is the ultimate aim of this research project.

5.3 Materials and methods

5.3.1 Overview of the EPID transit dosimetry model

A detailed description of a novel 2D EPID transit dosimetry model was provided in Chapter 4. Briefly, the 2D EPID transit dosimetry model was based on a quadratic equation (Swindell, 1983) that relates the reduction in intensity, represented by the ratio of exit (M) to entrance (M0) dose, to the water-equivalent thickness or EPL of the attenuator.

$$-\ln\left[\frac{M(i,j)}{M0(i,j)}\right] = A(i,j) \times EPL(i,j) + B(i,j) \times EPL^2(i,j) \qquad (5\text{-}1)$$

(Equation 4-4, Chapter 4)

where 'A' and 'B' are the coefficients and (i,j) is the coordinate of pixels in a 2D plane. The linear coefficient, A, reflects the linear attenuation coefficients of the attenuator while the quadratic coefficient, B, describes the non-linear relationship due to spectral variation in a photon beam (Swindell, 1983).

The commissioning of the EPID dosimetry model involved the derivation of the A and B coefficients in the quadratic equation from a set of M and M0 calibration dose planes measured for homogeneous phantoms with known water-equivalent thicknesses under reference conditions. By fitting Equation 5-1, pixel-by-pixel, to the set of calibration dose planes measured with phantoms of different thicknesses, A and B coefficients can be obtained. With the A and B coefficients, the EPL of any attenuator can be calculated from Equation 5-2 (inversion of Equation 5-1) if given the amount of reduction in intensity (M/M0).

$$EPL(i,j) = \frac{-A(i,j) \pm \sqrt{A^2(i,j) - 4B(i,j) \times \ln\{FSF(i,j) \times [M(i,j)/M0(i,j)]\}}}{2B(i,j)} \quad (5\text{-}2)$$

(Equation 4-7, Chapter 4)

where FSF is the field size correction factor, defined as the ratio of dose for the reference field size to dose for other field sizes of interest. The FSF was tabulated from 2D dose planes measured for a range of field sizes as a function of attenuator thicknesses and the correction was applied based on the individual pixel location (i,j).

The calculated 2D EPL map, which is a property of the attenuator and independent of the measuring system, is then used as a bridge to translate between the two different dosimetry systems, EPID and TPS. For the dosimetry model to work, two sets of quadratic equations coefficients must be derived separately for the EPID and TPS because of the differential response and scatter characteristics of the EPID. With two sets of coefficients, the EPL can be calculated from either the EPID or TPS dose planes for the treatment field to be investigated, giving the model a dual nature. Also, the two sets of coefficients, together with the calculated EPL, are required in the dose reconstruction/prediction process, as previously illustrated in Figure 4-3 and with the updated version shown below in Figure 5-3.

5.3.2 Commissioning process: Calibration dose planes for A and B derivation

In the EPID transit dosimetry model described in Chapter 4, the two sets of coefficients, $(A \text{ and } B)_{EPID}$ and $(A \text{ and } B)_{TPS}$, were derived from calibration dose planes measured with EPID and computed with TPS respectively. The calibration dose planes were measured and computed for the same reference beam (6 MV, 200 MU and field size 20 x 20 cm^2) and the same set of water-equivalent homogeneous phantoms of known thicknesses (PT: 0 cm to 35 cm) placed at the isocentre. The study was performed in two separate and independent institutions equipped with Varian and Elekta linacs and TPSs to demonstrate the generic nature of the proposed dosimetry model.

The study described in this chapter was only performed in Institution A with Varian Clinac 21EX linac and Eclipse TPS (Palo Alto, CA, USA). The same reference beam parameters and homogeneous phantom thicknesses were used to derive the calibration dose planes in this study. While the EPID measurements of calibration dose planes remained largely the same as before, the TPS computed calibration dose planes were replaced with IC measurements in water. Methods to measure the calibration dose planes are provided in the following sub-sections, briefly for the EPID measurements and with more detail for the IC measurements in water.

5.3.2.1 Measurements of EPID calibration dose planes to derive $(A \text{ and } B)_{EPID}$

The experimental methods to measure EPID calibration dose planes were described explicitly in Chapter 4, sub-Section 4.3.3.1. In short, EPID images were captured with an aS500 a-Si EPID (Varian, Palo Alto, CA, USA) that had 384 x 512 pixels using standard manufacturer's software, IAS3. All images were captured using default manufacturer's settings that automatically perform dark field, flood field and defect pixel corrections as part of the standard image processing procedure in the clinical mode. The distance from source to EPID was fixed at 140 cm. The EPID panel was used unmodified, as supplied by the manufacturer, for practical implementation. The M0 dose planes were captured without a phantom in the beam (0 cm) while M dose planes were captured with water-equivalent solid phantom (density 1.04 g/cm^3, Gammex Inc., Middleton, WI, USA) of different thicknesses (5 cm to 35 cm) placed isocentrically (SAD) at 100 cm. The experimental set-up for the EPID measurements was shown in Figure 4-1 and is reiterated below in Figure 5-1a for easy reference. Although the EPID signal was not absolutely calibrated to dose, the term EPID dose plane was used for a more consistent description with the IC and TPS dose planes.

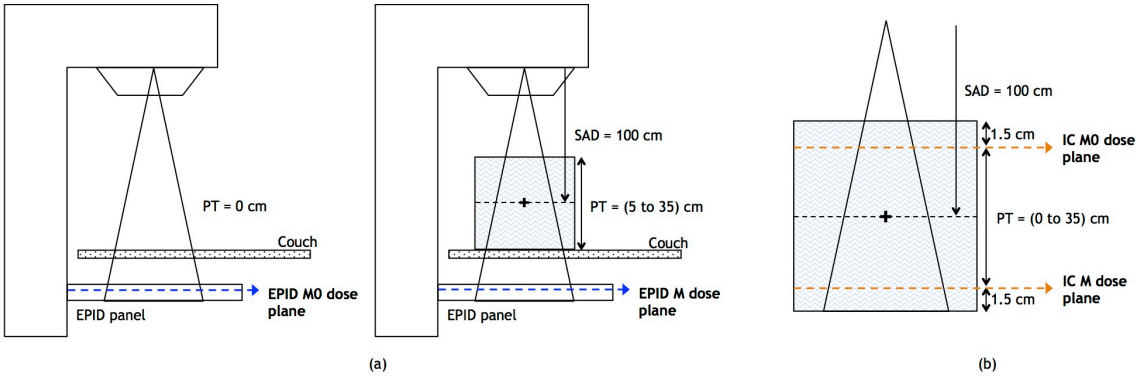

Figure 5-1 Set-up for EPID and IC calibration dose planes. (a) Experimental set-up for the EPID entrance (M0) and exit (M) calibration dose planes measurements. (b) Set-up dimension for the IC entrance (M0) and exit (M) calibration dose planes. Additional 1.5 cm build up was required for the IC set-up dimension to provide adequate electronic equilibrium for the 6 MV beam used in this study while an additional 1.5 cm backscatter was chosen for a symmetric geometry. The ratio of M to M0, for both EPID and IC set-up, included the same set of water-equivalent phantom thicknesses (PT: 0 cm to 35 cm).

5.3.2.2 Measurements of IC calibration dose planes to derive $(A \text{ and } B)_{IC}$

The first objective of this study was to replace the TPS calibration dose planes, described in Chapter 4, sub-Section 4.3.3.2, with dose planes derived from IC measurements in water. The IC calibration dose planes were derived to simulate the isocentric set-up shown in Figure 5-1b. This set-up was similar to the TPS virtual phantom set-up shown in Figure 4-2. As with the TPS calibration dose planes, the IC M0 and M were defined as doses at depth 1.5 cm from the beam entrance and exit surface in a phantom respectively. The 1.5 cm build up for the M0 was necessary to provide reasonable electronic equilibrium conditions for the 6 MV beam used in this study and the 1.5 cm backscatter was chosen for a symmetric geometry. As a result, the vertical dimension of the water phantom was effectively (1.5+'PT'+1.5) cm, where 'PT' ranged from 0 cm to 35 cm.

To derive the IC calibration dose planes, cross-line and in-line profiles were measured with a CC04 IC (IBA Dosimetry, Schwarzenbruck, Germany) in a scanning water tank (IBA Dosimetry, Schwarzenbruck, Germany) at different depths from 1.5 cm to 36.5 cm. All measured profiles were normalised to the central axis. After that, each of the 1D relative profiles was duplicated to fill a 2D matrix of 512 x 512 dimension. For each scan depth, there were two matrices representing the in-line and cross-line directions. Then, the in-line and cross-line matrices for the same scan depth were multiplied to generate a 2D relative dose plane. The 2D relative dose plane was cropped to 384 (rows) x 512 (columns) to

match the EPID dimension. Finally, all the 2D relative dose planes at different depths were converted into 2D absolute dose planes by multiplication with the central axis dose calculated from percentage depth dose (PDD).

Since the PDDs, by definition, were measured at a fixed source to surface distance (SSD) of 100 cm and with full backscatter, two corrections were required to account for: (1) the varying SSD due to the isocentric set-up, and (2) the difference in backscatter thickness at the entrance and exit levels. Figure 5-2 shows the two corrections to translate PDD measurements in a scanning water tank with a fixed SSD of 100 cm and with full scatter condition, to the IC calibration dose planes with isocentric set-up and with limited backscattering material.

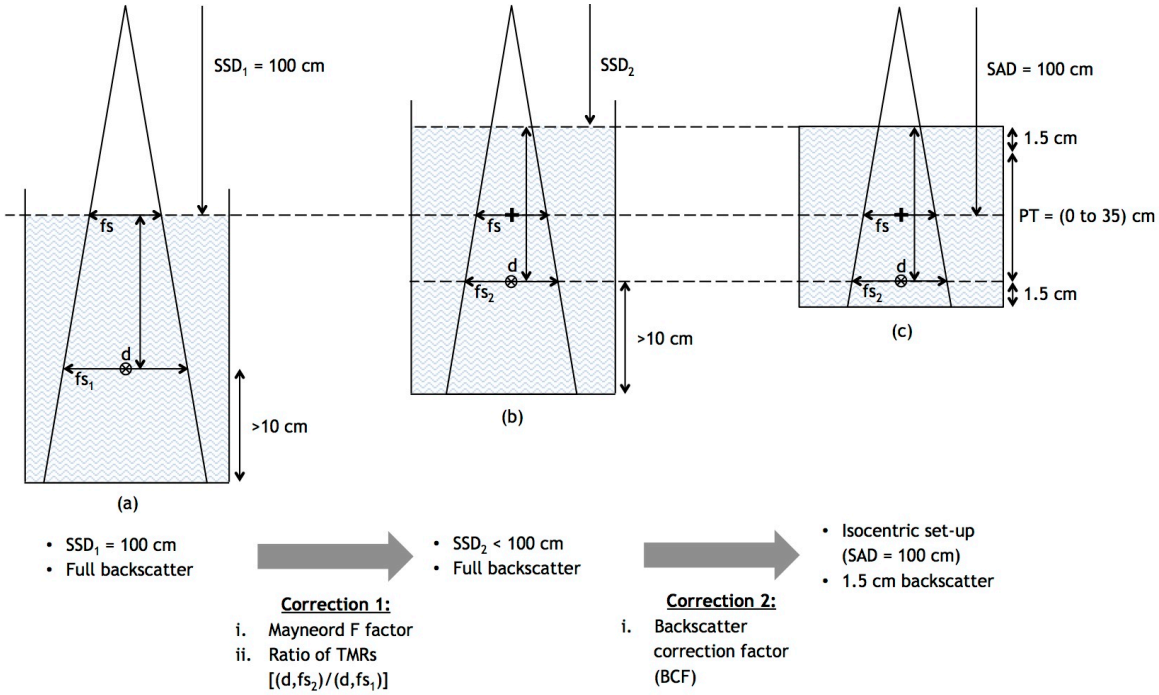

Figure 5-2 Conversion of dose calculated from PDD to isocentric dose with 1.5 cm backscatter. Steps to translate dose calculated from PDD, measured in a scanning water tank with a fixed SSD of 100 cm and with full scatter condition (diagram a), to the dose with isocentric set-up and with 1.5 cm backscatter (diagram c). The first corrections, with Mayneord F factor and ratios of TMRs, were used to quantify the change in PDD with non-standard SSD. The Mayneord F factor and ratios of TMRs account for the inverse square effect and variation in phantom scatter respectively. The second correction, BCF, defined as the ratio of dose without full backscatter to dose with full backscatter, was used to quantify the reduction in backscattered photon due to the different amount of underlying material. Corrections 1 and 2 are given in Equations 5-3 and 5-5 respectively in the text.

The first correction was to quantify the change in PDD with SSD due to the isocentric set-up required in this study. The PDD, which is the dose at any depth relative to the dose at a fixed reference point, decreases with decrease in SSD. This is because the reduction in dose between two points due to the inverse square law effect is more rapid nearer to the source as opposed to further away (Khan, 2010a). The Mayneord F factor (Mayneord & Lamerton, 1941), shown in the second term of Equation 5-3, was used to account for this effect. However, the Mayneord F factor correction assumes that the field size at the surface, and consequently the amount of phantom scatter at depth, remains the same with different SSD and only strictly corrects for the inverse square law effect. Since the field size stated in this study is defined at 100 cm, the change in phantom scatter at depth with different SSD was accounted for using a ratio of TMRs (Varian Medical Systems, 2008), shown in the third term of Equation 5-3.

$$PDD_2 = PDD_1 \times \left[\left(\frac{SSD_2 + dmax}{SSD_1 + dmax}\right)^2 \times \left(\frac{SSD_1 + d}{SSD_2 + d}\right)^2\right] \times \left[\frac{TMR(d,fs_2)}{TMR(d,fs_1)}\right] \quad (5\text{-}3)$$

where subscript ‘1’ and ‘2’ indicates the fixed SSD and isocentric set-up respectively, ‘dmax’ is the depth of maximum dose, ‘d’ is the depth of interest, ‘fs_1’ and ‘fs_2’ are the field sizes at depth ‘d’.

Subsequently, the PDD_2 is used to calculate the dose at depth ‘d’ with the SSD_2 of the isocentric set-up. The formula for dose calculation is given in Equation 5-4.

$$Dose_{fs}^{d} = PDD_2 \times D_{dmax} \times OF_{fs} \times \left(\frac{SSD_1 + dmax}{SSD_2 + dmax}\right)^2 \quad (5\text{-}4)$$

where ‘d’ is the depth at which dose is calculated, ‘fs’ is the field size at distance 100 cm, ‘D_{dmax}’ is the dose at depth of maximum for reference field size (usually 10 x 10 cm^2) and ‘OF_{fs}’ is the field size output factor. The last term of Equation 5-4 is to correct for change in D_{dmax} for different SSD due to the inverse square effect.

Up to this point, the dose calculated from scanning water tank measurements represents full scatter conditions. A second correction, the backscatter

correction factor (BCF), was required to account for the effect of reduced backscatter thickness to satisfy the condition of IC M0 and M calibration dose planes as shown in Figure 5-1b, where the backscatter thickness for M0 varies with different phantom thickness and the backscatter thickness for M was only 1.5 cm. The BCF, defined as the ratio of dose without full backscatter to dose with full backscatter, was measured at the central axis with IC in water-equivalent solid phantoms. Details of the experimental methods and series of BCF values as a function of field size, backscatter thickness and depth for the 6 MV beam investigated can be found in Chapter 3 and Tan et al. (2014). Since the BCF is independent of SSD (Lambert et al., 1983, Tan et al., 2014), the BCF value was taken from Table 3-1 of Chapter 3 and incorporated into Equation 5-4 to yield Equation 5-5.

$$Dose_{fs}^{d} = PDD_2 \times D_{dmax} \times OF_{fs} \times \left(\frac{SSD_1 + dmax}{SSD_2 + dmax}\right)^2 \times BCF \qquad (5\text{-}5)$$

Finally, before the IC dose planes were used to derive the $(A \text{ and } B)_{IC}$ coefficients, all the M0 and M dose planes were scaled to the same reference level using inverse square distance correction. The isocentre (100 cm from source), which is also the mid-plane of the phantom, was chosen as the reference level. The inverse square distance scaling was done so that the ratio of M and M0 will reflect the reduction of dose due to object attenuation entirely without the effect of distance.

The derived $(A \text{ and } B)_{IC}$ coefficients were then used to replace the $(A \text{ and } B)_{TPS}$ described in Chapter 4. The updated EPID transit dosimetry model is illustrated in Figure 5-3 below.

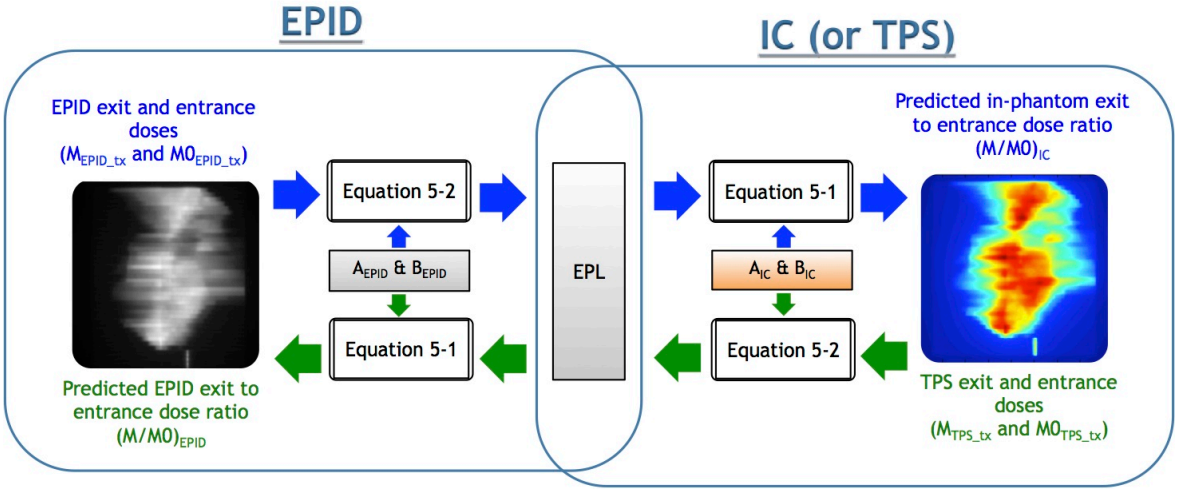

Figure 5-3 The role of quadratic equation coefficients (A and B) and EPL in relating two different dosimetry systems, EPID and IC (or TPS). The diagram is similar to Figure 4-3, except that the $(A \text{ and } B)_{TPS}$ were replaced by $(A \text{ and } B)_{IC}$. Equations 5-1 and 5-2 are given in the text. From left to right is the path (Path 1) to predict in-phantom dose ratio $(M/M0)_{IC}$ from EPID measured dose planes. From right to left is the path (Path 2) to predict EPID dose ratio $(M/M0)_{EPID}$ from TPS exported dose planes. The predicted dose ratios $(M/M0)_{IC}$ and $(M/M0)_{EPID}$ were used to derive in-phantom exit dose and EPID transit dose respectively, as described in Sections 5.3.3 and 5.3.4.

5.3.3 Path 1: Reconstruction of in-phantom exit dose

5.3.3.1 Open field

Figure 5-3, from left to right, shows the flow to predict the in-phantom exit to entrance dose ratio $(M/M0)_{IC}$ from EPID measured dose planes. The process of predicting in-phantom exit dose for open fields was basically the same as that described in sub-Section 4.3.5. In short, two EPID dose planes, measured with (M_{EPID_tx}) and without ($M0_{EPID\_tx}$) the presence of an attenuator for the treatment field to be investigated, together with the $(A \text{ and } B)_{EPID}$ coefficients, were used to calculate the attenuator's EPL according to Equation 5-2. All EPID images were smoothed with a moving average filter (Smith, 2003) using a window size of eight pixels. Smoothing was applied to the EPID images to reduce random signal of low magnitude observed with modulated fields, possibly introduced by MLC interleaf leakage that was not accounted for in the Eclipse TPS. The FSF_{EPID} was required in Equation 5-2 to correct for treatment fields with field size other than the reference 20 x 20 cm^2. The FSF_{EPID} is the field size correction factor tabulated from EPID measured 2D dose planes for a range of field sizes (5 x 5 cm^2 to 20 x 20 cm^2) and attenuator thicknesses (0 cm to 35 cm) and corrected based on pixel location. Then, the calculated 2D EPL matrix was used in

combination with (A and B)$_{IC}$ coefficients, instead of (A and B)$_{TPS}$ in Chapter 3, to calculate the equivalent IC ratio (M/M0)$_{IC}$ using Equation 5-1. Consequently, the in-phantom exit dose ($M_{IC\ pred}$) can be reconstructed by multiplying this equivalent IC ratio with an (reference field size 20 x 20 cm^2) IC entrance dose plane ($M0_{IC\ ref}$) previously derived as part of the commissioning process. An inverse square correction was also added to scale dose from the reference level (100 cm) to the exit level.

$$M_{IC\ pred} = \left(\frac{M}{M0}\right)_{IC} \times M0_{IC\ ref} \div FSF_{IC} \times \left(\frac{100}{SDD}\right)^2 \quad (5\text{-}6)$$

where 'SDD' is the source to exit distance. 'FSF_{IC}' is the field size correction factor tabulated from IC derived 2D dose planes for a range of field sizes (5 x 5 cm^2 to 20 x 20 cm^2) and attenuator thicknesses (0 cm to 35 cm).

The reconstructed in-phantom exit dose was compared to TPS dose computed for the treatment field and exported at the exit level of the phantom, to verify the accuracy of treatment delivery.

5.3.3.2 Modulated field (wedge and IMRT)

The effect of beam modulation will not be reflected in the $M_{IC\ pred}$ from Equation 5-6. This is because the ratio of M_{EPID_tx} to $M0_{EPID\_tx}$ was used to derive the equivalent IC ratio and the division of two identical modulated fields with and without an object in the beam would have cancelled out the modulation effect. Therefore, for verification of modulated treatment fields, an additional modulation factor (MF) defined as the ratio of modulated to non-modulated dose plane was used (Equation 5-7). The modulated dose plane ($M0_{EPID\_tx}$) was the EPID dose plane measured for the treatment field without an object in the beam. The non-modulated dose plane ($M0_{EPID\_openFSx}$) was the EPID dose plane, also measured without an object in the beam, for a reference open field (100 MU, 20 x 20 cm^2) that was subsequently corrected with FSF_{EPID} based on the field size of the treatment field. The effective field size of irregular treatment fields was calculated according to the methods described by Monti et al. (1995) with the irregular field area for an IMRT delivery defined as the region with dose greater than 50% of the maximum dose. Since both the modulated and non-modulated fields were measured by the EPID without an object in the beam and

preferably during the same session, the MF is a relative factor that can be used to quantify beam modulation in a field. The MF needs to be derived only once for each modulated treatment field.

$$MF_{EPID} = \frac{M0_{EPID\_tx}}{M0_{EPID\_openFSx}} \quad (5\text{-}7)$$

Equation 5-6 was modified to include MF, as shown in Equation 5-8, for the prediction of in-phantom exit dose for modulated fields.

$$M_{IC\ pred} = \left(\frac{M}{M0}\right)_{IC} \times M0_{IC\ ref} \div FSF_{IC} \times \left(\frac{100}{SDD}\right)^2 \times MF_{EPID} \quad (5\text{-}8)$$

In the above description, MF from EPID measurements was used to quantify beam modulation for the prediction of TPS in-phantom exit doses. Although the MF is a relative factor, the MF from EPID measurements (MF_{EPID}) was found to be slightly different from the MF from IC measurements (MF_{IC}). Figure 5-4 shows the comparisons of MF_{EPID} and MF_{IC} for enhanced dynamic wedge (EDW) 60 degree (EDW60) and 15 degree (EDW15) fields. MapCHECK2 (Sun Nuclear, Melbourne, FL, USA) measurements were used to represent the IC dose planes to save measurement time. It can be observed from Figure 5-4 that the discrepancies between MF_{EPID} and MF_{IC} were more prominent for EDW60 compared to EDW15. The difference between MF_{EPID} and MF_{IC} and the effect of different wedge angles could be due to variation of EPID response with the changing field size and dose rate during delivery. To account for this effect, a generic correction was derived to convert MF_{EPID} to MF_{IC} for all wedge angles. This generic correction was derived from MF_{EPID} and MF_{IC} measured for the EDW60 field. A graph of MF_{EPID} against MF_{IC} for the EDW60 field was plotted and a linear fit was derived (Figure 5-5). The fitting formula was used to correct the MF_{EPID} to the equivalent of MF_{IC}, ($MF_{EPID\rightarrow IC}$). Two fitting formulae are shown in Figure 5-5, representing the EDW60 fields for field size 10 x 10 cm^2 and 20 x 20 cm^2. Depending on the field size of the test field, the appropriate fitting formula was used for the correction. For wedge fields of other angles (θ), a weighting factor (W) was calculated and used to determine the fraction of total MF to be corrected (Equations 5-9 and 5-10). The weighting calculation was adapted from the concept of achieving a desired effective wedge angle by varying the proportion

of open field irradiation and nominal wedge field irradiation (Tatcher, 1970, Zwicker et al., 1985).

$$\text{Weighting, } W = \frac{\left(\frac{\tan\theta}{\tan 60}\right) \div WF}{\left(\frac{\tan\theta}{\tan 60} \div WF\right) + \left(1 - \frac{\tan\theta}{\tan 60}\right)} \tag{5-9}$$

where 'WF' is the conventional wedge factor, defined as the ratio of central axis dose measured with wedge 60 degree and open field.

$$MF^{EPID}_{corrected} = [MF_{EPID \rightarrow IC} \times W] + [MF_{EPID} \times (1-W)] \tag{5-10}$$

where 'MF_{EPID}' is the uncorrected MF from EPID measurements as defined in Equation 5-7 and the '$MF_{EPID \rightarrow IC}$' is the MF_{EPID} corrected to the equivalent of MF_{IC} using the fitting formula shown in Figure 5-5. Accordingly, the mathematical expression to predict in-phantom exit dose for EDW fields was modified from Equation 5-8 to become Equation 5-11.

$$M_{IC\ pred} = \left(\frac{M}{M0}\right)_{IC} \times M0_{IC\ ref} \div FSF_{IC} \times \left(\frac{100}{SDD}\right)^2 \times MF^{EPID}_{corrected} \tag{5-11}$$

As for IMRT fields, the in-phantom exit dose was also predicted using Equation 5-11. The MF correction was applied but with the W in Equation 5-10 assumed to be one (W = 1).

Finally, the reconstructed in-phantom exit dose for wedge and IMRT fields were compared to TPS computed exit doses to verify the accuracy of treatment delivery.

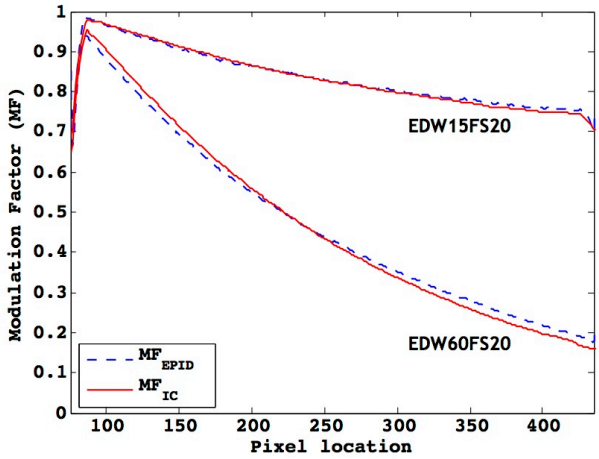

Figure 5-4 Comparisons of MF_{EPID} and MF_{IC} for enhanced dynamic wedge field. The comparisons are for EDW15FS20 (wedge angle 15 degree, field size 20 x 20 cm^2) and EDW60FS20 (wedge angle 60 degree, field size 20 x 20 cm^2) fields. The MF_{EPID} is the modulation factor derived from EPID measurements while the MF_{IC} is the modulation factor derived from IC measurements, represented by MapCHECK2 measurements.

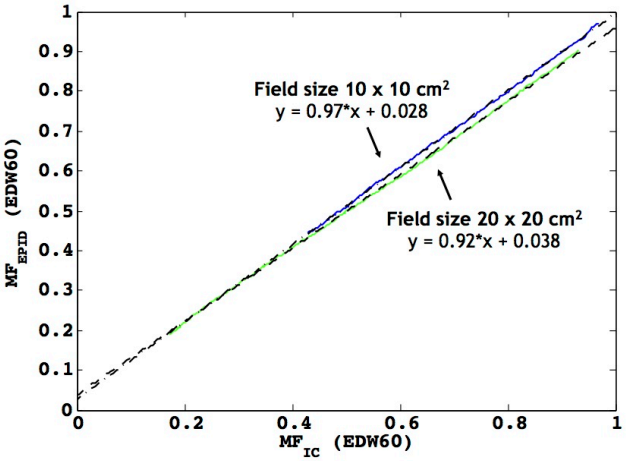

Figure 5-5 Plot of MF_{EPID} versus MF_{IC} for EDW60 field and a linear fit of data. Two plots are shown, representing EDW60 field with field size 10 x 10 cm^2 and 20 x 20 cm^2. The linear equation was used to convert MF derived from EPID to the equivalent of IC (or TPS) and vice versa, $MF_{EPID \Leftrightarrow IC}$.

5.3.4 Path 2: Prediction of EPID transit dose

5.3.4.1 Open field

Figure 5-3, from right to left, shows the flow to predict EPID transit dose from TPS exported dose planes. The treatment plans in this study were computed using the Eclipse AAA algorithm from Varian (version 10.0.28, Palo Alto, CA, USA) with 0.1 cm grid size. All TPS exported M0 and M dose planes were scaled to the same reference level (100 cm) using inverse square distance correction.

The entrance ($M0_{TPS\_tx}$) and exit (M_{TPS_tx}) dose planes for the treatment field to be verified along with the (A and B)$_{IC}$ coefficients, instead of the (A and B)$_{TPS}$ as previously described in Chapter 4, were used to calculate EPL of the attenuator from Equation 5-2. The FSF_{IC} was also required in Equation 5-2 to correct for treatment fields with field size other than the reference 20 x 20 cm^2. The FSF_{IC} was the field size correction factor tabulated from IC derived 2D dose planes for a range of field sizes (5 x 5 cm^2 to 20 x 20 cm^2) and attenuator thicknesses (0 cm to 35 cm). Subsequently, the methods to predict EPID transit dose from the calculated 2D EPL matrix remained the same as described in Chapter 3, sub-Section 4.3.6. Briefly, the EPL together with (A and B)$_{EPID}$ were used to calculate the equivalent EPID ratio (M/M0)$_{EPID}$ using Equation 5-1. As shown in Equation 5-12 below, which is similar to Equation 4-11, the EPID transit dose ($M_{EPID\ pred}$) can be predicted by multiplying this equivalent EPID ratio with an EPID dose plane captured with 20 x 20 cm^2 open field without a phantom in the beam ($M0_{EPID\ ref}$).

$$M_{EPID\ pred} = \left(\frac{M}{M0}\right)_{EPID} \times M0_{EPID\ ref} \div FSF_{EPID} \qquad (5\text{-}12)$$

where FSF_{EPID} is the field size correction factor tabulated from EPID dose planes measured for a range of field sizes (5 x 5 cm^2 to 20 x 20 cm^2) and attenuator thicknesses (0 cm to 35 cm).

The predicted EPID transit dose was directly compared to the EPID measured dose to verify the accuracy of treatment delivery.

5.3.4.2 Modulated field (wedge and IMRT)

In the prediction of EPID transit dose from TPS dose planes, the MF for beam modulation quantification was computed from modulated and non-modulated dose planes exported from the TPS at the entrance level:

$$MF_{IC} = \frac{M0_{TPS\_tx}}{M0_{TPS\_openFSx}} \qquad (5\text{-}13)$$

As described in sub-Section 5.3.3.2, the MF derived from TPS was corrected to the equivalent MF of EPID using the same linear equations shown in Figure 5-5.

This corrected MF was then incorporated into Equation 5-12 to predict EPID transit dose for modulated fields:

$$M_{EPID\,pred} = \left(\frac{M}{M0}\right)_{EPID} \times M0_{EPID\,ref} \div FSF_{EPID} \times MF^{IC}_{corrected} \quad (5\text{-}14)$$

In this case, the $MF^{IC}_{corrected}$ is:

$$MF^{IC}_{corrected} = [MF_{IC\rightarrow EPID} \times W] + [MF_{IC} \times (1\text{-}W)] \quad (5\text{-}15)$$

where 'MF_{IC}' is the uncorrected MF from TPS exported dose planes as defined in Equation 5-13 and the '$MF_{IC\rightarrow EPID}$' is the MF_{IC} corrected to the equivalent of MF_{EPID} using the fitting formula shown in Figure 5-5. 'W' is the weighting calculated according to Equation 5-9 for EDW fields with different wedge angles. For the prediction of EPID transit dose for IMRT fields, W was taken to be one.

Finally, the predicted EPID transit doses for modulated fields were directly compared to the EPID measured dose planes to verify the accuracy of treatment delivery.

5.3.5 Phantom measurements

The accuracy of the model was tested on both homogeneous and heterogeneous slab phantoms (Figure 5-6). The homogeneous phantom was a 15 cm thick water-equivalent solid phantom (density 1.04 g/cm^3, Gammex Inc., Middleton, WI, USA). The heterogeneous phantom, also with a total physical thickness of 15 cm, included an RMI 467 phantom (Gammex Inc., Middleton, WI, USA) placed between two slabs of water-equivalent solid phantoms. The RMI phantom had cylindrical rods (2.8 cm in diameter and 7 cm in height) with electron densities relative to water (ρ_e) that ranged from 0.001 to 1.69 (air to cortical bone) to simulate all possible densities in a human body.

For dose computations with the TPS, the phantoms were CT-scanned (Discovery CT590 RT, GE Healthcare, UK) and the CT images were imported into the TPS. An additional 1.5 cm of water-equivalent material was added to the top and bottom surfaces of both phantoms to provide adequate electronic equilibrium

and a symmetric geometry, similar to the condition used in the commissioning process.

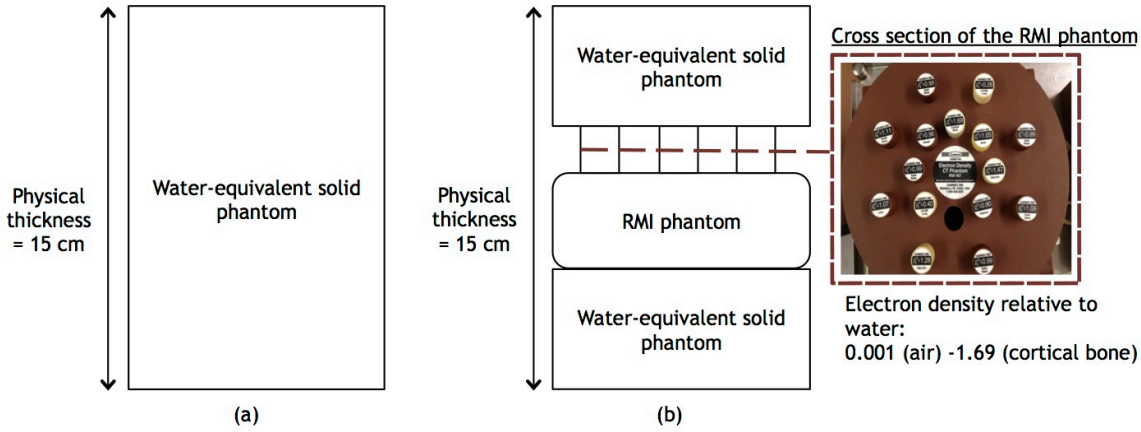

Figure 5-6 Experimental slab phantoms. (a) Homogeneous slab phantom and (b) Heterogeneous slab phantom comprised of RMI phantom with rods with electron density ranging from 0.001 (air) to 1.69 (cortical bone) placed between two slabs of water-equivalent solid phantoms. The cross section of the RMI phantom is shown in the inset. For dose computations with the TPS, an additional 1.5 cm of water-equivalent material was added to the top and bottom surfaces of both phantoms to provide adequate electronic equilibrium and a symmetric geometry, similar to the condition used in the commissioning process.

Non-modulated and modulated fields were tested on both phantoms. Non-modulated fields were open fields 10 x 10 cm^2 and 20 x 20 cm^2. Modulated fields comprised of five enhanced dynamic wedge fields (wedge angle 15, 45 and 60 degree with field size 10 x 10 cm^2; and wedge angle 45 and 60 degree with field size 20 x 20 cm^2) and seven IMRT fields (three prostate and four head and neck fields). The IMRT fields were delivered with 200 MU using the sliding window technique with the number of segments in each field ranging from 114 to 178. The extent of MLC travel distance for the seven IMRT fields ranged from 10.8 cm to 18.5 cm while the Y-jaw opening ranged from 10.5 cm to 18 cm. All beams were delivered at a fixed gantry angle of zero degrees and with the phantoms positioned at the isocentre. Results were analysed with the Varian Portal Dosimetry software (version 10.0, Palo Alto, CA, USA) using 2D global gamma analysis in absolute mode. The area of analysis was taken to be 100% of the field area for regular fields (open and wedge fields) and defined by the 20% threshold for irregular fields (IMRT fields). A dose threshold method was used for irregular fields to automatically demarcate the region of interest in a systematic way. The 20% value was chosen for IMRT fields to include a larger area of analysis,

considering the dose variation in the field and at the same time, to exclude very low dose region that may artificially improve the gamma analysis results due to global calculation of percentage dose difference.

5.3.6 Independent verification with 2D array

The phantom measurements described in sub-Section 5.3.5 were repeated on the same day with a MapCHECK2 device to independently verify results from this model. The same homogeneous and heterogeneous phantoms were placed on top of the MapCHECK2 device (Figure 5-7). For consistency, MapCHECK2 dose planes were interpolated using a bilinear method to match the EPID resolution and comparisons between MapCHECK2 measured dose planes and TPS computed dose planes were also analysed with the Varian Portal Dosimetry software using 2D global gamma analysis in absolute mode.

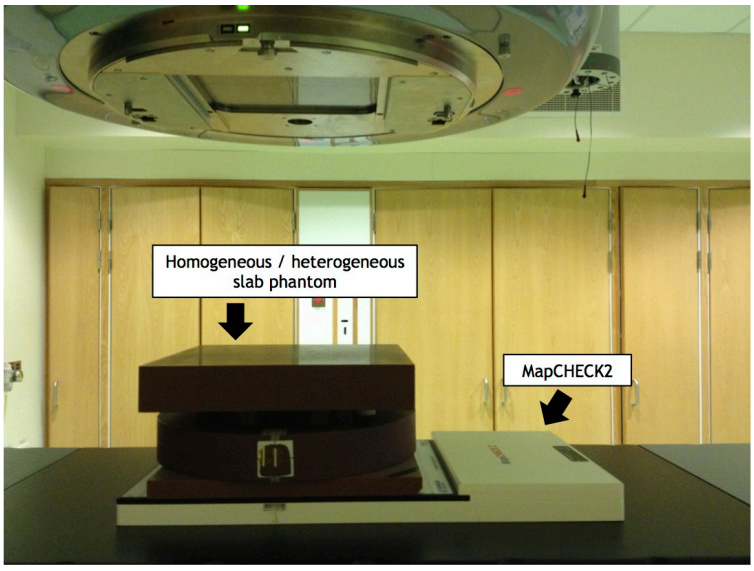

Figure 5-7 Experimental set-up for independent verifications with 2D array device.

5.4 Results

5.4.1 Comparisons of in-phantom exit dose: Reconstructed versus TPS

5.4.1.1 Open field

Figure 5-8a and 5-8b show comparisons of reconstructed and TPS computed in-phantom exit dose profiles for a 20 x 20 cm^2 open field tested on the homogeneous and heterogeneous phantoms respectively. At the central axis, the TPS computed exit dose was found to be higher than the reconstructed dose by

3.5% for the homogeneous phantom and 1.5% for the heterogeneous phantom. Additional central axis measurements with IC placed at the exit level of the two phantoms showed the same trend and confirmed that the TPS over-estimated the exit doses by 3.8% for the homogeneous phantom and 0.8% for the heterogeneous phantom. The same IC verification with a 10 x 10 cm^2 open field showed a similar finding. From IC measurements at the central axis, the TPS was found to over- and under-estimate the exit dose by 2.8% and 0.6% for the homogeneous and heterogeneous phantoms respectively. These TPS inaccuracies were reflected in the results of this EPID dosimetry model. As can be seen from the profiles comparisons in Figure 5-8c and 5-8d for the 10 x 10 cm^2 test field, the TPS computed exit dose was 2.4% higher and 1.7% lower than the reconstructed dose for the homogeneous and heterogeneous phantom respectively. The agreement between doses reconstructed from this model and doses physically measured by IC in the phantom proved that this EPID dosimetry model could accurately reflect the actual discrepancies between delivered and TPS planned dose.

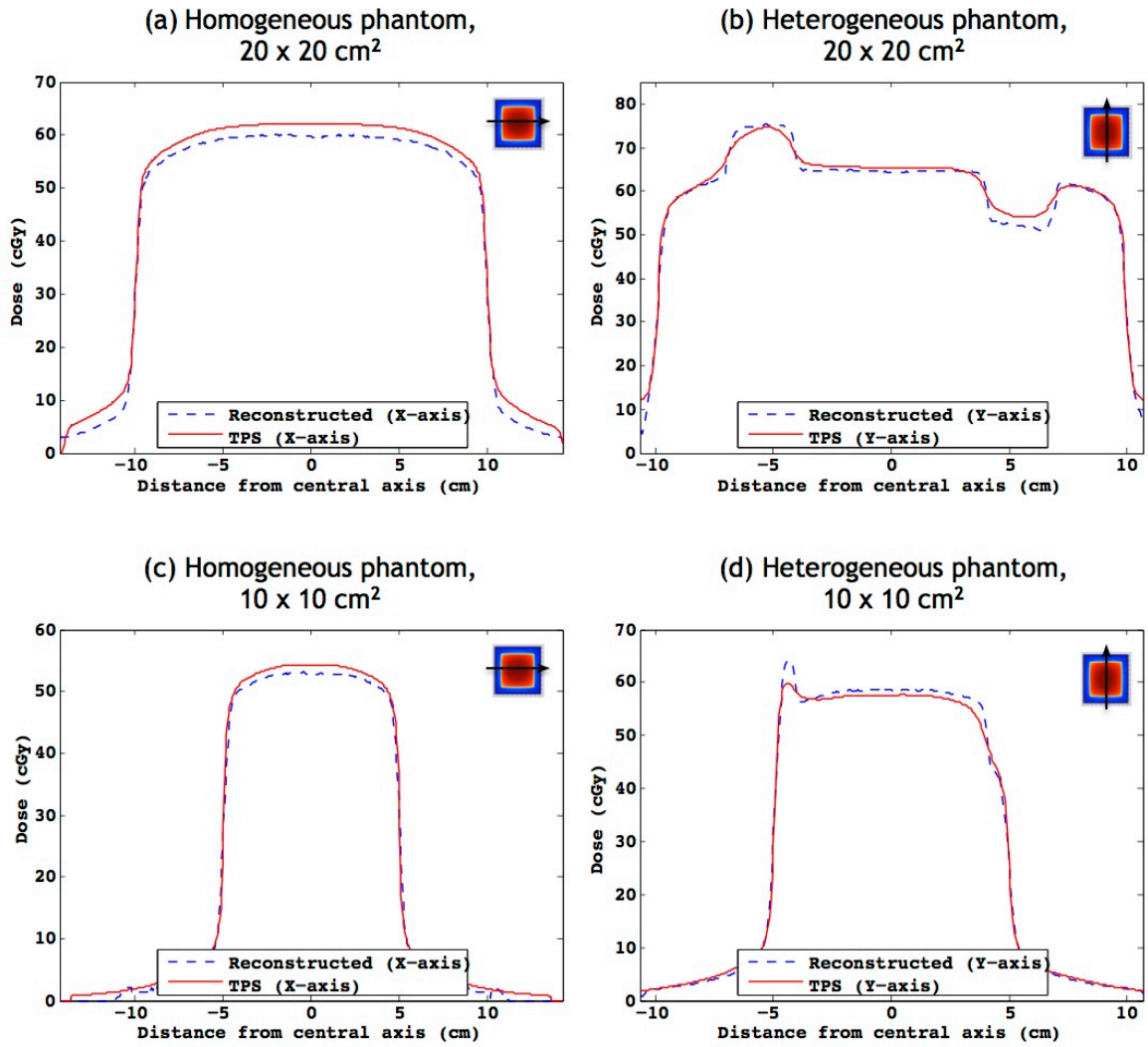

Figure 5-8 Profiles comparisons between TPS computed and EPID reconstructed in-phantom exit dose for open fields. Comparisons between TPS computed (red solid line) and reconstructed in-phantom exit dose (blue dashed line) are for: (a) 20 x 20 cm^2 open field tested on homogeneous phantom, (b) 20 x 20 cm^2 open field tested on heterogeneous phantom, (c) 10 x 10 cm^2 open field tested on homogeneous phantom and (d) 10 x 10 cm^2 open field tested on heterogeneous phantom. TPS inaccuracy in computing exit doses was found to have contributed to the observed offsets of the profiles.

The profiles in Figure 5-8a were normalised to the central axis and shown in Figure 5-9a as relative profiles comparisons between TPS and EPID reconstructed exit dose. The TPS computed relative profile was also compared to the IC relative profile measured in a scanning water tank at the same depth (Figure 5-9b). For clearer visualisation of the relative profiles comparisons, a section of the graphs was magnified and compared together (TPS computed, IC measured and EPID reconstructed) in the inset indicated as Figure 5-9c. Within the field, minor discrepancies between TPS and EPID reconstructed relative profiles were observed at the penumbra region (indicated by arrows in Figure 5-9c). The same

mismatch was also observed between the TPS and IC relative profile, proving that the discrepancies were inherent to the TPS and did not arise from the EPID dosimetry model.

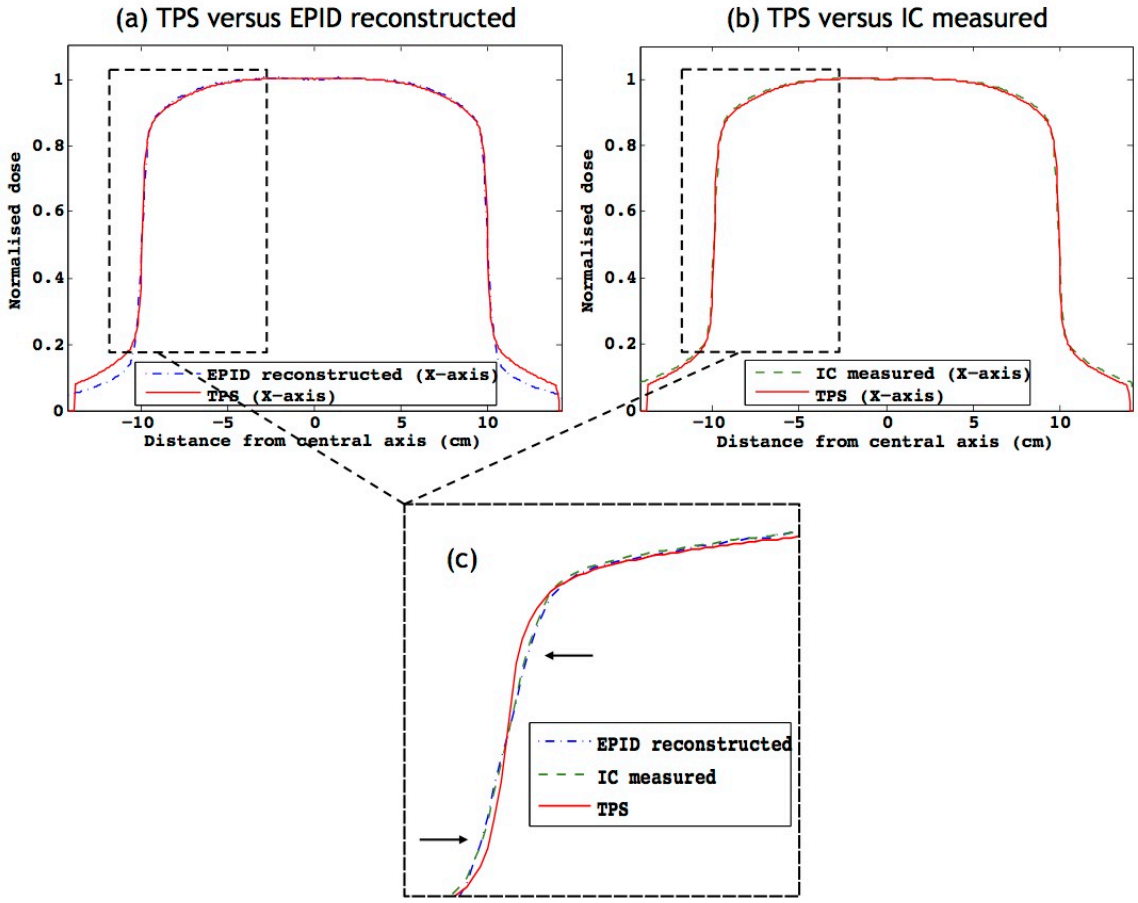

Figure 5-9 Relative profiles comparisons between TPS computed, EPID reconstructed and IC measured. (a) TPS computed (solid line) versus EPID reconstructed (dashed line) and (b) TPS computed (solid line) versus IC measured in a scanning water tank (dashed line). Section of profiles from (a) and (b) were magnified and compared together in the inset (c). The good agreement between EPID reconstructed and IC measured relative profiles as well as the consistent mismatches between these profiles and the TPS computed relative profiles at the penumbra region (indicated by arrows) imply that the discrepancies were inherent to the TPS and did not arise from the EPID dosimetry model.

The ability of this dosimetry model to reflect actual discrepancies between delivered and TPS planned dose, confirmed by on- and off-axis IC measurements as described above, is an advantage. However, the common use of gamma criteria of 3%/3mm could be a problem because the TPS inaccuracy at the exit level could be more than 3% in some cases. Without correcting for the inaccuracy of TPS in computing exit doses, the gamma pass rate using 3%/3mm criterion was as low as 85.4% (for the 20 x 20 cm^2 field tested on homogeneous

phantom, with a central axis dose difference of 3.5%). However, when the TPS computed exit doses were corrected, the pass rates were above 95.7% for all open fields tested on both phantoms. The TPS computed exit dose planes were corrected as an overall offset based on IC measurements at the central axis. The minor TPS inaccuracy at the penumbra region was not corrected.

5.4.1.2 Modulated field (wedge and IMRT)

TPS computed exit doses for modulated fields were also corrected based on IC point dose measurements at the central axis. However, instead of performing IC measurements for each wedge and IMRT field on the different phantoms, the inaccuracies of TPS computed exit doses for these modulated fields were only approximated from IC measurements of open fields with the same field size as the modulated fields and on the same phantom. For example, the effective field size for test field IMRT8 was 10.6 x 10.6 cm^2, and from the IC measurement with open field 10 x 10 cm^2 at the exit level of the homogeneous phantom, it was found that the TPS over-estimated the exit dose by 3%. Subsequently, the TPS computed exit dose for field IMRT8 on the homogeneous phantom was corrected as an overall offset of 3% before comparison was performed with the EPID reconstructed dose. Results for gamma comparisons between EPID reconstructed and TPS computed exit doses corrected for inaccuracies are given in the column 'With Dose Correction' in Table 5-1. Results for gamma comparisons for the same fields but without correcting for TPS inaccuracies are also presented in Table 5-1 under the column 'Without Dose Correction'. MapCHECK2 results are included in the table for reference.

Table 5-1 Gamma analysis results for comparisons between EPID reconstructed and TPS computed in-phantom exit dose with and without correcting for TPS exit dose inaccuracy. MapCHECK2 results were included for reference.

	Homogeneous Phantom 3%/3mm gamma pass rate (%)			Heterogeneous Phantom 3%/3mm gamma pass rate (%)		
	Without Dose Correction	With Dose Correction	MapCHECK2	Without Dose Correction	With Dose Correction	MapCHECK2
EDW15FS10	99.8	99.9	99.9	87.8	95.2	97.5
EDW45FS10	99.0	99.1	100.0	93.1	96.6	98.1
EDW60FS10	100.0	99.8	100.0	94.0	96.5	98.1
EDW45FS20	98.1	98.3	99.9	97.7	96.2	97.6
EDW60FS20	95.6	98.5	100.0	99.6	99.0	99.1
Mean Wedge:	**98.5**	**99.1**	**100.0**	**94.4**	**96.7**	**98.1**
IMRT1	99.5	99.4	98.2	94.7	95.2	95.2
IMRT2	90.2	96.9	97.9	97.1	97.4	96.8
IMRT3	81.2	96.2	98.4	95.1	95.1	97.1
IMRT4	87.9	97.9	99.0	97.0	97.3	95.8
IMRT5	85.8	97.0	98.6	96.0	95.3	95.3
IMRT6	91.1	97.7	97.0	95.3	93.5	94.2
IMRT7	88.8	97.1	97.7	92.8	93.5	90.9
Mean IMRT:	**89.2**	**97.5**	**98.1**	**95.4**	**95.3**	**95.0**
Mean Overall:	**93.1**	**98.2**	**98.9**	**95.0**	**95.9**	**96.3**

Comparisons between EPID reconstructed and TPS corrected in-phantom exit dose for wedge fields resulted in 3%/3mm gamma agreement that ranged from 95.2% to 100% with a mean of 99.1% for homogeneous phantom and 96.7% for heterogeneous phantom. As for IMRT fields, the gamma pass rates ranged from 93.5% to 99.4% with a mean of 97.5% for homogeneous phantom and 95.3% for heterogeneous phantom. The IMRT fields with pass rates below 95% concur with results from MapCHECK2 measurements. The overall mean gamma pass rate (all modulated fields on both phantoms) from this model was 97.0%, in good agreement with MapCHECK2 measurement results of 97.6%. Figure 5-10 shows comparisons of EPID reconstructed and TPS corrected in-phantom exit dose for an EDW15FS10 field, an EDW60FS10 field and an IMRT field (IMRT1) tested on the heterogeneous phantom.

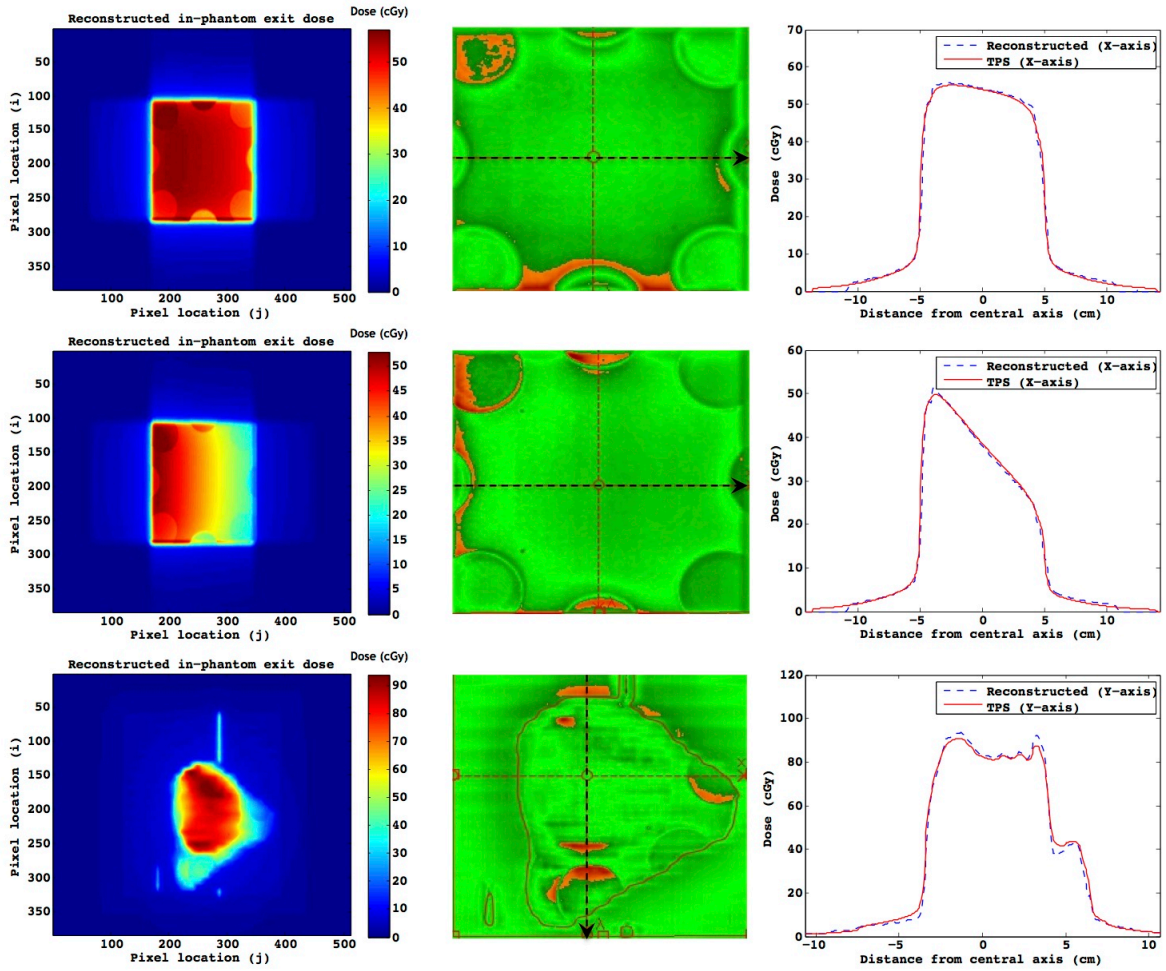

Figure 5-10 Examples of results from comparisons between EPID reconstructed and TPS corrected in-phantom exit dose. Comparisons between EPID reconstructed and TPS corrected in-phantom exit dose for an EDW15FS10 field (top row), EDW60FS10 field (middle row) and IMRT1 field (bottom row) tested on the heterogeneous phantom. From left to right is the reconstructed in-phantom exit dose plane, 3%/3mm gamma comparison result (red indicating areas that failed the gamma criteria) and profiles comparisons between reconstructed (dashed line) and TPS computed (solid line) in-phantom exit dose across the axis indicated by the arrow. The percentages of points that passed the gamma criterion were 95.2%, 96.5% and 95.2% for the EDW15FS10 field (top row), EDW60FS10 field (middle row) and IMRT1 field (bottom row) respectively.

5.4.2 Comparisons of EPID transit dose: Predicted versus measured

5.4.2.1 Open field

Comparisons between the EPID measured transit dose and that predicted by this model from TPS exported dose planes showed good agreement for open fields. The TPS exported exit dose planes were corrected for inaccuracies quantified from IC central axis dose measurements before the dose planes were used as input for the prediction of EPID transit dose. After correcting for TPS inaccuracy, the percentage of points that passed gamma criteria of 3%/3mm was above 98.9% for all open fields tested on both homogeneous and heterogeneous

phantoms. Without correcting for TPS inaccuracy at the exit level, the lowest pass rate was 33.6% (for the 20 x 20 cm^2 field tested on homogeneous phantom, with a central axis dose difference of 4.2%).

5.4.2.2 Modulated field (wedge and IMRT)

Table 5-2 gives the wedge and IMRT gamma comparisons results between the EPID measured transit dose planes and that predicted by this model from TPS exported dose planes with and without correction for TPS inaccuracy at the exit level. After correcting for TPS exit dose inaccuracy based on IC measured dose, the predicted EPID transit dose agreed well with EPID measured dose for all modulated fields on both phantoms. The gamma pass rate with 3%/3mm criterion for wedge fields ranged from 95.8% to 100% with a mean value of 98.6% and 98.0% for homogeneous and heterogeneous phantom respectively. For IMRT fields, the percentage of points that passed the gamma criteria ranged from 88.6% to 98.5% with a mean pass rate of 96.2% (homogeneous phantom) and 94.4% (heterogeneous phantom). The overall mean gamma pass rate from this model was 96.5% (MapCHECK2, 97.6%). Figure 5-11 shows comparisons of measured and predicted EPID transit dose for an EDW45FS20 field, an EDW60FS20 field and an IMRT field (IMRT4) tested on the heterogeneous phantom.

Table 5-2 Gamma analysis results for comparisons between EPID measured transit dose and predicted from TPS dose planes with and without correcting for TPS exit dose inaccuracy. MapCHECK2 results are included for reference and are identical to those presented in Table 5-1.

	Homogeneous Phantom 3%/3mm gamma pass rate (%)			Heterogeneous Phantom 3%/3mm gamma pass rate (%)		
	Without Dose Correction	With Dose Correction	MapCHECK2	Without Dose Correction	With Dose Correction	MapCHECK2
EDW15FS10	99.4	98.6	99.9	93.2	97.5	97.5
EDW45FS10	97.3	99.1	100.0	92.7	97.4	98.1
EDW60FS10	95.4	99.4	100.0	98.8	98.8	98.1
EDW45FS20	85.5	95.8	99.9	98.3	97.0	97.6
EDW60FS20	78.9	100.0	100.0	99.7	99.1	99.1
Mean Wedge:	**91.3**	**98.6**	**100.0**	**96.5**	**98.0**	**98.1**
IMRT1	99.1	97.3	98.2	96.0	96.7	95.2
IMRT2	89.9	98.0	97.9	98.1	98.5	96.8
IMRT3	79.0	97.1	98.4	96.3	96.3	97.1
IMRT4	82.3	97.0	99.0	97.0	97.2	95.8
IMRT5	81.2	96.5	98.6	94.7	95.3	95.3
IMRT6	86.4	93.9	97.0	89.2	87.9	94.2
IMRT7	83.4	93.4	97.7	89.1	88.6	90.9
Mean IMRT:	**85.9**	**96.2**	**98.1**	**94.3**	**94.4**	**95.0**
Mean Overall:	**88.2**	**97.2**	**98.9**	**95.3**	**95.9**	**96.3**

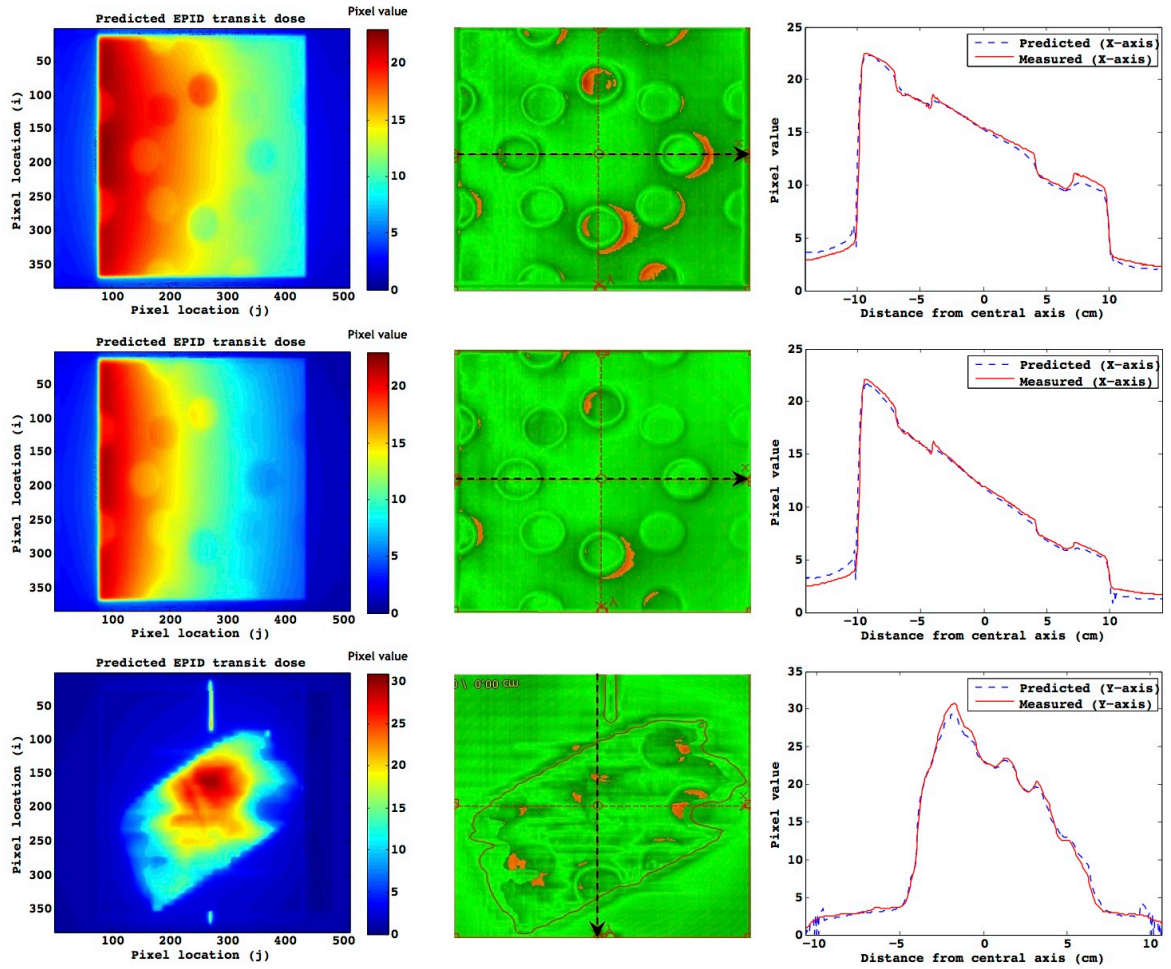

Figure 5-11 Examples of results from comparisons between measured and predicted EPID transit dose. Comparisons between measured and predicted EPID transit dose for an EDW45FS20 field (top row), EDW60FS20 field (middle row) and IMRT4 field (bottom row) tested on the heterogeneous phantom. The EPID transit dose was predicted after correcting for TPS inaccuracy. From left to right is the predicted EPID transit dose plane, 3%/3mm gamma comparison result (red indicating areas that failed the gamma criteria) and profiles comparisons between measured (solid line) and predicted (dashed line) EPID transit dose across the axis indicated by the arrow. The percentages of points that passed the gamma criterion were 97.0%, 99.1% and 97.2% for the EDW45FS20 field (top row), EDW60FS20 field (middle row) and IMRT4 field (bottom row) respectively.

5.5 Discussion

The first objective of this study was to replace TPS calibration dose planes with IC in water calibration dose planes for the commissioning of this EPID dosimetry model. Although the methods to derive IC calibration dose planes required more effort, this was justified because the TPS computed calibration dose planes exported at the entrance and exit level of a phantom could contain inaccuracies. Inaccuracies in calibration data could propagate to the end results and may mask real discrepancies between planned and delivered dose. For

example, the results in Chapter 3 confirmed that the Eclipse AAA failed to account properly for the backscatter effect and, as a result, caused a 3.8% over-estimation of dose at the exit level of a 15 cm thick water-equivalent phantom for a 6 MV, 20 x 20 cm^2 field. However, this TPS inaccuracy was not reflected in the EPID dosimetry result in Chapter 4, where the difference between EPID reconstructed and TPS computed in-phantom exit dose for the same beam and phantom thickness was only 0.4%. By using IC calibration dose planes in the commissioning process, the EPID dosimetry model was able to reveal real differences between measured and TPS planned dose. As shown in the results section of this chapter, the TPS dose computed at the exit level of the 15 cm thick water-equivalent phantom for a 20 x 20 cm^2 field was higher than the EPID reconstructed dose by 3.5%, in closer agreement with the findings in Chapter 3. This result proves that the use of accurate calibration data, independent of the TPS, is essential in ensuring that the EPID dosimetry model can reflect actual discrepancies between measured and TPS planned doses.

The inaccuracy of exit dose computed by the Eclipse AAA algorithm could be as much as 5% at large depth (31.5 cm) and large field size (20 x 20 cm^2) (Tan 2014). In the case where the TPS exit dose error was more than 3%, the use of common 3%/3mm gamma criterion to evaluate the agreement of measured and planned exit dose planes would result in a disproportionately high rate of failure and make it difficult to retrieve meaningful information from the comparison results. In this study, additional IC measurements were done at the exit level of both phantoms and the inaccuracy of TPS computed exit doses were quantified and corrected. The IC measurements were done only for open fields. The TPS exit dose inaccuracies for modulated fields were approximated from the open fields measurements of the closest setting. To ensure a reasonable approximation, the parameters that affect the amount of backscattered photons such as beam energy, field size, phantom type and measurement depth were chosen from the open field measurements that would represent the conditions of the modulated fields. Two sets of comparisons, with and without correcting for TPS inaccuracies, were presented in the results section. The purpose of presenting the results with TPS dose correction was to evaluate the effect of TPS exit dose inaccuracy on the results of this model. It can be observed from Tables 5-1 and 5-2 that the 3%/3mm gamma comparisons results generally improved

after accounting for TPS computed exit dose inaccuracies. However, the additional IC measurement at the exit level is not practical for routine clinical practice. In the case where IC measurements at the exit level are not possible, a higher gamma criterion should be considered. Table 5-3 presents results for comparisons of in-phantom exit dose and comparisons of EPID transit dose using a 4%/4mm criterion, without any correction to the TPS computed exit dose. The criterion was chosen based on previous IC measurements, which showed that the inaccuracy of Eclipse AAA computed exit dose for both phantoms were within 4%. Using this 4%/4mm criterion, all the fields tested on both phantoms had more than 90% gamma pass rate. For the in-phantom exit dose comparisons, the minimum gamma pass rate was 94.3% with an overall mean of 98.9% for the homogeneous phantom and 99.0% for the homogeneous phantom. As for the comparisons of EPID transit dose, the minimum gamma pass rate was 91.7% with an overall mean of 97.1% and 99.1% for the homogeneous and heterogeneous phantom respectively.

Table 5-3 Gamma analysis results, with 4%/4mm criterion, for comparisons of in-phantom exit dose and comparisons of EPID transit dose. No correction was applied to the TPS computed exit dose.

	Comparisons of in-phantom exit dose: Reconstructed versus TPS		Comparisons of EPID transit dose: Predicted versus Measured	
	4%/4mm gamma pass rate (%)		4%/4mm gamma pass rate (%)	
	Homogeneous Phantom	Heterogeneous Phantom	Homogeneous Phantom	Heterogeneous Phantom
Open 10 x 10 cm^2	100.0	99.2	99.8	99.7
Open 20 x 20 cm^2	100.0	99.2	97.4	99.7
Mean Open:	**100.0**	**99.2**	**98.6**	**99.7**
EDW15FS10	100.0	97.2	100.0	98.7
EDW45FS10	100.0	97.8	100.0	98.3
EDW60FS10	100.0	97.5	100.0	100.0
EDW45FS20	100.0	99.9	97.1	100.0
EDW60FS20	99.9	100.0	95.4	100.0
Mean Wedge:	**100.0**	**98.5**	**98.5**	**99.4**
IMRT1	100.0	97.6	100.0	99.6
IMRT2	98.4	99.5	98.6	99.8
IMRT3	94.3	99.2	93.7	99.7
IMRT4	98.7	99.9	96.3	99.9
IMRT5	96.9	99.4	94.6	99.3
IMRT6	98.8	99.8	95.1	96.5
IMRT7	97.4	99.1	91.7	96.5
Mean IMRT:	**97.8**	**99.2**	**95.7**	**98.8**
Mean Overall:	**98.9**	**99.0**	**97.1**	**99.1**

As with any other empirical model, the limited number of measurements that can be practically carried out require certain assumptions to be made that may affect the accuracy of results. In this model, two assumptions were made in using MF, defined as the ratio of modulated to non-modulated dose planes at the same level, to quantify beam modulation. First, the MF was assumed to be similar for both EPID and IC (or TPS). Second, the MF derived at the entrance level was assumed to be representative of the MF at the exit level.

For this first assumption, a minor correction was made, as described in sub-Section 5.3.3.2, to convert MF derived from EPID to the equivalent of IC and vice versa. This correction was derived from EDW60 measurements and used as a generic correction for all modulated fields, including IMRT. Without accounting for the difference in dose rate between EDW60 and IMRT delivery, the same generic MF correction derived from EDW60 measurements was applied to the IMRT fields. Figure 5-12 shows the comparisons of MF derived from TPS dose planes (MF_{IC}) and EPID dose planes (MF_{EPID}), for IMRT fields. It can be observed that the agreement between MF derived from TPS and EPID improved after applying the generic correction ($MF^{EPID}_{corrected}$). The generic MF correction was applied according to Equation 5-8 and W in the equation was taken to be one for IMRT fields. The $MF^{EPID}_{corrected}$ agreed well with the MF_{IC} despite using a general correction derived from EDW60 measurements for IMRT fields.

For the second assumption, the MF at the entrance level was assumed to be the same as the MF at the exit level. This assumption is illustrated in Figures 5-13, which show comparisons of MF derived from entrance dose planes versus MF derived from exit dose planes. The comparisons of MF at the two levels are shown for both TPS and EPID dose planes. Within the field of interest, the MFs derived at two different levels were reasonably comparable.

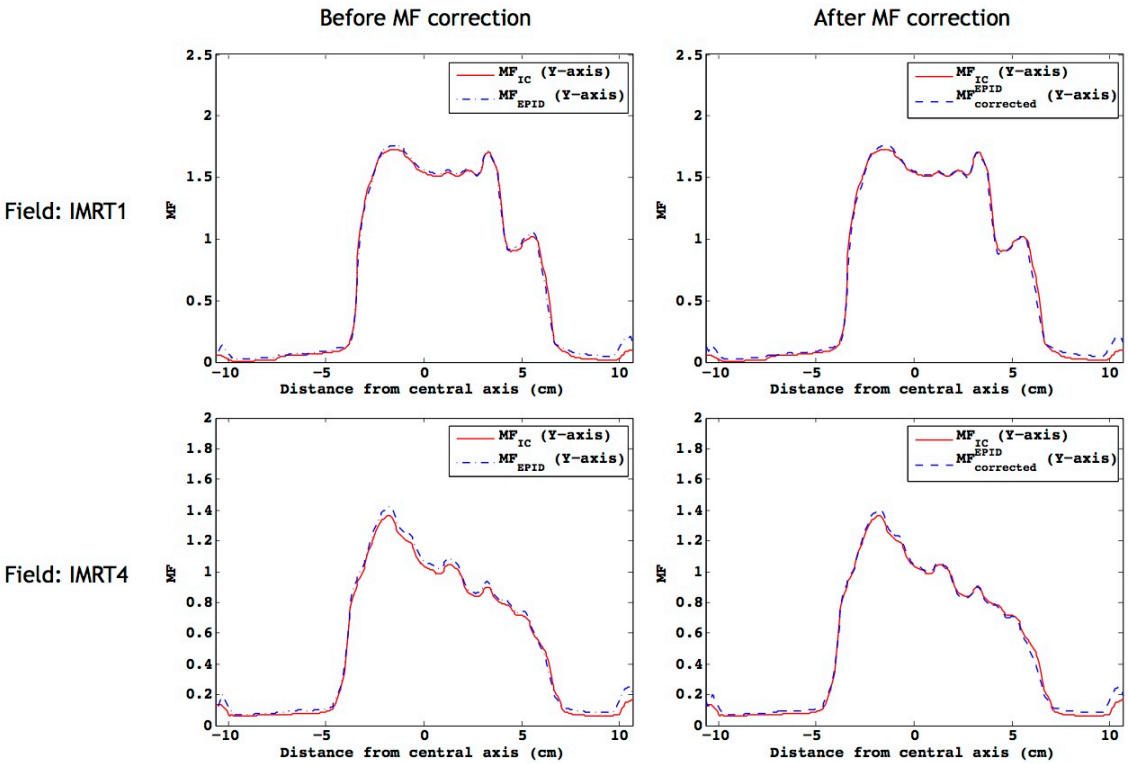

Figure 5-12 Comparisons of MFs derived from TPS dose planes and EPID dose planes and the effect of generic MF correction. MFs derived from TPS dose planes, MF_{IC}, are represented by solid line and MFs derived from EPID dose planes, MF_{EPID}, are represented by dashed line. Examples are given for field IMRT1 (top row) and field IMRT4 (bottom row). Agreement between the two MFs improved after applying the generic MF correction ($MF^{EPID}_{corrected}$), according to Equation 5-8 with W taken to be one for IMRT fields.

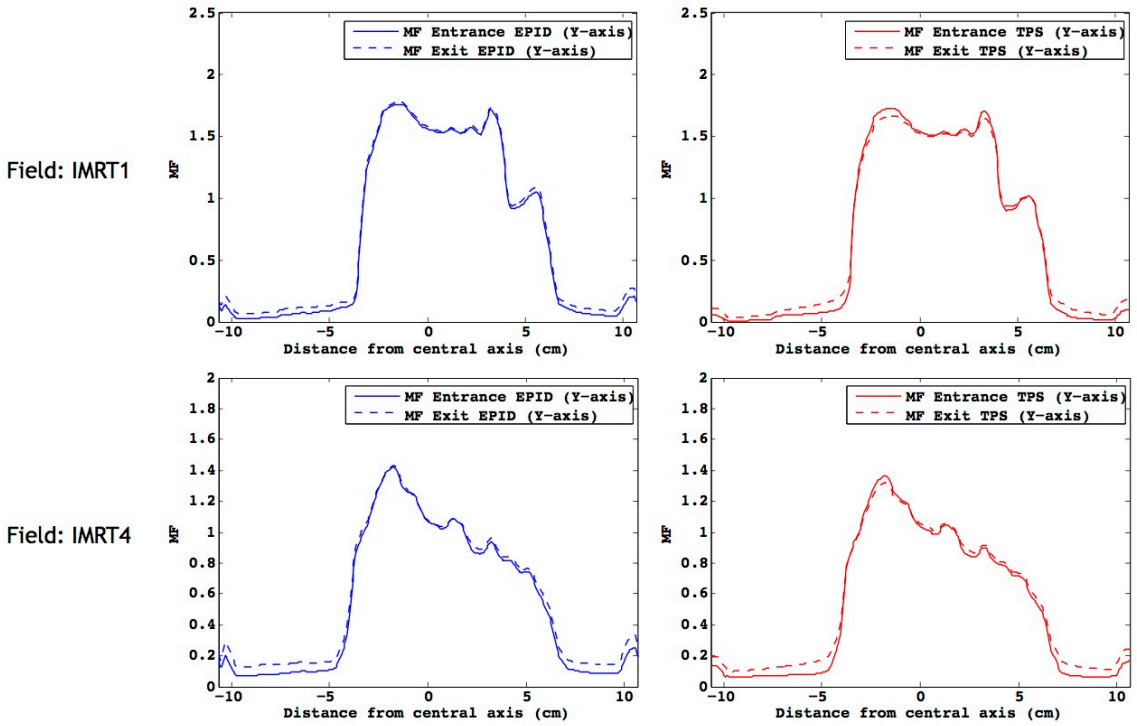

Figure 5-13 Comparisons of MFs derived from entrance dose planes and exit dose planes. Solid lines represent MFs derived from entrance dose planes and dashed lines represent MFs derived from exit dose planes. Examples are given for field IMRT1 (top row) and field IMRT4 (bottom row). The comparisons were performed for both EPID measured dose planes (left column) as well as TPS computed dose planes (right column).

5.6 Conclusions

An empirical 2D EPID transit dosimetry model, commissioned with data independent of the TPS, was described and proven to be capable of revealing actual discrepancies between measured and planned doses. The dosimetry model was tested with open, wedge and IMRT fields on both homogeneous and heterogeneous slab phantoms. Results showed that by taking into account the TPS exit dose inaccuracies, the 3%/3mm gamma pass rates for open fields were above 95.7% for in-phantom exit dose comparisons and above 98.6% for EPID transit dose comparisons. As for the modulated fields (wedge and IMRT), the overall mean gamma pass rate was 97.0% (range: 93.5% to 99.9%) for in-phantom exit dose comparisons and 96.5% (range: 87.9% to 100.0%) for EPID transit dose comparisons. The overall results compared favourably with independent verification using a commercial 2D array device, with an overall mean of 97.6% (range: 90.9% to 100.0%). Without accounting for TPS exit dose inaccuracies and with a higher gamma criterion of 4%/4mm, the mean gamma pass rate for all

fields tested on both phantoms was 98.9% (range: 94.3% to 100.0%) for in-phantom exit dose comparisons and 98.1% (range: 91.7% to 100.0%) for EPID transit dose comparisons.

The 2D EPID transit dosimetry model developed up to this stage can only be used for slab phantoms and with the gantry angle fixed at zero degrees, thus limiting its application to pre-treatment verification only. The requirement for the incident beam to be perpendicular to a flat surface is to allow the direct export of TPS entrance and exit dose planes, at a distance of 1.5 cm from the beam entry and exit surface of a phantom. With a non-flat object, the entrance or exit doses are no longer located at the same plane and cannot be easily exported from the TPS. A solution to this problem will be presented in the next chapter, with the aim of extending the current EPID dosimetry model to verification of actual patient treatment delivery.

Chapter 6: Clinical feasibility of a dual 2D EPID transit dosimetry model for actual treatment verification

6.1 Publication/presentation arising from work in this chapter

- **A dual 2D EPID transit dosimetry model for actual treatment verification**, Tan, Y., Metwaly, M., Glegg, M., Baggarley, S. & Elliott, A., 2015, Poster presentation, *3rd ESTRO Forum, European Society for Radiotherapy and Oncology*, Barcelona, Spain.

6.2 Introduction

A dual 2D EPID transit dosimetry model, commissioned with data independent of the TPS, was described in Chapter 5 and shown to be effective in reflecting real discrepancies between measured and planned doses. In addition to simple non-modulated square fields, the dosimetry model was also proven to be capable of reconstructing and predicting doses for modulated fields such as enhanced dynamic wedge (EDW) and IMRT fields. The non-modulated and modulated fields were systematically tested on both homogeneous and heterogeneous slab phantoms. Using a gamma criterion of 4%/4mm, comparisons of in-phantom dose at the exit level (1.5 cm upstream from the beam exit surface of the phantom) between TPS computed and reconstructed from EPID measured dose planes (Path 1) showed an overall mean gamma pass rates of 98.9% (range: 94.3% to 100.0%) for the homogeneous slab phantom and 99.0% (range: 97.2% to 100.0%) for the heterogeneous slab phantom. As well as in-vivo dose comparison at the exit level, the dosimetry model also allowed transit dose comparison at the EPID level. The overall mean gamma pass rates for EPID transit dose comparisons between measured and predicted from TPS exported dose planes (Path 2) was 97.1% (range: 91.7% to 100.0%) for the homogeneous slab phantom and 99.1% (range: 96.5% to 100.0%) for the heterogeneous slab phantom. Instead of the more common 3%/3mm criterion, a higher gamma criterion of 4%/4mm was necessary because the TPS computed exit dose was found to contain inaccuracies that may exceed 3% for large fields and thick phantoms, as confirmed by IC measurements presented in Chapters 3 and 5.

The EPID dosimetry model developed in this study is a transit model, where a phantom or patient can be present in the beam during the EPID measurement. Unlike non-transit models, which require measurements through air and are therefore only applicable to pre-treatment verification, the transit model can be utilised for both pre-treatment and actual treatment verification. Actual treatment verification is especially valuable as a final check to confirm the safe delivery of radiotherapy and is highly recommended for routine use in all radiotherapy centres (The Royal College of Radiologists et al., 2008). In addition to the errors that can be detected by pre-treatment QA, actual treatment verification can also detect anatomical changes, obstruction from immobilisation devices or table structures, machine performance variation on a particular treatment day, set-up error and other types of operator errors (van Elmpt et al., 2008a). In a study by Ford et al. (2012) that quantified the efficacy of 15 common QA checks, pre-treatment QA ranked the lowest with an effectiveness score of only 1.4% while EPID dosimetry for actual treatment verification ranked much higher at fifth place, with an effectiveness score of 33.0%. The author also studied the effectiveness of different combinations of QA checks. By combining the EPID dosimetry for actual treatment verification with only one other QA check (physics chart review), the error detection rate was as high as 80%. In addition, Mans et al. (2010b) also found that the EPID dosimetry for actual treatment verification was more effective in detecting errors compared to pre-treatment QA. Nine out of 17 serious errors that were detected by EPID dosimetry would have been missed by pre-treatment QA.

Recognising the value of EPID dosimetry for actual treatment verification, the ultimate aim of this study was to develop an EPID dosimetry model that could be used for this purpose. Although the EPID dosimetry model described in the previous chapters is a transit model, all experiments were performed with a fixed gantry angle of zero degrees using slab phantoms with a flat surface, restricting its application to pre-treatment verification only. The requirement for the incident beam to be perpendicular to a flat surface was because the entrance (M0) or exit (M) dose points across the field must be located at the same plane in the attenuating object to enable direct export from the TPS. Since the entrance and exit doses were defined as dose at 1.5 cm from the beam entry and exit surface of the object respectively, the M0 or M dose points across

the field would not be located at the same plane if the beam were incident on a non-flat or irregular surface.

The first objective of this chapter was to develop a method that could extract M0 and M dose planes for objects with an irregular surface without relying on the direct export of 2D dose planes from the TPS. Since the patient's surface is clearly irregular, the proper extraction of TPS M0 and M dose planes is necessary to enable the application of the EPID transit dosimetry model for actual treatment verification. The method must also incorporate steps to deal with irradiation from different gantry angles, as would be encountered in an actual treatment delivery.

In one of the proposed EPID transit dosimetry model pathways, Path 1, the EPID measured dose planes were used to reconstruct dose at 1.5 cm upstream from the beam exit surface of the phantom, the exit level. The second objective of this chapter was to extend the methods in Path 1 to reconstruct in-phantom/in-vivo dose at other levels besides the exit level. By extending the model to reconstruct dose at other levels, users would be able to choose a location that is more clinically relevant (such as at the tumour level or critical organ level) for the dose verification.

The extended 2D EPID transit dosimetry model was initially evaluated with an anthropomorphic phantom using open, 3D conformal, EDW and IMRT fields at cardinal and oblique gantry angles. Tests with an anthropomorphic phantom and irradiation at variable gantry angles provided a more complete and realistic evaluation of the EPID transit dosimetry model before it was used for actual patient treatment verification.

Finally, clinical feasibility of the 2D EPID transit dosimetry model for actual treatment verification was assessed. Results from a pilot study with patients undergoing radiotherapy to the pelvic region are presented. Practical issues related to the clinical workflow are discussed also.

6.3 Materials and methods

6.3.1 Extracting TPS M0 and M dose planes

As described in Chapters 4 and 5, the TPS M0 and M dose planes were required for reference comparisons in Path 1 (Comparisons of in-phantom/in-vivo dose: EPID reconstructed versus TPS computed) and as input for the prediction of EPID transit dose in Path 2 (Comparisons of EPID transit dose: TPS predicted versus EPID measured). Since the TPS M0 and M dose planes were defined as dose at 1.5 cm from the beam entry and exit surface of the attenuating object (either phantom or patient), the M0 or M points across the field area would not be located in the same plane normal to the beam if the surface were not flat. This condition is clearly illustrated in Figure 6-1 for two objects with (a) a flat surface and (b) an irregular surface.

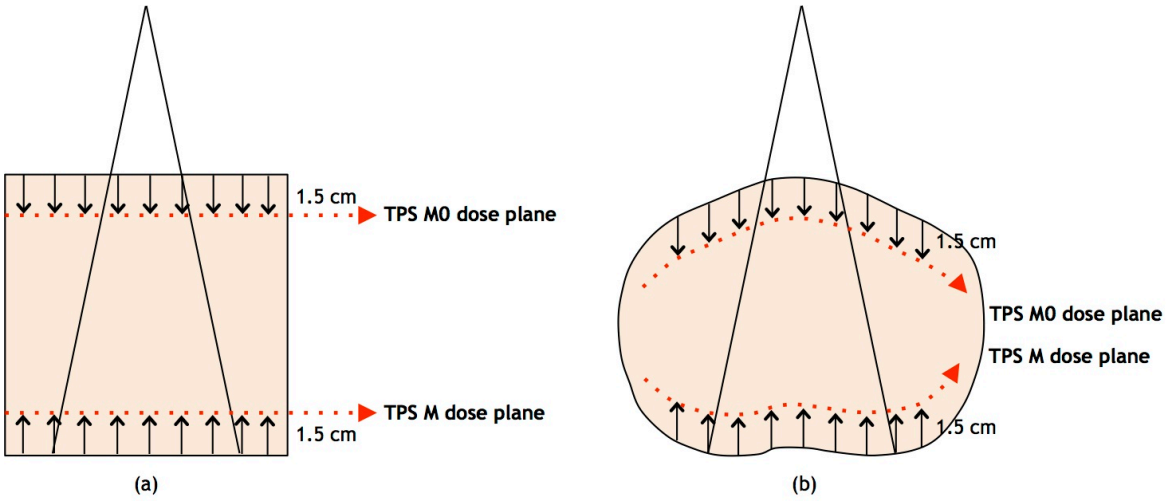

Figure 6-1 Location of entrance (M0) and exit (M) doses, 1.5 cm from beam entry and exit surface of the phantom respectively. For an object with a flat surface (a), the M0 or M doses across the field area are located in the same plane (indicated by the straight arrows in red) and can be directly exported from the TPS as 2D dose planes. However, for an object with an irregular surface (b), the M0 or M doses are not located in the same plane across the field area (indicated by the curved arrows in red) and cannot be directly exported from the TPS as 2D dose planes.

When the M0 or M doses across the field area are not located in the same plane, they cannot be directly exported from the TPS as 2D dose planes. As a solution to this problem, a Matlab code was written to extract 2D M0 and M dose planes from 3D 'Structure' and 'Dose' DICOM files exported from the TPS. The 'Structure' DICOM file contains information on the location of the external body

contour on each slice of the CT scan, which is outlined for all phantoms/patients during the planning stage. The 'Dose' DICOM file, meanwhile, contains information on the 3D dose distribution for a particular treatment field planned and computed for the phantom/patient. From these two DICOM files exported from the TPS, the 2D M0 and M dose planes were extracted following the steps illustrated in Figure 6-2.

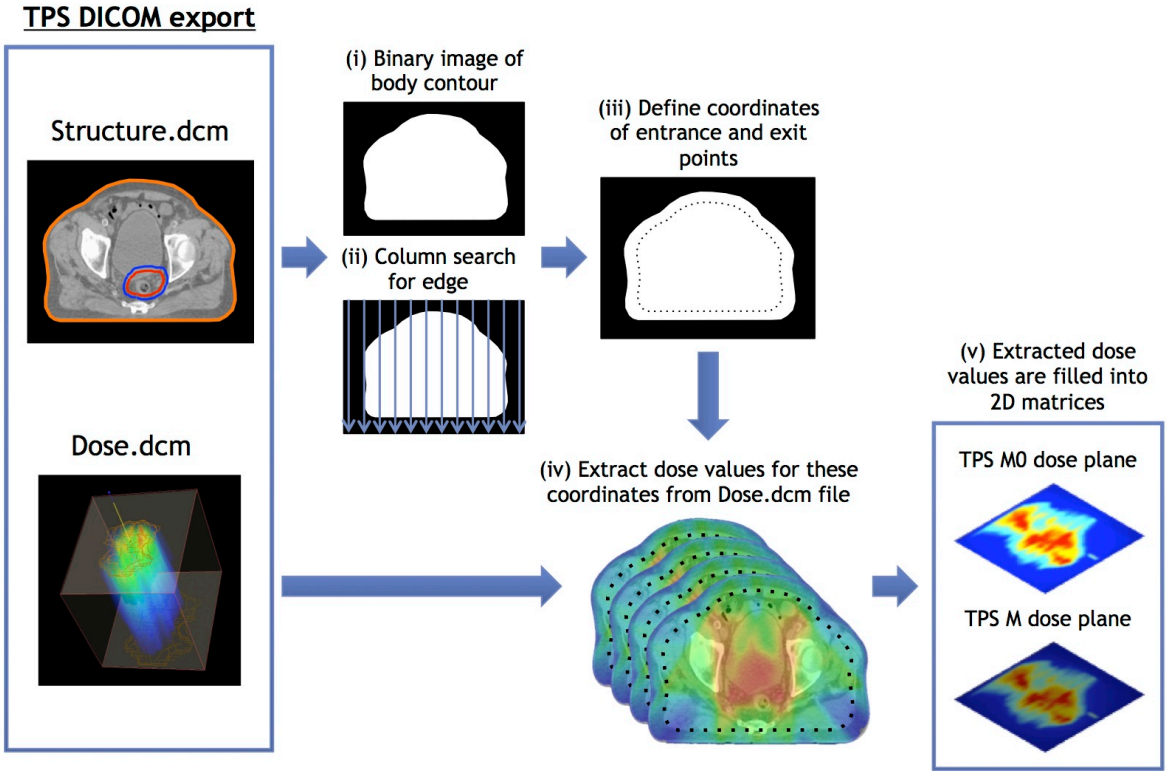

Figure 6-2 Steps to extract 2D M0 and M dose planes from 3D 'Structure' and 'Dose' DICOM files exported from the TPS. The 'Structure' DICOM file contains information on the location of the body contour on each slice of the CT scan and the 'Dose' DICOM file contains information on the 3D dose distribution for the treatment field calculated for the phantom/patient.

First, the external body contour in the 'Structure' DICOM file was used to create a binary image. Then, a column-by-column search was done on the binary image to locate the edge of the body contour (the surface). The coordinates of the entrance and exit points, defined as 1.5 cm from the surface, can then be determined from the location of the edge. After that, dose values for these coordinates were extracted from the 'Dose' DICOM file. These steps were repeated for all slices. The dose values for the entrance and exit coordinates from each slice were then used to fill a 2D matrix, with each row representing one slice, to create the TPS M0 and M dose planes.

For treatment fields with gantry angle other than zero degrees, both the 'Structure' and 'Dose' DICOM files were rotated around the field isocentre before the column search for body edge was performed. The image rotation based on field gantry angle was necessary so that the column search would correctly identify the coordinates of the entrance and exit points, which were dependent on the point of beam entry and exit surface respectively. Figure 6-3 shows an example of a treatment field with a gantry angle of 90 degrees. Without rotating the 'Structure' and 'Dose' files, the coordinates identified from the column search were not in the direction of the beam and, therefore, incorrect (Figure 6-3a). By rotating the 'Structure' and 'Dose' files according to the field gantry angle in the anti-clockwise direction, the correct coordinates can be identified using the column search technique (Figure 6-3b).

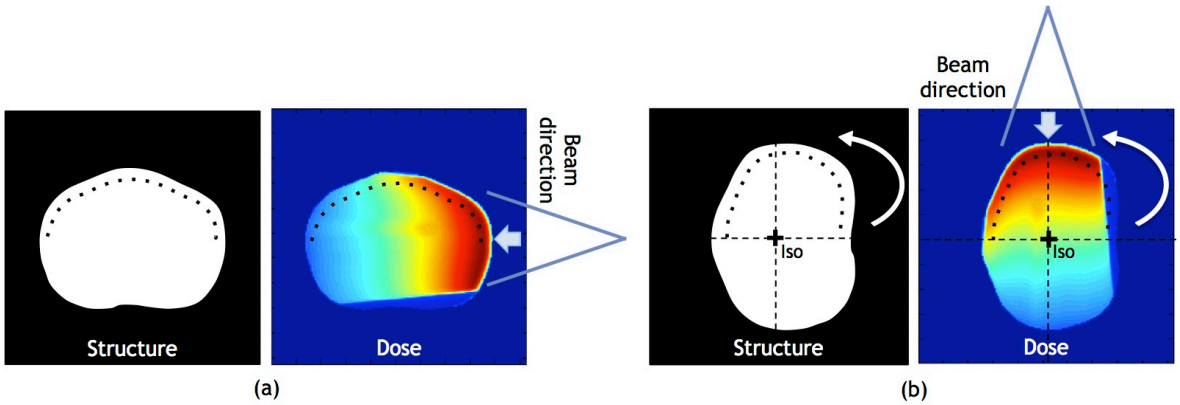

Figure 6-3 Example of 'Structure' and 'Dose' DICOM images for a treatment field with a gantry angle of 90 degrees. The dotted line represents the entrance coordinates identified using the column search technique. (a) Without rotating the DICOM images, the coordinates identified were not in the direction of the beam entry surface; (b) After rotating the DICOM images around the beam isocentre (Iso) based on the gantry angle, the correct coordinates can be identified.

6.3.2 Path 1: Reconstruction of in-phantom/in-vivo dose

6.3.2.1 Exit level

The method used to reconstruct in-phantom exit dose from EPID measured dose planes was previously described in detail in Chapter 5 (sub-Section 5.3.3). Briefly, EPID dose planes measured for the treatment field with (M_{EPID_tx}) and without ($M0_{EPID\_tx}$) phantom/patient in the beam and (A and B)$_{EPID}$ were used to calculate a 2D EPL map. Subsequently, the 2D EPL map, in combination with the

$(A \text{ and } B)_{IC}$, were used to calculate the equivalent dose ratio $(M/M0)_{IC}$. This equivalent dose ratio was used in the final reconstruction of in-phantom/in-vivo exit. Finally, the reconstructed exit dose was compared to TPS computed exit dose, extracted as described in sub-Section 6.3.1, to verify the accuracy of treatment delivery.

6.3.2.2 '*X*' level

Besides reconstructing dose at the exit level as summarised above, the EPID measured dose planes could also be used to reconstruct in-phantom/in-vivo dose at other levels ('*X*'), for example at the isocentre plane. For this purpose, a 'CT number' to 'EPL relative to water' (EPL_{rel}) calibration curve must be established. A tissue characterisation phantom, RMI 467 phantom (Gammex Inc., Middleton, WI, USA), which consisted of multiple cylindrical rods made of materials with relative electron densities ranging from 0.001 to 1.69 (air to cortical bone, including solid water), was used to establish this curve (Figure 6-4a).

First, the RMI phantom was placed vertically on the CT couch and scanned with a CT simulator (Discovery CT590 RT, GE Healthcare, UK) at 120 kVp to get the CT number in Hounsfield units (HU) for each rod material in the phantom (Figure 6-4b). This was the same CT simulator and energy setting used to scan all phantoms/patients for the treatment planning process. Then, the CT number was correlated to the EPL_{rel}. To get the EPL_{rel}, the same RMI phantom was positioned flat on the linac couch and irradiated with the reference beam (6 MV, 100 MU and field size 20 x 20 cm^2). The EPID transit dose plane measured for the RMI phantom was used to calculate the 2D EPL map (Figure 6-4c) with the quadratic equation (Swindell, 1983). The EPL for each rod material was normalised to the EPL for the rod with water density to obtain the EPL relative to water (EPL_{rel}).

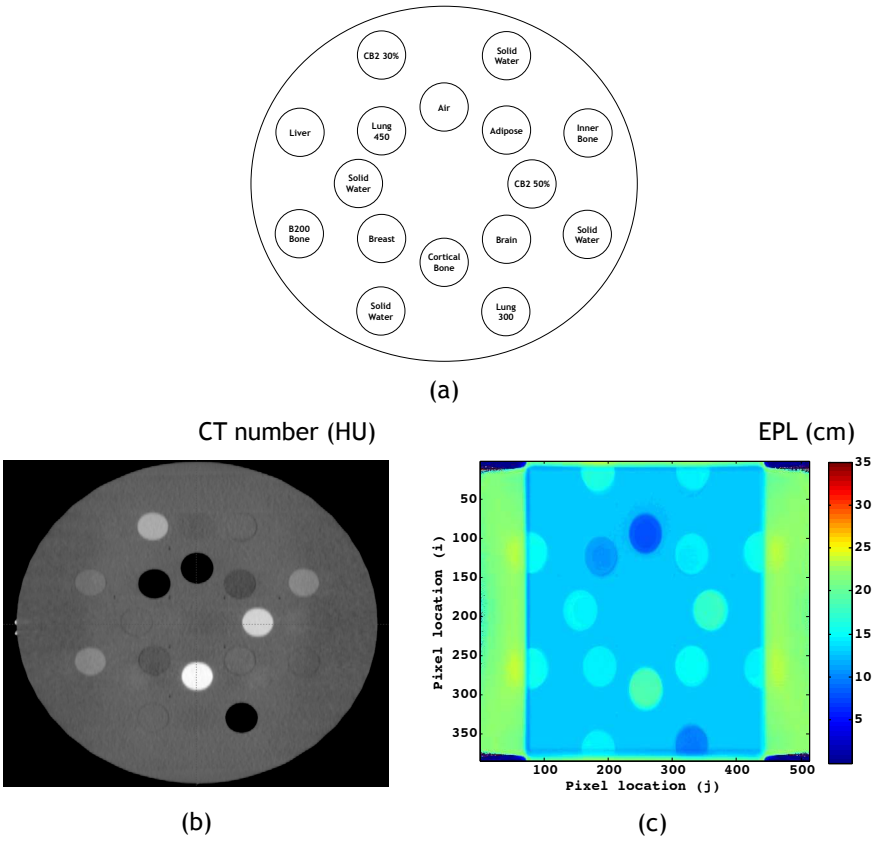

Figure 6-4 Cross-section of RMI 467 phantom, CT axial image and 2D EPL map of the phantom. (a) Cross-section of RMI 467 phantom and the arrangement of rods representing materials of different densities. Details of the rod materials are given in Table 6-1. (b) CT image of the RMI 467 phantom that was used to derive the CT number (HU) for rods with different densities. (c) 2D EPL map of the same RMI 467 phantom calculated with the quadratic equation using EPID dose planes measured for a reference beam (6 MV, 100 MU and field size 20 x 20 cm^2) with and without the RMI phantom in the beam.

Table 6-1 lists the CT number and EPL_{rel} values for various rods in the RMI phantom that were made of materials with different densities. A plot of the CT number versus EPL_{rel} is shown in Figure 6-5. The plot shows a discontinuity and therefore, must be fitted with two linear equations that have different slopes. This pattern of plot is characteristic of the relationship between electron density relative to water and CT number (HU), with the point of inflection and slopes specific to each CT scanner (Constantinou et al., 1992).

Table 6-1 List of rod materials and the respective electron density relative to water. The CT number (HU) and EPL (cm) for each rod material were obtained using methods described in sub-Section 6.3.2.2. The physical length of all rods was 7 cm.

Rod materials	Physical density (g/cm^3)	Electron density relative to water	CT number (HU)	EPL (cm)	EPL relative to water, EPL_{rel}
Air	0.00	0.00	-900	0.00	0.00
Lung 300	0.30	0.29	-600	2.00	0.29
Lung 450	0.41	0.40	-450	3.10	0.46
Adipose	0.92	0.90	20	6.40	0.94
Breast	0.98	0.96	50	6.50	0.96
Solid Water	1.02	0.99	100	6.80	1.00
Brain	1.05	1.05	130	7.10	1.04
Liver	1.11	1.07	150	7.30	1.07
Inner Bone	1.14	1.09	250	7.50	1.10
B200 Bone	1.16	1.11	260	7.60	1.12
CB2 30%	1.34	1.28	500	8.50	1.25
CB2 50%	1.56	1.47	800	9.70	1.43
Cortical Bone	1.82	1.69	1160	10.90	1.60

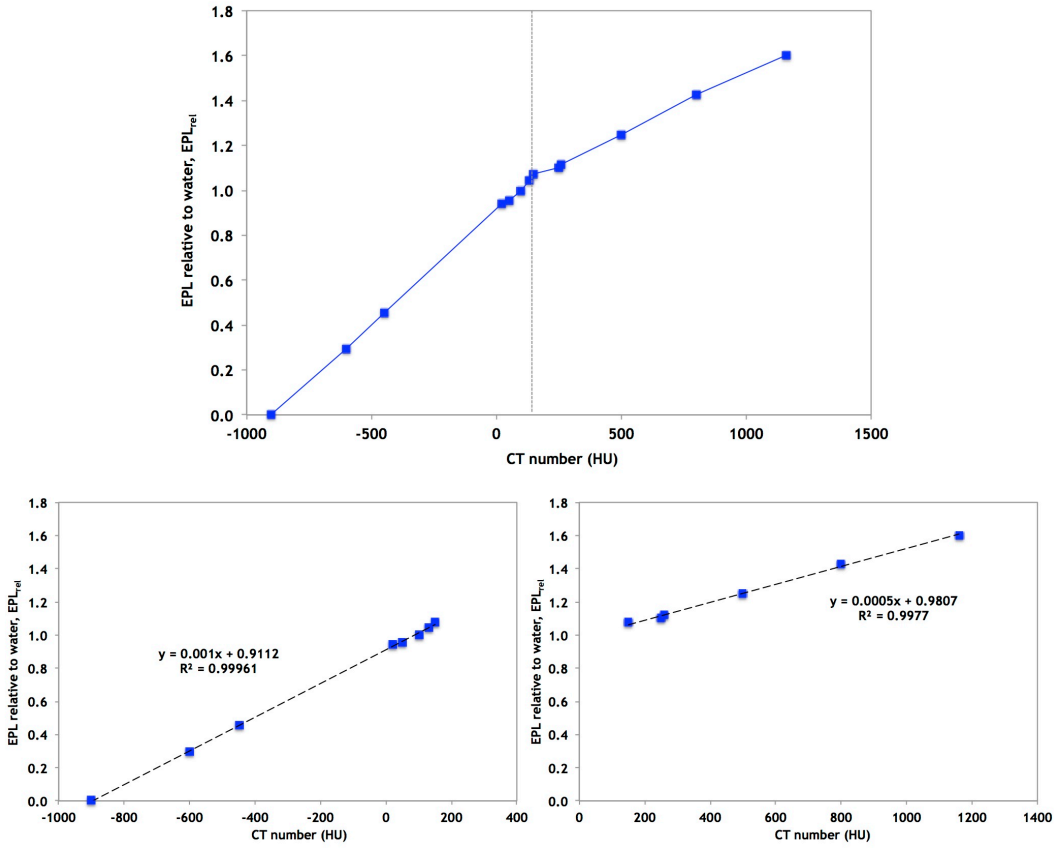

Figure 6-5 CT number to EPL relative to water calibration curve. The CT number (HU) to EPL relative to water, EPL_{rel}, calibration curve is plotted for materials of different relative electron densities (top row). The vertical line marks the point of inflection in the graph (at 150 HU). The data to the left and right of that point were separately fitted with a linear equation (bottom row).

The two linear equations derived from the CT number to EPL_{rel} calibration curve were:

$$EPL_{rel} = \begin{cases} 0.0010\,HU + 0.91 & HU \leq 150 \\ 0.0005\,HU + 0.98 & HU > 150 \end{cases} \quad (6\text{-}1)$$

Using these linear equations, the CT number (HU) for each pixel on the phantom's/patient's CT simulation images was converted into an EPL_{rel} value. Then, EPL_{rel} value for all pixels along a column (j) from the entrance to the level of interest, '*X*', was summed ($\sum_{i=Entrance}^{'X'} EPL_{rel}(i)$). The EPL_{rel} value from entrance to the exit level was also summed in the same way ($\sum_{i=Entrance}^{Exit} EPL_{rel}(i)$). The summation processes were repeated for all CT slices, with the value for each slice (z) occupying a row on a 2D matrix. Then, the two 2D matrices were divided to become a new parameter, termed as the EPL ratio:

$$EPL\ ratio\ (z,j) = \frac{\left[\sum_{i=Entrance}^{'X'} EPL_{rel}(i)\right](z,j)}{\left[\sum_{i=Entrance}^{Exit} EPL_{rel}(i)\right](z,j)} \quad (6\text{-}2)$$

The effect of beam divergence was neglected in the derivation of EPL ratio. Thus, the EPL ratio was regarded as a close approximation. Figure 6-6 illustrates the derivation of the 2D EPL ratio from a patient's CT images. The example shown is for a treatment field with gantry at zero degrees. For fields with other gantry angles, the patient's CT images were rotated around the isocentre according to the treatment gantry angle and in the anti-clockwise direction before the EPL_{rel} values were summed.

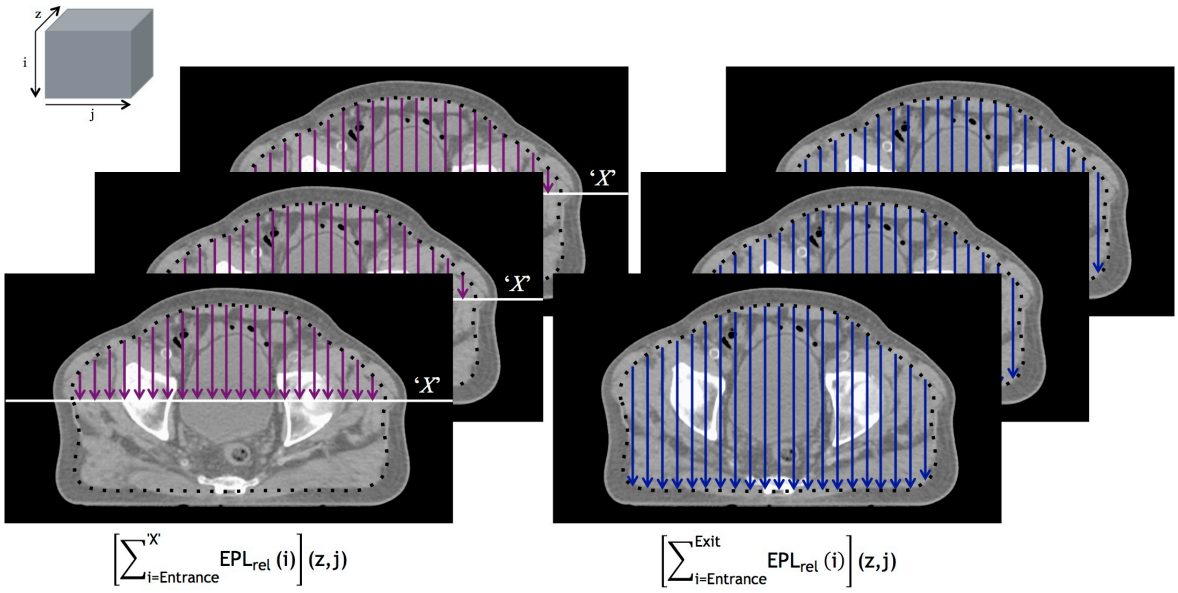

$$\text{EPL ratio } (z,j) = \frac{\left[\sum_{i=Entrance}^{'X'} EPL_{rel}(i)\right](z,j)}{\left[\sum_{i=Entrance}^{Exit} EPL_{rel}(i)\right](z,j)}$$

Figure 6-6 Derivation of 2D EPL ratio from CT simulation images. The calibration curve was first used to convert CT number (HU) in the images to EPL_{rel} value. Then, the EPL_{rel} value for pixels along each column (j) was summed from the entrance to '*X*' level as well as from the entrance to exit level. The dotted contour marked the entrance and exit location, 1.5 cm from the surface. The process was repeated for each CT slice (z), resulting in two 2D matrices that were subsequently divided to get the EPL ratio.

Since the EPID can only measure radiation after it traverses the full vertical length of the phantom/patient, the EPL calculated from EPID measured dose planes will always represent the path length from the entrance to the exit level of the phantom/patient. The function of the 2D EPL ratio was to scale the full EPL so that the EPL now represents the path length from the entrance to '*X*' level, as required in the reconstruction of in-phantom/in-vivo dose at the '*X*' plane. Figure 6-7 shows the pathway to reconstruct in-phantom/in-vivo '*X*' dose from EPID measured dose planes. As can be seen from the figure, the initial steps leading to the calculation of EPL from EPID measured M0 and M dose planes remained the same as that for exit dose reconstruction (Figure 5-3, Path 1). After that, the full EPL calculated from EPID measured dose planes was multiplied to the EPL ratio. By using this scaled EPL for the subsequent calculation of the equivalent in-phantom/in-vivo dose ratio $(M/M0)_{IC}$, the M now would represent the dose at '*X*' instead of exit dose and the equivalent dose ratio can be rewritten as $(M_{'X'}/M0)_{IC}$.

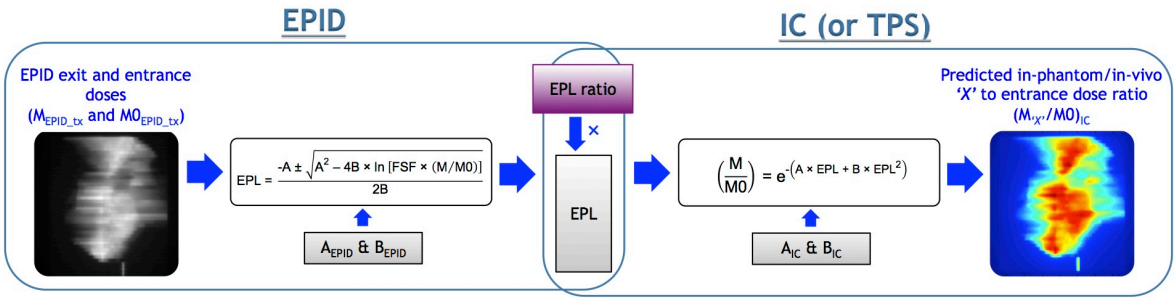

Figure 6-7 Pathway to predict in-phantom/in-vivo dose ratio $(M_{'X'}/M0)_{IC}$ from EPID measured dose planes. The EPL ratio was used to scale the EPL calculated from EPID dose planes, so that the EPL would represents the path length from the entrance to '*X*' level of the phantom/patient. With this scaled EPL, the in-phantom/in-vivo '*X*' to entrance dose ratio $(M_{'X'}/M0)_{IC}$ can be calculated. The dose ratio was used in the final reconstruction of dose at '*X*' for comparison with TPS computed dose. The '*X*' could be any plane inside the phantom/patient as chosen by the user. All parameters are in 2D and the (i,j) coordinates have been omitted for clearer illustration.

After that, the calculated dose ratio, $(M_{'X'}/M0)_{IC}$, was used to reconstruct in-phantom/in-vivo dose at '*X*' ($M_{IC\ pred\ ('X')}$) according to Equation 6-3. This equation was very similar to the equation previously described for exit dose reconstruction (Chapter 5, Equation 5-11). But because the dose ratio was calculated from the EPL representing the path length from the entrance to '*X*' level, the resultant reconstructed dose is that at the '*X*' plane.

$$M_{IC\ pred\ ('X')} = \left(\frac{M_{'X'}}{M0}\right)_{IC} \times M0_{IC\ ref} \div FSF_{IC} \times \left(\frac{100}{SDD}\right)^2 \times MF^{EPID}_{corrected} \qquad (6\text{-}3)$$

where '$M0_{IC\ ref}$' is the IC entrance dose plane for a 20 x 20 cm^2 reference beam that was previously derived as part of the commissioning process, 'FSF_{IC}' is the field size correction factor tabulated from IC measured 2D dose planes to correct for treatment fields with non-reference field size and 'SDD' is the distance from source to '*X*' plane. The $MF^{EPID}_{corrected}$ is the modulation factor acquired by dividing the EPID dose plane measured for a modulated treatment field by EPID dose plane measured for a non-modulated reference field corrected for field size. Both the modulated and non-modulated EPID dose planes used to derive the MF were measured through air. A general correction, described in Chapter 5 (sub-Section 5.3.3.2), was applied to account for differences between MF acquired from EPID measured dose planes and IC

measured dose planes. For a treatment field without modulation, the $MF^{EPID}_{corrected}$ was equal to unity.

Finally, the reconstructed in-phantom/in-vivo dose at *'X'* plane was compared to the TPS planned dose to verify the accuracy of treatment delivery.

6.3.3 Path 2: Prediction of EPID transit dose

A detailed description of the methods to predict EPID transit dose from TPS dose planes was provided in Chapter 5 (sub-Section 5.3.4). In short, TPS entrance ($M0_{TPS\_tx}$) and exit (M_{TPS_tx}) dose planes, defined as dose at 1.5 cm from the beam entry and exit surface of the phantom/patient respectively, were extracted from 3D 'Structure' and 'Dose' DICOM files exported from the TPS according to the steps elaborated in sub-Section 6.3.1. Then, the $M0_{TPS\_tx}$ and M_{TPS_tx}, together with $(A \text{ and } B)_{IC}$, were used to calculate the 2D EPL map of the phantom/patient. Subsequently, the 2D EPL map and the $(A \text{ and } B)_{EPID}$ were used to derive the equivalent EPID dose ratio $(M/M0)_{EPID}$. Finally, the $(M/M0)_{EPID}$ was used to predict the EPID transit dose for direct comparison with the EPID dose plane captured during treatment delivery.

6.3.4 Evaluation with anthropomorphic phantom

The dual 2D EPID transit dosimetry model was first evaluated using an anthropomorphic pelvic phantom (The Phantom Laboratory, NY, USA), shown in Figure 6-8. The pelvic phantom was scanned with the CT simulator and the images were sent to Eclipse TPS (Varian, Palo Alto, CA, USA) for treatment planning. Various non-modulated and modulated treatment fields were planned for the phantom. The non-modulated treatment field consisted of two simple square fields and three 3D conformal fields, while the modulated treatment field consisted of three EDW fields and three IMRT prostate fields. The IMRT fields were delivered using the sliding window technique, each with 114 segments. These 11 types of treatment fields were planned for different locations on the phantom and with variable gantry and collimator angles, resulting in a total of 65 test fields for evaluations. Details of the test fields are given in Table 6-2.

Table 6-2 Information on the test fields used for evaluation with the anthropomorphic phantom.

	Field name	Field number	[a]Isocentre	Gantry angle (degree)	Collimator angle (degree)	Jaw positions X1 (cm)	X2 (cm)	Y1 (cm)	Y2 (cm)	MLC	[b]Equivalent square (cm^2)	MU
Open	FS10	1 - 8	A	0, 45, 90, 135, 180, 225, 270, 315	0	5.0	5.0	5.0	5.0	None	10.0^2	100
		9 - 12	B	0, 90, 180, 270	0	5.0	5.0	5.0	5.0	None	10.0^2	100
		13 - 17	C	0, 45, 135, 180, 225	0	5.0	5.0	5.0	5.0	None	10.0^2	100
	FS20	18 - 21	A	0, 90, 180, 270	0	10.0	10.0	10.0	10.0	None	20.0^2	100
3D conformal	Conform 1	22 - 23	A	0, 45	0	10.0	5.0	10.0	7.5	Static	13.4^2	100
	Conform 2	24 - 25	A	0, 135	0	5.0	5.0	5.0	5.0	Static	7.6^2	100
	Conform 3	26 - 27	A	0, 315	0	5.0	5.0	5.5	5.5	Static	7.6^2	100
Wedge	EDW60FS10	28 - 31	A	0, 90, 180, 270	90 or 270	5.0	5.0	5.0	5.0	None	10.0^2	100
		32 - 35	B	0, 90, 180, 270	90 or 270	5.0	5.0	5.0	5.0	None	10.0^2	100
	EDW15FS20	36 - 37	A	0, 180	90 or 270	10.0	10.0	10.0	10.0	None	20.0^2	100
	EDW60FS20	38 - 41	A	0, 90, 180, 270	90 or 270	10.0	10.0	10.0	10.0	None	20.0^2	100
IMRT	IMRT 1	42 - 45	A	0, 135, 180, 315	0	7.5	7.5	7.5	7.5	Dynamic	6.6^2	200
		46 - 49	B	0, 135, 180, 315	0	7.5	7.5	7.5	7.5	Dynamic	6.6^2	200
	IMRT 2	50 - 53	A	0, 45, 180, 225	0	7.5	7.5	7.5	7.5	Dynamic	6.3^2	200
		54 - 57	B	0, 45, 180, 225	0	7.5	7.5	7.5	7.5	Dynamic	6.3^2	200
	IMRT 3	58 - 61	A	0, 135, 180, 225	0	7.5	7.5	7.5	7.5	Dynamic	6.8^2	200
		62 - 65	B	0, 135, 180, 225	0	7.5	7.5	7.5	7.5	Dynamic	6.8^2	200

[a] Location of field isocentre (lateral, vertical, longitudinal): A = (0 cm, 0 cm, 0 cm), B = (0 cm, 0 cm, -7 cm), C = (4 cm, 0 cm, 0 cm). These isocentres are visually indicated in Figure 6-8.
[b] The equivalent square field size for an irregularly shaped field was calculated using the method described by Monti et al. (1995). The field area for 3D conformal fields was defined by positions of the MLC leaves retrieved from MLC files exported from the TPS. For the IMRT fields, the field area was defined as the region with dose greater than 50% of the maximum dose, following the common definition of field size.

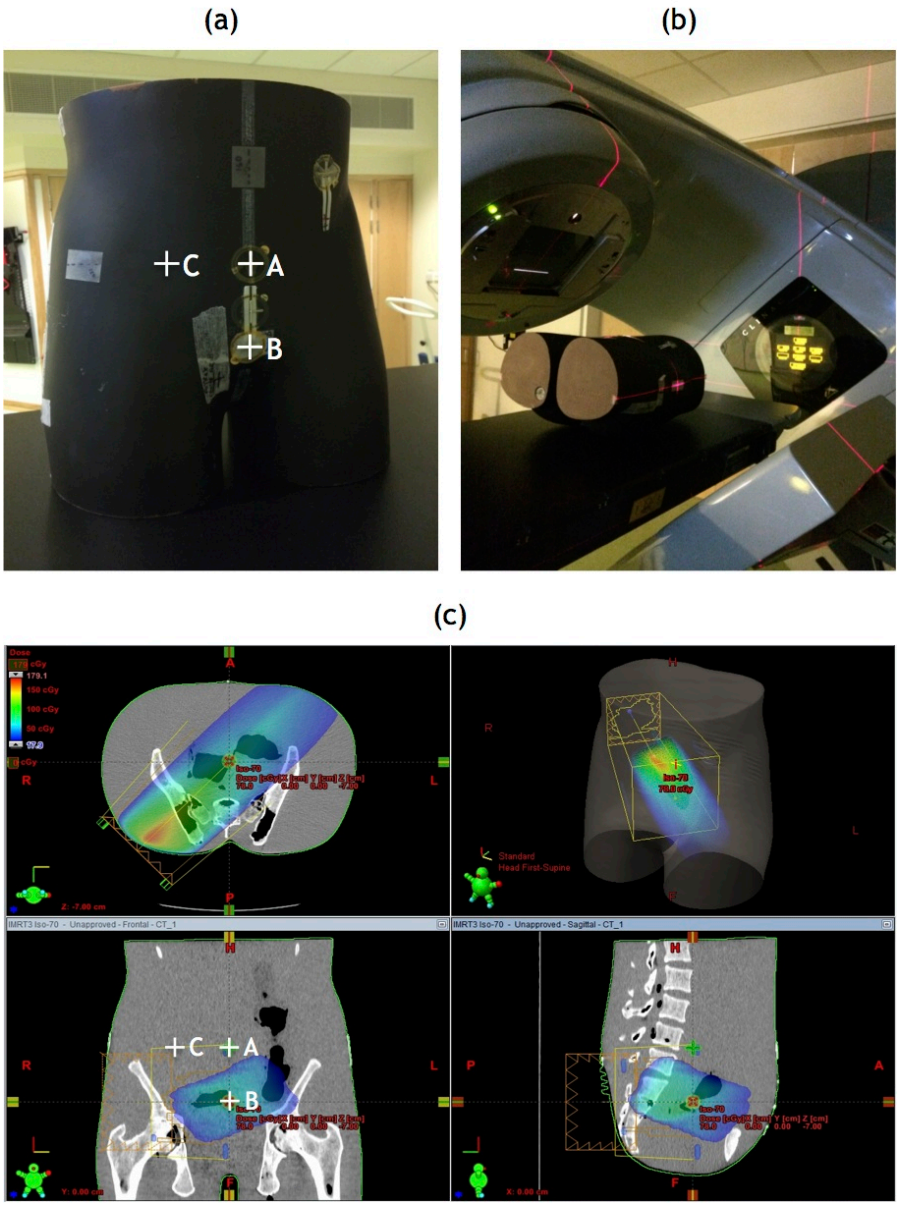

Figure 6-8 Anthropomorphic pelvic phantom and beam arrangements. (a) Anthropomorphic pelvic phantom. (b) Anthropomorphic pelvic phantom positioned on the linac couch for EPID measurements. (c) CT images of the phantom imported into the TPS for treatment planning. The 'A', 'B' and 'C' marked different locations where test fields were centred.

6.3.5 Actual treatment verification of patients

After a thorough evaluation with the anthropomorphic phantom, the 2D EPID transit dosimetry model was used for actual treatment verification of three patients undergoing radiotherapy to the pelvic area. The treatment plans for the three patients comprised of 11 3D conformal and EDW fields with irradiation from different gantry angles. Details of the treatment fields are given in Table 6-3. During treatment delivery, the radiation beam after transiting the patient

was passively captured with the EPID panel. A total of 18 analyses were performed with some fields captured on two different treatment days. The treatment verification was carried out on random treatment days and might not be consecutive. No IMRT fields could be evaluated on patients because the department now routinely uses VMAT instead of IMRT for clinical treatment.

Table 6-3 Treatment field information for the three patients included in this study.

	Field name	Gantry angle (degree)	Collimator angle (degree)	Wedge angle (degree)	Jaw positions				MLC	[c]Equivalent square field size (cm^2)	MU
					X1 (cm)	X2 (cm)	Y1 (cm)	Y2 (cm)			
Patient 1	**Field 1**	0	0	15	7.9	7.3	9.8	7.3	Static	14.9^2	110
	Field 2	90	90	60	9.6	7.1	4.0	8.9	Static	13.3^2	112
	Field 3	270	90	60	9.6	7.1	8.9	4.0	Static	13.3^2	110
Patient 2	**Field 4**	0	0	None	5.4	6.0	4.3	6.0	Static	9.8^2	113
	Field 5	180	0	None	5.9	5.4	4.3	6.0	Static	9.6^2	115
	Field 6	90	90	30	4.3	6.0	4.0	9.1	Static	10.0^2	105
	Field 7	270	90	45	4.3	6.0	9.4	4.1	Static	10.1^2	108
Patient 3	**Field 8**	0	0	None	6.3	7.3	6.1	5.5	Static	11.5^2	113
	Field 9	180	0	None	7.4	6.5	6.0	5.5	Static	11.5^2	108
	Field 10	90	90	10	6.0	5.5	7.4	7.1	Static	11.9^2	96
	Field 11	270	90	10	6.0	5.5	7.0	7.4	Static	11.8^2	97

[c] The equivalent square field size for an irregularly shaped field was calculated using the method described by Monti et al. (1995). Positions of the MLC leaves were determined from MLC files exported from the TPS.

6.3.6 Treatment planning, EPID measurement and evaluation of result

Following the routine clinical practice of the department, all treatment plans were computed using the Eclipse AAA algorithm (version 10.0.28) with 0.25 cm grid size. Treatments were delivered with a Varian Clinac 21EX linac. The aS500 EPID panel, attached to the linac, was extended to a vertical distance of 140 cm to measure radiation exiting the phantom/patient. No modification was done to the EPID panel. The measurements were performed in the integrated mode using the manufacturer's default settings. The EPID signal was not absolutely calibrated to dose although the term 'EPID dose plane' was used for a more consistent description with IC and TPS dose planes. Image processing and dose reconstruction/prediction for the 2D EPID transit dosimetry model was performed using the MATLAB software (R2011a Student version, The MathWorks, Natick, MA). The agreement between two dose planes was evaluated on the

Varian Portal Dosimetry platform (version 10.0) using 2D global gamma analysis in absolute mode. The gamma criterion was set to 4%/4mm for the phantom assessments and 5%/5mm for patient's actual treatment verifications. A less stringent criterion was selected for patient verification in anticipation of day-to-day variation in positioning and anatomical changes; the 5% criterion was also in accordance with ICRU recommendation (ICRU Report No. 24, 1976). For both phantom and patient, the area of analysis was taken to be 100% of the field area for regular shaped fields. As for irregularly shaped fields, a dose threshold of 50% and 20% was used for non-modulated and modulated fields respectively. The dose threshold method was required for irregularly shaped fields to allow automatic demarcation of the region of interest in a systematic way. The 50% value for non-modulated fields was used following the common definition of field size. Meanwhile, the 20% value for modulated fields was chosen to include a larger area, considering the dose modulation in the field and at the same time, to exclude very low dose regions that may artificially improve the gamma analysis results due to global calculation of dose difference.

6.4 Results

6.4.1 Anthropomorphic phantom

A total of 65 fields were evaluated with the anthropomorphic phantom. The percentage gamma pass rates with 4%/4mm criterion for all the test fields are summarised in the figures below. Figure 6-9 shows the results for comparisons of in-phantom dose (Path 1) at the exit level, between reconstructed from EPID dose planes versus computed by the TPS. The overall mean gamma pass rate for exit dose comparisons was 97.6%, ranging from 90.0% to 100%. When categorised into non-modulated (open and 3D conformal fields) and modulated fields (EDW and IMRT fields), the mean gamma pass rates were 98.1% (range: 92.9% to 100%) and 97.3% (range: 90.0% to 100%) respectively.

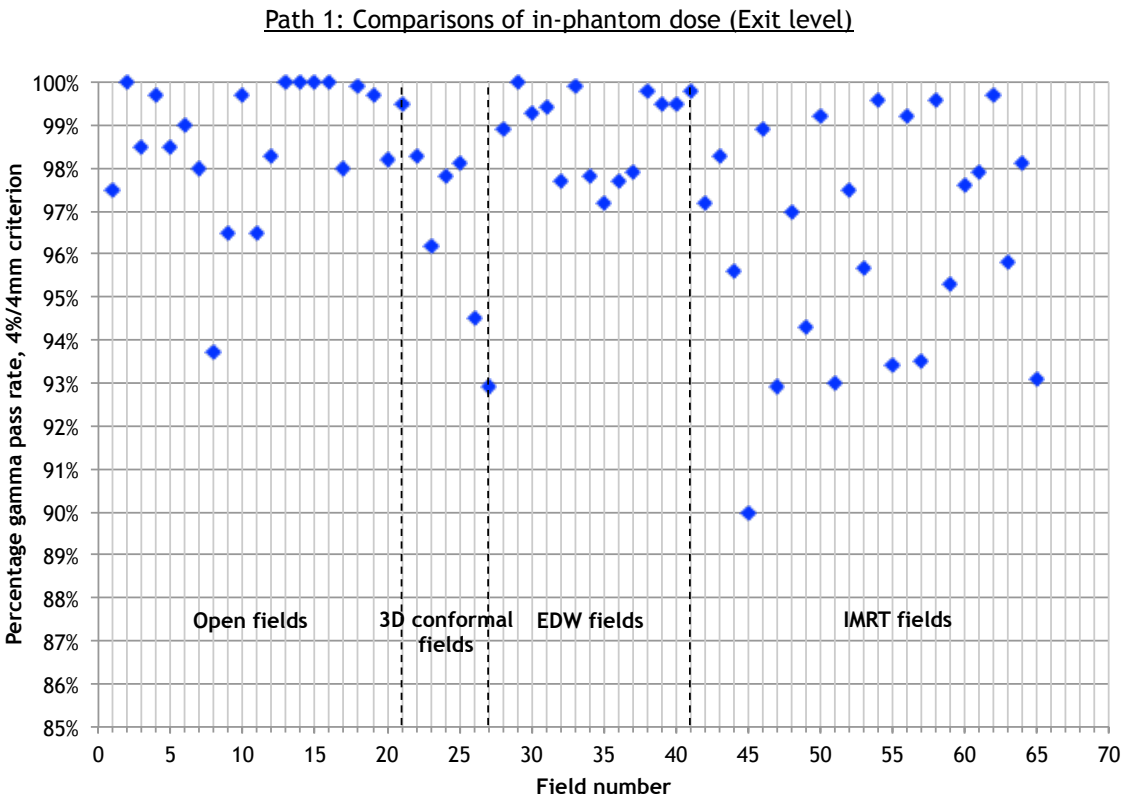

Figure 6-9 Percentage gamma pass rates for in-phantom dose comparisons at the exit level, between EPID reconstructed versus TPS computed. The field number corresponds to field listed in Table 6-2.

Besides verifying doses at the exit level, the dose agreements were also evaluated at another level, '*X*', in the phantom. In this study, level '*X*' was chosen to be the isocentre. Figure 6-10 shows the gamma pass rates for comparisons between EPID reconstructed and TPS computed in-phantom doses at the isocentre level. The overall mean gamma pass rate for the same criterion of 4%/4mm was marginally higher than comparisons at the exit level, at 98.2% with the pass rates ranging from 91.7% to 100%. Between non-modulated and modulated fields, the mean gamma pass rates were 98.3% (range: 93.1% to 100%) and 98.2% (range: 91.7% to 100%) respectively.

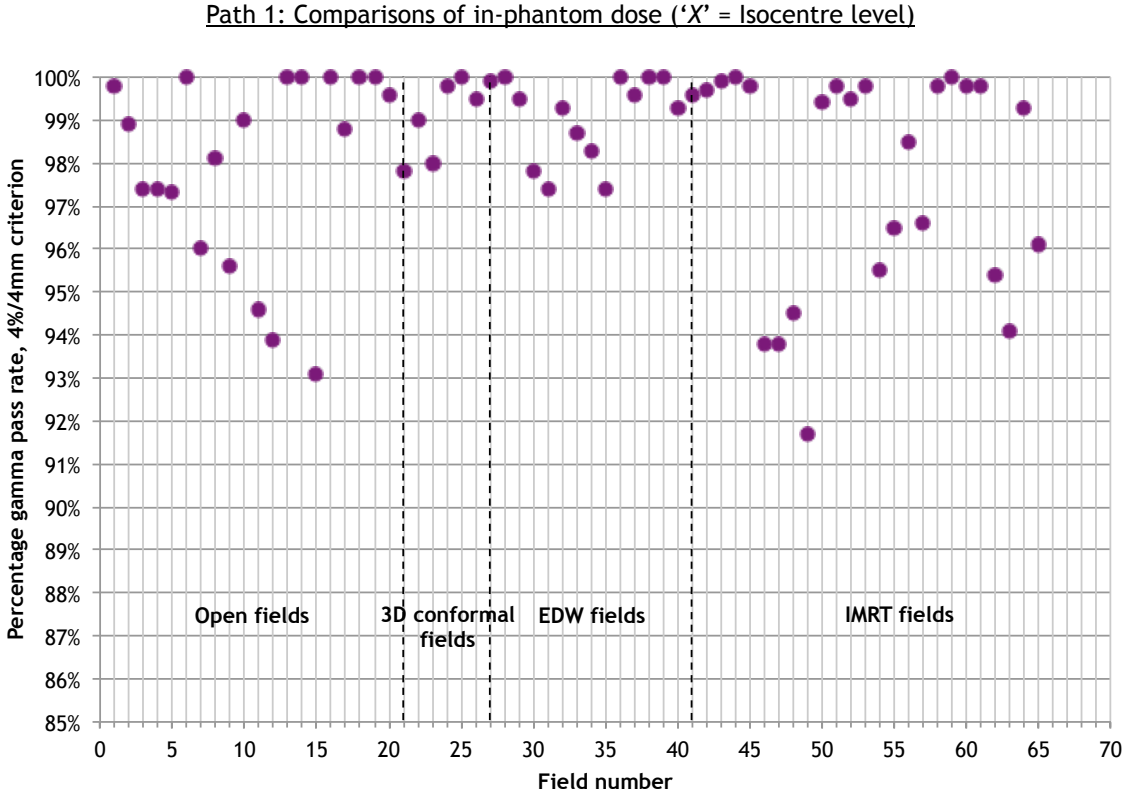

Figure 6-10 Percentage gamma pass rates for in-phantom dose comparisons at the isocentre level, between EPID reconstructed versus TPS computed. The field number corresponds to field listed in Table 6-2.

Alternatively, the TPS computed dose planes could be used to predict EPID transit dose for direct comparison with EPID dose plane measured during treatment delivery (Path 2). Figure 6-11 shows the gamma results for comparisons between predicted and measured EPID transit dose planes. Using a gamma criterion of 4%/4mm, the overall mean gamma pass rate was 97.1% with a minimum and maximum of 92.9% and 99.8% respectively. For comparisons of non-modulated fields, the mean gamma pass rate was 97.3% (range: 93.2% to 99.8%). As for modulated fields, the mean gamma pass rate was 96.9% (range: 92.9% to 99.6%).

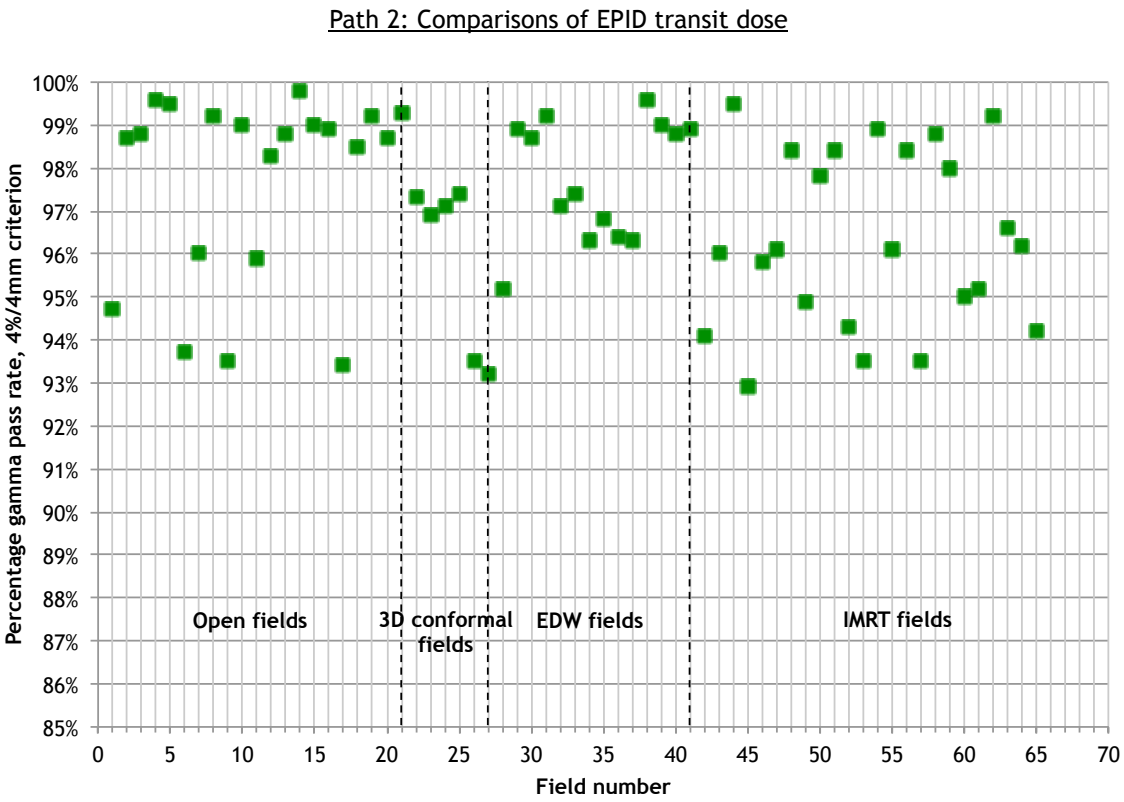

Figure 6-11 Percentage gamma pass rates for EPID transit dose comparisons, between predicted from TPS dose planes versus measured. The field number corresponds to field listed in Table 6-2.

Examples of comparisons at different levels (comparison in-phantom at the exit level, comparison in-phantom at the isocentre level and comparison at the EPID level) for various test fields are illustrated in Figure 6-12. From the figure, it can be observed that the areas that failed gamma comparisons mostly coincided with the location of air cavities, especially in the case of lateral fields (Figure 6-12a and 6-12b) where the beam passed through a large amount of air in the phantom cavity representative of the transverse colon. In these cases, the TPS computed doses were lower than the doses reconstructed from the EPID measured dose planes.

Path 1: In-phantom dose comparison (Exit level), Reconstructed versus TPS computed

(a) Open (Field name: FS10), gantry 90°

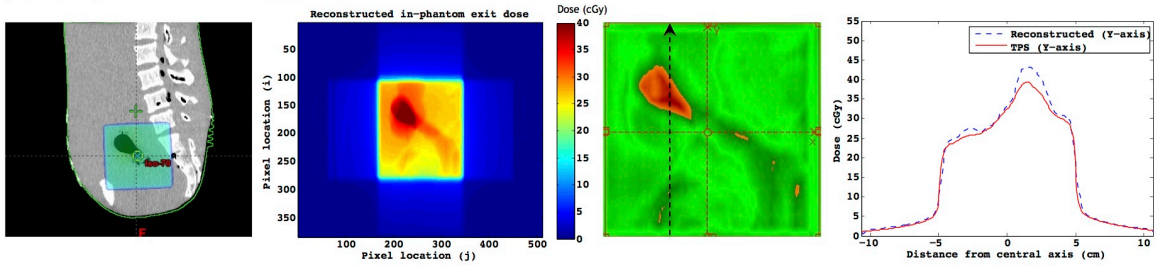

Path 1: In-phantom dose comparison ('*X*' = Isocentre level), Reconstructed versus TPS computed

(b) Wedge (Field name: EDW60FS10), gantry 270°

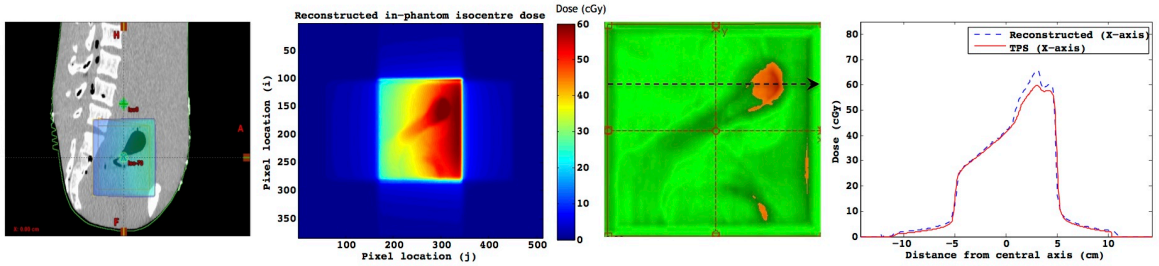

(c) 3D conformal (Field name: Conform 3), gantry 315°

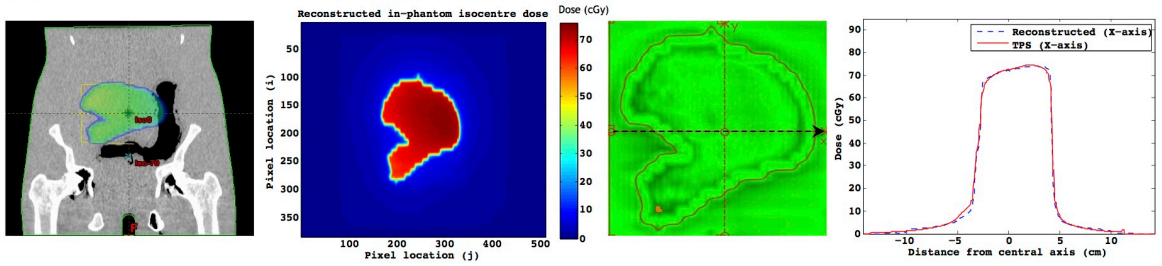

Path 2: EPID transit dose comparison, Predicted versus Measured

(d) IMRT (Field name: IMRT 2), gantry 0°

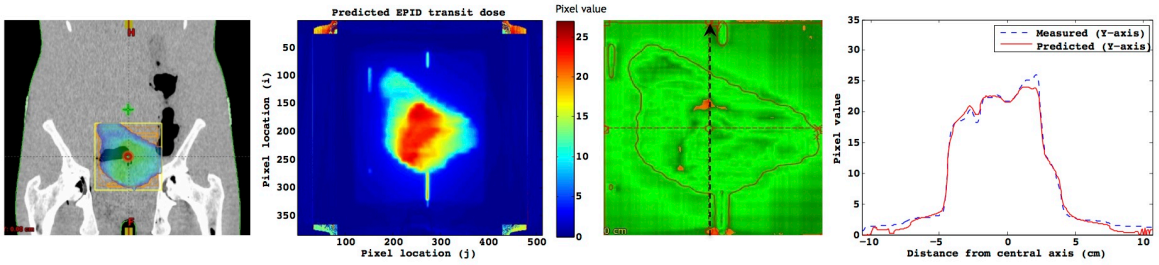

Figure 6-12 Examples of various dose comparisons performed on the anthropomorphic phantom. (a) Comparison of EPID reconstructed and TPS computed in-phantom exit dose for a 10 x 10 cm^2 field with 90° gantry angle. (b) Comparison of EPID reconstructed and TPS computed in-phantom isocentre dose for an EDW 60°, field size 10 x 10 cm^2 field with 270° gantry angle (c) and a 3D conformal field with 315° gantry angle. (d) Comparison of predicted and measured EPID transit dose for an IMRT field with 0° gantry angle. Figures from left to right are the CT simulation images with the planned fields, reconstructed/predicted dose planes, 4%/4mm gamma comparisons results (red indicating areas that failed the gamma criteria) and the profiles comparisons across the axis indicated by the arrows. The percentages of points that passed the specified gamma criterion for the different comparisons were (a) 96.5%, (b) 97.4%, (c) 99.9% and (d) 98.9%.

6.4.2 Actual treatment verification of patients

Table 6-4 lists the actual treatment verification results for three patients treated for cancers in the pelvic area. The percentage gamma pass rates were presented for (Path 1) in-vivo dose comparisons as well as (Path 2) EPID transit dose comparisons. Similar to the assessment with the anthropomorphic phantom, the in-vivo dose comparisons were performed at two levels, the exit level and the isocentre level. Although the dose could be reconstructed and compared at any level in-vivo, the isocentre plane was chosen because it intersects the target volume for all three patients and therefore, represents the most clinically relevant plane to be verified.

Table 6-4 Gamma analysis results, with 5%/5mm criterion, for in-vivo dose comparisons (at the exit level and isocentre level) and EPID transit dose comparisons. 11 treatment fields (details given in Table 6-3) for three patients were verified. The treatment verification process was repeated for two of the patients on different treatment days, resulting in a total of 18 analyses.

Treatment field			Path 1 In-vivo dose comparisons: Reconstructed versus TPS 5%/5mm gamma pass rate (%)		Path 2 EPID transit dose comparisons: Predicted versus Measured 5%/5mm gamma pass rate (%)
			Exit level	Isocentre level	
Patient 1	**Field 1**	**Verify 1**	98.4	99.6	95.1
		[d]Verify 2	92.4	99.2	90.7
	Field 2	**Verify 1**	95.8	96.1	94.6
		[d]Verify 2	97.0	98.2	92.2
	Field 3	**Verify 1**	98.0	96.3	95.5
		[d]Verify 2	96.6	98.9	95.4
Patient 2	**Field 4**	**Verify 1**	99.5	97.9	98.5
		[d]Verify 2	97.3	96.6	95.9
	Field 5	**Verify 1**	94.8	100.0	93.7
		[d]Verify 2	96.9	100.0	93.9
	Field 6	**Verify 1**	99.6	99.4	97.5
		[d]Verify 2	97.7	96.1	94.9
	Field 7	**Verify 1**	94.3	99.6	94.9
		[d]Verify 2	99.1	99.4	97.7
Patient 3	**Field 8**	**Verify 1**	95.8	98.8	96.1
	Field 9	**Verify 1**	96.3	99.9	95.8
	Field 10	**Verify 1**	98.7	99.8	98.8
	Field 11	**Verify 1**	97.3	99.6	99.9
		Mean	**97.0**	**98.6**	**95.6**

[d] Treatment verification was repeated on another treatment day.

The 5%/5mm gamma pass rates for in-vivo comparisons between EPID reconstructed and TPS computed dose planes at the exit level ranged from 92.4% to 99.6% with a mean of 97.0%. Comparisons at the isocentre level resulted in a mean pass rate of 98.6%, ranging from 96.1% to 100%. As for the comparisons between measured and predicted EPID transit dose, the overall mean gamma pass rate was 95.6% with a minimum pass rate of 90.7% and a maximum pass rate of 99.9%. The treatment verification was repeated for seven fields (n = 7) from two of the patients on different treatment days (Verify 1 and Verify 2). Statistical analyses with paired T-test (IBM SPSS Statistics, version 22.0, Armonk, NY, USA) showed no statistically significant difference in the mean of gamma pass rates between “Verify 1” and “Verify 2” for comparisons at all levels (using a significance level of 0.05 and a two-tailed test). The *p*-values were 0.726, 0.928 and 0.203 for dose comparisons at the exit level, isocentre level and EPID level respectively. However, the statistical analysis may be limited to only detecting large differences because of the small sample size. Detailed results of the statistical analyses are provided in Appendix C.

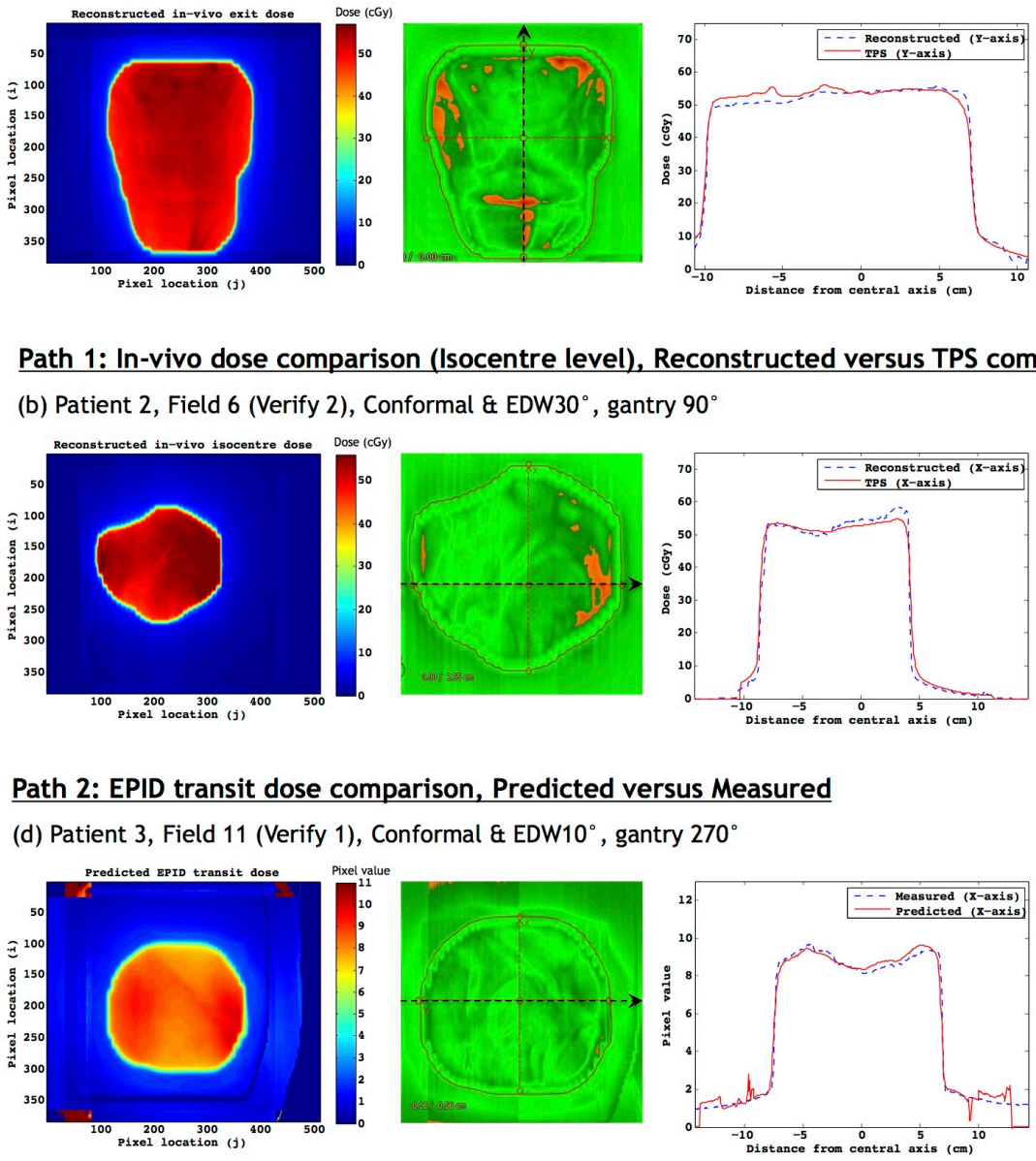

Figure 6-13 Examples of actual treatment verifications of patients. (a) comparison of in-vivo dose at the exit level, (b) comparison of in-vivo dose at the isocentre level and (c) comparison of EPID transit dose. Figures from left to right are the reconstructed/predicted dose planes, 5%/5mm gamma comparisons results (red indicating areas that failed the gamma criteria) and the profiles comparisons across the axis indicated by the arrows. The percentages of points that passed the specified gamma criterion for the different comparisons were (a) 92.4%, (b) 96.1% and (c) 99.9%.

6.5 Discussion

The anthropomorphic pelvic phantom has a hollow cavity that mimics the colon and rectum structures of the human anatomy. The cavity can be filled with water or contrast media but it was left empty for this study. Several test fields

were planned in such a way that the beam passed through the whole transverse length of the air-filled colon structure, which was approximately 12 cm in physical length. An example of such a beam arrangement is shown in Figure 6-14a. The dose comparison result for this particular test field was previously presented in Figure 6-12a and again in Figure 6-14a below for ease of reference. From the results, it could be observed that the points that failed gamma comparisons were at the area where the air-filled transverse colon was located. The profiles comparison revealed that the dose reconstructed from this EPID dosimetry model was higher than the TPS computed dose. This over-estimation of dose in the presence of air cavity could possibly be a weakness of the EPID dosimetry model that uses EPL for heterogeneity correction. It is well known that the EPL correction method only accounts for changes in primary beam and ignores variations in scatter contribution from materials of different densities (Rosenwald et al., 2007). In the case of air cavities, the reduced scatter contribution from air relative to water could not be properly accounted for by the EPL method, which could explain the over-estimation of dose seen in the results. However, this scenario of having the whole colon filled with air is not clinically realistic. A much smaller amount of gas would be expected in a real patient. Figure 6-14b shows the same lateral beam planned on a different part of the pelvic phantom, now passing through the descending colon with a smaller cross-section of air cavity (approximately 2.5 cm in diameter). As can be seen in the profiles and gamma comparison, the reconstructed dose was still higher than the TPS computed dose but the dose discrepancies were less and mostly within the 4%/4mm gamma criterion. It would be of future interest to evaluate the performance of the EPID dosimetry model with an anthropomorphic chest phantom, which has a large volume of low-density lung tissues. Williams et al. (1991) suggested the use of modified limit for lung treatments in their independent dose verification program. Without accounting for dose inhomogeneity, a wide tolerance of 5% to 15% was adopted instead of the standard ±2%. Later, in a modified version of the software program, the thickness of overlying lung was used as a form of inhomogeneity correction and a stricter tolerance was used (the exact tolerance was not stated). In our case, the EPL was a form of simple inhomogeneity correction and a stricter tolerance should be adequate. The appropriate tolerance could only be determined with further experiment with low-density phantoms. Also, the current model could

potentially be improved to better account for inhomogeneity correction. A better understanding on the weakness of the EPID dosimetry model is crucial to ensure appropriate judgement when interpreting gamma comparison results. This also implies that careful investigation of gamma results and the corresponding CT images is necessary to help ascertain the reason of gamma failures.

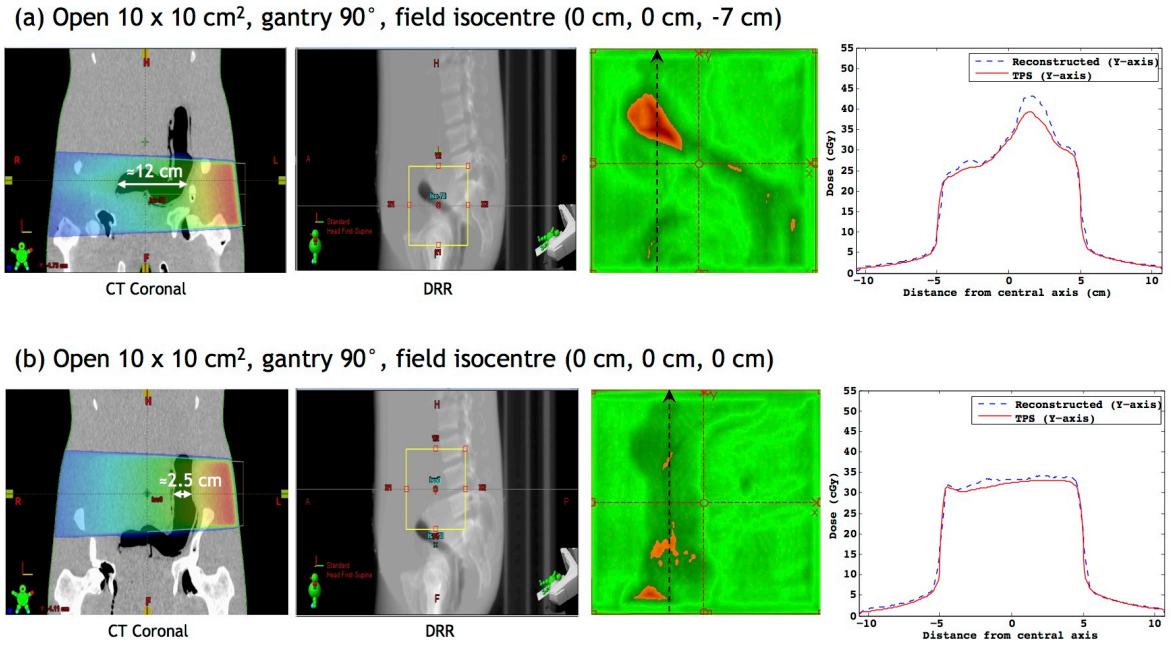

Figure 6-14 In-phantom exit dose comparisons for two identical fields (open 10 x 10 cm^2, gantry 90°) planned and irradiated at different parts of the pelvic phantom. (a) Field passed through the air-filled transverse colon with a physical length of approximately 12 cm and (b) Field passed through the air-filled descending colon with an approximate diameter of 2.5 cm. The columns from left to right are the coronal view of the CT plan, field location (yellow box) shown on digitally reconstructed radiograph (DRR), 4%/4mm gamma comparisons results (red indicating areas that failed the gamma criteria) and the profiles comparisons across the axis indicated by the dashed arrows. The percentage gamma pass rates were (a) 96.5% and (b) 98.5%.

One of the issues that arise when performing treatment verification from different gantry angles is the attenuation by couch structures. The Exact treatment couch (Varian, Palo Alto, CA, USA) installed in the linac treatment room has a pair of metal sliding support rails below the carbon fibre couch top. The beam attenuation by these metal rails is not negligible. Li et al. (2011) reported a maximum attenuation of 14.4% when the metal rails at the section of the couch near the pelvic region were in the path of a 6 MV 10 x 10 cm^2 field. As far as patient dose is concerned, the metal rails only affect posterior/posterior

oblique fields and the therapists must move the rails to a position out of the beam pathway if they were not included in the treatment plan. However, for the purpose of EPID dose measurements, where dose is measured after the beam transits both the patient and couch, the position of the metal rails affects not only the posterior/posterior oblique fields but also the anterior/anterior oblique fields. Figure 6-15 shows the effect of rail attenuation if they were accidentally left in the beam pathway. The example given is for a 10 x 10 cm^2 field irradiated from gantry 135° using the anthropomorphic phantom. The 4%/4mm gamma pass rate for comparison between EPID reconstructed and TPS computed exit dose was only 89.2%, with a distinct rectangular area of gamma failure at the side of the field that resembled the metal rail. Comparison of profiles showed that at the region of gamma failure, the dose reconstructed from EPID transit dose plane was lower than the TPS computed dose by as much as 10%. This was consistent with attenuation by the metal rail that was measured by the EPID but not accounted for in the treatment planning. If this EPID dosimetry result were to appear in the actual treatment verification of patients, it would have highlighted to the users that an incident had occurred that might have compromised the patient's treatment. But the same EPID dosimetry results for an anterior/anterior oblique field would not have impacted the patient's treatment. Instead, it would mean that the EPID transit dose plane was not properly captured and the EPID verification result must be interpreted with caution. This issue is not unique to couch structure but also applies to any other objects that may be present in the beam pathway, for example certain radiopaque parts of patient immobilisation devices. Also, it is important that users should always inspect the verification result to look for any suspicious pattern of failure. If the affected area is not as large, for example small metal joints in an immobilisation device, the gamma pass rate alone may not be indicative of a problem and the consistent error may be overlooked.

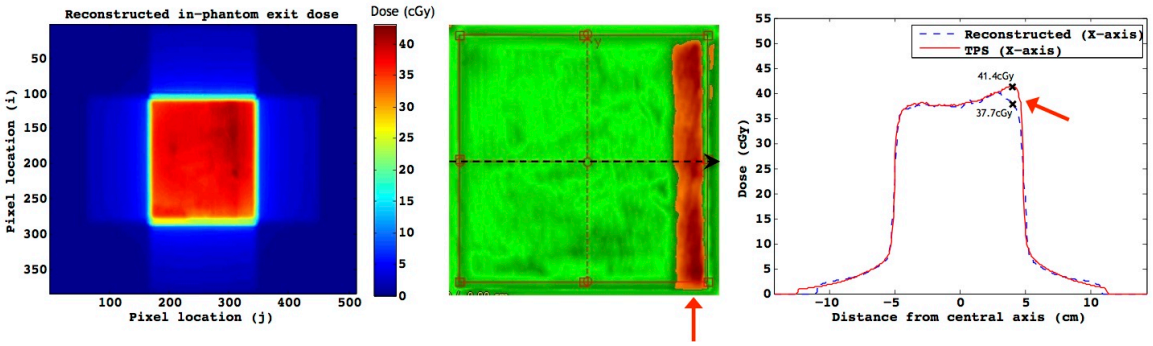

Figure 6-15 Effect of beam attenuation by couch metal rail. The effect of rail attenuation (indicated by red arrows) is shown for a 10 x 10 cm^2 field irradiated from gantry 135° for the anthropomorphic phantom. The metal rail was in the beam pathway during the treatment delivery and the reduced transmission was measured by the EPID. The in-phantom exit dose reconstructed from the EPID measured dose plane (left column) was compared with the TPS computed dose. But because the metal rail was not included in the treatment plan, the discrepancy in measured and planned dose, of up to approximately 10%, was reflected as a region of failure in the 4%/4mm gamma comparisons (centre column, red indicating areas that failed the gamma criteria). As a result, the gamma pass rate was only 89.2%. Profiles comparison across the axis indicated by the dashed arrows is shown in the right column.

Besides detecting unexpected beam obstruction during treatment delivery, the EPID dosimetry model could also indicate changes in patient position or anatomy. This can be seen in the results for actual treatment verification performed on two different treatment days for the same patient. Figure 6-16 shows an example of how the presence of bowel gas on a certain treatment day could be reflected in the EPID treatment verification results.

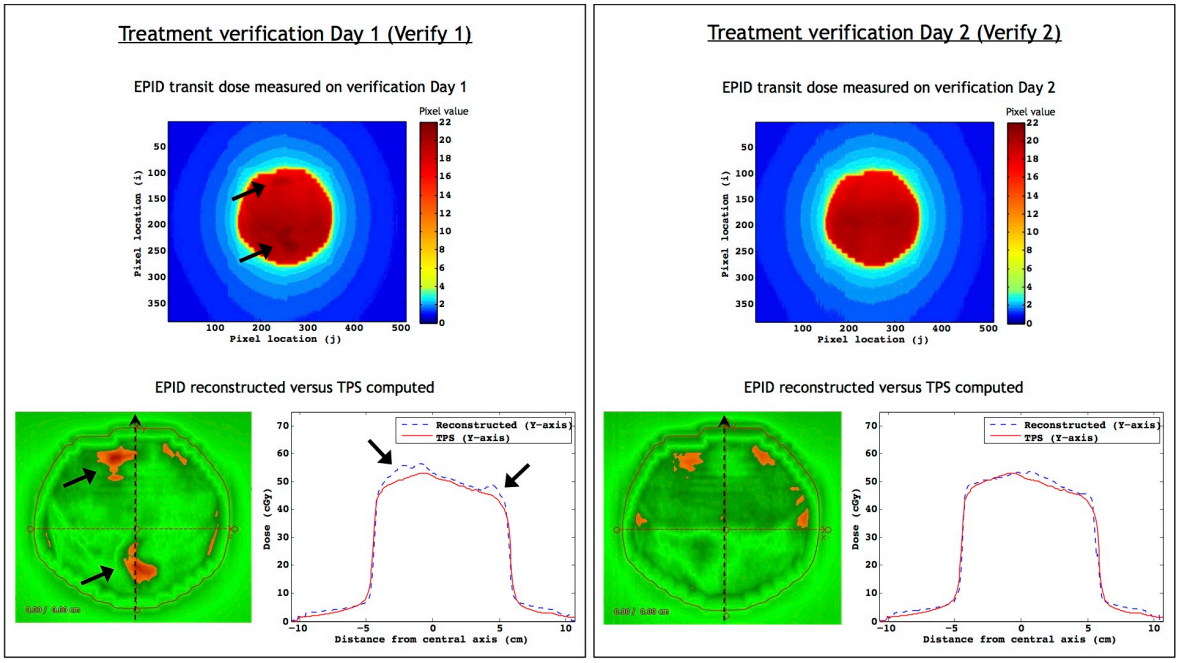

Figure 6-16 Effect of change in patient's anatomy. The effect of change in patient's anatomy can be seen in the in-vivo exit dose verification results on two different treatment days (Patient 2, Field 5). On the first day of treatment verification (Verify 1), pockets of high dose region (indicated by solid arrows) were visible on the EPID transit dose plane measured during treatment delivery, which subsequently led to areas of gamma failures (red indicating areas that failed the gamma criterion of 5%/5mm) when the EPID reconstructed dose plane was compared to TPS computed dose plane. Profiles comparison across the axis indicated by the dashed arrow showed that the EPID reconstructed dose (blue dashed line) was higher than the TPS computed dose (red solid line) at the region of gamma failure, possibly indicating that the discrepancies were due to the presence of bowel gas on treatment day that was not there during CT simulation. The areas of high dose were no longer noticeable on the EPID transit dose plane measured on another treatment day (Verify 2), leading to better agreement with the TPS computed dose. The percentage gamma pass rates for the first and second verification were 94.8% and 96.9% respectively.

Despite having demonstrated that EPID dosimetry for actual treatment verification is useful to detect inconsistency in treatment delivery, the additional time and effort required to implement an EPID dosimetry program must also be considered for practical reasons. The commissioning process for this EPID dosimetry model involved measuring two sets of calibration dose planes with the EPID as well as IC in water. The methods to acquire these calibration dose planes were explicitly described in Chapter 5 (sub-Section 5.3.2). The measurements of EPID calibration dose planes took approximately two hours to complete, requiring a total of 32 EPID images measured for water-equivalent solid phantom of eight different thicknesses (0 cm to 35 cm, in 5 cm increment) and beams with four different field sizes (5 x 5 cm^2 to 20 x 20 cm^2, in 5 cm

increment). These images were inclusive of those needed for tabulation of field size correction factors (FSF). Because the EPID response is fairly stable, with less than 1% to 2% variation over a year (Van Esch et al., 2004, Winkler & Georg, 2006), the re-measurements of EPID calibration dose plane will be infrequent. As for the IC calibration dose planes, the required PDD and profiles were taken from the original linac commissioning measurements performed in a scanning water tank. If the PDD and profiles must be measured, the time required is estimated to be four hours, including the time taken to set-up the water tank. Since measurements in a scanning water tank represent full scatter condition, an additional backscatter correction factor (BCF) was used to account for the reduced backscatter, especially at the exit level where the thickness of underlying material was only 1.5 cm. The measurements of BCF values with IC in solid water phantoms, with different backscatter thicknesses and depths (1.5 cm to 36.5 cm) as a function of field size (5 x 5 cm^2 to 20 x 20 cm^2), took approximately three hours to complete. However, the BCF values for 6 MV beams were found to be very similar for linacs from different manufacturers and these values have been published Tan et al. (2014). Moreover, it is very unlikely that any of the IC measurements will have to be repeated as long as the linac's dosimetric performance remained the same. Once the EPID dosimetry model had been properly commissioned, the subsequent dose reconstruction/prediction took less than five minutes to complete for a typical conformal or IMRT field.

The clinical workflows for actual treatment verification with the proposed EPID dosimetry model are shown in the figures below. Figure 6-17 illustrates the workflow for Path 1, where the EPID measured dose planes were used to reconstruct in-vivo dose for comparison with TPS computed dose, to verify the accuracy of treatment delivery. First, a plan was scheduled in the Aria oncology information system (Varian, Palo Alto, CA, USA) to capture an EPID integrated image. On the day of treatment, the patient was set up to the usual treatment position. After that, the EPID panel was extended to the calibration position (140 cm was used in this study). The EPID detectors then passively capture radiation that transits the patient during treatment delivery. Upon completion of treatment, the captured EPID transit dose plane (M_{EPID_tx}) was exported from the Aria system for the reconstruction of in-vivo dose using an in-house code written with the Matlab software. In addition to the EPID transit dose plane

measured during treatment delivery, another EPID dose plane measured for the same treatment field but without the patient on couch ($M0_{EPID\_tx}$) was required. The $M0_{EPID\_tx}$ can either be measured once for repeated use in the subsequent dose reconstruction or a new dose plane can be captured each time on the day of verification. By using the latter, machine output variation for the day was taken into account and would not be reflected in the results. Although the measurement of $M0_{EPID\_tx}$ is relatively easy to perform, it is the intention of future study to remove this measurement and minimise the additional workload associated with the implementation of EPID transit dosimetry. Finally, the reconstructed in-vivo dose was imported into the Varian Portal Dosimetry workspace. The TPS computed dose, exported from the TPS and extracted according to the steps described in sub-Section 6.3.1, was also imported into the Portal Dosimetry workspace as a reference for the gamma analysis.

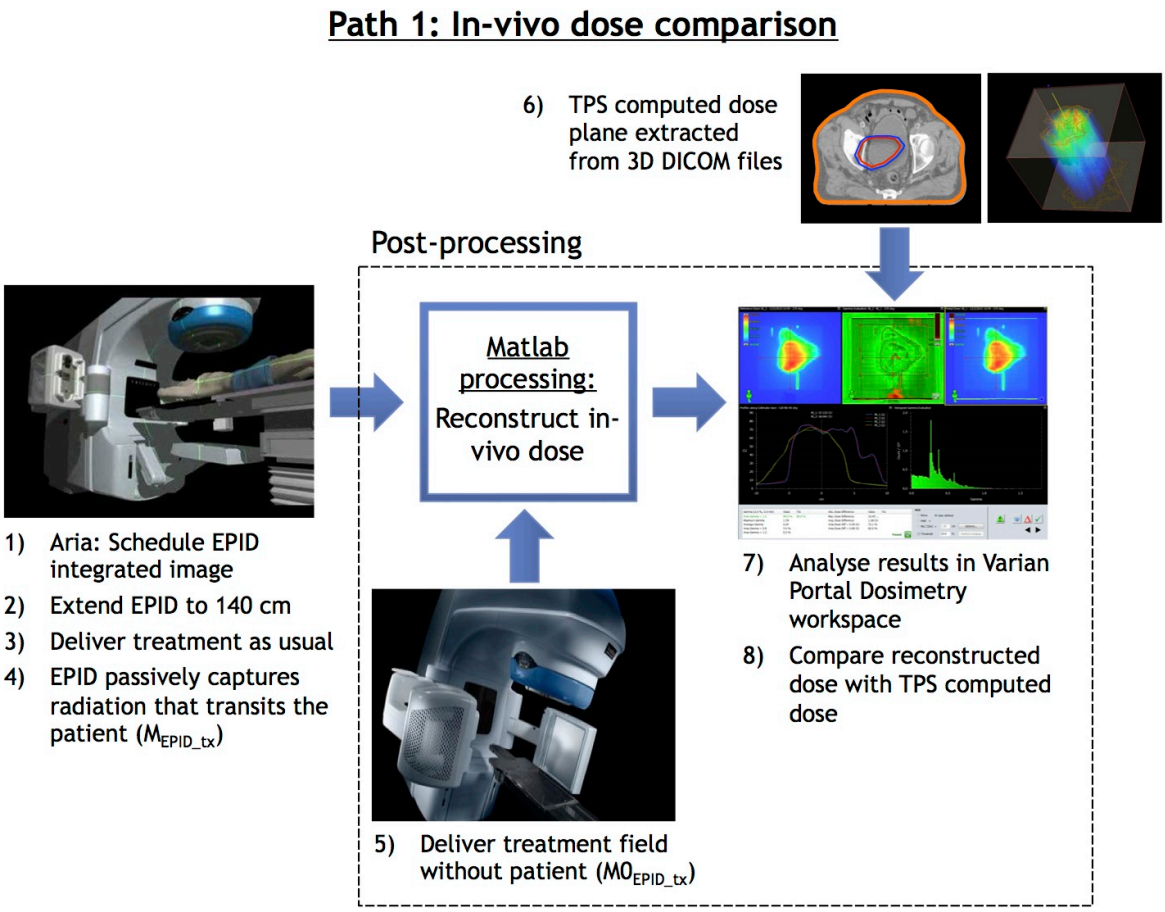

Figure 6-17 Clinical workflow for actual treatment verification with EPID (Path 1). The illustrated workflow is for Path 1 of the dual EPID transit dosimetry model, where EPID measured dose planes were used to reconstruct in-vivo dose for comparison with TPS computed dose.

Figure 6-18 illustrates the clinical workflow for Path 2, where the TPS computed dose planes were used to predict EPID transit dose for direct comparison with the EPID transit dose plane measured on the day of treatment. Prior to the treatment day, dose planes for the patient treatment plan were exported from the TPS ($M0_{TPS\_tx}$ and M_{TPS_tx}) and used to predict the EPID transit dose with an in-house Matlab code. Then, the predicted EPID transit dose was imported into the Varian Portal Dosimetry workspace. In preparation for the treatment verification, a plan was scheduled in the Aria system to capture an EPID integrated image. On the day of treatment, the EPID panel was extended to the calibration position after patient set-up. The EPID transit dose plane measured during treatment was saved automatically in the Portal Dosimetry workspace and was immediately compared to the predicted EPID transit dose plane. As opposed to Path 1, where the EPID dose plane must be exported for post-processing and causes a delay in the result, this pathway allows the immediate analysis of the accuracy of treatment. Furthermore, the prediction of EPID transit dose from TPS dose planes is only performed once for each treatment field and therefore, requires less time compared to Path 1 where the reconstruction of in-vivo dose from EPID transit dose plane, measured during treatment, must be performed for each verification session. However, evaluation in pixel value at the EPID level may be clinically less meaningful compared to in-vivo evaluation.

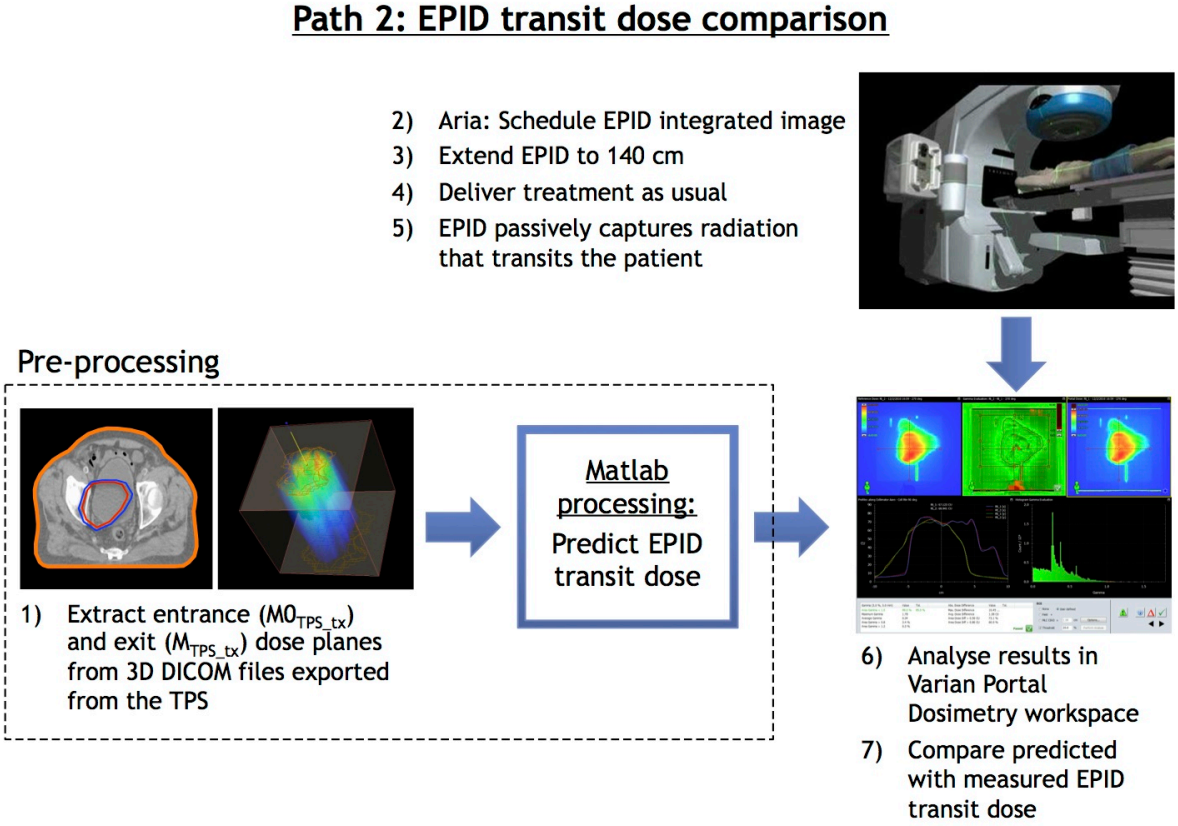

Figure 6-18 Clinical workflow for actual treatment verification with EPID (Path 2). The illustrated workflow is for Path 2 of the dual EPID transit dosimetry model, where TPS computed dose planes were used to predict EPID transit dose for direct comparison with EPID transit dose plane measured during treatment.

6.6 Conclusions

The study described in this chapter focuses on the application of a dual 2D EPID transit dosimetry model for actual treatment verification. Initial assessment with an anthropomorphic pelvic phantom using open, 3D conformal, EDW and IMRT fields resulted in a mean 4%/4mm gamma pass rate of 97.6% (range: 90.0% to 100%) for comparisons of in-phantom dose at the exit level (Path 1) and 97.1% (range: 92.9% to 99.8%) for comparisons of transit dose at the EPID level (Path 2). The original method in Path 1 was further extended to reconstruct dose at other levels besides the exit level. With the extended dose reconstruction, verification at the isocentre level resulted in a mean gamma pass rate of 98.2% (range: 91.7% to 100%).

Clinical feasibility of the EPID dosimetry model was demonstrated with three patients undergoing pelvic radiotherapy. The patients' treatments consisted of

3D conformal and wedge fields. Gamma analyses with a 5%/5mm criterion resulted in a mean pass rate of 97.0% (range: 92.4% to 99.6%) and 98.6% (range: 96.1% to 100%) for in-vivo comparisons at the exit level and isocentre level respectively (Path 1). The mean gamma pass rate for EPID transit dose comparisons (Path 2) was 95.6% (range: 90.7% to 99.9%). No IMRT fields could be evaluated on patients because the department now routinely uses VMAT instead of IMRT for clinical treatment.

In conclusion, the dual 2D EPID transit dosimetry model developed in this study has been proven to be clinically feasible for actual treatment verification. The model is a useful tool that could detect deviation in delivered dose from the intended treatment, as shown by the examples given in the discussion section for beam obstruction and changes in patient's anatomy. From a practical viewpoint, the EPID transit dosimetry model is suitable for routine clinical implementation because the extra workload incurred is minimal once the model has been properly commissioned. Therefore, with the implementation of this EPID transit dosimetry model, the accuracy of treatment delivered to patient could be checked without adding too much burden on the department.

Chapter 7: Conclusion

7.1 Summary of thesis

The broad theme of this thesis is improving safety in radiotherapy. Chapter 1 briefly outlined the risk of radiotherapy and the role of the QA program, particularly patient-specific QA, in ensuring safe and accurate delivery of treatment to patients. There are many variations to the practice of patient-specific QA. It can be performed either before treatment (pre-treatment QA) or during the actual treatment delivery to the patient (actual treatment verification). The role of pre-treatment QA is to test the deliverability of a treatment plan, while actual treatment verification confirms that the treatment has been accurately delivered to the patient. Ideally, both pre-treatment and actual treatment verifications should be performed to check different aspects of the radiotherapy process. However, this may not be always possible due to the additional cost, manpower and time required to implement these QA procedures. Thus, the challenge is to find a cost effective tool and an efficient way to carry out these patient-specific QA checks.

Among the different types of radiation measuring devices, EPID is the most favourable in terms of cost effectiveness and efficiency. EPID is cost effective because it is readily available as an attachment on most linacs and efficient because it can be set-up effortlessly using the linac controls. Moreover, the EPID produces an immediate high-resolution 2D digital image that does not require cumbersome manual processing. But the EPID, which was originally designed for imaging purposes, exhibits different scatter and dose response characteristics compared to a water-equivalent detector. In Chapter 2, a literature review on various methods to overcome the dosimetric challenges of a-Si EPID was presented. The literature review included non-transit and transit EPID dosimetry models but the focus of this thesis was on the transit model, which could be used for both pre-treatment QA as well as actual treatment verification. From the literature review, it became apparent that there were few studies on using an empirical approach for EPID transit dosimetry, especially for 2D or 3D verifications of IMRT or VMAT fields. The transit dosimetry model based on empirical methods is advantageous because it involves only general

measurements and, thus, is easier to replicate. The limited publications on empirical-based 2D EPID transit dosimetry model and the lack of reliable commercial software have made it difficult for clinical departments with scarce resources to use EPID for the verification of patients' actual treatment delivery.

The aim of this research was to develop an empirical-based 2D EPID transit dosimetry model that was practical, generic and flexible, to facilitate implementation in a wide range of radiotherapy centres with very different equipment and work practices. In Chapter 4, a novel concept was introduced that used the water-equivalent path length or EPL of the phantom/patient to relate the non-water equivalent EPID detector and the water-based TPS. The EPL was calculated using a quadratic equation (Swindell, 1983) based on the amount of beam attenuation, as quantified by the ratio of exit (M) to entrance (M0) doses. Coefficients in the quadratic equation were separately derived from EPID and TPS entrance and exit calibration dose planes for the same reference beam (6 MV, 20 x 20 cm^2, 100 MU) and homogeneous water phantom of known thicknesses (0 cm to 35 cm). With two sets of coefficients, the EPL could be calculated from either EPID or TPS M0 and M dose planes for the treatment field. The EPID M0 and M dose planes were measured without and with the phantom/patient in the beam respectively, while, the TPS M0 and M dose planes were defined as dose at 1.5 cm from the beam entrance and exit surfaces of the phantom/patient respectively. The calculated EPL, which is a property of the attenuating object and independent of the dosimeter, provided a link to the two different dosimetry systems and allowed a two-way relationship for the: (Path 1) Reconstruction of in-phantom/in-vivo exit dose from EPID measured dose planes; and (Path 2) Prediction of EPID transit dose from TPS computed dose planes. The validity of the concept was initially proven with simple square fields of various field sizes and homogeneous slab phantoms of different thicknesses. To show that the proposed method was generic, the experiment was performed on linacs and TPS from different manufacturers: Varian (Clinac/Eclipse AAA) and Elekta (Synergy/XiO Superposition).

Because the entrance and exit doses were extensively used in the EPID dosimetry model, a study was described earlier on in Chapter 3 to evaluate the accuracies of six algorithms from three TPSs (Eclipse, XiO, Monaco) in computing

doses at these levels. While the entrance doses computed by all algorithms agreed with the measured values to within 2%, discrepancies of up to 5% were observed for exit doses computed by the Eclipse PBC and Eclipse AAA algorithms. By using TPS computed entrance and exit calibration dose planes to derive the quadratic equation coefficients in the commissioning stage, inaccuracies from the TPS algorithm would become inherent in the EPID dosimetry model. In Chapter 5, the TPS calibration dose planes were replaced with dose planes derived from IC measurements in water. Although the methods were more cumbersome, they were justified because results from the EPID dosimetry could now accurately reflect discrepancies between planned and delivered doses. Apart from improvement in the commissioning process, the EPID dosimetry model was also extended to include verification of modulated wedge and IMRT fields. The updated model was tested with homogeneous and heterogeneous slab phantoms on the Varian system (Clinac/Eclipse AAA).

Due to difficulties in directly exporting M0 and M dose planes from the TPS for objects with irregular surface, the experiments so far were restricted to slab phantoms with irradiation at gantry zero degrees. Instead of relying on the 2D export function of the TPS, a method was described in Chapter 6 to extract dose planes from 3D 'structure' and 'dose' DICOM files from the TPS. The extraction process also took into account the effect of different gantry angles. This was a crucial development that enabled the application of the proposed EPID transit dosimetry model for the verification of actual treatment delivery to patients. In addition, the original method in Path 1 was extended to reconstruct dose at any other planes in-phantom/in-vivo, besides the exit plane. This was achieved by quantifying the fractional EPL, from the entrance to the plane of interest, using a new parameter, EPL ratio, derived from patients' CT simulation images and a 'CT to relative EPL' calibration curve. The ability to reconstruct dose at any chosen plane allows users to verify dose at a more clinically relevant location, such as the isocentre plane that intersects the target volume. Moreover, the ability to reconstruct dose at multiple planes in-vivo/in-phantom would make it possible for 3D dose reconstruction in the future. The expanded model was extensively tested with different fields (open, 3D conformal, wedge and IMRT fields at different gantry angles) using an anthropomorphic pelvic phantom. Finally, clinical feasibility of the 2D EPID transit dosimetry model was

demonstrated for three patients who were undergoing radiotherapy of the pelvic region.

7.2 Study limitations

The study conducted in this research has some limitations. First, the EPID panel was always positioned at the central position of the beam axis for all the experiments. Test fields were created such that the field area was always contained within the EPID active area without having to re-position the panel away from the beam centre in the lateral or longitudinal directions. Similarly, only patients with treatment fields located within the EPID active area, when the panel was at the central position, were selected for the pilot study. Since the EPID A and B coefficients were derived, pixel-by-pixel, from a set of calibration dose planes measured for a reference beam with the EPID fixed at the central position, the coefficients for each pixel may no longer be appropriate for measurement at other EPID positions. The effect of changes in EPID position on the accuracy of the dosimetry model has not yet been studied. Besides that, the mid-plane of the phantom/patient always coincided with the isocentre of the beam, which was similar to the reference set-up used in the commissioning process. Other phantom/patient position that resulted in non-reference vertical distance (air gap) between the exit surface and the EPID detector, and consequently the amount of scattered photons that reaches the EPID, was not investigated. Restriction in panel position and phantom/patient position limits the type of treatment fields that can be verified with this EPID transit dosimetry model at present.

Second, validity of the EPID transit dosimetry model has been proven only for the pelvic region, where tissue compositions are relatively homogeneous compared to, for example, the chest region. Performance of the EPID dosimetry model was not assessed in the presence of large amounts of low-density tissues such as lung. Systematic evaluation with a chest phantom is mandatory before the EPID transit dosimetry model could be used to verify the accuracy of treatment delivered to patients with cancers in the chest region. Evaluation with a chest phantom could not be performed in this research because the phantom was not available.

Lastly, the number of patients included in the clinical feasibility study is very small, with only three patients verified. Moreover, all three patients were treated with very similar treatment technique, either a three-field or four-field box technique. The small number of patients with very similar treatment techniques does not adequately represent the diverse treatment types and beam configurations encountered in the clinic. Including more patients with different treatment techniques and sites may help to reveal problems that are not obvious at this point. Also, verification of IMRT fields could only be tested on phantoms in this study because the department now routinely uses VMAT rather than IMRT for modulated treatment delivery. It would have been more interesting if the verification of highly modulated treatment fields could be reported for patient's actual treatment delivery. The current formulation of the EPID transit dosimetry model cannot reconstruct/predict VMAT treatment fields.

7.3 Suggestions for future study

VMAT is a treatment technique that continuously delivers radiation while rotating the gantry and varying the gantry speed, dose rate and MLC leaves positions to achieve highly conformal dose distributions. This complex delivery technique is becoming more popular and in some cases, replacing the IMRT technique. This trend was reflected in the results of a survey of 65 UK radiotherapy centres that showed a considerable increase in VMAT treatment from 34% to 74% in the period of 2012 to 2014 (Abolaban et al., 2015). Therefore, it would be of great interest to develop the EPID transit dosimetry model further for verification of VMAT delivery in the future. In the current model, the EPID captures one integrated image for each treatment field that is planned and delivered with a fixed gantry angle. For VMAT delivery with continuous gantry rotation, capturing one integrated image per treatment field, per gantry angle is no longer applicable. Instead, the EPID acquisition must be in cine (continuous) mode where a series of images are captured and saved as a function of time. The gantry angle for each cine image must be known to enable dose reconstruction/prediction with the EPID transit dosimetry model. Different methods to retrieve this information have been suggested for the Varian system (Woodruff et al., 2013, McCowan et al., 2014) and the Elekta system (Mans et

al., 2010a), including the correction strategies required to address the issue of time lag that caused inaccurate gantry angle information. In addition, the effect of panel sag due to gravitational force at different gantry angles is more complex for VMAT verification than for fixed-gantry IMRT verification. Panel sag and its effect on each cine image acquired at different gantry angles must be investigated (Rowshanfarzad et al., 2012) and corrected (Mans et al., 2010a) to ensure that the final cumulated verification is not compromised. Another issue that must be considered with VMAT verification is the time required to reconstruct/predict the doses. With the angle-resolved acquisition, the dose reconstruction/prediction process must be repeated for a large number of images before a complete result can be produced. Taking account of these problems, it is feasible to extend the current EPID transit dosimetry model for VMAT verification; this would require further research on image acquisition technique in continuous mode and a faster way to accomplish the dose reconstruction/prediction process.

Another interesting aspect for future development is 3D dose reconstruction. In the current EPID transit dosimetry model, Path 1 offers 2D in-vivo dose reconstruction from EPID measured dose planes. The 2D dose plane can be reconstructed in any chosen plane inside the patient that is parallel to the EPID. In theory, there is no limit to the number of 2D dose planes that can be reconstructed using this technique. So, by reconstructing multiple parallel 2D dose planes with acceptably small spacing between them, it would then result in a 3D dose reconstruction. From here, the model can be further diversified to allow composite treatment verification rather than just a field-by-field verification, which is the case for the current model. Composite dose verification can possibly be done by assigning a grid system and summing up the dose reconstructed for all treatment fields. If information on the target and OARs are available, then DVH can also be produced from the reconstructed 3D composite dose. The reconstructed DVH for each structure can be compared with TPS planned dose and decisions can be made based on the planning criteria. This provides an alternative way to evaluate the accuracy of treatment that is more clinically relevant than gamma analysis. Also, to produce a more accurate reflection of the treated dose, the 3D dose should ideally be reconstructed on cone-beam computed tomography (CBCT) images acquired on

the treatment day rather than CT simulation images. However, there are still a few issues pertaining CBCT, such as HU calibration, HU stability, effect of object scatter and image artefacts, which require further research before the images can be used for dosimetric purpose. There are several studies that investigated the feasibility of using CBCT images for treatment planning and provide useful information for future research on 3D dose verification with CBCT. For example, the study by Yoo & Yin (2006) and Yang et al. (2007) showed that the HU values from Varian KV CBCT were very similar to a conventional CT simulator in the absence of motion. The difference in dose computed on the two sets of images agreed to within 1%. This result is a promising indication that the Varian KV CBCT images may be suitable for 3D dose reconstruction. However, a much larger dose difference of approximately 15% was observed between dose calculated on the Elekta KV CBCT images versus CT simulation images (Richter et al., 2008). The author proposed the use of a site-specific CBCT calibration curve to reduce the dose difference to less than 2%. The large variability in characteristics between different models of CBCT necessitates a careful investigation before the images can be used for 3D dose verification of actual treatment delivery.

So far, the verification of actual treatment delivery refers to the checking of dose post-treatment (offline verification). This is adequate assuming that the error detected after the delivery of a single fraction can be compensated in the subsequent fractions. However, to guard against error that is too large to be compensated, a more appropriate strategy would be online treatment verification. Online verification is the real-time monitoring of dose during treatment, where results of comparisons between delivered and expected doses are constantly updated while the treatment is ongoing. With real-time verification, the most important factor is processing speed. Therefore, the methods in Path 2 of the current model, where EPID transit dose is predicted only once beforehand and saved in a database for immediate comparison with measured EPID transit dose, is possibly more suitable for further development as a real-time verification tool. An international multi-centre research project on real-time 2D EPID transit dosimetry (watchDOG), headed by researchers from the University of Newcastle, Australia, used a synchronisation method to match, and then compare, measured cine EPID images with a reference dataset of

predicted cine EPID images. The methods were described by Fuangrod et al. (2013) in a feasibility study with dynamic IMRT delivery, which showed that synchronisation based on MLC positions could correctly pair the measured and predicted cine EPID images in the database and the subsequent comparisons could detect a simulated MU dose error of 10% within 10 s and systematic MLC leaf positional error of 4 mm within 2.5 s. A brief example on the clinical application of this real-time EPID treatment verification was presented for a lung stereotactic treatment in a conference abstract, Greer et al. (2015). Reports from the watchDOG project could provide invaluable information for the future development of our model towards real-time treatment verification.

Another important subject that requires further study is the search for an appropriate indicator parameter and action level to define when a treatment should be deemed unacceptable. This subject is important for both online and offline verification strategies. In an online treatment verification system, the feedback mechanism should preferably interrupt the treatment delivery automatically when a certain parameter exceeds the specified threshold. Thus, a robust parameter and threshold would be crucial to ensure that the monitoring system is sensitive enough to catch all true positive events and at the same time specific enough to avoid false positive detection that disrupts the treatment workflow unnecessarily. As for the offline treatment verification system, determining an appropriate parameter and action level are especially important if the analysis of results were automated and users were only notified if a treatment fraction exceeds the specified threshold. The automation of offline analysis and reporting is inevitable for large-scale routine clinical implementation of EPID treatment verification to minimise its impact on workload. A threshold that is too sensitive and lacks specificity would defeat the purpose of reducing workload. On the other hand, all positive events must be detected to ensure the reliability of the system. At present, there is no clear recommendation on the best parameter and action level to use for EPID treatment verification. Studies on this subject are still in the preliminary stage with no conclusive results. For example, Rozendaal et al. (2015) suggested a method that searched for the presence of hot spots in the in-vivo verification result, but retrospective analysis of 1095 cases showed a high rate of false positive detections, which hampered its clinical implementation. Alternatively,

Fuangrod et al. (2015) proposed the use of statistical process control to derive site-specific action level for comparisons between measured and predicted EPID transit dose planes. The suggested action level for percentage pass rate with 4%/4mm criterion (determined from a pool of 10 IMRT patients per site, using three standard deviations from mean) was 67% and 50% for prostate and head and neck cases respectively. Proposals by different investigators should be further studied to determine the best indicator parameter and appropriate action level that presents the highest sensitivity and specificity.

One of the important factors to consider for broad-scale implementation of EPID transit dosimetry in different departments is the ease of commissioning. The commissioning process for the EPID transit dosimetry model proposed in this study involves measuring two sets of dose planes, separately with EPID and IC in water, to derive the A and B quadratic equation coefficients, field size correction factors and backscatter correction factors (for IC in water only). The full commissioning process could take up to approximately seven hours to complete. Future study could explore the possibility of deriving a generalised set of commissioning data for use with different EPIDs and TPSs. The idea is for different departments to use a generalised dataset and only perform a limited number of measurements to account for variation in EPID sensitivity or to confirm the agreement between general and locally measured data. Researchers from Università Cattolica del Sacro Cuore, Rome, Italy, had reported an example of such approach by deriving generalised correlation functions from measurements on three linacs for each manufacturer: Varian (Fidanzio et al., 2011a), Elekta (Cilla et al., 2011) and Siemens (Fidanzio et al., 2011b). The use of generalised correlation functions for their single point EPID transit dosimetry model eliminates the need for local IC measurements on every linac and greatly simplifies the commissioning process. A more recent report by Tielenburg et al. (2015) showed that the generalised approach was also possible for their 2D EPID transit dosimetry model, with initial investigation yielding very comparable results between doses reconstructed from a generic dataset versus a full commissioning dataset. Future study on establishing a generic dataset could reduce the amount of time required to commission the EPID transit dosimetry model and thus, makes it more attractive for implementation in different departments.

Future study should also look into the application of the EPID transit model for the flattening filter free (FFF) treatment technique, which is becoming more common in newer linac models. The FFF beam, produced without the flattening filter, can deliver radiation at a very high dose rate (typically up to 2400 MU/min) and has different beam characteristics compared to the conventional flattened-beam. This relatively new technology is most often used for high dose stereotactic body radiotherapy (SBRT) and stereotactic radiosurgery (SRS) treatments, mainly because the high dose rate of FFF beam shortens the treatment time and as a consequence, leads to improved patient comfort and better motion management. Since SBRT and SRS treatments deliver a very high dosage over a very limited number of fractions, performing actual treatment verification of these treatments in real time, in addition to pre-treatment QA, will be most beneficial. A recent report on the new aS1200 EPID (Varian, Palo Alto, CA, USA) was encouraging, with no saturation effect observed when tested with an FFF beam at the highest dose rate (Nicolini et al., 2015). The response of other versions of EPID to an FFF beam must be further investigated so that the EPID transit dosimetry model can be used to verify the accuracy of, but not limited to, SBRT and SRS treatments with FFF beams.

Finally, future development of the EPID transit dosimetry model must be accompanied by research aimed to improve the speed of the verification process. The development of VMAT verification, real-time verification and 3D dose reconstructions, mentioned in the above paragraphs, can only be practically realised if the verification speed is improved. For example, the current EPID transit dosimetry model takes about 5 min to reconstruct/predict one 2D dose plane for an IMRT field on a personal computer with Intel Core i5, 2.3 GHz CPU and 8 GB RAM. At this speed, the reconstruction/prediction of a single arc VMAT treatment, with 36 cine images saved at every 10° of gantry rotation, would take approximately 180 min to complete. The use of a graphic processing unit (GPU) to improve computational speed (Zhu et al., 2015) may offer a possible solution to this problem and should be further explored.

7.4 Final conclusion

> "It is now possible to use EPIDs to measure the dose absorbed by the patient (transit dosimetry). This technology is still being developed and is not routinely available. … Research into these technologies should be encouraged and supported." (The Royal College of Radiologists et al., 2008)

It is clear that EPID transit dosimetry has many advantages and potentials. In this research, a 2D EPID transit dosimetry model based on empirical methods has been successfully developed and proven to be valid for application with different treatment fields including IMRT. In addition to pre-treatment verification with phantoms, the developed model was also shown to be suitable for actual treatment verification of patients.

To allow broad-scale implementation, the model used methods that are generic and practical, involving only general measurements and does not require modification to the EPID panel or measurements under non-clinical settings. The model has a unique feature, which allows users to choose either to verify dose in-vivo (Path 1) or at the EPID level (Path 2). While verification in-vivo is more clinically relevant, verification at the EPID level is more efficient as the prediction process is only performed once and therapists can evaluate the accuracy of delivery immediately after treatment. The choice of two pathways makes it easier for different departments to integrate the EPID transit dosimetry program into their existing clinical workflow depending on the local preference and clinical needs. Furthermore, the versatility provides greater capacity for future development of the current model into a more comprehensive verification system for safer radiotherapy.

Appendix A: Beam divergence correction

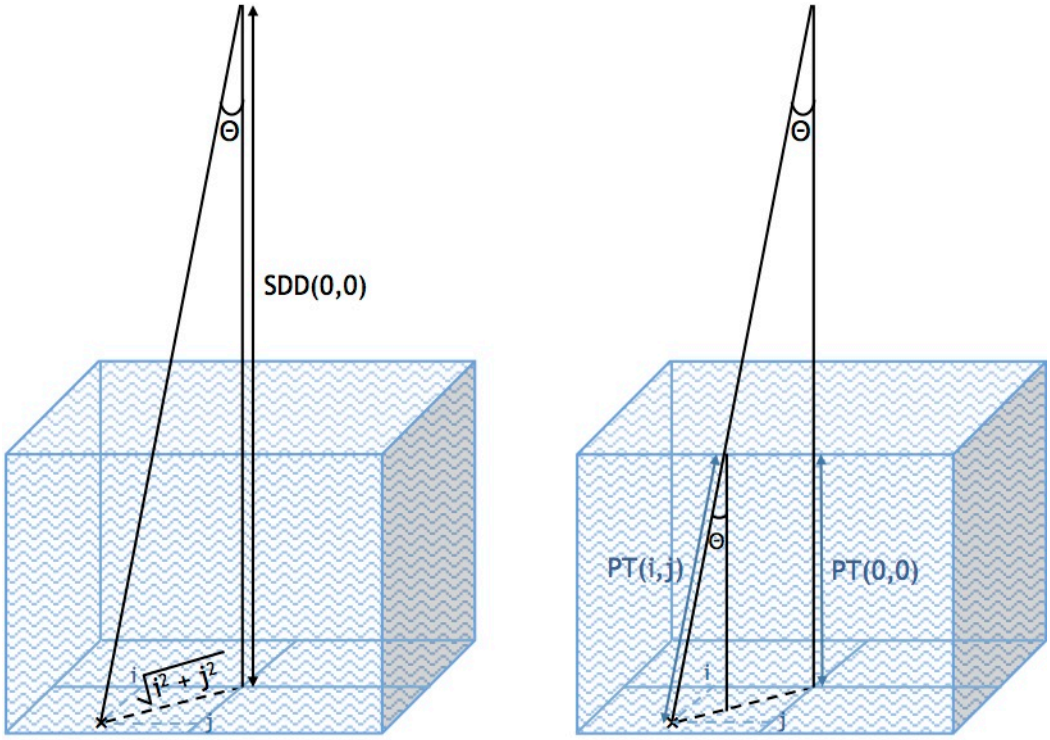

Figure A-1 Accounting for the effect of beam divergence in phantom thickness.

Where:

PT(0,0) = phantom thickness at the central axis,

PT(i,j) = phantom thickness corrected for beam divergence at point (i,j),

SDD(0,0) = source to detector (or exit plane) distance at the central axis,

Θ = angle between the central axis ray and the divergent ray.

From Figure A-1 (left), the angle between the central axis ray and divergent ray can be calculated according to Equation A-1:

$$\theta = \tan^{-1}\left[\frac{\sqrt{i^2+j^2}}{SDD(0,0)}\right] \qquad \text{(A-1)}$$

With the angle Θ known, phantom thickness corrected for beam divergence at point (i,j) can be calculated with Equation A-2, as illustrated in Figure A-1 (right):

$$PT(i,j) = \frac{PT(0,0)}{\cos\theta} \qquad \text{(A-2)}$$

Appendix B: Numerical iteration

The quadratic equation is given in Equation B-1:

$$AT + BT^2 + \ln\left(\frac{M}{M0}\right) = 0 \qquad \text{(B-1)}$$

Where:

A = coefficient of the linear term,

B = coefficient of the quadratic term,

T = thickness of attenuator (or EPL),

M = exit dose,

M0 = entrance dose.

(Note: the Cartesian coordinates (i,j) have been removed for clarity)

Equation B-1 can be re-written according to the steps below to arrive at the final Equation B-5, used for the iterative calculation:

$$AT + BT^2 = -\ln\left(\frac{M}{M0}\right) \qquad \text{(B-2)}$$

$$AT + 2BT^2 = BT^2 - \ln\left(\frac{M}{M0}\right) \qquad \text{(B-3)}$$

$$T\,(A + 2BT) = BT^2 - \ln\left(\frac{M}{M0}\right) \qquad \text{(B-4)}$$

$$T = \frac{BT^2 - \ln\left(\frac{M}{M0}\right)}{A + 2BT} \qquad \text{(B-5)}$$

Appendix C: Statistical analysis

(Software: IBM SPSS Statistics, version 22.0, Armonk, NY, USA)

C.1 Normality tests of differences

H_0: Differences between Verify 1 and Verify 2 are normally distributed
H_1: Differences between Verify 1 and Verify 2 are not normally distributed

Shapiro-Wilk (Difference Verify 1 – Verify 2)		Test statistic	df	Significance (*p*-value)	Decision (α = 0.05, 2-tailed)	
Pair 1	Path 1: In-vivo dose comparisons at the exit level	0.974	7	0.926	*p*-value > 0.05	Accept H_0
Pair 2	Path 1: In-vivo dose comparisons at the isocentre level	0.949	7	0.718	*p*-value > 0.05	Accept H_0
Pair 3	Path 2: EPID transit dose comparisons	0.932	7	0.570	*p*-value > 0.05	Accept H_0

[a] Verify 1 and Verify 2 are verification results (percentage gamma pass rates) for two different treatment days.

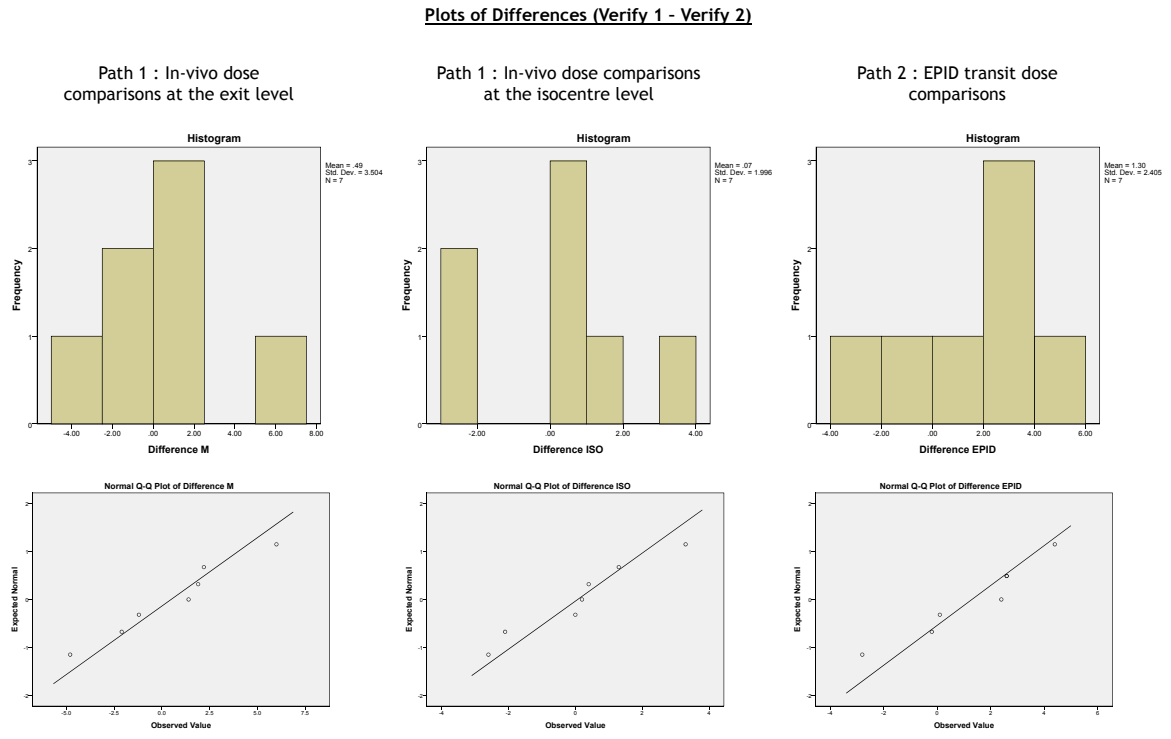

Figure C-1 Histograms and Q-Q plots of differences.

Interpretation of statistical results:

The differences between Verify 1 and Verify 2 are normally distributed for all comparisons (*p*-value > 0.05). However, the statistical analyses may be affected by the small sample size (n = 7).

C.2 Paired t-test

Justification for using paired t-test:

1. The variables are continuous (from 0 to 100).
2. The independent variable consists of two related groups, with the same subjects present in both groups.
3. There is no obvious outlier in the differences between the two related groups.
4. Differences between the two related groups are approximately normally distributed.

H_0: There is no difference in the mean gamma pass rates for verification performed on two different days, "Verify 1" versus "Verify 2"
H_1: There is a difference in the mean gamma pass rates for verification performed on two different days, "Verify 1" versus "Verify 2"

Paired T-test (Difference Verify 1 – Verify 2)		Mean difference	Standard deviation	95% Confidence Interval of the difference		Test statistics	df	Significance (*p*-value)	Decision (α = 0.05, 2-tailed)	
				Lower	Upper					
Pair 1	Path 1: In-vivo dose comparisons at the exit level	0.4857	3.5035	-2.7545	3.7259	0.367	6	0.726	*p*-value > 0.05	Accept H_0
Pair 2	Path 1: In-vivo dose comparisons at the isocentre level	0.0714	1.9964	-1.7750	1.9178	0.095	6	0.928	*p*-value > 0.05	Accept H_0
Pair 3	Path 2: EPID transit dose comparisons	1.3000	2.4049	-0.9241	3.5241	1.430	6	0.203	*p*-value > 0.05	Accept H_0

Interpretation of statistical results:

The verification results for two treatment days are not significantly different for all comparisons (*p*-value > 0.05). However, the statistical analyses may be limited to only detecting large differences because of the small sample size (n = 7).

References

Abolaban, F., Zaman, S., Cashmore, J., Nisbet, A. & Clark, C. 2015. How has IMRT verification practice in the UK changed over the last two years? *Radiotherapy and Oncology,* 115 (Supplement 1), S433-S434, http://www.sciencedirect.com/science/article/pii/S0167814015408461 [Accessed 14 May 2015].

Alecu, R., Feldmeier, J. J. & Alecu, M. 1997. Dose perturbations due to in vivo dosimetry with diodes. *Radiotherapy and Oncology,* 42 (3), 289-291.

Alhakeem, E., Alshaikh, S., Rosenfeld, A. B. & Zavgorodni, S. 2012. Experimental and Monte Carlo verification of Acuros XB calculations near low and high density heterogeneities. *Medical Physics,* 39 (7), 4619, http://scitation.aip.org/content/aapm/journal/medphys/39/7/10.1118/1.4740086 [Accessed 27 June 2013].

Ansbacher, W. 2006. Three-dimensional portal image-based dose reconstruction in a virtual phantom for rapid evaluation of IMRT plans. *Medical Physics,* 33 (9), 3369-3382.

Antonuk, L. E., El-Mohri, Y., Huang, W., Jee, K. W., Siewerdsen, J. H., Maolinbay, M., Scarpine, V. E., Sandler, H. & Yorkston, J. 1998. Initial performance evaluation of an indirect-detection, active matrix flat-panel imager (AMFPI) prototype for megavoltage imaging. *International Journal of Radiation Oncology Biology Physics,* 42 (2), 437-454.

Antonuk, L. E., Yorkston, J., Huang, W. D., Siewerdsen, J. H., Boudry, J. M., Elmohri, Y. & Marx, M. V. 1995. A real-time, flat-panel, amorphous-silicon, digital X-ray imager. *Radiographics,* 15 (4), 993-1000.

Arjomandy, B., Tailor, R., Anand, A., Sahoo, N., Gillin, M., Prado, K. & Vicic, M. 2010. Energy dependence and dose response of Gafchromic EBT2 film over a wide range of photon, electron, and proton beam energies. *Medical Physics,* 37 (5), 1942-1947.

Baek, T. S., Chung, E. J., Son, J. & Yoon, M. 2014. Feasibility study on the verification of actual beam delivery in a treatment room using EPID transit dosimetry. *Radiation Oncology,* 9 (273), 1-8.

Berry, S. L., Polvorosa, C. S. & Wuu, C. S. 2010. A field size specific backscatter correction algorithm for accurate EPID dosimetry. *Medical Physics,* 37 (6), 2425-2434.

Berry, S. L., Sheu, R. D., Polvorosa, C. S. & Wuu, C. S. 2012. Implementation of EPID transit dosimetry based on a through-air dosimetry algorithm. *Medical Physics,* 39 (1), 87-98.

Boellaard, R., Van Herk, M. & Mijnheer, B. J. 1996. The dose response relationship of a liquid-filled electronic portal imaging device. *Medical Physics,* 23 (9), 1601-1611.

Borca, V. C., Pasquino, M., Russo, G., Grosso, P., Cante, D., Sciacero, P., Girelli, G., La Porta, M. R. & Tofani, S. 2013. Dosimetric characterization and use of GAFCHROMIC EBT3 film for IMRT dose verification. *Journal of Applied Clinical Medical Physics,* 14 (2), 158-171.

Boyer, A. L., Antonuk, L., Fenster, A., Van Herk, M., Meertens, H., Munro, P., Reinstein, L. E. & Wong, J. 1992. A review of electronic portal imaging devices (EPIDs). *Medical Physics,* 19 (1), 1-16.

Buchauer, K., Hillbrand, E. & De Vries, A. 2009. Gafchromic® EBT photospectral dose response dependence on temperature and implications for flat bed scanning. *Medical Physics,* 36 (11), 5044-5051.

Bush, K., Gagne, I. M., Zavgorodni, S., Ansbacher, W. & Beckham, W. 2011. Dosimetric validation of Acuros (R) XB with Monte Carlo methods for photon dose calculations. *Medical Physics,* 38 (4), 2208-2221.

Butson, M. J., Cheung, T. & Yu, P. K. N. 2006. Scanning orientation effects on Gafchromic EBT film dosimetry. *Australasian Physical and Engineering Sciences in Medicine,* 29 (3), 281-284.

Butson, M. J., Cheung, T. & Yu, P. K. N. 2009. Evaluation of the magnitude of EBT Gafchromic film polarization effects. *Australasian Physical and Engineering Sciences in Medicine,* 32 (1), 21-25.

Camilleri, J., Mazurier, J., Franck, D., Dudouet, P., Latorzeff, I. & Franceries, X. 2014. Clinical results of an EPID-based in-vivo dosimetry method for pelvic cancers treated by intensity-modulated radiation therapy. *Physica Medica,* 30 (6), 690-695.

Capote, R., Sánchez-Doblado, F., Leal, A., Lagares, J. I., Arráns, R. & Hartmann, G. H. 2004. An EGSnrc Monte Carlo study of the microionization chamber for reference dosimetry of narrow irregular IMRT beamlets. *Medical Physics,* 31 (9), 2416-2422.

Carrasco, P., Jornet, N., Latorre, A., Eudaldo, T., Ruiz, A. & Ribas, M. 2012. 3D DVH-based metric analysis versus per-beam planar analysis in IMRT pretreatment verification. *Medical Physics,* 39 (8), 5040-5049.

Chang, J., Mageras, G. S., Chui, C. S., Ling, C. C. & Lutz, W. 2000. Relative profile and dose verification of intensity-modulated radiation therapy. *International Journal of Radiation Oncology Biology Physics,* 47 (1), 231-240.

Chang, J. W., Mageras, G. S. & Ling, C. C. 2003. Evaluation of rapid dose map acquisition of a scanning liquid-filled ionization chamber electronic portal imaging device. *International Journal of Radiation Oncology Biology Physics,* 55 (5), 1432-1445.

Chen, J., Chuang, C. F., Morin, O., Aubin, M. & Pouliot, J. 2006. Calibration of an amorphous-silicon flat panel portal imager for exit-beam dosimetry. *Medical Physics,* 33 (3), 584-594.

Cheung, T., Butson, M. J. & Yu, P. K. N. 2004. Effects of temperature variation on MOSFET dosimetry. *Physics in Medicine and Biology,* 49 (13), N191-N196.

Childress, N., Chen, Q. & Rong, Y. 2015. Parallel/Opposed: IMRT QA using treatment log files is superior to conventional measurement-based method. *Journal of Applied Clinical Medical Physics,* 16 (1), 4-7.

Childress, N. L., Dong, L. & Rosen, I. I. 2002. Rapid radiographic film calibration for IMRT verification using automated MLC fields. *Medical Physics,* 29 (10), 2384-2390.

Chytyk, K. & Mccurdy, B. M. C. 2009. Comprehensive fluence model for absolute portal dose image prediction. *Medical Physics,* 36 (4), 1389-1398.

Cilla, S., Fidanzio, A., Greco, F., Sabatino, D., Russo, A., Gargiulo, L., Azario, L. & Piermattei, A. 2011. Correlation functions for Elekta aSi EPIDs used as transit dosimeter for open fields. *Journal of Applied Clinical Medical Physics,* 12 (1), 218-233.

Coleman, L. & Skourou, C. 2013. Sensitivity of volumetric modulated arc therapy patient specific QA results to multileaf collimator errors and correlation to dose volume histogram based metrics. *Medical Physics,* 40 (11), 1117151-1117157.

Constantinou, C., Harrington, J. C. & Dewerd, L. A. 1992. An electron density calibration phantom for CT – based treatment planning computers. *Medical Physics,* 19 (2), 325-327.

Curtin-Savard, A. J. & Podgorsak, E. B. 1999. Verification of segmented beam delivery using a commercial electronic portal imaging device. *Medical Physics,* 26 (5), 737-742.

Danciu, C., Proimos, B. S., Rosenwald, J. C. & Mijnheer, B. J. 2001. Variation of sensitometric curves of radiographic films in high energy photon beams. *Medical Physics,* 28 (6), 966-974.

De Boer, J. C. J., Heijmen, B. J. M., Pasma, K. L. & Visser, A. G. 2000. Characterization of a high-elbow, fluoroscopic electronic portal imaging device for portal dosimetry. *Physics in Medicine and Biology,* 45 (1), 197-216.

Derreumaux, S., Etard, C., Huet, C., Trompier, F., Clairand, I., Bottollier-Depois, J. F., Aubert, B. & Gourmelon, P. 2008. Lessons from recent accidents in radiation therapy in France. *Radiation Protection Dosimetry,* 131 (1), 130-135.

Devic, S., Seuntjens, J., Sham, E., Podgorsak, E. B., Schmidtlein, C. R., Kirov, A. S. & Soares, C. G. 2005. Precise radiochromic film dosimetry using a flat-bed document scanner. *Medical Physics,* 32 (7), 2245-2253.

Dirkx, M. L. P. 1995. Daily dosimetric quality control of the MM50 Racetrack Microtron using an electronic portal imaging device. *Radiotherapy and Oncology,* 37 (1), 55-60.

Edwards, C. R., Green, S., Palethorpe, J. E. & Mountford, P. J. 1997. The response of a MOSFET, p-type semiconductor and LiF TLD to quasi-monoenergetic x-rays. *Physics in Medicine and Biology,* 42 (12), 2383-2391.

Essers, M., Hoogervorst, B. R., Vanherk, M., Lanson, H. & Mijnheer, B. J. 1995. Dosimetric characteristics of a liquid-filled electronic portal imaging device. *International Journal of Radiation Oncology Biology Physics,* 33 (5), 1265-1272.

Essers, M. & Mijnheer, B. J. 1999. In vivo dosimetry during external photon beam radiotherapy. *International Journal of Radiation Oncology Biology Physics,* 43 (2), 245-259.

Evans, P. M., Donovan, E. M., Partridge, M., Bidmead, A. M., Garton, A. & Mubata, C. 1999. Radiological thickness measurement using a liquid ionization chamber electronic portal imaging device. *Physics in Medicine and Biology,* 44 (6), N89-N97.

Evans, P. M., Hansen, V. N., Mayles, W. P. M., Swindell, W., Torr, M. & Yarnold, J. R. 1995. Design of compensators for breast radiotherapy using electronic portal imaging. *Radiotherapy and Oncology,* 37 (1), 43-54.

Ezzell, G. A., Galvin, J. M., Low, D., Palta, J. R., Rosen, I., Sharpe, M. B., Xia, P., Xiao, Y., Xing, L. & Yu, C. X. 2003. Guidance document on delivery, treatment planning, and clinical implementation of IMRT: Report of the IMRT subcommittee of the AAPM radiation therapy committee. *Medical Physics,* 30 (8), 2089-2115.

Fidanzio, A., Azario, L., Greco, F., Cilla, S. & Piermattei, A. 2015. Routine EPID in-vivo dosimetry in a reference point for conformal radiotherapy treatments. *Physics in Medicine and Biology,* 60 (8), N141-N150.

Fidanzio, A., Cilla, S., Greco, F., Gargiulo, L., Azario, L., Sabatino, D. & Piermattei, A. 2011a. Generalized EPID calibration for in vivo transit dosimetry. *Physica Medica,* 27 (1), 30-38.

Fidanzio, A., Greco, F., Gargiulo, L., Cilla, S., Sabatino, D., Cappiello, M., Di Felice, C., Di Castro, E., Azario, L., Russo, M., Pompei, L., D'onofrio, G. & Piermattei, A. 2011b. A generalized calibration procedure for in vivo transit dosimetry using siemens electronic portal imaging devices. *Medical and Biological Engineering and Computing,* 49 (3), 373-383.

Fidanzio, A., Porcelli, A., Azario, L., Greco, F., Cilla, S., Grusio, M., Balducci, M., Valentini, V. & Piermattei, A. 2014. Quasi real time in vivo dosimetry for VMAT. *Medical Physics,* 41 (6), 0621031-0621039.

Fielding, A. L., Evans, P. M. & Clark, C. H. 2002. The use of electronic portal imaging to verify patient position during intensity-modulated radiotherapy delivered by the dynamic MLC technique. *International Journal of Radiation Oncology Biology Physics,* 54 (4), 1225-1234.

Fogliata, A., Nicolini, G., Clivio, A., Vanetti, E. & Cozzi, L. 2011. Dosimetric evaluation of Acuros XB advanced dose calculation algorithm in heterogeneous media. *Radiation Oncology,* 6 (82), 1-15.

Fogliata, A., Nicolini, G., Clivio, A., Vanetti, E. & Cozzi, L. 2012. Critical appraisal of Acuros XB and anisotropic analytic algorithm dose calculation in advanced non-small-cell lung cancer treatments. *International Journal of Radiation Oncology Biology Physics,* 83 (5), 1587-1595.

Fogliata, A., Vanetti, E., Albers, D., Brink, C., Clivio, A., Knoos, T., Nicolini, G. & Cozzi, L. 2007. On the dosimetric behaviour of photon dose calculation algorithms in the presence of simple geometric heterogeneities: Comparison with Monte Carlo calculations. *Physics in Medicine and Biology,* 52 (5), 1363-1385.

Ford, E. C., Gaudette, R., Myers, L., Vanderver, B., Engineer, L., Zellars, R., Song, D. Y., Wong, J. & Deweese, T. L. 2009. Evaluation of safety in a radiation oncology setting using failure mode and effects analysis. *International Journal of Radiation Oncology Biology Physics,* 74 (3), 852-858.

Ford, E. C., Terezakis, S., Souranis, A., Harris, K., Gay, H. & Mutic, S. 2012. Quality Control Quantification (QCQ): A tool to measure the value of quality control checks in radiation oncology. *International Journal of Radiation Oncology Biology Physics,* 84 (3), e263-e269.

Francois, P., Boissard, P., Berger, L. & Mazal, A. 2011. In vivo dose verification from back projection of a transit dose measurement on the central axis of photon beams. *Physica Medica,* 27 (1), 1-10.

Franken, E. M., De Boer, J. C. J., Barnhoorn, J. C. & Heijmen, B. J. M. 2004. Characteristics relevant to portal dosimetry of a cooled CCD camera-based EPID. *Medical Physics,* 31 (9), 2549-2551.

Franken, E. M., De Boer, J. C. J. & Heijmen, B. J. M. 2006. A novel approach to accurate portal dosimetry using CCD-camera based EPIDs. *Medical Physics,* 33 (4), 888-903.

Fuangrod, T., Woodruff, H., Greer, P. B. & Middleton, R. 2015. Development of action levels for patient error detection for an EPID based real-time delivery verification system. *Radiotherapy and Oncology,* 115 (Supplement 1), S270, http://www.sciencedirect.com/science/article/pii/S016781401540550X [Accessed 14 May 2015].

Fuangrod, T., Woodruff, H. C., Van Uytven, E., Mccurdy, B. M. C., Kuncic, Z., O'connor, D. J. & Greer, P. B. 2013. A system for EPID-based real-time

treatment delivery verification during dynamic IMRT treatment. *Medical Physics,* 40 (9), 0919071-09190711.

Garavaglia, G., Johansson, K. A., Leunens, G. & Mijnheer, B. 1993. The role of in vivo dosimetry. *Radiotherapy and Oncology,* 29 (2), 281-282.

Gimeno, J., Pujades, M. C., García, T., Carmona, V., Lliso, F., Palomo, R., Candela-Juan, C., Richart, J. & Perez-Calatayud, J. 2014. Commissioning and initial experience with a commercial software for in vivo volumetric dosimetry. *Physica Medica,* 30 (8), 954-959.

Greco, F., Piermattei, A., Azario, L., Placidi, L., Cilla, S., Caivano, R., Fusco, V. & Fidanzio, A. 2013. aSi-EPID transit signal calibration for dynamic beams: a needful step for the IMRT in vivo dosimetry. *Medical and Biological Engineering and Computing,* 51 (10), 1137-1145.

Greer, P. B. 2005. Correction of pixel sensitivity variation and off-axis response for amorphous silicon EPID dosimetry. *Medical Physics,* 32 (12), 3558-3568.

Greer, P. B., Cadman, P., Lee, C. & Bzdusek, K. 2009. An energy fluence-convolution model for amorphous silicon EPID dose prediction. *Medical Physics,* 36 (2), 547-555.

Greer, P. B. & Popescu, C. C. 2003. Dosimetric properties of an amorphous silicon electronic portal imaging device for verification of dynamic intensity modulated radiation therapy. *Medical Physics,* 30 (7), 1618-1627.

Greer, P. B., Woodruff, H. & Simpson, J. 2015. Real-time EPID based delivery verification during lung stereotactic body radiotherapy: Initial experience. *Radiotherapy and Oncology,* 115 (Supplement 1), S65-S66, http://www.sciencedirect.com/science/article/pii/S0167814015401367 [Accessed 14 May 2015].

Grein, E. E., Lee, R. & Luchka, K. 2002. An investigation of a new amorphous silicon electronic portal imaging device for transit dosimetry. *Medical Physics,* 29 (10), 2262-2268.

Han, T., Mikell, J. K., Salehpour, M. & Mourtada, F. 2011. Dosimetric comparison of Acuros XB deterministic radiation transport method with Monte Carlo and model-based convolution methods in heterogeneous media. *Medical Physics,* 38 (5), 2651-2664.

Han, T., Mourtada, F., Kisling, K., Mikell, J., Followill, D. & Howell, R. 2012. Experimental validation of deterministic Acuros XB algorithm for IMRT and VMAT dose calculations with the Radiological Physics Center's head and neck phantom. *Medical Physics,* 39 (4), 2193-2202.

Hartmann, B., Martišíková, M. & Jäkel, O. 2010. Technical note: Homogeneity of gafchromic® EBT2 film. *Medical Physics,* 37 (4), 1753-1756.

Heijmen, B. J., Pasma, K. L., Kroonwijk, M., Althof, V. G., De Boer, J. C., Visser, A. G. & Huizenga, H. 1995. Portal dose measurement in radiotherapy using an electronic portal imaging device (EPID). *Physics in Medicine and Biology,* 40 (11), 1943-1955.

Herman, M. G., Balter, J. M., Jaffray, D. A., Mcgee, K. P., Munro, P., Shalev, S., Van Herk, M. & Wong, J. W. 2001. Clinical use of electronic portal imaging: Report of AAPM radiation therapy committee Task Group 58. *Medical Physics,* 28 (5), 712-737.

Hu, Y. & Zhu, T. C. 2011. Backscatter correction factor for megavoltage photon beam. *Medical Physics,* 38 (10), 5563-5568.

IAEA Human Health Reports No. 8 2013. Development of procedures for in vivo dosimetry in radiotherapy. Vienna, Austria: International Atomic Energy Agency, IAEA.

IAEA Technical Reports Series No. 398 2000. Absorbed dose determination in external beam radiotherapy. An international code of practice for dosimetry based on standards of absorbed dose to water. Vienna, Austria: International Atomic Energy Agency, IAEA.

Ibbott, G. S., Followill, D. S., Molineu, H. A., Lowenstein, J. R., Alvarez, P. E. & Roll, J. E. 2008. Challenges in credentialing institutions and participants in advanced technology multi-institutional clinical trials. *International Journal of Radiation Oncology Biology Physics,* 71 (Supplement 1), S71-S75.

Ibbott, G. S., Molineu, A. & Followill, D. S. 2006. Independent evaluations of IMRT through the use of an anthropomorphic phantom. *Technology in Cancer Research and Treatment,* 5 (5), 481-487.

ICRP Publication 112 2010. Preventing accidental exposures from new external beam radiation therapy technologies. International Commission on Radiological Protection, ICRP.

ICRU Report No. 24 1976. Determination of absorbed dose in a patient irradiated by beams of X and gamma rays in radiotherapy procedures. *ICRU Report No 24.* Washington: International Commission on Radiation Units and Measurements, ICRU.

Jarry, G. & Verhaegen, F. 2007. Patient-specific dosimetry of conventional and intensity modulated radiation therapy using a novel full Monte Carlo phase space reconstruction method from electronic portal images. *Physics in Medicine and Biology,* 52 (8), 2277-2299.

Johns, H. E., Bruce, W. R. & Reid, W. B. 1958. The dependence of depth dose on focal skin distance. *British Journal of Radiology,* 31 (365), 254-260.

Jornet, N., Carrasco, P., Jurado, D., Ruiz, A., Eudaldo, T. & Ribas, M. 2004. Comparison study of MOSFET detectors and diodes for entrance in vivo dosimetry in 18 MV x-ray beams. *Medical Physics,* 31 (9), 2534-2542.

Jursinic, P. A. 2010. Changes in optically stimulated luminescent dosimeter (OSLD) dosimetric characteristics with accumulated dose. *Medical Physics,* 37 (1), 132-140.

Kairn, T., Cassidy, D., Sandford, P. M. & Fielding, A. L. 2008. Radiotherapy treatment verification using radiological thickness measured with an amorphous silicon electronic portal imaging device: Monte Carlo simulation and experiment. *Physics in Medicine and Biology,* 53 (14), 3903-3919.

Kairn, T., Warne, D., Kenny, J. & Dwyer, M. 2011. Accurately simulating the production of radiotherapy portal images using non-zero beam angles. *Radiation Measurements,* 46 (12), 1967-1970.

Kappas, K. & Rosenwald, J. C. 1991. Analytic representation of the backscatter correction factor at the exit of high energy photon beams. *Radiotherapy and Oncology,* 21 (2), 128-134.

Kavuma, A., Glegg, M., Currie, G. & Elliott, A. 2008. Assessment of dosimetrical performance in 11 Varian a-Si-500 electronic portal imaging devices. *Physics in Medicine and Biology,* 53 (23), 6893-6909.

Kavuma, A., Glegg, M., Metwaly, M., Currie, G. & Elliott, A. 2010. A novel method for patient exit and entrance dose prediction based on water equivalent path length measured with an amorphous silicon electronic portal imaging device. *Physics in Medicine and Biology,* 55 (2), 435-452.

Kavuma, A., Glegg, M., Metwaly, M., Currie, G. & Elliott, A. 2011. Calculation of exit dose for conformal and dynamically-wedged fields, based on water-equivalent path length measured with an amorphous silicon electronic portal imaging device. *Journal of Applied Clinical Medical Physics,* 12 (3), 44-60.

Kerns, J. R., Kry, S. F., Sahoo, N., Followill, D. S. & Ibbott, G. S. 2011. Angular dependence of the nanoDot OSL dosimeter. *Medical Physics,* 38 (7), 3955-3962.

Khan, F. M. 2010a. Chapter 9: Dose distribution and scatter analysis, In: Khan, F. M. (ed.) *The Physics of Radiation Therapy,* 4th edition. Philadelphia, USA, Lippincott Williams and Wilkins.

Khan, F. M. 2010b. Chapter 5: Interactions of ionizing radiation, In: Khan, F. M. (ed.) *The Physics of Radiation Therapy,* 4th edition. Philadelphia, USA, Lippincott Williams and Wilkins.

Khan, F. M. 2010c. Chapter 8: Measurement of absorbed dose, In: Khan, F. M. (ed.) *The Physics of Radiation Therapy,* 4th edition. Philadelphia, USA, Lippincott Williams and Wilkins.

Khan, R. F. H., Ostapiak, O. Z. & Szabo, J. J. 2008. An empirical model of electronic portal imager response implemented within a commercial treatment planning system for verification of intensity-modulated radiation therapy fields. *Journal of Applied Clinical Medical Physics,* 9 (4), 135-150.

Kirkby, C. & Sloboda, R. 2005. Consequences of the spectral response of an a-Si EPID and implications for dosimetric calibration. *Medical Physics,* 32 (8), 2649-2658.

Knoos, T., Wieslander, E., Cozzi, L., Brink, C., Fogliata, A., Albers, D., Nystrom, H. & Lassen, S. 2006. Comparison of dose calculation algorithms for treatment planning in external photon beam therapy for clinical situations. *Physics in Medicine and Biology,* 51 (22), 5785-5807.

Ko, L., Kim, J. O. & Siebers, J. V. 2004. Investigation of the optimal backscatter for an aSi electronic portal imaging device. *Physics in Medicine and Biology,* 49 (9), 1723-1738.

Kry, S. F., Molineu, A., Kerns, J. R., Faught, A. M., Huang, J. Y., Pulliam, K. B., Tonigan, J., Alvarez, P., Stingo, F. & Followill, D. S. 2014. Institutional patient-specific IMRT QA does not predict unacceptable plan delivery.

International Journal of Radiation Oncology Biology Physics, 90 (5), 1195-1201.

Kutcher, G. J., Coia, L., Gillin, M., Hanson, W. F., Leibel, S., Morton, R. J., Palta, J. R., Purdy, J. A., Reinstein, L. E., Svensson, G. K., Weller, M. & Wingfield, L. 1994. Comprehensive QA for radiation oncology: Report of AAPM radiation therapy committee Task Group 40. *Medical Physics,* 21 (4), 581-618.

Lambert, G. D., Liversage, W. E., Hirst, A. M. & Doughty, D. 1983. Exit dose studies in megavoltage photon therapy. *British Journal of Radiology,* 56 (665), 329-334.

Lanson, J. H., Essers, M., Meijer, G. J., Minken, A. W. H., Uiterwaal, G. J. & Mijnheer, B. J. 1999. In vivo dosimetry during conformal radiotherapy. Requirements for and findings of a routine procedure. *Radiotherapy and Oncology,* 52 (1), 51-59.

Laub, W. U. & Wong, T. 2003. The volume effect of detectors in the dosimetry of small fields used in IMRT. *Medical Physics,* 30 (3), 341-347.

Lee, C., Menk, F., Cadman, P. & Greer, P. B. 2009. A simple approach to using an amorphous silicon EPID to verify IMRT planar dose maps. *Medical Physics,* 36 (3), 984-992.

Li, H., Lee, A. K., Johnson, J. L., Zhu, R. X. & Kudchadker, R. J. 2011. Characterization of dose impact on IMRT and VMAT from couch attenuation for two Varian couches. *Journal of Applied Clinical Medical Physics,* 12 (3), 23-31.

Lin, H., Huang, S., Deng, X., Zhu, J. & Chen, L. 2014. Comparison of 3D anatomical dose verification and 2D phantom dose verification of IMRT/VMAT treatments for nasopharyngeal carcinoma. *Radiation Oncology,* 9 (71), 1-7.

Lin, M.-H., Chao, T.-C., Lee, C.-C., Tung, C.-J., Yeh, C.-Y. & Hong, J.-H. 2009. Measurement-based Monte Carlo dose calculation system for IMRT pretreatment and on-line transit dose verifications. *Medical Physics,* 36 (4), 1167-1175.

Loncol, T., Greffe, J. L., Vynckier, S. & Scalliet, P. 1996. Entrance and exit dose measurements with semiconductors and thermoluminescent

dosemeters: A comparison of methods and in vivo results. *Radiotherapy and Oncology,* 41 (2), 179-187.

Lonsdale, A. P. M. 2012. Multistage evaluation and commissioning of a pre-calibrated, single-use OneDosePlus MOSFET system for in vivo dosimetry in a radiotherapy department. *British Journal of Radiology,* 85 (1012), 451-457.

Low, D. A., Harms, W. B., Mutic, S. & Purdy, J. A. 1998. A technique for the quantitative evaluation of dose distributions. *Medical Physics,* 25 (5), 656-661.

Mackay, R. I. & Williams, P. C. 2009. The cost effectiveness of in vivo dosimetry is not proven. *British Journal of Radiology,* 82 (976), 265-266.

Mans, A., Remeijer, P., Olaciregui-Ruiz, I., Wendling, M., Sonke, J. J., Mijnheer, B., Van Herk, M. & Stroom, J. C. 2010a. 3D dosimetric verification of volumetric-modulated arc therapy by portal dosimetry. *Radiotherapy and Oncology,* 94 (2), 181-187.

Mans, A., Wendling, M., Mcdermott, L. N., Sonke, J. J., Tielenburg, R., Vijlbrief, R., Mijnheer, B., Van Herk, M. & Stroom, J. C. 2010b. Catching errors with in vivo EPID dosimetry. *Medical Physics,* 37 (6), 2638-2644.

Martens, C., Claeys, I., De Wagter, C. & De Neve, W. 2002. The value of radiographic film for the characterization of intensity-modulated beams. *Physics in Medicine and Biology,* 47 (13), 2221-2234.

Mayneord, W. V. & Lamerton, L. F. 1941. A survey of depth dose data. *British Journal of Radiology,* 14 (164), 255-264.

Mccowan, P. M., Rickey, D. W., Rowshanfarzad, P., Greer, P. B., Ansbacher, W. & Mccurdy, B. M. 2014. An investigation of gantry angle data accuracy for cine-mode EPID images acquired during arc IMRT. *Journal of Applied Clinical Medical Physics,* 15 (1), 187-201.

Mccurdy, B. M. C., Luchka, K. & Pistorius, S. 2001. Dosimetric investigation and portal dose image prediction using an amorphous silicon electronic portal imaging device. *Medical Physics,* 28 (6), 911-924.

Mccurdy, B. M. C. & Pistorius, S. 2000. A two-step algorithm for predicting portal dose images in arbitrary detectors. *Medical Physics,* 27 (9), 2109-2116.

Mcdermott, L. N., Louwe, R. J. W., Sonke, J. J., Van Herk, M. B. & Mijnheer, B. J. 2004. Dose-response and ghosting effects of an amorphous silicon electronic portal imaging device. *Medical Physics,* 31 (2), 285-295.

Mcdermott, L. N., Nijsten, S. M. J. J. G., Sonke, J. J., Partridge, M., Van Herk, M. & Mijnheer, B. J. 2006a. Comparison of ghosting effects for three commercial a-Si EPIDs. *Medical Physics,* 33 (7), 2448-2451.

Mcdermott, L. N., Wendling, M., Nijkamp, J., Mans, A., Sonke, J. J., Mijnheer, B. J. & Van Herk, M. 2008. 3D in vivo dose verification of entire hypo-fractionated IMRT treatments using an EPID and cone-beam CT. *Radiotherapy and Oncology,* 86 (1), 35-42.

Mcdermott, L. N., Wendling, M., Sonke, J. J., Van Herk, M. & Mijnheer, B. J. 2007. Replacing pretreatment verification with in vivo EPID dosimetry for prostate IMRT. *International Journal of Radiation Oncology Biology Physics,* 67 (5), 1568-1577.

Mcdermott, L. N., Wendling, M., Van Asselen, B., Stroom, J., Sonke, J. J., Van Herk, M. & Mijnheer, B. J. 2006b. Clinical experience with EPID dosimetry for prostate IMRT pre-treatment dose verification. *Medical Physics,* 33 (10), 3921-3930.

Meertens, H., Van Herk, M. & Weeda, J. 1985. A liquid ionisation detector for digital radiography of therapeutic megavoltage photon beams. *Physics in Medicine and Biology,* 30 (4), 313-321.

Mijnheer, B., Beddar, S., Izewska, J. & Reft, C. 2013. In vivo dosimetry in external beam radiotherapy. *Medical Physics,* 40 (7), 0709031-07090319.

Mijnheer, B. & Georg, D. 2008. *Guidelines for the verification of IMRT,* 1st edition. Brussels, Belgium, European Society for Radiotherapy and Oncology, ESTRO.

Mijnheer, B., Mans, A., Olaciregui-Ruiz, I., Sonke, J. J., Tielenburg, R., Van Herk, M., Vijlbrief, R. & Stroom, J. 2010. 2D and 3D dose verification at The Netherlands Cancer Institute-Antoni van Leeuwenhoek Hospital using EPIDs. *Journal of Physics: Conference Series,* 250 (1), 0120201-0120206, http://iopscience.iop.org/article/10.1088/1742-6596/250/1/012020/meta [Accessed 1 December 2011].

Molineu, A., Followill, D. S., Balter, P. A., Hanson, W. F., Gillin, M. T., Huq, M. S., Eisbruch, A. & Ibbott, G. S. 2005. Design and implementation of an

anthropomorphic quality assurance phantom for intensity-modulated radiation therapy for the Radiation Therapy Oncology Group. *International Journal of Radiation Oncology Biology Physics,* 63 (2), 577-583.

Monti, A. F., Ostinelli, A., Frigerio, M. & Gelosa, S. 1995. An equivalent square method for irregular photon fields. *Medical Dosimetry,* 20 (4), 275-277.

Moran, J. M., Dempsey, M., Eisbruch, A., Fraass, B. A., Galvin, J. M., Ibbott, G. S. & Marks, L. B. 2011. Safety considerations for IMRT: Executive summary. *Medical Physics,* 38 (9), 5067-5072.

Morton, E. J., Swindell, W., Lewis, D. G. & Evans, P. M. 1991. A linear array, scintillation crystal-photodiode detector for megavoltage imaging. *Medical Physics,* 18 (4), 681-691.

Munro, A. J. 2007. Hidden danger, obvious opportunity: Error and risk in the management of cancer. *British Journal of Radiology,* 80 (960), 955-966.

Nelms, B. E., Rasmussen, K. H. & Tome, W. A. 2010. Evaluation of a fast method of EPID-based dosimetry for intensity-modulated radiation therapy. *Journal of Applied Clinical Medical Physics,* 11 (2), 140-157.

Nelms, B. E., Zhen, H. & Toḿ, W. A. 2011. Per-beam, planar IMRT QA passing rates do not predict clinically relevant patient dose errors. *Medical Physics,* 38 (2), 1037-1044.

Nicolini, G., Clivio, A., Vanetti, E., Tomatis, S., Reggiori, G., Cozzi, L. & Fogliata, A. 2015. Dosimetric testing of the new aS1200 MV imager with FF and FFF beams. *Radiotherapy and Oncology,* 115 (Supplement 1), S439, http://www.sciencedirect.com/science/article/pii/S0167814015408552 [Accessed 14 May 2015].

Nicolini, G., Fogliata, A., Vanetti, E., Clivio, A. & Cozzi, L. 2006. GLAaS: An absolute dose calibration algorithm for an amorphous silicon portal imager. Applications to IMRT verifications. *Medical Physics,* 33 (8), 2839-2851.

Nijsten, S. M. J. J. G., Van Elmpt, W. J. C., Jacobs, M., Mijnheer, B. J., Dekker, A. L. a. J., Lambin, P. & Minken, A. W. H. 2007. A global calibration model for a-Si EPIDs used for transit dosimetry. *Medical Physics,* 34 (10), 3872-3884.

Nilsson, B., Rudén, B. I. & Sorcini, B. 1988. Characteristics of silicon diodes as patient dosemeters in external radiation therapy. *Radiotherapy and Oncology,* 11 (3), 279-288.

Niroomand-Rad, A., Blackwell, C. R., Coursey, B. M., Gall, K. P., Galvin, J. M., Mclaughlin, W. L., Meigooni, A. S., Nath, R., Rodgers, J. E. & Soares, C. G. 1998. Radiochromic film dosimetry: Recommendations of AAPM radiation therapy committee Task Group 55. *Medical Physics,* 25 (11), 2093-2115.

Nyc Department of Health and Mental Hygiene 2005. *ORH information notice 2005-01,* New York, NY, Office of Radiological Health, NYC Department of Health and Mental Hygiene.

Olaciregui-Ruiz, I., Rozendaal, R., Mijnheer, B., Van Herk, M. & Mans, A. 2013. Automatic in vivo portal dosimetry of all treatments. *Physics in Medicine and Biology,* 58 (22), 8253-8264.

Oldham, M., Thomas, A., O'daniel, J., Juang, T., Ibbott, G., Adamovics, J. & Kirkpatrick, J. P. 2012. A quality assurance method that utilizes 3D dosimetry and facilitates clinical interpretation. *International Journal of Radiation Oncology Biology Physics,* 84 (2), 540-546.

Oldham, M. & Webb, S. 1997. Intensity-modulated radiotherapy by means of static tomotherapy: A planning and verification study. *Medical Physics,* 24 (6), 827-836.

Orton, C. G. 2007. 17: Fractionation: Radiobiologic principles and clinical practice, In: Khan, F. M. (ed.) *Treatment planning in radiation oncology,* 2nd edition. Philadelphia, PA, USA, Lippincott Williams & Wilkins.

Paelinck, L., De Neve, W. & De Wagter, C. 2007. Precautions and strategies in using a commercial flatbed scanner for radiochromic film dosimetry. *Physics in Medicine and Biology,* 52 (1), 231-242.

Pai, S., Das, I. J., Dempsey, J. F., Lam, K. L., Losasso, T. J., Olch, A. J., Palta, J. R., Reinstein, L. E., Ritt, D. & Wilcox, E. E. 2007. TG-69: Radiographic film for megavoltage beam dosimetry. *Medical Physics,* 34 (6), 2228-2258.

Palm, Å. & Losasso, T. 2005. Influence of phantom material and phantom size on radiographic film response in therapy photon beams. *Medical Physics,* 32 (8), 2434-2442.

Parent, L., Fielding, A. L., Dance, D. R., Seco, J. & Evans, P. M. 2007. Amorphous silicon EPID calibration for dosimetric applications: Comparison of a method based on Monte Carlo prediction of response with existing techniques. *Physics in Medicine and Biology,* 52 (12), 3351-3368.

Parent, L., Seco, J., Evans, P. M., Fielding, A. & Dance, D. R. 2006. Monte Carlo modelling of a-Si EPID response: The effect of spectral variations with field size and position. *Medical Physics,* 33 (12), 4527-4540.

Parsaei, H., El-Khatib, E. & Rajapakshe, R. 1998. The use of an electronic portal imaging system to measure portal dose and portal dose profiles. *Medical Physics,* 25 (10), 1903-1909.

Partridge, M., Evans, P. M. & Symonds-Tayler, J. R. N. 1999. Optical scattering in camera-based electronic portal imaging. *Physics in Medicine and Biology,* 44 (10), 2381-2396.

Pasma, K. L., Kroonwijk, M., De Boer, J. C. J., Visser, A. G. & Heijmen, B. J. M. 1998. Accurate portal dose measurement with a fluoroscopic electronic portal imaging device (EPID) for open and wedged beams and dynamic multileaf collimation. *Physics in Medicine and Biology,* 43 (8), 2047-2060.

Patient Safety in Radiotherapy Steering Group 2010. *Patient safety in radiotherapy steering group activity (November 2007 - March 2010)* Oxfordshire, Health Protection Agency Centre for Radiation, Chemical and Environmental Hazards.

Patient Safety in Radiotherapy Steering Group 2012. *Data report on radiotherapy errors and near misses (December 2009 - November 2011),* Oxfordshire, Health Protection Agency Centre for Radiation, Chemical and Environmental Hazards.

Patient Safety in Radiotherapy Steering Group 2014. *Data report on radiotherapy errors and near misses (December 2011 - November 2013),* Oxfordshire, Health Protection Agency Centre for Radiation, Chemical and Environmental Hazards.

Pawlicki, T., Yoo, S., Court, L. E., Mcmillan, S. K., Rice, R. K., Russell, J. D., Pacyniak, J. M., Woo, M. K., Basran, P. S., Shoales, J. & Boyer, A. L. 2009. Moving from IMRT QA measurements toward independent computer calculations using control charts. *Radiotherapy and Oncology,* 89 (3), 330-337.

Peca, S. & Brown, D. W. 2014. Two-dimensional in vivo dose verification using portal imaging and correlation ratios. *Journal of Applied Clinical Medical Physics,* 15 (4), 117-128.

Piermattei, A., Fidanzio, A., Azario, L., Grimaldi, L., D'onofrio, G., Cilla, S., Stimato, G., Gaudino, D., Ramella, S., D'angelillo, R., Cellini, F., Trodella, L., Russo, A., Iadanza, L., Zucca, S., Fusco, V., Di Napoli, N., Gambacorta, M. A., Balducci, M., Cellini, N., Deodato, F., Macchia, G. & Morganti, A. G. 2007. Application of a practical method for the isocenter point in vivo dosimetry by a transit signal. *Physics in Medicine and Biology,* 52 (16), 5101-5117.

Piermattei, A., Fidanzio, A., Stimato, G., Azario, L., Grimaldi, L., D'onofrio, G., Cilla, S., Balducci, M., Gambacorta, M. A., Di Napoli, N. & Cellini, N. 2006. In vivo dosimetry by an aSi-based EPID. *Medical Physics,* 33 (11), 4414-4422.

Piermattei, A., Greco, F., Azario, L., Porcelli, A., Cilla, S., Zucca, S., Russo, A., Castro, E. D., Russo, M., Caivano, R., Fusco, V., Morganti, A. & Fidanzio, A. 2012. A national project for in vivo dosimetry procedures in radiotherapy: First results. *Nuclear Instruments and Methods in Physics Research Section B: Beam Interactions with Materials and Atoms,* 274 42-50.

Podgorsak, E. B. 2005. Chapter 1: Basic radiation physics, In: Podgorsak, E. B. (ed.) *Radiation oncology physics: A handbook for teachers and students,* Vienna, International Atomic Energy Agency.

Ramaseshan, R., Kohli, K. S., Zhang, T. J., Lam, T., Norlinger, B., Hallil, A. & Islam, M. 2004. Performance characteristics of a microMOSFET as an in vivo dosimeter in radiation therapy. *Physics in Medicine and Biology,* 49 (17), 4031-4048.

Ramsey, C., Dube, S. & Hendee, W. R. 2003. It is necessary to validate each individual IMRT treatment plan before delivery. *Medical Physics,* 30 (9), 2271-2273.

Rangaraj, D., Zhu, M., Yang, D., Palaniswaamy, G., Yaddanapudi, S., Wooten, O. H., Brame, S. & Mutic, S. 2013. Catching errors with patient-specific pretreatment machine log file analysis. *Practical Radiation Oncology,* 3 (2), 80-90.

Reft, C. S. 2009. The energy dependence and dose response of a commercial optically stimulated luminescent detector for kilovoltage photon,

megavoltage photon, and electron, proton, and carbon beams. *Medical Physics,* 36 (5), 1690-1699.

Reinhardt, S., Hillbrand, M., Wilkens, J. J. & Assmann, W. 2012. Comparison of Gafchromic EBT2 and EBT3 films for clinical photon and proton beams. *Medical Physics,* 39 (8), 5257-5262.

Renner, W. D., Norton, K. & Holmes, T. 2005. A method for deconvolution of integrated electronic portal images to obtain incident fluence for dose reconstruction. *Journal of Applied Clinical Medical Physics,* 6 (4), 22-39.

Richter, A., Hu, Q., Steglich, D., Baier, K., Wilbert, J., Guckenberger, M. & Flentje, M. 2008. Investigation of the usability of conebeam CT data sets for dose calculation. *Radiation Oncology,* 3 (42), 1-13.

Robar, J. L. & Clark, B. G. 1999. The use of radiographic film for linear accelerator stereotactic radiosurgical dosimetry. *Medical Physics,* 26 (10), 2144-2150.

Rosca, F. & Zygmanski, P. 2008. An EPID response calculation algorithm using spatial beam characteristics of primary, head scattered and MLC transmitted radiation. *Medical Physics,* 35 (6), 2224-2234.

Rosenwald, J. C., Rosenberg, I. & Shentall, G. 2007. Chapter 26: Patient dose computation for photon beams, In: Mayles, P., Nahum, A. & Rosenwald, J. C. (eds.) *Handbook of Radiotherapy Physics: Theory and practice,* Florida, USA, Taylor & Francis Group, LLC.

Rowbottom, C. G. & Jaffray, D. A. 2004. Characteristics and performance of a micro-MOSFET: An "imageable" dosimeter for image-guided radiotherapy. *Medical Physics,* 31 (3), 609-615.

Rowshanfarzad, P., Mccurdy, B. M. C., Sabet, M., Lee, C., O'connor, D. J. & Greer, P. B. 2010. Measurement and modeling of the effect of support arm backscatter on dosimetry with a Varian EPID. *Medical Physics,* 37 (5), 2269-2278.

Rowshanfarzad, P., Sabet, M., O'connor, D. J., Mccowan, P. M., Mccurdy, B. M. C. & Greer, P. B. 2012. Detection and correction for EPID and gantry sag during arc delivery using cine EPID imaging. *Medical Physics,* 39 (2), 623-635.

Rozendaal, R., Spreeuw, H., Mijnheer, B., Mans, A., Gonzalez, P., Olaciregui-Ruiz, I. & Van Herk, M. 2015. Hot-spot analysis for incident detection in real-time 3D EPID-based in vivo dosimetry. *Radiotherapy and Oncology,* 115 (Supplement 1), S427-S428, http://www.sciencedirect.com/science/article/pii/S0167814015408357 [Accessed 14 May 2015].

Sabet, M., Rowshanfarzad, P., Menk, F. W. & Greer, P. B. 2014. Transit dosimetry in dynamic IMRT with an a-Si EPID. *Medical and Biological Engineering and Computing,* 52 (7), 579-588.

Saini, A. S. & Zhu, T. C. 2004. Dose rate and SDD dependence of commercially available diode detectors. *Medical Physics,* 31 (4), 914-924.

Sánchez-Doblado, F., Hartmann, G. H., Pena, J., Capote, R., Paiusco, M., Rhein, B., Leal, A. & Lagares, J. I. 2007. Uncertainty estimation in intensity-modulated radiotherapy absolute dosimetry verification. *International Journal of Radiation Oncology Biology Physics,* 68 (1), 301-310.

Scalchi, P., Francescon, P. & Rajaguru, P. 2005. Characterization of a new MOSFET detector configuration for in vivo skin dosimetry. *Medical Physics,* 32 (6), 1571-1578.

Seco, J., Clasie, B. & Partridge, M. 2014. Review on the characteristics of radiation detectors for dosimetry and imaging. *Physics in Medicine and Biology,* 59 (20), R303-R347.

Shafiq, J., Barton, M., Noble, D., Lemer, C. & Donaldson, L. J. 2009. An international review of patient safety measures in radiotherapy practice. *Radiotherapy and Oncology,* 92 (1), 15-21.

Siebers, J. V., Kim, J. O., Ko, L., Keall, P. J. & Mohan, R. 2004. Monte Carlo computation of dosimetric amorphous silicon electronic portal images. *Medical Physics,* 31 (7), 2135-2146.

Siewerdsen, J. H. & Jaffray, D. A. 1999. A ghost story: Spatio-temporal response characteristics of an indirect-detection flat-panel imager. *Medical Physics,* 26 (8), 1624-1641.

Siochi, R., Huang, Y. & Bayouth, J. 2008. Assessment of an in – house independent phantom dose calculation algorithm for IMRT QA. *Medical Physics,* 35 (6), 2944,

http://scitation.aip.org/content/aapm/journal/medphys/35/6/10.1118/1.2962735 [Accessed 8 October 2014].

Siochi, R. A., Pennington, E. C., Waldron, T. J. & Bayouth, J. E. 2009. Radiation therapy plan checks in a paperless clinic. *Journal of Applied Clinical Medical Physics,* 10 (1), 43-62.

Siochi, R. a. C., Molineu, A. & Orton, C. G. 2013. Patient-specific QA for IMRT should be performed using software rather than hardware methods. *Medical Physics,* 40 (7), 0706011-0706013.

Smith, J. C., Dieterich, S. & Orton, C. G. 2011. It is STILL necessary to validate each individual IMRT treatment plan with dosimetric measurements before delivery. *Medical Physics,* 38 (2), 553-555.

Smith, S. W. 2003. Digital filters, *Digital signal processing: A practical guide for engineers and scientists,* Burlington, MA, USA, Newnes.

Soubra, M., Cygler, J. & Mackay, G. 1994. Evaluation of a dual bias dual metal oxide-silicon semiconductor field effect transistor detector as radiation dosimeter. *Medical Physics,* 21 (4), 567-572.

Stasi, M., Bresciani, S., Miranti, A., Maggio, A., Sapino, V. & Gabriele, P. 2012. Pretreatment patient-specific IMRT quality assurance: A correlation study between gamma index and patient clinical dose volume histogram. *Medical Physics,* 39 (12), 7626-7634.

Steciw, S., Warkentin, B., Rathee, S. & Fallone, B. G. 2005. Three-dimensional IMRT verification with a flat-panel EPID. *Medical Physics,* 32 (2), 600-612.

Swindell, W. 1983. A 4-MV CT scanner for radiation therapy: Spectral properties of the therapy beam. *Medical Physics,* 10 (3), 347-351.

Symonds-Tayler, J. R. N., Partridge, M. & Evans, P. M. 1997. An electronic portal imaging device for transit dosimetry. *Physics in Medicine and Biology,* 42 (11), 2273-2283.

Talamonti, C., Casati, M. & Bucciolini, M. 2006. Pretreatment verification of IMRT absolute dose distributions using a commercial a-Si EPID. *Medical Physics,* 33 (11), 4367-4378.

Tan, Y. I., Metwaly, M., Glegg, M., Baggarley, S. P. & Elliott, A. 2014. Evaluation of six TPS algorithms in computing entrance and exit doses. *Journal of Applied Clinical Medical Physics,* 15 (3), 229-240.

Tatcher, M. 1970. A method for varying the effective angle of wedge filters. *Radiology,* 97 (1), 132.

The Royal College of Radiologists, Society and College of Radiographers, Institute of Physics and Engineering in Medicine, National Patient Safety Agency & British Institute of Radiology 2008. *Towards safer radiotherapy,* London, The Royal College of Radiologists.

Thwaites, D. I., Mijnheer, B. J. & Mills, J. A. 2005. Quality assurance of external beam radiotherapy, In: Podgorsak, E. B. (ed.) *Review of radiation oncology physics: A handbook for teachers and students,* Vienna, Austria, IAEA.

Tielenburg, R., Olaciregui-Ruiz, I., Rozendaal, R., Mijnheer, B. & Van Herk, M. 2015. Derivation of a universal dataset for commissioning of an EPID-based dosimetry system. *Radiotherapy and Oncology,* 115 (Supplement 1), S421-S422, http://www.sciencedirect.com/science/article/pii/S0167814015408266 [Accessed 14 May 2015].

Van Elmpt, W., Mcdermott, L., Nijsten, S., Wendling, M., Lambin, P. & Mijnheer, B. 2008a. A literature review of electronic portal imaging for radiotherapy dosimetry. *Radiotherapy and Oncology,* 88 (3), 289-309.

Van Elmpt, W., Nijsten, S., Mijnheer, B., Dekker, A. & Lambin, P. 2008b. The next step in patient-specific QA: 3D dose verification of conformal and intensity-modulated RT based on EPID dosimetry and Monte Carlo dose calculations. *Radiotherapy and Oncology,* 86 (1), 86-92.

Van Elmpt, W. J. C., Nijsten, S. M. J. J. G., Dekker, A. L. a. J., Mijnheer, B. J. & Lambin, P. 2007. Treatment verification in the presence of inhomogeneities using EPID-based three-dimensional dose reconstruction. *Medical Physics,* 34 (7), 2816-2826.

Van Elmpt, W. J. C., Nijsten, S. M. J. J. G., Schiffeleers, R. F. H., Dekker, A. L. a. J., Mijnheer, B. J., Lambin, P. & Minken, A. W. H. 2006. A Monte Carlo based three-dimensional dose reconstruction method derived from portal dose images. *Medical Physics,* 33 (7), 2426-2434.

Van Esch, A., Depuydt, T. & Huyskens, D. P. 2004. The use of an aSi-based EPID for routine absolute dosimetric pre-treatment verification of dynamic IMRT fields. *Radiotherapy and Oncology,* 71 (2), 223-234.

Van Esch, A., Tillikainen, L., Pyykkonen, J., Tenhunen, M., Helminen, H., Siljamaki, S., Alakuijala, J., Paiusco, M., Iori, M. & Huyskens, D. P. 2006. Testing of the analytical anisotropic algorithm for photon dose calculation. *Medical Physics,* 33 (11), 4130-4148.

Van Esch, A., Vanstraelen, B., Verstraete, J., Kutcher, G. & Huyskens, D. 2001. Pre-treatment dosimetric verification by means of a liquid-filled electronic portal imaging device during dynamic delivery of intensity modulated treatment fields. *Radiotherapy and Oncology,* 60 (2), 181-190.

Van Herk, M. 1991. Physical aspects of a liquid-filled ionization chamber with pulsed polarizing voltage. *Medical Physics,* 18 (4), 692-702.

Van Herk, M. & Meertens, H. 1988. A matrix ionisation chamber imaging device for on-line patient setup verification during radiotherapy. *Radiotherapy and Oncology,* 11 (4), 369-378.

Varian Medical Systems 2008. *Dose calculation with PBC algorithm*, Varian Medical Systems, Inc.

Vial, P., Gustafsson, H., Oliver, L., Baldock, C. & Greer, P. B. 2009. Direct-detection EPID dosimetry: Investigation of a potential clinical configuration for IMRT verification. *Physics in Medicine and Biology,* 54 (23), 7151-7169.

Visser, A. G., Huizenga, H., Althof, V. G. M. & Swanenburg, B. N. 1990. Performance of a prototype fluoroscopic radiotherapy imaging system. *International Journal of Radiation Oncology Biology Physics,* 18 (1), 43-50.

Warkentin, B., Steciw, S., Rathee, S. & Fallone, B. G. 2003. Dosimetric IMRT verification with a flat-panel EPID. *Medical Physics,* 30 (12), 3143-3155.

Wendling, M., Louwe, R. J. W., Mcdermott, L. N., Sonke, J. J., Van Herk, M. & Mijnheer, B. J. 2006. Accurate two-dimensional IMRT verification using a back-projection EPID dosimetry method. *Medical Physics,* 33 (2), 259-273.

Wendling, M., Mcdermott, L. N., Mans, A., Olaciregui-Ruiz, I., Pecharroman-Gallego, R., Sonke, J. J., Stroom, J., Van Herk, M. & Mijnheer, B. J. 2012. In aqua vivo EPID dosimetry. *Medical Physics,* 39 (1), 367-377.

Wendling, M., Mcdermott, L. N., Mans, A., Sonke, J. J., Van Herk, M. & Mijnheer, B. J. 2009. A simple backprojection algorithm for 3D in vivo EPID dosimetry of IMRT treatments. *Medical Physics,* 36 (7), 3310-3321.

Williams, J. R., Bradnam, M. S., Mccurrach, G. M., Deehan, C. & Johnston, S. 1991. A system for the quality audit of treatment dose delivery in radiotherapy. *Radiotherapy and Oncology,* 20 (3), 197-202.

Williams, M. V. & Mckenzie, A. 2008. Can we afford not to implement in vivo dosimetry? *British Journal of Radiology,* 81 (969), 681-684.

Winkler, P. & Georg, D. 2006. An intercomparison of 11 amorphous silicon EPIDs of the same type: Implications for portal dosimetry. *Physics in Medicine and Biology,* 51 (17), 4189-4200.

Winkler, P., Hefner, A. & Georg, D. 2005. Dose-response characteristics of an amorphous silicon EPID. *Medical Physics,* 32 (10), 3095-3105.

Woodruff, H. C., Fuangrod, T., Rowshanfarzad, P., Mccurdy, B. M. C. & Greer, P. B. 2013. Gantry-angle resolved VMAT pretreatment verification using EPID image prediction. *Medical Physics,* 40 (8), 0817151-0817159.

Yang, Y., Schreibmann, E., Li, T., Wang, C. & Xing, L. 2007. Evaluation of on-board kV cone beam CT (CBCT)-based dose calculation. *Physics in Medicine and Biology,* 52 (3), 685-705.

Yeo, I. J., Beiki-Ardakani, A., Cho, Y. B., Heydarian, M., Zhang, T. & Islam, M. 2004. EDR2 film dosimetry for IMRT verification using low-energy photon filters. *Medical Physics,* 31 (7), 1960-1963.

Yin, F. F., Schell, M. C. & Rubin, P. 1994. Input/output characteristics of a matrix ion-chamber electronic portal imaging device. *Medical Physics,* 21 (9), 1447-1454.

Yoo, S. & Yin, F.-F. 2006. Dosimetric feasibility of cone-beam CT-based treatment planning compared to CT-based treatment planning. *International Journal of Radiation Oncology Biology Physics,* 66 (5), 1553-1561.

Yukihara, E. G., Mardirossian, G., Mirzasadeghi, M., Guduru, S. & Ahmad, S. 2008. Evaluation of Al2O3: C optically stimulated luminescence (OSL)

dosimeters for passive dosimetry of high-energy photon and electron beams in radiotherapy. *Medical Physics,* 35 (1), 260-269.

Zhen, H. M., Nelms, B. E. & Tomeacute, W. A. 2011. Moving from gamma passing rates to patient DVH-based QA metrics in pretreatment dose QA. *Medical Physics,* 38 (10), 5477-5489.

Zhu, J., Chen, L., Chen, A., Luo, G., Deng, X. & Liu, X. 2015. Fast 3D dosimetric verifications based on an electronic portal imaging device using a GPU calculation engine. *Radiation Oncology,* 10 (85), 1-11.

Zhu, Y., Jiang, X. Q. & Van Dyk, J. 1995. Portal dosimetry using a liquid ion chamber matrix: Dose response studies. *Medical Physics,* 22 (7), 1101-1106.

Zhu, Y., Kirov, A. S., Mishra, V., Meigooni, A. S. & Williamson, J. F. 1997. Quantitative evaluation of radiochromic film response for two-dimensional dosimetry. *Medical Physics,* 24 (2), 223-231.

Zwicker, R. D., Shahabi, S., Wu, A. & Sternick, E. S. 1985. Effective wedge angles for 6-MV wedges. *Medical Physics,* 12 (3), 347-349.